

NATIONAL INSTITUTE FOR FUSION SCIENCE

平成 11 年度核融合科学研究所共同研究 研究会
「プラズマ閉じ込めに関連する数値計算手法の研究」
Proceeding of 1999-Workshop on MHD Computations
"Study on Numerical Methods Related to Plasma Confinement"

研究代表者 加古 孝 (電気通信大学)
所内世話人 渡辺 二太
Ed. by T. Kako and T. Watanabe
(Received - June 6, 2000)

NIFS-PROC-46

June 2000

This report was prepared as a preprint of work performed as a collaboration research of the National Institute for Fusion Science (NIFS) of Japan. This document is intended for information only and for future publication in a journal after some rearrangements of its contents.

Inquiries about copyright and reproduction should be addressed to the Research Information Center, National Institute for Fusion Science, Oroshi-cho, Toki-shi, Gifu-ken 509-5292 Japan.

RESEARCH REPORT
NIFS-PROC Series

Proceeding of 1999-Workshop on MHD Computations
“Study on Numerical Methods related to Plasma Confinement”

Edited by T. Kako and T. Watanabe

November 8 – 10, 1999
National Institute for Fusion Science
Toki, Japan

Abstract

This is the proceeding of “ Study on Numerical Methods related to Plasma Confinement ” held in National Institute for Fusion Science. In this workshop, theoretical and numerical analyses of possible plasma equilibria with their stability properties are presented. There are also various lectures on mathematical as well as numerical analyses related to the computational methods for fluid dynamics and plasma physics.

Key Words: magnetohydrodynamics, MHD, plasma confinement, equilibrium, stability analysis, helical system, resistive plasma, magnetic reconnection, charge simulation method, neural networks, Newmark’s method, Lyapunov exponent, HTS plate, FEM-FSM combined method

研究代表者 加古 孝（電気通信大学） 所内世話人 渡辺二太

平成 11 年度 核融合科学研究所共同研究〔研究会〕

「プラズマ閉じ込めに関連する数値計算手法の研究」

T. Kako and T. Watanabe (Eds.)

Proceeding of 1999-Workshop on MHD Computations

“Study on Numerical Methods related to Plasma Confinement”

Nov. 1999

Preface

This volume contains 19 papers contributed at the 1999-Workshop on MHD Computations held in Toki, November 8-10, 1999. This workshop was held as one of the collaboration research projects of the National Institute of Fusion Sciences (NIFS). This is also the continuation of the workshop activity on numerical computations related to the thermonuclear fusion research that has been continued for more than eighteen years by researchers in plasma physics and applied mathematics.

The purpose of this workshop is to study various possible plasma behaviors and its controllability in fusion research focused on LHD device in NIFS. The main basic mathematical model treated in the workshop was Magneto-Hydro-dynamics (MHD). There were also several lectures related to various mathematical models of plasma such as kinematic models and particle simulations.

There were more than 30 participants in the workshop, and we had 19 contributed talks under the following themes: 1) Study of plasma equilibria and its stability analysis for helical system; 2) Study of various resistive effect in plasma behavior; 3) Proposal of new numerical methods and simulation techniques related to fluid dynamics and electromagnetism.

Organizers

IMAI, Hitoshi (Tokushima University, Tokushima, Tokushima 770)

USHIJIMA, Teruo (Univ. Electro-Communications., Chofu, Tokyo 182-8585)

KAKO, Takashi (University of Electro-Communications., Chofu, Tokyo 182-8585)

TANABE, Kunio (Institute of Statistical Mathematics, Minato-ku, Tokyo 106)

TODOROKI, Jiro (National Institute for Fusion Science, Toki, Gifu 509-5292)

HAMADA, Shigeo (Nihon University, Chiyoda-ku, Tokyo 101)

WAKATANI, Masahiro (Kyoto University, Uji, Kyoto 611)

WATANABE, Tsuguhiro (National Inst. for Fusion Science, Toki, Gifu 509-5292)

Contents

Analytical model of LHD divertor plasma T. Watanabe, Y. Matsumoto and S. Oikawa	1
Construction of generalized magnetic coordinates by B-spline expansion M. Kurata and J. Todoroki	11
On numerical computation of Lyapunov exponent of attractors in free boundary problems H. Imai, T. Takeuchi, S.S. Shanta and N. Ishimura	21
MHD stability analysis of herical system plasmas Y. Nakamura	30
New applications of neural networks for computational sciences T. Takeda, X.-F. Ma, A. Liaqat and M. Fukuhara	40
A new scheme for MHD stability analysis S. Tokuda, T. Watanabe and A. Ishizawa	54
Influence of numerical integration on convergence of eigenvalues in the MHD stability analysis A. Ida, J. Todoroki and H. Sanuki	64
Effect of linear shear flow on interchange modes T. Tatsuno, F. Volponi and Z. Yoshida	72
Comparison of shear flow formation between resonant and non-resonant resistive interchange type modes T. Unemura, S. Hamaguchi and M. Wakatani	82
Gyro-kinetic simulation of self-generated radial electric field induced by kinetic $m=1$ internal kink mode T. Matsumoto, S. Tokuda, Y. Kishimoto and H. Naitou	90
MHD simulation study of compact toroid injection into magnetized plasmas Y. Suzuki, T. Hayashi and Y. Kishimoto	98
Nonlinear density wave theory for the spiral structure of galaxies S. Kondoh, R. Teramoto and Z. Yoshida	104
Investigation on application of multigrid method to MHD equilibrium analysis S. Ikuno	114

Error analysis of Newmark's method for the second order equation with inhomogeneous term	
F. Chiba and T. Kako	120
Numerical conformal mapping by the charge simulation method	
K. Amano, D. Okano and H. Ogata	130
Forced magnetic reconnection due to boundary perturbation	
A. Ishizawa and S. Tokuda	137
Frequency dependence of magnetic shielding performance of HTS plates in mixed states	
A. Kamitani and T. Yokono	147
On the structure of numerical solutions of flow simulation by implicit scheme	
I. Hataue	151
On FEM-FSM combined method applied to 2D exterior Laplace and Helmholtz problems	
T. Ushijima	165

List of Participants

Amano, Kaname	Ehime University
Chiba, Fumihiro	The University of Electro-Communications
Hamada, Shigeo	Nihon University
Hataue, Itaru	Kumamoto University
Ida, Akihiro	Nagoya University
Ikuno, Soichiro	Tokyo University of Technology
Imai, Hitoshi	Tokushima University
Ishizawa, Akihiro	Japan Atomic Energy Research Institute
Kako, Takashi	The University of Electro-Communications
Kamitani, Atsushi	Yamagata University
Kondoh, Shigeo	The University of Tokyo
Kurata, Michinari	Nagoya University
Masuda, Shigeru	The University of Electro-Communications
Matsumoto, Taro	Japan Atomic Energy Research Institute
Nakajima, Noriyoshi	National Institute for Fusion Science
Nakajima, Satoshi	Nagoya University
Nakamura, Yuji	Kyoto University
Nakazawa, Shinji	National Institute for Fusion Science
Numata, Ryusuke	The University of Tokyo
Okamura, Shoichi	National Institute for Fusion Science

Sanuki, Heiji	National Institute for Fusion Science
Suzuki, Yasuhiro	Kyoto University
Suzuki Yoshio	Japan Atomic Energy Research Institute
Takaku, Yuichi	Nihon University
Takeda, Tatsuoki	The University of Electro-Communications
Tatsuno, Tomoya	The University of Tokyo
Todoroki, Jiro	National Institute for Fusion Science
Unemura, Takeshi	Kyoto University
Ushijima, Teruo	The University of Electro-Communications
Wakatani, Masahiro	Kyoto University
Watanabe, Tsuguhiro	National Institute for Fusion Science
Yamagishi, Osamu	Kyoto University
Yamamoto, Satoshi	National Institute for Fusion Science

Analytical Model of LHD Divertor Plasma

Tsuguhiro WATANABE

National Institute for Fusion Science,

Oroshicho, Toki, 509-5292 JAPAN

TEL: 81-0572-58-2283 FAX: 81-0572-58-2630 e-mail wata@nifs.ac.jp

Yutaka MATSUMOTO and Shun-ichi OIKAWA

Graduate School of Engineering, Hokkaido University,

Kita-13, Nishi-8, Kitaku, Sapporo, 060-8628, JAPAN

概要

Details of magnetic field structure of LHD are shown. The connection length of divertor field lines are of the order of 10 km. Based on these characteristics of the peripheral magnetic field structure, it is proposed an analytical model for divertor plasma of LHD. Heat flow in chaotic field line region is analyzed and criterion for detached divertor plasma is obtained.

Keywords : LHD, divertor plasma, detached divertor, chaos, fractal, SOL plasma

I 序

「フラクタル上の解析学」[1]と題した講演が日本応用数学会(1999年度年会)で行われた。フラクタル構造をしている幾何学的図形の各辺には抵抗、各頂点はコンデンサーを通して接地する電気回路を想定し、電位の伝播を記述する方程式を導くものであった。さらにこの講演では、携帯電話のアンテナにフラクタル構造の実用化が進んでいることも紹介された。[2] 携帯電話のアンテナに要求される無指向性、広帯域特性には、アンテナが点対称であること、自己相似特性を持つことが要求され、高効率のためには長いアンテナ長が要求される。これらの要求はアンテナがフラクタル形状であることで満たされる。

核融合発電炉の実用化には、炉心から流出するプラズマ熱エネルギーの合理的処理が不可欠である。それには、フラクタル構造をしている磁力線構造を利用する方策があると指摘するのがこの論文の目的である。炉心プラズマの周囲を取り巻く磁力線がフラクタル構造をしているときには、プラズマが容器壁にたどり着くまでの磁力線長(磁力線結合長)が極端に長くなることを利用する。

炉心プラズマ・ダイバータ板間の温度差とその間に流

れる熱流の関係は単純に磁力線長に比例するものではないことを類似の例(導体棒の両端の電位差とその間に流れる電流との関係)で示そう。断面積 S_0 長さ L_0 の導体棒を考えよう。表面は絶縁物で被覆されているとする。棒の両端の電位差 φ と流れる電流 I_0 の間には

$$I_0 = S_0 \sigma \varphi / L_0 \quad (1)$$

の関係が成立する。この棒をたたいて引き延ばし折り曲げるという工程を繰り返そう。その結果断面積が S 長さが L となったとする。棒の物性値(電気伝導度 σ)は普遍であると仮定すると流れる電流 I は

$$I = S \sigma \varphi / L \quad (2)$$

となる。棒の引き延ばし・折り曲げ工程は導体の体積を不変に保つので、

$$S_0 \times L_0 = S \times L \quad (3)$$

が成立する。よって棒の両端の電位差が同一の時は(1,2)より、

$$\frac{I}{I_0} = \left(\frac{L_0}{L} \right)^2 \quad (4)$$

の関係を得る。すなわち棒に流れる電流は棒の全長の二乗に逆比例する。

文部省核融合科学研究所に建設された LHD の磁力線構造については文献 [7] に詳述されている。閉じた磁気面の外側にカオス磁力線領域が存在し、カオス磁力線領域からヒゲ磁力線が伸び、その内の最も外側に位置するものがダイバータ磁力線として真空容器壁に到達する。カオス磁力線領域、ヒゲ磁力線領域では、磁力線の引き延ばし、折り畳み過程が繰り返され、磁力線結合長は十分に長い。すなわち、LHD の炉心プラズマはフラクタル構造の磁力線で取り巻かれていることを示した。これに対して、ヒゲ磁力線間を出発する磁力線の挙動は規則的であり、結合長は短いことを明らかにしている。

LHD は 1998 年 3 月末の放電開始以来、閉じこめプラズマのパラメータを順調に向上させている。エネルギー閉じこめ時間 τ_E は従来の比例則から予測される数値の 1.5 から 2 倍に達している。[3] この LHD プラズマの際だった特徴は周辺プラズマの構造に現れている。

- (1) 接線方向からの可視光 CCD カメラ画像によれば、プラズマへの加熱入力が継続しているときには、磁気面領域内は透明なのに対してカオス磁力線領域内のみが青白い色で発光している。発光部分がカオス磁力線領域内に限定されていることは磁力線追跡結果と発光部分との比較で確認されている。[4] 基底状態にある原子の励起・電離に伴う発光が主体ならば、相対的に低次数エネルギー準位からの発光が多く、赤く光るはずである。LHD の可視光 CCD カメラ画像が赤みを帯びるのは、加熱開始直後の極く短時間と、加熱入力停止後プラズマが崩壊する直前だけである。
- (2) 発光部分の幾何学的構造 (位置、厚み等) は加熱方法、加熱電力には依存していない。磁場強度にも依存していないように見える。また、発光部分の境界

は極めて明瞭で、長時間放電の際にも時間の経過につれて境界が滲むという傾向は見られない。

- (3) ダイバータ板への熱入力は予測を下回るレベルにある。[5]
- (4) ダイバータ板に埋め込まれた静電プローブ計測によれば、周辺プラズマの温度が低い時点ではダイバータプラズマの密度は極めて低く、周辺プラズマの温度上昇と連動してダイバータ板へのプラズマ流入が観測される。[6] このときプローブ信号には強い揺動が存在する。

これらの状況を総合的に理解する理論モデルを組み立てることも目標である。手がかりは特徴 (2) にある。発光を支えているプラズマの形状が磁場を横切る拡散課程支配されているなら時刻の経過とともに滲むはずである。磁場を横切る拡散速度が沿磁力線拡散速度に比べて極端に遅いためほぼ磁力線形状が現れているとするならば両者の比はプラズマの温度・密度あるいは磁場強度等に依存するので、発光プラズマの形状もこれへの依存性が現れはずである。プラズマの形状を支配し、プラズマの温度・密度あるいは磁場強度等に全く無関係な幾何学的要素としては磁力線形状がある。LHD の磁力線の特徴は閉じた磁気面の外側に明瞭なカオス磁力線領域が存在することである。[8][7] カオス磁力線領域は適当な厚みがあり、磁力線結合長 L_{cml} は十分に長い。カオス磁力線構造のみが発光プラズマの形状を決めているとする仮説は特徴 (1) をよく説明する。

第 II 章においては LHD の磁場・磁力線構造の特徴を要約し磁力線結合長の計算例を示す。

第 III 章においては LHD の周辺部プラズマの理論モデルを提案し、LHD において非接触ダイバータプラズマ (detached plasma) を実現する条件を導く。第 IV 章はまとめと議論に当てられる。

II LHD の磁場・磁力線構造

LHD は $\ell = 2$ のヘリカルヘリオトロン磁場方式を用いたプラズマ実験装置である。その磁場構造の特徴は

1. 周辺磁場領域には強い磁気シアが存在すること、
2. ダイバータ磁力線がきれいに畳み込まれていること、
3. トロイダル磁場コイルが存在しないこと、

の 3 点に要約される。これらが LHD プラズマの挙動に深く関わっていることを最初に指摘しておこう。

強い磁気シアが存在する領域では磁場の回転変換 $l/2\pi$ が値を大きく変化させていることを意味するので、必然

的に様々な m, n (整数: ポロイダル方向, トロイダル方向のモード数) の値を持つ有理面、それに伴う磁気島が層状に多数配置することになる。最外殻磁気面の内側領域ではこれらの磁気島は互いに孤立しており、磁気面の整列している層で互いに隔てられている。最外殻磁気面の外側のカオス磁力線領域にも、また、大小さまざまな磁気島が埋め込まれているが数値計算で確認されている。LHD 標準磁場配位の下における比較的大きな磁気島の存在状況を FIG.1 に示す。

ISLANDS OF LINES OF FORCE

M/N = (11/10, 10/10, 9/10, 8/10, 15/20, 7/10, 6/10)

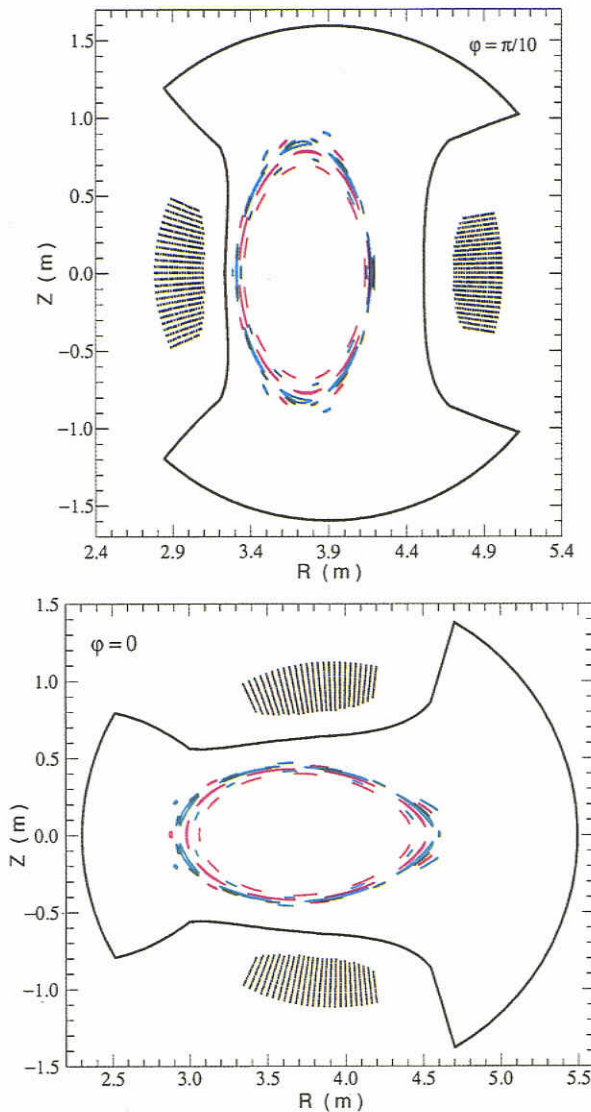


Fig.1 LHD 標準磁場配位における磁気島の配置状況 (磁気面が横長、縦長となる断面 (トロイダル角 $\varphi = 0, \pi/10$) とで示す。磁力線追跡の出発地点を 1mm 単位に動かして最大サイズとなった磁気島が描かれている。ヘリカルコイルと真空容器の断面も示す。

従来トラス型プラズマ閉じこめ装置では、同一磁気面上では密度、温度等は一定となることが前提され、磁気面の垂直方向 (径方向) のみを拡散現象ととらえていた。拡散係数 D は、粒子軌道のステップ幅 Δr と衝突時間 τ を用いて、

$$D = \frac{\langle \Delta r^2 \rangle}{\tau} \quad (5)$$

と評価できることから、粒子軌道のステップ幅を増大させる磁気島の存在は直接的にプラズマ閉じこめ性能の劣化を招くものとされてきた。

これに対して、LHD の周辺部に配置された磁気島は、互いに孤立した関係を維持しながら、多数存在することで、拡散現象との関わり合いには再考が必要であろう。このような状況では拡散現象が進行する空間は次元が縮退していることに相当するからである。LHD の周辺部では局所的に高温となっても、それが直ちに磁気面上に瞬時に広がるということとはなくなり、拡散速度の低下 (プラズマ閉じこめ性能の向上) が期待できる。

LHD 型磁場 (ヘリオトロン型磁場) では、磁場のシアがプラズマの安定に寄与することは従来から指摘されてきた。FIG.1 に示された磁気島の配置を眺めれば、これらの磁気島群は周辺プラズマを安定化させる「タガ」の役割を果たしているように見える。すなわち、LHD 磁場の強い磁気シアは、プラズマ輸送と安定性の面から、周辺プラズマの輸送に深く関わっていると予想される。

強い磁気シアがもたらす大小さまざまな磁気島がカオス磁力線領域に埋め込まれていることは、LHD の磁力線結合長が 10km にも及ぶきわめて長いものとした。磁気シアの存在しない (あるいは弱い) プラズマ閉じこめ配位では、最外殻磁気面外を出発する磁力線は直接真空容器壁へと向かっていくので、磁力線結合長は短い。これに対し、LHD においては真空容器壁に到達するまでには無数の磁気島の間隙を縫っていく必要があるため、磁力線結合長は長いものとなる。LHD の標準磁場配位における磁力線結合長の計算例を FIG.2 に示す。

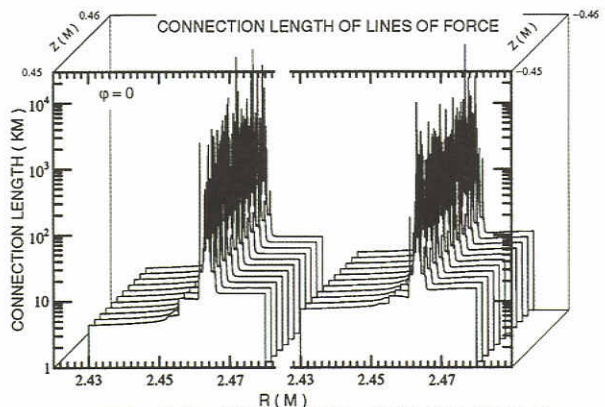


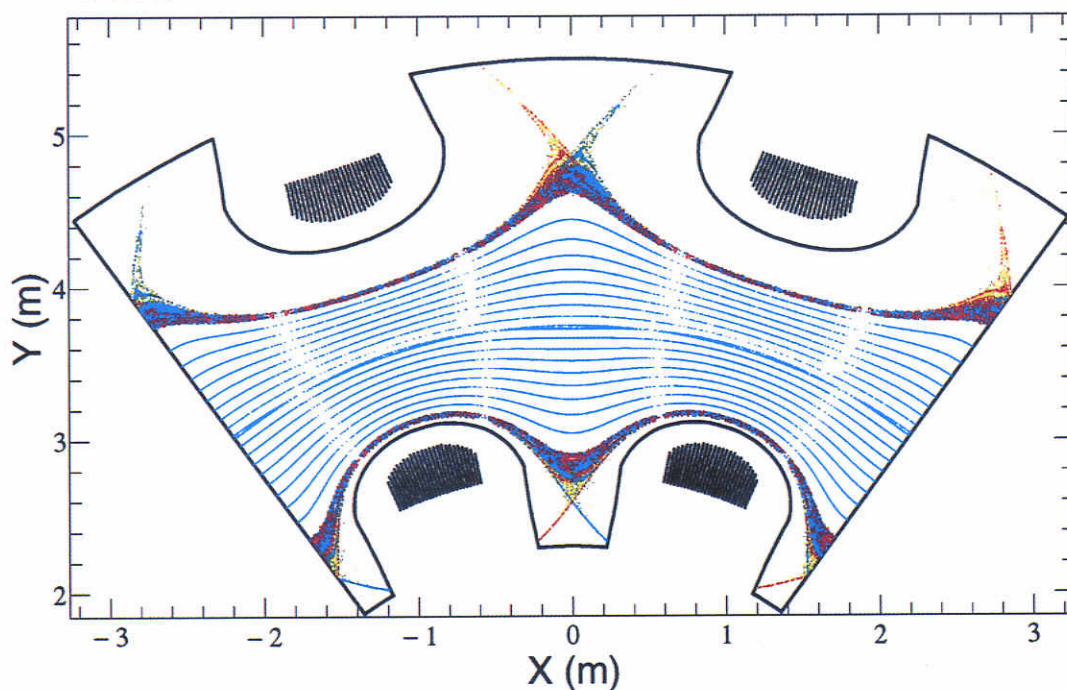
FIG.2 LHD 標準磁場配位における磁力線結合長の計算例。トロイダル角 $\varphi = 0$ の断面におけるダイバータ磁力線終端部 (ただしトラス内側) に磁力線追跡の出発点 (R, Z) を並べたときの真空容器壁に到達するまでの磁力線長を示す。

FIG.3 に LHD における磁力線貫通図を示す。カオス磁力線領域を特定するためには、最外殻磁気面を跨ぐ複数個 (縦長断面で 4 個、横長断面で 4 個の合計 8 個) の長方形領域内部に磁力線追跡の出発地点を稠密に設定した数値計算を行った。磁力線結合長をトラス周回数で表したとき、結合長が 0.36 以下のものはカオス磁力線ではないと判断して作図しない (直接壁に到達する磁力

線と判断する。これによりカオス磁力線領域の外周が定まる)。逆にトーラス周回数が 50 を越える磁力線も、磁気面を形成している磁力線と判断して作図しない(これにより最外殻磁気面とカオス磁力線領域に埋め込まれている比較的大きな磁気島が浮かび上がる)。作図される磁力線結合長の下限を 0.36 と比較的小く設定したのはダイバータ磁力線をよく見えるようにするためである。たとえば作図する磁力線結合長の下限を 1 と設定してもカオス磁力線領域、ダイバータ磁力線の形状はほとんど変わらないのに、ダイバータ磁力線上の貫通点密度

が極端に減少する。ただし磁力線結合長が 0.36 以下のものまで作図すると、ダイバータ磁力線以外に、出発地点から直接壁に到達する磁力線群が現れる。またトーラス周回数の上限を 50 と比較的小く設定したのは計算時間、および作図時間を節約するためである。トーラス周回数の上限を 200 と設定しても最外殻磁気面の形状は変わらない。また、FIG.2 のダイバータ磁力線の結合長を計算したときの磁力線貫通図も FIG.3 のカオス磁力線領域を再現したことを確認している。

POINCARÉ PLOT OF LINES OF FORCE ON EQUITROPICAL PLANE



POINCARÉ PLOT OF LINES OF FORCE

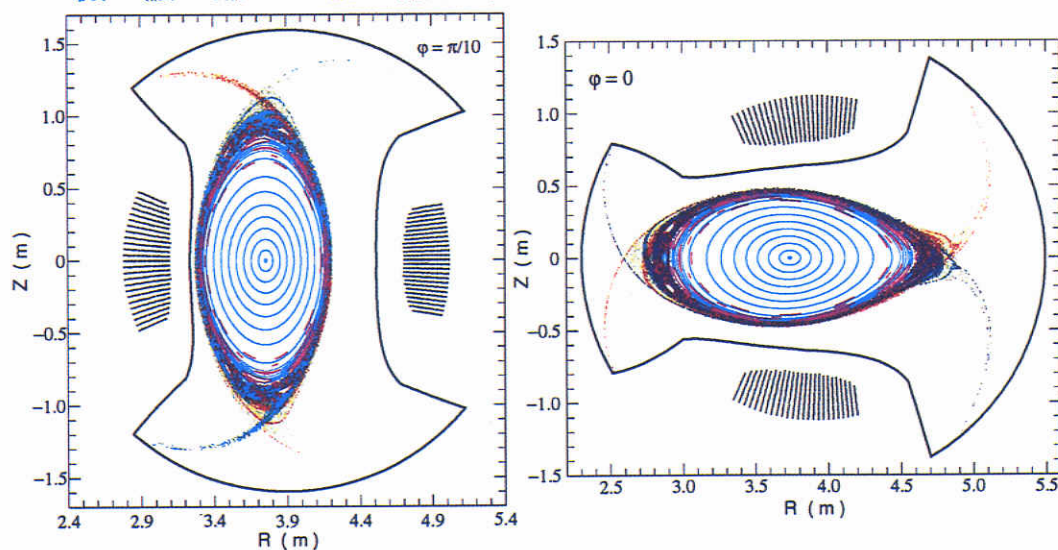
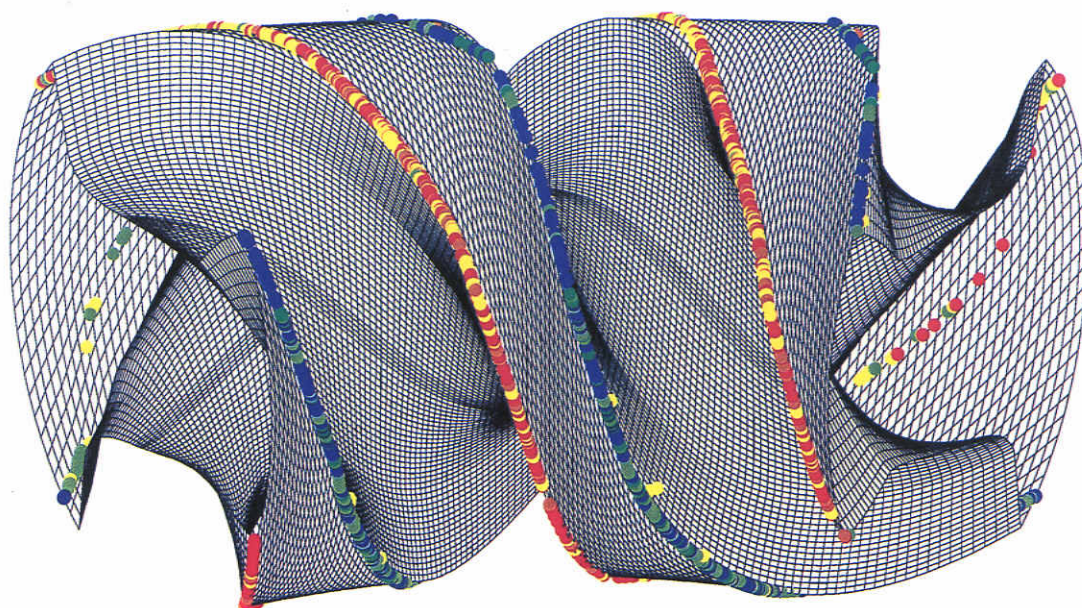




FIG.3 LHD 標準磁場配位における磁力線貫通図。トロイダル角 $\varphi = 0, = \pi/10$ のポロイダル断面、および、 $z = 0$ の赤道面上での磁力線貫通図を示す。カオス磁力線の貫通図は磁力線方向と磁力線結合長とで色分けされている。



DIVERTOR TRACE OF LINES OF FORCE

CNL (TOROIDAL TURNS) :  < -2  < -1  $< -0.36, 0.36 <$  < 1  $2 <$ 

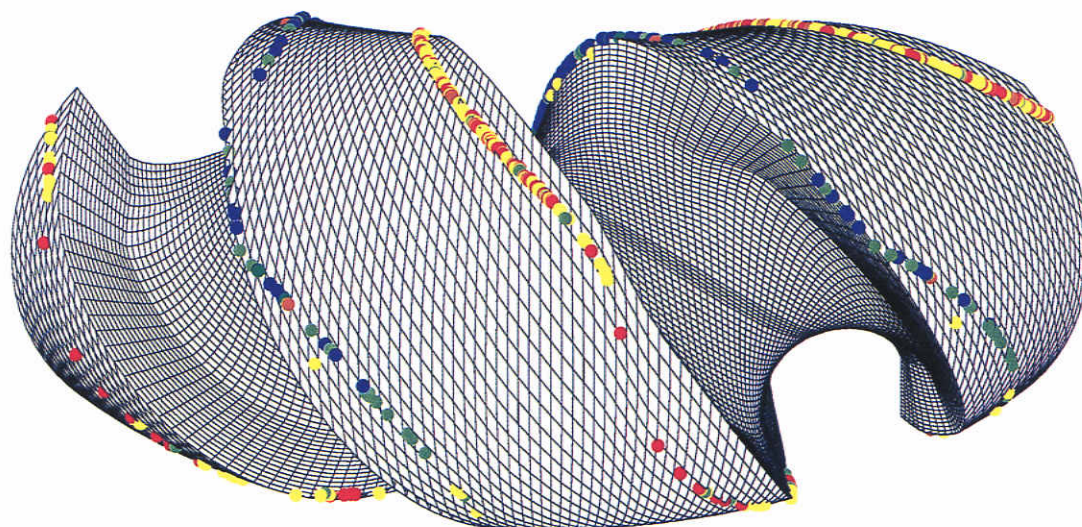


FIG.4 LHD 標準磁場配位におけるダイバータ磁力線が真空容器に到達する地点. トーラス内周側 (上図) と外周側 (下図) とから見た図を示す. 磁力線方向と磁力線結合長とで色分けされている.

ダイバータ磁力線が真空容器壁に到達する地点を FIG.4 に示す. 内周側ではコイルを埋め込むために作られた真空容器の溝の上辺部にダイバータ磁力線が到達する. 外周側では真空容器壁上のダイバータトレースは大きなうねりを示す. ダイバータ磁力線がきれいに整列していることは, 今後 LHD を閉ダイバータ配位にするときに大きな利点となるであろう.

LHD にトロイダル磁場コイルが存在しないことは, 他のトーラス型プラズマ閉じこめ装置に見られない利点である. たとえば, トカマクにおいてはトロイダル磁場コイルの作り出す磁場強度の変化 (トロイダルリップル) は, ピッチ角の立った粒子 (磁力線方向と粒子の速

度ベクトルとで作られる角度が $\pi/2$ 近辺の粒子) は隣接したトロイダルコイルの中間域に運動可能領域が制限され, $B \times \nabla B$ ドリフトにより真空容器壁に流出してしまう.[14] 閉じこめ性能の劣化だけでなく, 第一壁上の局在化した熱負荷をもたらす. これに対し, LHD ではトロイダルコイルがないのでピッチ角の立った粒子でも, 無衝突ならば, バナナ形状のドリフト面を描き磁場に完全に保持される. 特に, 最外殻磁気面の外側領域では, 磁力線に沿って走る粒子 (通過粒子) は, 磁力線とともにダイバータに流出するのに対して, ピッチ角の立った粒子はヘリカルコイル間でミラー反射を繰り返すことになるので (通過粒子に比べて反射粒子は運動の 1 周期長

が半減するので) 粒子軌道運動の断熱性が高く、完全保持粒子となることが可能である ($B \times \nabla B$ ドリフト速度が小さい低エネルギー粒子ほど顕著となる)。すなわち、LHD の最外殻磁気面の外側領域 (カオス磁力線領域) はミラープラズマ (開放端プラズマ) と同様のプラズマになる。このことは、最外殻磁気面外側のカオス磁力線領域に低温プラズマが効率的に保持できることを意味し、磁気面内に保持されている高温プラズマの荷電損失交換を引き起こす中性原子の浸透を妨げる働きが期待できるようになる。外殻磁気面の外側に出発地点を選んでも、LHD 磁場に完全に保持されている粒子軌道 (バナナ軌道) の存在は軌道計算で確認している。

III LHD 周辺部プラズマの理論モデル

まず最初に周辺部プラズマ密度を考察しよう。最も簡単なモデルとして、炉心からのプラズマの供給とダイバータへの流出とで密度は定まっているとし中性原子の役割は無視する。磁場は、LHD の標準磁場配位にあるとする。このときには、磁気面領域の体積 V_{CORE} とカオス磁力線領域の体積 V_C は次のようになる。

$$V_{CORE} \simeq 27.7 \text{ m}^3$$

$$V_C \simeq 9.3 \text{ m}^3$$

磁気面領域のプラズマ密度を n_{CORE} 、周辺部のプラズマ密度を n_{SOL} と記す。 n_{SOL} はカオス磁力線領域の磁力線結合長 L_{cni} が長いために維持されるプラズマ密度 n_C とピッチ角の立っているためカオス磁力線領域に保持されるミラープラズマ (反射粒子で構成されるプラズマ) n_M の和となる。

$$n_{SOL} = n_C + n_M \quad (6)$$

磁場強度が高くなるヘリカルコイル直近にはミラープラズマが存在しないので、ミラープラズマ保持領域の体積 V_M はカオス磁力線領域のほぼ 1/2 と仮定する。

$$V_M \simeq V_C/2$$

磁気面領域から流出するプラズマの内の、ミラー保持されるものの割合を $1 - \alpha$ としよう。このプラズマはピッチ角散乱後には磁力線にそって流出するカオス磁力線領域保持プラズマとなる。よって、粒子数保存則は次のようになる。(炉心プラズマの粒子閉じこめ時間を τ_{CORE} とする)

$$V_C \frac{dn_C}{dt} = \alpha \frac{V_{CORE} n_{CORE}}{\tau_{CORE}} + \frac{V_M n_M}{\tau_M} - \frac{V_C n_C}{\tau_C} \quad (7)$$

$$V_M \frac{dn_M}{dt} = (1 - \alpha) \frac{V_{CORE} n_{CORE}}{\tau_{CORE}} - \frac{V_M n_M}{\tau_M} \quad (8)$$

LHD の炉心領域からの高エネルギーイオン排出流は文献 [15] に詳述した。磁場強度が特別に弱い状況でなければ高エネルギーイオン排出流はすべてダイバータ磁力線に沿っていることが計算機解析によって示されている。ここで特に注意すべきは、高エネルギーイオンが排出されるのはピッチ角が通過粒子と、反射粒子の境界域に位置するときであり、反磁力線方向に走行するとき磁気面よりも外側に軌道が膨らむ性質により、高エネルギーイオンの排出流は磁力線を遡行する方向に行われることである。すなわち、炉心からの高エネルギーイオンの排出は 4 本のダイバータ磁力線のうち、2 本にだけ集中する。

磁力線結合長 L_{cni} が長いために維持されるプラズマの寿命 τ_C は走行時間で定まるので

$$\tau_C \simeq \frac{L_{cni}}{\sqrt{T_C/M}} \quad (9)$$

となる。ミラー保持されているプラズマはピッチ角散乱で寿命が定まるので

$$\begin{aligned} \tau_M &\simeq \tau_{ii} \ln(R) \\ &\simeq 5.6 \cdot 10^{-9} \frac{T_M^{3/2}}{n_{SOL}/10^{20}} \ln(R) \end{aligned}$$

で近似される。ここで R はカオス磁力線領域のミラー比で LHD 標準磁場配位においてはほぼ 2 である。

$$R \simeq 2 \quad (10)$$

定常を仮定すると磁力線結合長 L_{cni} が長いために維持されるプラズマ密度 n_C とピッチ角の立っているためカオス磁力線領域に保持されるミラープラズマ (反射粒子で構成されるプラズマ) n_M が求まる。

$$\begin{aligned} n_M^2 + \alpha \frac{V_{CORE}}{V_C} \frac{L_c/\sqrt{T_C/M}}{\tau_{CORE}} n_{CORE} n_M \\ \simeq 5.6 \times 10^{11} T_M^{3/2} \ln(R) (1 - \alpha) \frac{V_{CORE}}{V_M} n_{CORE} / \tau_{CORE} \end{aligned}$$

磁力線結合長 L_{cni} が長いために維持されるプラズマの温度 T_C とピッチ角の立っているためカオス磁力線領域に保持されるミラープラズマの温度 T_M はともに等しいと仮定し T_{SOL} と表す。さらに、磁気面領域から流出するプラズマの内の、ミラー保持されるものの割合も 1/2 ($\alpha = 1/2$) と仮定しよう。 T_{sol} の上昇は n_C の低下をもたらす、 n_M の上昇を引き起こす (FIG.5)

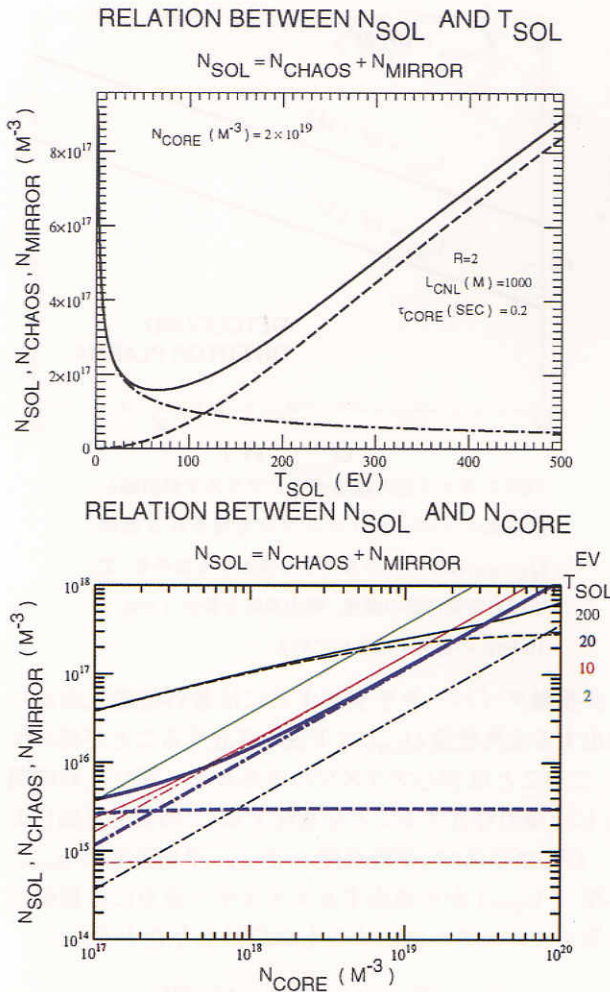


FIG.5 周辺プラズマの温度と密度および炉心プラズマの密度との関係. 計算に使用したパラメータは図中に記されている.

次に、カオス磁力線領域のプラズマと熱の流れを記述するモデルを組み立てる. ただし以下では簡単のためミラー保持プラズマの効果は無視する. さらに、磁場を横切る熱伝導係数 χ_{\perp} は沿磁力線熱伝導係数 χ_{\parallel} に比べて遙かに小さいので最初は磁力線に沿う熱の流れのみを考察する. また、カオス磁力線領域の厚みは十分な厚みがあるので、大部分のカオス磁力線はプラズマ中を走行しているとして、中性原子との相互作用は無視しよう. 最外殻磁気面から流出したプラズマの熱と粒子は半径 a の磁力管内を流れるとする. 最外殻最外殻磁気面には N 本の磁力管が開いているとする. 磁力管に沿った長さを ℓ とすると、磁力管内の粒子、運動量、熱の流れを記述する方程式は次のようになる.[9],[10]

$$\frac{\partial n}{\partial t} + \frac{\partial(nu)}{\partial \ell} = -\alpha_{ei}n^3 \quad (11)$$

$$Mn \left(\frac{\partial u}{\partial t} + u \frac{\partial u}{\partial \ell} \right) + 2 \frac{\partial(nT)}{\partial \ell} = 0 \quad (12)$$

$$3n \left(\frac{\partial T}{\partial t} + u \frac{\partial T}{\partial \ell} \right) + 2nT \frac{\partial u}{\partial \ell} - \frac{\partial}{\partial \ell} \left(\chi_{e\parallel} \frac{\partial T}{\partial \ell} \right) = 0 \quad \text{条件} \quad (13)$$

ただし、ここではカオス磁力線領域における磁場強度変動効果、およびそれに伴う磁力管断面の変動は簡単のため無視し、電子とイオン間のクーロン衝突による沿磁力線方向熱伝導 (熱伝導係数 $= \chi_{e\parallel}$) と 3 体衝突による電離再結合過程 (再結合係数 $= \alpha_{ei}$) のみを取り入れた. 電子とイオンの密度 ($= n$), 速度 ($= u$), 温度 $= T$ はともに等しいと仮定し、比熱の比 ($= \gamma$) は $5/3$ とした. M はイオンの質量を表し、電子とイオンの質量比の平方根 ($= \sqrt{m/M}$) に相当する微量は無視している. 電子による熱伝導係数 $\chi_{e\parallel}$ には次式を採用する.[11],[12] ただし、以下では、温度は eV 単位で記述し、それ以外は国際単位系 (SI 単位系) を採用する.

$$\chi_{e\parallel} = 3.16 \frac{T}{m} n \tau_{ei} \quad (14)$$

$$= 2.4 \times 10^{22} [T(\text{eV})]^{5/2} m^{-1} \text{sec}^{-1} \quad (15)$$

Braginskii の衝突時間 τ_{ei} に含まれているクーロン対数は 20 と設定した.

3 体衝突の電離再結合係数 α_{ei} としては、文献 [13] のグラフに示されている低温時の漸近表式

$$\alpha_{ei} \simeq 0.8 \times 10^{-39} T^{-9/2} \quad (16)$$

を採用する. 以下では定常流を仮定して議論する.

まず最初に磁力管中のプラズマ流速を無視できる場合 ($u < C_s$ の場合: $C_s = \sqrt{2T/M}$) を考察しよう. このときには、

$$\chi_0 \equiv 2.4 \times 10^{22} \quad (17)$$

とおくと、熱流の式 (13) より、

$$T(\ell)^{7/2} = T(0)^{7/2} - \frac{7}{2} \frac{q_0}{1.6021 \times 10^{-19} \chi_0} \ell \quad (18)$$

の関係を得る. ここで q_0 は開口部での熱流を表し開口部での温度勾配と関係づけられているが、プラズマの真空中への膨張速度が音速であることを考慮すると、 q_0 に上限が存在する.

$$q_0 = -1.6021 \times 10^{-19} \chi_0 T(0)^{5/2} \frac{\partial T(0)}{\partial \ell} < 4.7 \times 10^{-15} \frac{n(0) T(0)^{3/2}}{\sqrt{M/M_p}} \quad (19)$$

ここで、 M_p 陽子の質量を表す.

関係式 (18) は、磁力管の長さが十分に長ければプラズマの温度が 0 となり得ることを示している. この磁力管の長さを L_{crit} と定義しよう.

$$L_{crit} = \frac{2}{7} T(0)^{7/2} \frac{1.6021 \times 10^{-19} \chi_0}{q_0} \quad (20)$$

条件

$$L_{crit} < L_{cnl} \quad (21)$$

が成立するならば、ダイバータ板に到達する前にプラズマ温度は十分に低下し運動方程式 (12) から導かれる結論

$$n(l)T(l) = \text{一定} \quad (22)$$

の関係でプラズマ密度は急上昇する。密度の上昇と温度低下で 3 体再結合過程が進行しプラズマの消滅が期待される。

カオス磁力線領域中でプラズマが消滅し、非接触ダイバータプラズマの実現される条件は (19, 20, 21) より次のようになる (FIG.6)。

$$\frac{T(0)^2 \sqrt{M/M_p}}{n(0)L_{cni}} < 4.27 \times 10^{-18} \quad (23)$$

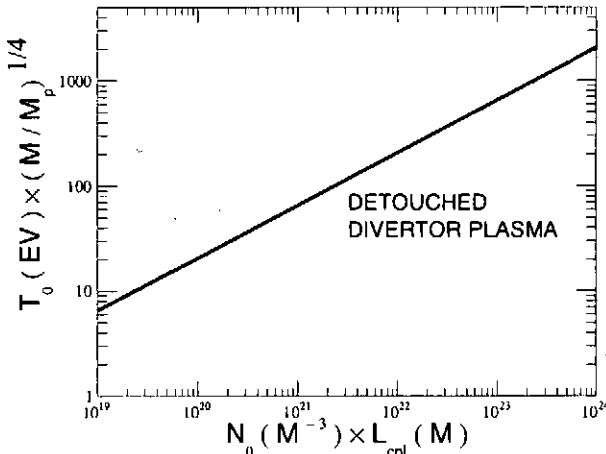


FIG.6 カオス磁力線領域中でプラズマが消滅し、非接触ダイバータプラズマの実現される条件。\$N_0\$, \$T_0\$ 磁力管開口部の密度、温度、\$L_{cni}\$ 磁力管開口部からダイバータ板までの距離 (磁力線結合長) は示す。

次に非接触ダイバータプラズマが実現しているとき最外殻磁気面から流出する全熱流量 \$Q_{loss}\$ を評価しよう。最外殻磁気面には半径 \$a\$ の磁力管が \$N\$ 本開口していると仮定したので (20,21) より、

$$\begin{aligned} Q_{loss} &= \pi a^2 q_0 N \\ &> 1.1 \times 10^3 \frac{N \pi a^2 T(0)^{7/2}}{L_{cni}} \end{aligned} \quad (24)$$

の関係が導かれる。カオス磁力線領域の体積を \$V_{chaos}\$ とし、そこに半径 \$a\$ 長さ \$L_{cni}\$ 磁力管が稠密に埋め込まれていると考え、

$$V_{chaos} = N \pi a^2 L_{cni} \quad (25)$$

の関係が成立するのでこの関係から \$N \pi a^2\$ を求め、(24) に代入すると

$$Q_{loss} > 1.1 \times 10^3 \frac{V_{chaos} T(0)^{7/2}}{L_{cni}^2} (W), \quad (26)$$

となる (FIG.7)。

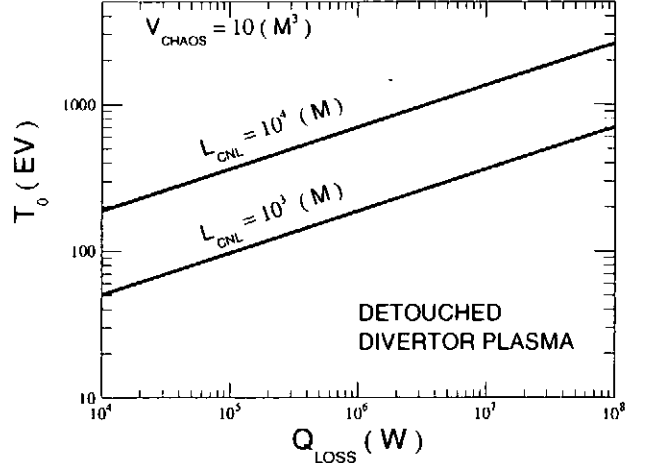


FIG.7 カオス磁力線領域中でプラズマが消滅し、非接触ダイバータプラズマの実現される条件。 Q_{LOSS} は炉心プラズマから流出する総熱量、\$T_0\$ は磁力管開口部の温度。磁力線結合長が 1 km, と 10 km, の場合が示されている。

非接触ダイバータを実現するには最外殻磁気面から流出する全熱流量 \$Q_{loss}\$ に下限の存在することが導かれた。このことは炉心プラズマのエネルギー閉じこめ時間 \$\tau_E\$ に上限の存在することを意味する。この値を評価しよう。炉心プラズマ (平均温度 = \$T_{core}\$, 平均密度 = \$n_{core}\$, 体積 = \$V_{core}\$) から流出するエネルギー流束には輻射損失等ダイバータへ流出するもの以外も存在するので

$$\tau_E < \frac{3n_{core}T_{core} \times 1.6021 \times 10^{-19}V_{core}}{Q_{loss}} \quad (27)$$

の不等式が導かれる。ここで、LHD においては密度分布が非常に平坦であることを考慮して

$$n_{core} = n_0 \quad (28)$$

と仮定し、\$Q_{loss}\$ の下限値 (26) を代入すると非接触ダイバータを実現しているプラズマの閉じこめ時間の上限が導かれる。

$$\tau_E < \frac{4.37 \times 10^{-22} n_0 T_{core} V_{core} L_{cni}^2}{V_{chaos} T(0)^{7/2}} \quad (29)$$

たとえば、LHD (\$V_{core} \simeq 30 (m^3)\$, \$V_{chaos} \simeq 10 (m^3)\$) において \$n_0 = 10^{20} (m^{-3})\$, \$T_{core} = 5 (keV)\$, \$T_0 = 1 (keV)\$, \$\tau_E = 1 (sec)\$ プラズマを非接触ダイバータで保持するためには、磁力線結合長 \$L_{cni}\$ に対して

$$L_{cni} > 6.95 (km) \quad (30)$$

の条件が要求される。

上記の解析結果では、プラズマの流速が音速以下であることを仮定し、熱伝導のみで炉心からダイバータ板へ熱が流れているとした。しかしながら、温度低下に伴う、

密度の上昇, 流速の低下は, 3 体再結合過程の進行で破綻する。3 体再結合によるプラズマの消滅は必然的に流速の上昇を引き起こす。プラズマ流速の上昇は熱の流れが熱伝導のみで表すことのできないことも引き起こす。よって, (11,12,13) の定常解を数値的に計算しよう。ただし, 炉心プラズマからの熱流出を促すため方程式 (13) の右辺には磁力管先端部でのエネルギー吸収項を人工的に設定した。FIG.8 に計算例を示す。計算に設定したパラメータは図中に記されている。炉心から流出する熱流束 Q_{EDGE} が閾値を越せば, ダイバータ板への粒子束の低下する非接触ダイバータへ移行する状況が示されている。

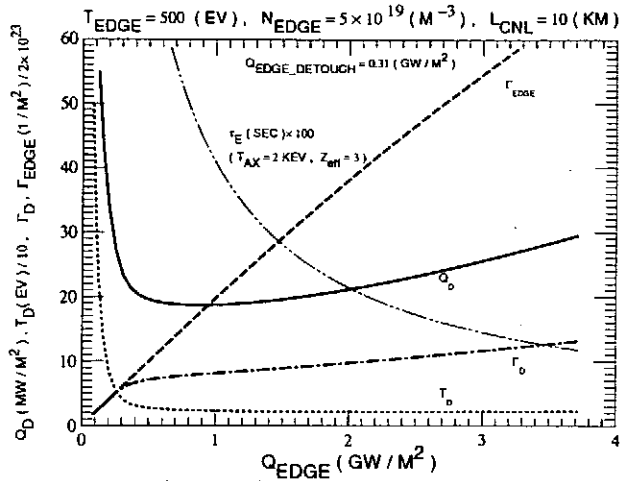


FIG.8 炉心から流出する熱流束 Q_{EDGE} と, ダイバータ板に到達するプラズマ流束, 熱流束, ダイバータプラズマ温度等の関係。計算に使用したパラメータは図中に記されている。

IV まとめと議論

LHD の磁場・磁力線構造を詳述し, 周辺プラズマの挙動に深く関わることを指摘した。

LHD は $\ell=2$ のヘリカルヘリオトロン磁場方式を用いたプラズマ実験装置であり, 周辺磁場領域には強い磁気シアが存在している。その結果, 周辺部磁力線はフラクタル構造を形成し, 磁力線結合長は 10km の程度にも達することを数値計算で明らかにした。プラズマの沿磁力線方向熱伝導係数がプラズマ温度に強く依存していることも取り入れ, プラズマの熱流と温度・密度との関係を解析することで, 磁力線結合長が 10km の程度になるならば, 磁力管先端部ではプラズマの再結合過程の進行が期待できることを導いた。このときには, 非接触ダイバータプラズマが実現される。LHD の磁場配位の下での非接触ダイバータの実現の条件を求めた。

さらに, LHD にはトロイダル磁場コイルが無いために, ピッチ角の立った粒子は最外殻磁気面の外のカオス磁力線領域でも完全に保持されることが明らかにされ

ている。これにより, LHD の磁気面領域を取り巻くプラズマは磁力線結合長が長いまま保持されているプラズマとミラー保持プラズマとで構成されていることを指摘した。

上記の特徴は, LHD では炉心プラズマが真空容器内に浮遊している中性原子との荷電交換で直接冷却されることを防ぐプラズマブランケットがカオス磁力線領域に実現可能であることを指摘した。このことは炉心プラズマ保持性能の大幅向上に寄与すると期待される。

当論文では, 周辺プラズマ流が定常であることを仮定して解析を進めたが時間発展の解析が次の課題である。さらに, 閉ダイバータ配位にして, ダイバータ磁力管の先端部で中性原子と強く相互作用する状況の解析が物理的にも, 実用的にもきわめて興味ある研究課題となる。

磁力管を横切る熱伝導, ミラー保持プラズマとの熱の授受等の解析も今後の課題である。

参考文献

- [1] 木上淳：日本応用数学会 1999 年度年会 (愛媛大学, 1999 年 10 月 4 日 A 会場)
- [2] MUSSER, Gerge：日経サイエンス (1999 年 9 月号) 10.
- [3] 核融合科学研究所 研究組織改善調査委員会編：核融合科学研究所大型ヘリカル研究部 外部評価報告書 (核融合科学研究所, 1999) 30～33.
- [4] 核融合科学研究所 研究組織改善調査委員会編：核融合科学研究所大型ヘリカル研究部 外部評価報告書 (核融合科学研究所, 1999) 40.
- [5] 核融合科学研究所 研究組織改善調査委員会編：核融合科学研究所大型ヘリカル研究部 外部評価報告書 (核融合科学研究所, 1999) 38.
- [6] 核融合科学研究所 研究組織改善調査委員会編：核融合科学研究所大型ヘリカル研究部 外部評価報告書 (核融合科学研究所, 1999) 35～38.
- [7] AKAO, H., J. Phys. Soc. JPN, **59** (1990) 1633.
- [8] 渡辺二太, 羽鳥尹承, 石田亨：核融合研究 **68** (1992) 298-327.
- [9] Nedospasov, A.V., and Tokar', M.Z. : Reviews of Plasma Physics (Edited by B.B. Kadomtsev, CONSULTANTS BUREAU, NewYork-London **18** (1996) 116).
- [10] Braginskii: S.I., Reviews of Plasma Physics (Edited by M.A. Leontvitch, CONSULTANTS BUREAU, NewYork **1** (1966) 211).
- [11] Braginskii: S.I., Reviews of Plasma Physics (Edited by M.A. Leontvitch, CONSULTANTS BUREAU, NewYork **1** (1966) 215).
- [12] 高村秀一：プラズマ加熱基礎論 (名古屋大学出版会 (1986) 36)
- [13] 高村秀一：プラズマ理工学入門 (森北出版 (1997) 46)
- [14] 飛田健次, 濱松清隆, 滝塚知典, 鈴木正信：プラズマ・核融合学会誌 **75** (1999) 582.
- [15] 藤原正己 編：大型ヘリカル装置実験計画検討作業会, 平成 8 年度報告書 (大型ヘリカル装置総合建設本部, 核融合科学研究所, 1997) 207.

B-スプライン展開による一般磁気座標の構築

Construction of Generalized Magnetic Coordinates by B-Spline Expansion

倉田道成（名古屋大学大学院工学研究科エネルギー理工学専攻）
等々力二郎（核融合科学研究所）

Michinari Kurata

Dept. of Energy Engineering and Science, Graduate School of Engineering, Nagoya University

and

Jiro Todoroki

National Institute for Fusion Science

Abstract

Generalized Magnetic Coordinates (GMC) are curvilinear coordinates (ξ, η, ζ) , in which the magnetic field is expressed in the form

$$\mathbf{B} = \nabla \Psi(\xi, \eta, \zeta) \times \nabla \zeta + H^{\zeta}(\xi, \eta) \nabla \xi \times \nabla \eta.$$

The coordinates are expanded in Fourier series in the toroidal direction and the B-spline function in other two dimensions to treat the aperiodic model magnetic field. The coordinates are well constructed, but are influenced by the boundary condition in the B-spline expansion.

Keywords:

generalized magnetic coordinates, GMC, magnetic flux coordinates, nested magnetic surface, breaking of magnetic surfaces, magnetic islands, ABC magnetic field, B-spline expansion

§ 1. 序論

浜田座標やブーザー(Boozer)座標[1,2]などでよく知られる磁気面を座標変数とする磁気面座標(flux coordinates)は、プラズマのMHD平衡や安定性の解析などに今日広く利用されている。これらの磁気面座標は座標変数として入れ子状の磁気面を必要とするが、磁気島による磁気面破壊や磁力線のカオス(chaos)領域、ストカスティック(stochastic)領域の存在のために、プラズマ中において生成可能な領域が限られる場合がある。従って、トーラス状のプラズマにおける最外殻磁気面の外側の領域のように本来入れ子状の磁気面が存在しない領域や大きな磁気島が発生して入れ子状の磁気面が破壊されている領域には生成できない。このような場合に、従来の磁気面座標を補完する座標として一般磁気座標(Generalized Magnetic Coordinates, 略してGMC)[3]が考案された。

一般磁気座標は、磁気面を座標変数としない座標系であるため、入れ子状の磁気面が存在しない領域に対しても生成可能な座標系である。そのため、一般磁気座標は磁気島により入れ子状の磁気面の一部が破壊されている領域や領域の一部に最外殻磁気面の外側の領域を含む場合に対しても生成可能である。一般磁気座標を構築するアルゴリズムは磁力線を追跡せずに磁気面を構成する新しいアルゴリズムであり、座標系の

変化に伴うベクトルポテンシャルの変換則から得られる[4,5]。

§2. 一般磁気座標の構成

一般磁気座標は曲線座標系であり、その座標変数を (ξ, η, ζ) と表すこととする。ヤコビアンを $\sqrt{g} = (\nabla\xi \cdot \nabla\eta \times \nabla\zeta)^{-1}$ 、磁場の反変成分を (B^ξ, B^η, B^ζ) 、磁場のベクトルポテンシャルの共変成分を (A_ξ, A_η, A_ζ) とし、磁場の誘導密度を $(H^\xi, H^\eta, H^\zeta) \equiv (\sqrt{g}B^\xi, \sqrt{g}B^\eta, \sqrt{g}B^\zeta)$ と定義すると、 H^ζ が ζ に依存しないとき、磁場は次式で表される。

$$\mathbf{B} = \nabla\Psi(\xi, \eta, \zeta) \times \nabla\zeta + H^\zeta(\xi, \eta) \nabla\xi \times \nabla\eta. \quad (1)$$

ここで、 Ψ はベクトルポテンシャルの共変成分 A_ζ である。もし A_ζ が ζ に依存しないならば、 $\mathbf{B} \cdot \nabla A_\zeta = 0$ となるので $A_\zeta(\xi, \eta) = \text{Const.}$ で表わされる面は厳密に磁気面を表わす。従って、 A_ζ の ζ に依存する部分は磁気面の破壊によるものと考えられる。そこで、 A_ζ の ζ 依存性が最小となるように一般磁気座標を構築することとする。ここで、ある物理量 F に対して、

$$\bar{F} \equiv \oint F d\zeta / \oint d\zeta, \quad \tilde{F} \equiv F - \bar{F}. \quad (2)$$

という記号を導入すると、一般磁気座標を構築するための条件は以下のように表される。

条件1: H^ζ が ζ に依存しない $\Leftrightarrow \tilde{H}^\zeta = 0$.

条件2: A_ζ の ζ 依存性を最小にする $\Leftrightarrow \bar{A}_\zeta$ を最小にする。

条件1より、

$$\tilde{H}^\xi = \frac{\partial \bar{A}_\zeta}{\partial \eta}, \quad \tilde{H}^\eta = -\frac{\partial \bar{A}_\zeta}{\partial \xi} \quad (3)$$

と表せると仮定すれば、条件2は $\tilde{H}^\xi, \tilde{H}^\eta$ を最小にすることを意味する。また、 $\bar{A}_\zeta(\xi, \eta) = \text{Const.}$ で表わされる面を平均磁気面と呼ぶこととする。

これまでの報告[4-6]において、非軸対称な周期的なモデル磁場に対して座標を3次元方向にフーリエ展開することによってGMCが構築できることが示された。また、入れ子状の磁気面領域の一部に明らかな磁気島を含む場合でもGMCを構築できることが示された[6]。ここでは、さらに非周期的磁場や不連続性の大きい磁場を取り扱うために、局所的な台(Support)を持つ区分多項式関数であるB-スプライン関数を用いてGMCを生成した結果を報告する。

§3. 実験モデル

モデル磁場としてトポロジカルに非軸対称磁場を表現できる以下のようなABC(Arnol'd-Beltrami Childress)磁場を用いた。デカルト座標系 (x, y, z) において、

$$\begin{aligned} B_x &= b \cos(2\pi y) + c \sin(2\pi z), \\ B_y &= c \cos(2\pi z) + a \sin(2\pi x), \\ B_z &= a \cos(2\pi x) + b \sin(2\pi y) + B_0. \end{aligned} \quad (4)$$

この磁場は全ての方向に周期 1 を持っている。ここで $a=0.2, b=0.1, c=0.6$ と選び、 $B_z > 0$ となるように z -方向に一様な磁場 $B_0 = 1.0$ を加える。デカルト座標系を GMC の座標変数 (ξ, η, ζ) を用いて、

$$\begin{aligned} x &= \xi + \sum_{l,m,n} \xi_{l,m,n} B_l(\xi) B_m(\eta) \exp(2\pi i n \zeta), \\ y &= \eta + \sum_{l,m,n} \eta_{l,m,n} B_l(\xi) B_m(\eta) \exp(2\pi i n \zeta), \\ z &= \zeta. \end{aligned} \quad (5)$$

と展開して GMC を生成する。ここで、 $B_l(\xi), B_m(\eta)$ は各々図 1 に示されるような 3 次の B-スプライン関数であり、座標格子点と B-スプライン関数の節点は一致させている。GMC の座標変数 (ξ, η, ζ) の各変域はすべて区間 $[0, 1]$ とした。 $z=\zeta$ 方向がトロイダル方向に対応し、 ζ -方向にフーリエ展開し、残りの 2 次元方向に B-スプライン展開を行う。未知数である展開係数 $\xi_{l,m,n}, \eta_{l,m,n}$ を決定して座標を生成する。 ζ -方向のフーリエモードとしては $-L \leq n \leq L$ と表して、 $L=10$ に固定した。フーリエモードの数を $L=1$ から $L=10$ に至るまで順次増やしていくと座標精度が良くなるが、それ以上モード数を増やしても座標はほとんど変化しなかったのがこのように固定した。また、トロイダル方向の $z=\zeta$ 方向は、40 メッシュに等分割した。この方向のメッシュ数を必要以上に増やしても座標は変化しなかったため固定した。 (ξ, η) 方向の各メッシュ数 M をパラメータとして、 $M=20 \sim 80$ まで変化させた。反復法により、座標系が十分収束するまで 15 回程度の繰り返し計算を行った。GMC において磁気面が ζ によらず (ξ, η) 平面上で一定の曲線となるように、すなわち磁気面が軸対称となるように座標系を構築した。

§ 4. 実験結果

図 4 は、デカルト座標系においてモデル磁場の磁力線のポアンカレ図とそれに対して生成した GMC の等間隔格子を重ねて示している。中央の入れ子状の磁気面に注目して GMC を生成し、 $z =$ 一定の平面として $z = 0, 0.25, 0.5, 0.75$ の 4 平面を代表して選んだ。磁気面の z 方向の変位に対応して GMC が生成されていることがわかる。

図 2 に $M=40$ のとき GMC において得られた $\bar{A}_\zeta(\xi, \eta) = \text{Const.}$ で表わされる平均磁気面を示した。取り扱ったモデル磁場は、比較的磁気面破壊が少ない磁場であり、このような場合には、平均磁気面と磁気面はよく一致するはずである。 (ξ, η) 平面上で平均磁気面に沿って線積分を行うとさまざまな磁気面量を比較的簡単に計算できるが、その代表として回転変換を計算した。図 3 は、デカルト座標系において磁力線追跡から求めた回転変換と図 2 に示した平均磁気面から求めた回転変換を示したグラフである。グラフの横軸はそれぞれ各座標系において磁気軸から座標軸 ξ または x と同一方向に取った有向線分上での距離で、デカルト座標系においては $z=0$ の平面上での距離である。このグラフを比較すると概形は一致していることがわかる。この平均磁気面から求めた回転変換は $M=40$ の場合のものであり、 $M=60$ 及び $M=80$ の場合のそれと有効数字 2 桁以上一致していて、 M に対する依存性は少なかった。

次に H^ζ の ζ 依存性を評価するために、次のノルムを計算する。

$$I_\zeta = \int_0^1 \int_0^1 \int_0^1 |\tilde{H}^\zeta|^2 d\xi d\eta d\zeta. \quad (6)$$

GMC は $\tilde{H}^\zeta = 0$ を座標の必要条件としているので、本来 $I_\zeta = 0$ とならなければならない。従って、 I_ζ は座標生成の精度の尺度となる量である。また、 $\tilde{H}^\xi, \tilde{H}^\eta$ を評価するために、次のノルムを計算する。

$$I_{\xi} = \int_0^1 \int_0^1 \int_0^1 |\tilde{H}^{\xi}|^2 d\xi d\eta d\zeta, \quad I_{\eta} = \int_0^1 \int_0^1 \int_0^1 |\tilde{H}^{\eta}|^2 d\xi d\eta d\zeta. \quad (7)$$

GMCは $\tilde{H}^{\xi}, \tilde{H}^{\eta}$ が最小となるように構築されており、もし座標生成の精度が良ければ、 $\tilde{H}^{\xi}, \tilde{H}^{\eta}$ は入れ子状の磁気面が存在しない領域や磁気島による磁気面破壊を反映する量と考えられる。

座標格子点上での物理量をB-スプライン関数 $B_l(\xi), B_m(\eta)$ によって展開する場合、 (ξ, η) の各方向についてB-スプライン関数のモード l, m の数が座標格子点より2個多いために展開のための条件が不足する。そこで境界条件として座標境界での物理量の2階微分値=0と3階微分値=0という2種類の条件をそれぞれ課すことにした。実験ではいずれの境界条件を課した場合でも、他の領域と比較して座標境界近傍の数メッシュにおいて、 $I_{\xi}, I_{\eta}, I_{\zeta}$ が各々数桁大きくなった。その理由は明らかではない。そこで、座標境界での影響を取り除いた次のノルムを計算する。

$$\hat{I}_{\xi} = \int_0^1 \int_{0.1}^{0.9} \int_{0.1}^{0.9} |\tilde{H}^{\xi}|^2 d\xi d\eta d\zeta, \quad \hat{I}_{\eta} = \int_0^1 \int_{0.1}^{0.9} \int_{0.1}^{0.9} |\tilde{H}^{\eta}|^2 d\xi d\eta d\zeta, \quad \hat{I}_{\zeta} = \int_0^1 \int_{0.1}^{0.9} \int_{0.1}^{0.9} |\tilde{H}^{\zeta}|^2 d\xi d\eta d\zeta. \quad (8)$$

図5に3階微分値=0の境界条件を課した場合の $I_{\xi}, I_{\eta}, I_{\zeta}$ 及び $\hat{I}_{\xi}, \hat{I}_{\eta}, \hat{I}_{\zeta}$ とメッシュ数 M との関係を示した。また、図6に2階微分値=0の境界条件を課した場合のそれを示した。座標境界部分を含むノルム $I_{\xi}, I_{\eta}, I_{\zeta}$ については、3階微分値=0の境界条件の場合の方が2階微分値=0の場合よりも小さい。しかし、座標境界部分を除いたノルム $\hat{I}_{\xi}, \hat{I}_{\eta}, \hat{I}_{\zeta}$ については $M=60$ ではほぼ同じ値となっているので結局、座標境界部分を取り除けば境界条件の影響はない。また、 $I_{\xi}, I_{\eta}, I_{\zeta}$ 及び $\hat{I}_{\xi}, \hat{I}_{\eta}, \hat{I}_{\zeta}$ は、 M に依存しなくなるまではほぼ同じ傾きで共に減少するが、これは座標を3次元方向にフーリエ展開した場合[4]と同様である。座標を3次元方向にフーリエ展開した場合と比較すると、 $\hat{I}_{\xi}, \hat{I}_{\eta}, \hat{I}_{\zeta}$ に着目すれば数桁減少しているので座標生成の精度が上がったことがわかる。図5を見ると、 $M=40$ 以上では $\hat{I}_{\xi}, \hat{I}_{\eta}, \hat{I}_{\zeta}$ は M に依存しなくなっているが、 \hat{I}_{ζ} が0に近づいて行かないのは座標生成精度の点から不都合な現象である。

そこで (ξ, η) 平面上での分布を見るために次の ζ に関するノルムを計算する。

$$E_{\zeta}(\xi, \eta) = \int_0^1 |\tilde{H}^{\zeta}|^2 d\zeta. \quad (9)$$

図7で E_{ζ} の鳥瞰図を、図8で E_{ζ} の等高線図を示す。但し、同様に座標境界での値を省いて示した。 $M=20$ のときは $(\xi, \eta) = (0.5, 0.55)$ の近くにある磁気軸に関してほぼ対称な形をしており、まだ減少できる可能性を示していると考えられる。 $M=40$ 以上では、どのパラメータでもほぼ同じ山の形となって、この頂上は磁気軸からずれた位置にあり、山は磁気軸に関して対称ではない。なお、山以外の背景の平地部分のオーダーは 10^{-14} である。この平地部分にも別の入れ子状の磁気面の一部が4個存在していることが図1よりわかるが、この部分は小さな値となっている。

また、 \tilde{A}_{ζ} と磁気面破壊との関係を見るために次の ζ に関するノルムを計算する。

$$E_{\xi\eta}(\xi, \eta) = \int_0^1 \left(|\tilde{H}^{\xi}|^2 + |\tilde{H}^{\eta}|^2 \right) d\zeta. \quad (10)$$

図9で $E_{\xi\eta}$ の鳥瞰図を、図10で $E_{\xi\eta}$ の等高線図を示す。また E_{ζ} と同様に座標境界での値を省いて示した。 $M=20$ のときは座標生成の精度が悪く $\tilde{H}^{\xi}, \tilde{H}^{\eta}$ の中に座標生成における誤差を含んでしまうために、それがノイズとなって磁気面破壊による部分は明らかでない。 $M=40$ 以上では、 $E_{\xi\eta}$ の形状はほぼ同じ山の形となったが、座標をフーリエ展開した場合に最外郭磁気面の近傍で大きな値を持ったのとは全く異なった形状となった。山以外の背景の平地部分のオーダーは 10^{-15} であり、 E_{ζ} の場合と同様にこの部分は小さな値となっている。また、この山の頂上は磁気軸からずれた位置にあるが、 E_{ζ} の山の頂上とは異なる位置にある。座

標を3次元方向にフーリエ展開した場合には $E_{\xi\eta}$ と E_{ζ} とはかなり類似していたが、ここでは $E_{\xi\eta}$ の形状は E_{ζ} と少し似ている程度である。Mが大きくなると $E_{\xi\eta}$ の形状の解像度が上がるが、たとえばM=80のときでさえ $E_{\xi\eta}$ はデルタ関数のように局所的な大小があるわけではなく、その点では磁気面破壊を反映する量として直接的に明らかに感じ取れるわけではない。すなわち、磁気面のある領域及び磁気島領域や磁気面が存在しない領域との関係はこのままでは明瞭ではない。この関係は平均磁気面上で \tilde{H}^E, \tilde{H}^I のフーリエ成分を求めて、有理面との共鳴関係などを調べることによって明らかになるかもしれない。ここで取り扱ったモデル磁場は本来磁気面破壊が小さいものであったので、今後磁気島の存在が明らかにわかるようなより磁気面破壊が明らかな磁場を取り扱ってその関係を明らかにする必要がある。

§5. まとめ

非周期的磁場や不連続性の大きい磁場を取り扱うために、モデル磁場に対してトロイダル方向にフーリエ展開し、残りの2次元方向に3次のB-スプライン関数を用いた展開を行って一般磁気座標を構築した。B-スプライン関数による展開の際に課される境界条件の影響によって座標境界での座標生成の誤差は顕著に大きくなるが、座標境界を除けば良好に座標を生成できた。これまでの座標を3次元方向にフーリエ展開した場合と比較すると、座標生成の精度が向上した。

磁気面のある領域及び磁気島領域や磁気面が存在しない領域と一般磁気座標における量との関係は未だ解明できない。この点に関しては、磁気面破壊がより明らかな場合を取り扱うことと同時に平均磁気面上でのフーリエ成分などを考える新たなアプローチが必要である。

また、一般磁気座標で得られた平均磁気面を用いて回転変換を求めたが、メッシュ幅への依存性は少なく、比較的簡単に求められた。

Reference

- [1] S.Hamada: Nucl. Fusion **2**, 23 (1962).
- [2] A.Boozer: Phys. of Fluids **24**, 1999 (1981).
- [3] J.Todoroki: 核融合研究における数値解析手法と最適化(統計数理研究所共同研究レポート**105**), 1997, pp.1-10.
- [4] J.Todoroki and M.Kurata: 核融合研究における数値解析手法と最適化(統計数理研究所共同研究レポート**110**), 1998, pp.1-10.
- [5] M.Kurata and J.Todoroki: J. Plasma Fusion Res. SERIES, Vol. **1** (1998) 491-494.
- [6] M.Kurata and J.Todoroki: プラズマ閉じ込めに関連する数値計算手法の研究 NIFS-PROC-40 (1999) 9-18.

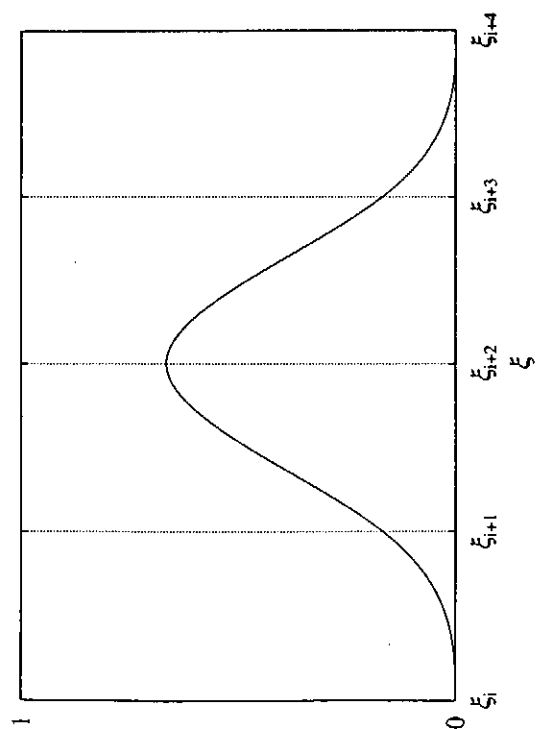


図 1. 3 次 B-スプライン関数 $B_1(\xi)$.

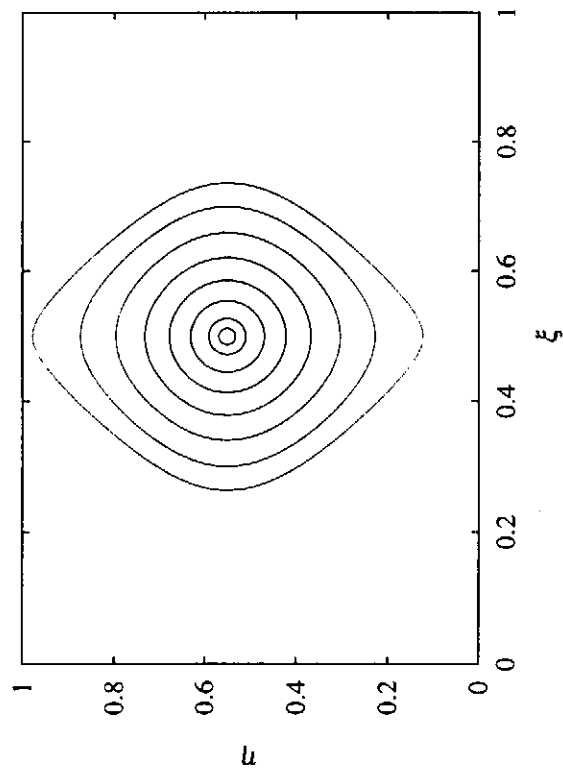


図 2. GMC における \bar{A}_c の等高線.

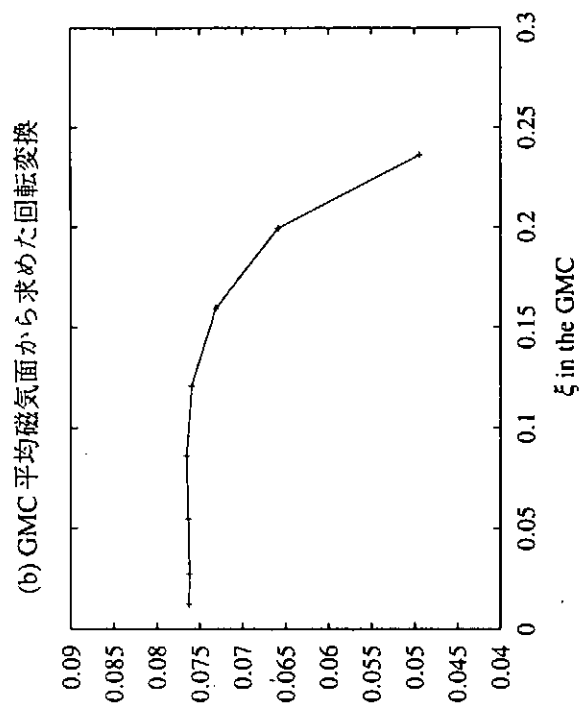
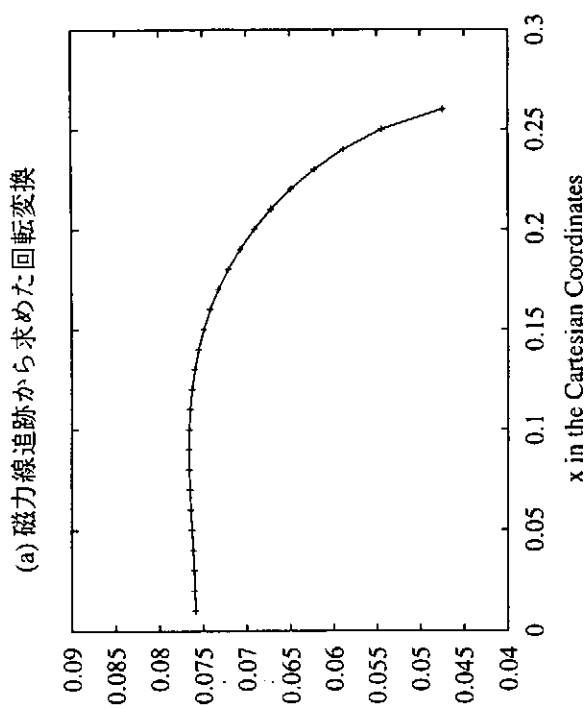


図 3. 回転変換.

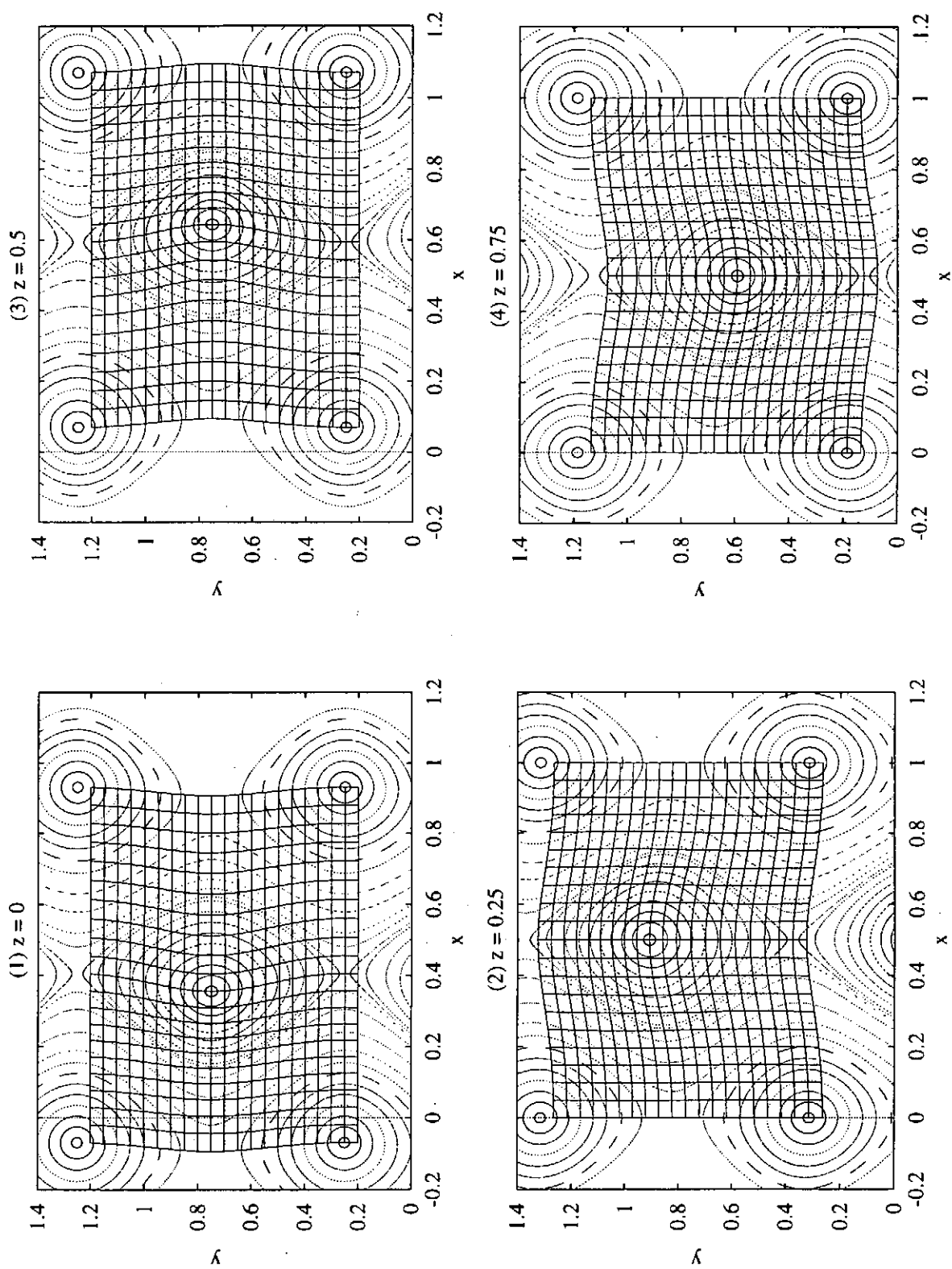
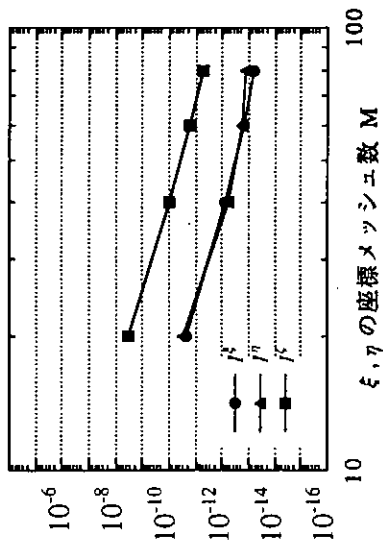


図4. 磁力線のポアンカレ図と「一般磁気座標」の等間隔格子.

(A) 境界部分を含む全座標領域での $\hat{f}^{\xi}, \hat{f}^{\eta}, \hat{f}^{\zeta}$



(B) 境界部分を除いた座標領域での $\hat{f}^{\xi}, \hat{f}^{\eta}, \hat{f}^{\zeta}$

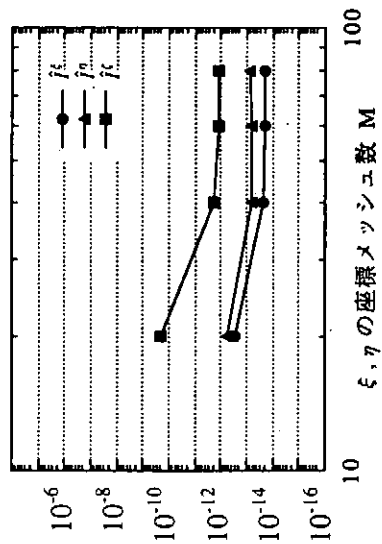
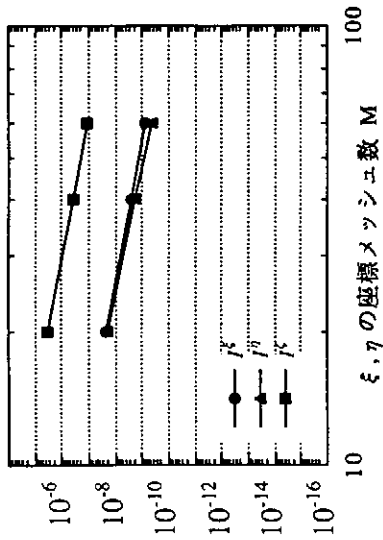


図5. $\hat{f}^{\xi}, \hat{f}^{\eta}, \hat{f}^{\zeta}$ 及び $\hat{f}^{\xi}, \hat{f}^{\eta}, \hat{f}^{\zeta}$
(境界条件: 3階微分=0の場合).

(A) 境界部分を含む全座標領域での $\hat{f}^{\xi}, \hat{f}^{\eta}, \hat{f}^{\zeta}$



(B) 境界部分を除いた座標領域での $\hat{f}^{\xi}, \hat{f}^{\eta}, \hat{f}^{\zeta}$

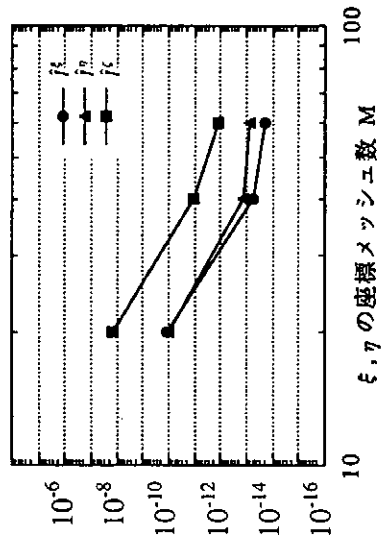


図6. $\hat{f}^{\xi}, \hat{f}^{\eta}, \hat{f}^{\zeta}$ 及び $\hat{f}^{\xi}, \hat{f}^{\eta}, \hat{f}^{\zeta}$
(境界条件: 2階微分=0の場合).

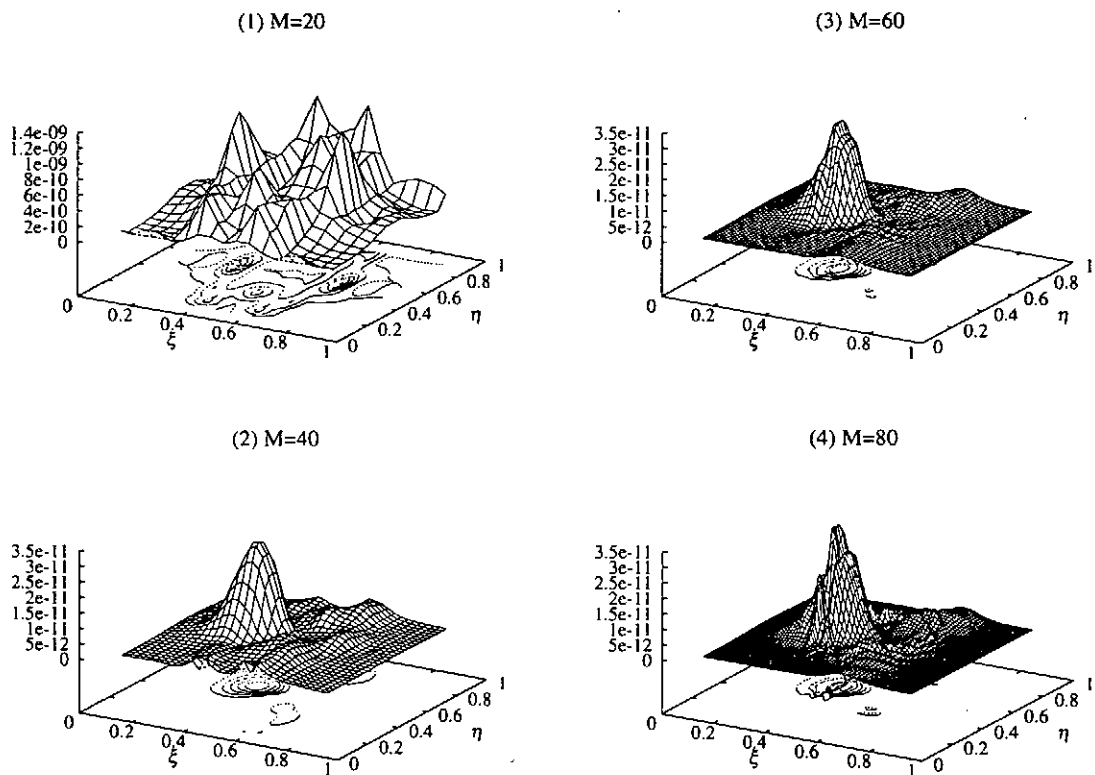


図7. $E_z(\xi, \eta)$ の鳥瞰図.

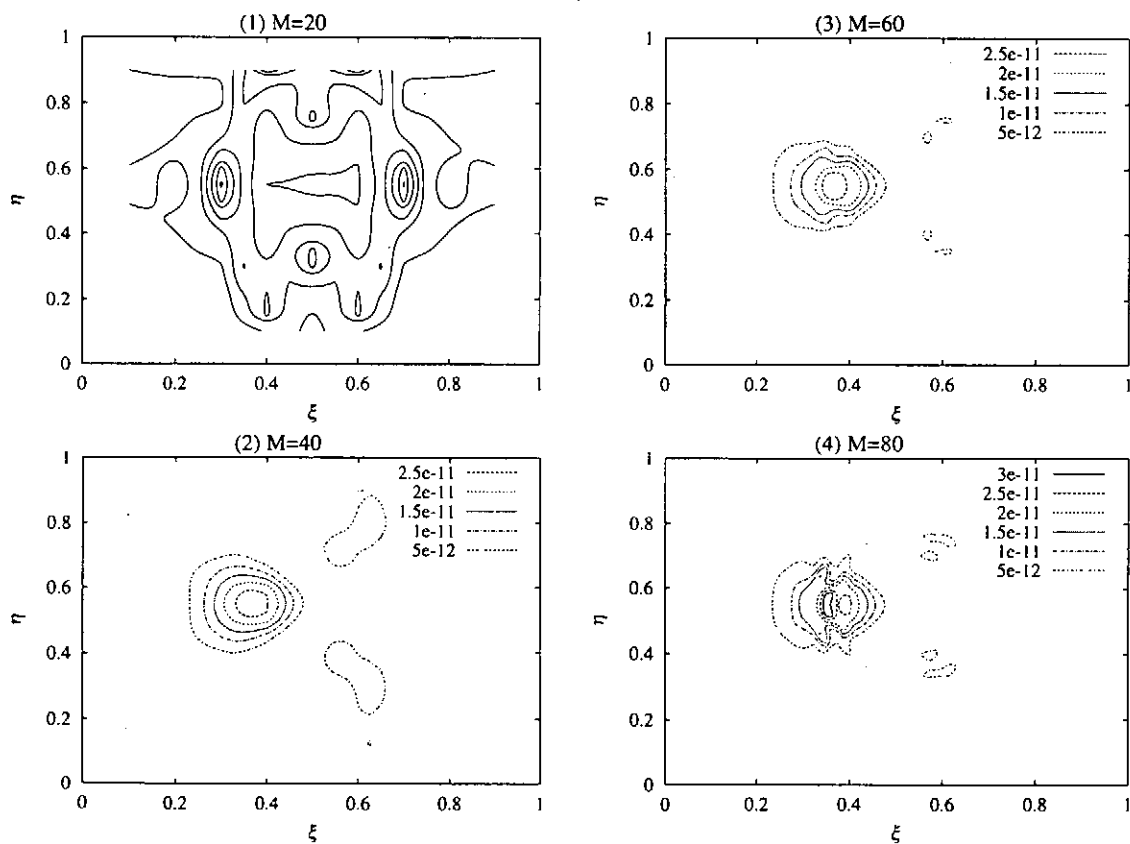


図8. $E_z(\xi, \eta)$ の等高線図.

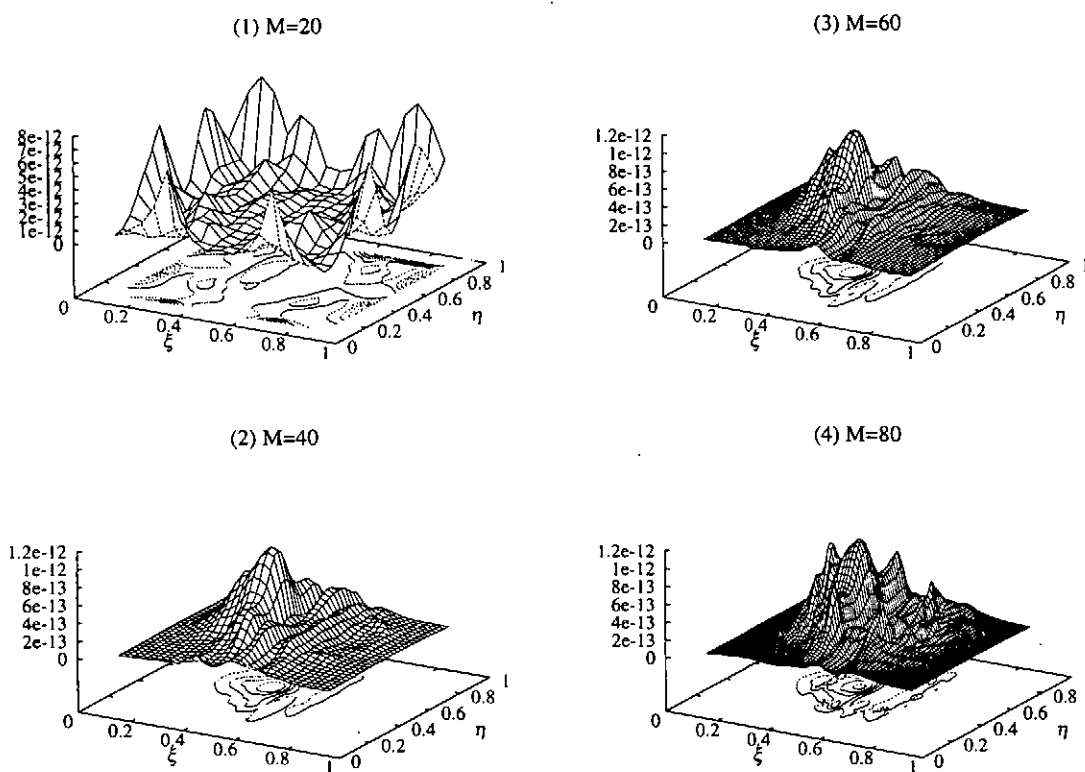


図 9. $E_{\xi\eta}(\xi, \eta)$ の鳥瞰図.

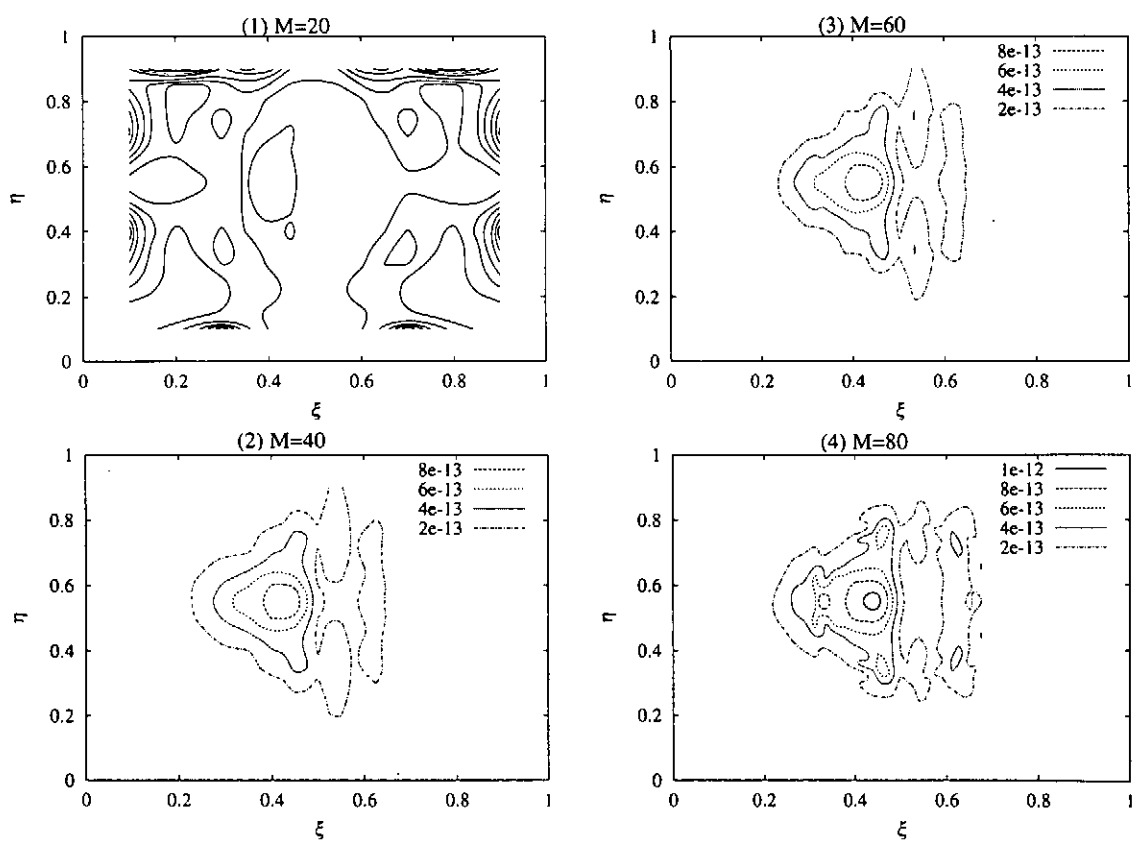


図 10. $E_{\xi\eta}(\xi, \eta)$ の等高線図.

On Numerical Computation of Lyapunov Exponents of Attractors in Free Boundary Problems*

Hitoshi IMAI¹, Toshiki TAKEUCHI¹, Shewli S. SHANTA²
and Naoyuki ISHIMURA³

¹*Faculty of Engineering, The University of Tokushima,*

²*Graduate School of Engineering, The University of Tokushima,*

³*Faculty of Economics, Hitotsubashi University,*

Abstract

In the paper a method for numerical computation of Lyapunov exponents of attractors in free boundary problems is presented. For one-dimensional free boundary problems it facilitates the derivation of ODE systems which are very useful in the concrete analysis. It is applied to a free boundary problem with some parameters. Various attractors are found numerically and their Lyapunov exponents are computed.

Key Words : free boundary, chaos, attractor, spectral method, Lyapunov exponent

1 Introduction

Free boundary problems are boundary value problems defined on domains whose boundaries are unknown and must be determined as the solution. Due to nonlinearity they easily involve chaotic phenomena. Free boundary problems are very important from the practical view point, so investigation of chaotic phenomena is very important.

The investigation is carried out via analysis of bifurcation and attractors. Bifurcation phenomena in a free boundary problem related to natural convection were analyzed numerically[9]. Attractors in free boundary problems were analyzed theoretically[1]. Such attractors are considered in the infinite-dimensional space. It is very difficult to carry out their concrete analysis.

*This work is partially supported by Grant-in-Aid for Scientific Research(Nos. 09440080 and 10354001). This work is also a collaboration with CCSE of Japan Atomic Energy Research Institute.

Attractors of the ODE system is very important. This is because it is useful for concrete analysis[7]. Numerical computation of Lyapunov exponents is easily carried out. If there exist positive Lyapunov exponents, chaotic phenomena exist. However, it is very difficult to derive the ODE system which approximates the PDE system describing a free boundary problem with chaotic phenomena.

In the paper a method for numerical computation of attractors in free boundary problems and their Lyapunov exponents is presented. To see the procedure of the method it is applied to a free boundary problem with some parameters which is of the type of a two-phase Stefan problem. The method consists of SCM(Spectral Collocation Method) and the fixed domain method. For one-dimensional free boudary problems it facilitate the derivation of ODE systems.

2 Test problem

We consider the following one-dimensional free boundary problem with some parameters.

Problem 1. For parameters $|\alpha^\pm|, |\beta|, |s_0| < 1$, $0 \leq r \leq 1$, q and ω^\pm , find $u^\pm(x, t)$ and $s(t)$ such that

$$\begin{aligned} u_t^\pm(x, t) &= u_{xx}^\pm(x, t) + g^\pm(x, t), & 0 < t, \quad 0 < x < s(t), \\ u^\pm(\mp 1, t) &= h^\pm(t), & 0 \leq t, \\ u^\pm(s(t), t) &= 0, & 0 \leq t, \\ u^+(x, 0) &= u^+(x), & -1 < x < s_0, \\ u^-(x, 0) &= u^-(x), & s_0 < x < 1, \\ \frac{d}{dt}s(t) &= -k^+(t)u_x^+(s(t), t) + k^-(t)u_x^-(s(t), t), & 0 < t, \\ s(0) &= s_0 \end{aligned}$$

where

$$\begin{aligned} k^\pm(t) &= r + (1-r) \frac{1}{2} \frac{1 \pm \beta \sin t}{\pm 1 + \alpha^\pm \sin t} \beta \cos t, \\ h^\pm(t) &= \pm 1 + \alpha^\pm \sin(\omega^\pm t), \\ g^\pm(x, t) &= q \left\{ \pm \frac{(\beta - \alpha^\pm) \cos t}{(1 \pm \beta \sin t)^2} (x - \beta \sin t) \pm \frac{\pm 1 + \alpha^\pm \sin t}{1 \pm \beta \sin t} \beta \cos t \right\}, \\ u^+(x) &= a(x - s_0)^2 + a(s_0 + 1)(x - s_0) - \frac{x - s_0}{s_0 + 1}, \\ u^-(x) &= b(x - s_0)^2 + b(s_0 - 1)(x - s_0) + \frac{x - s_0}{s_0 - 1}. \end{aligned}$$

Parameters a, b should be determined such that $u^+(x) \geq 0$, $u^-(x) \leq 0$.

Remark. For $a = b = s_0 = r = 0$, $\omega^\pm = 1$ and $q = 1$, there are exact solutions as follows:

$$\begin{aligned} s(t) &= s_p(t) \equiv \beta \sin t, \\ u^\pm(x, t) &= \frac{\mp h^\pm(t)}{1 \pm s_p(t)} (x - s_p(t)) = \mp \frac{\pm 1 + \alpha^\pm \sin t}{1 \pm \beta \sin t} (x - \beta \sin t). \end{aligned}$$

3 Our method

In analysis of chaotic phenomena attractor plays an very important role. Attractors in free boundary problems were analyzed theoretically[1]. Such attractors are considered in the infinite-dimensional space. It is very difficult to carry out concrete analysis to such attractors.

Attractors of the ODE system is very useful for concrete analysis. However, it is very difficult to derive the ODE system which approximates the PDE system describing a free boundary problem with chaotic phenomena.

In this section a method is presented. It consists of the fixed domain method and the spectral (collocation) method. To see its procedure it is applied to Problem 1.

3.1 Spectral collocation method

The spectral methods are superior in accuracy[3]. In particular, SCM(Spectral Collocation Method) is preferable to nonlinear problems.

In the paper, SCM using Chebyshev Polynomials and Chebyshev-Gauss-Lobatto case's collocation points is used. A function $u(x)$ in $[-1, 1]$ is approximated by the N the order Chebyshev Polynomials as follows:

$$u(x) = \sum_{k=0}^N \tilde{u}_k T_k(x), \quad T_k(x) = \cos(k \arccos x).$$

There is an inversion formula

$$u_j = \sum_{k=0}^N \tilde{u}_k T_k(x_j), \quad \tilde{u}_k = \frac{2}{N \bar{c}_k} \sum_{j=0}^N \frac{1}{\bar{c}_j} u_j T_k(x_j)$$

where

$$\bar{c}_j = \begin{cases} .2, & j = 0, N, \\ 1, & \text{otherwise} \end{cases}, \quad x_j = \cos \frac{j\pi}{N}, \quad j = 0, 1, \dots, N.$$

$\{x_j\}$ is called Chebyshev-Gauss-Lobatto case's collocation points. Derivatives at the collocation points are easily computed from $\{u_j\}$. These mean that it is easy to increase the order of the approximatin by increasing the number of collocation points. This feature is quite remarkable and different from other discretization mthods. By using this feature we developed IPNS(Infinite-Precision Numerical Simulation)[5, 6]. The application of SCM is similar to that of FDM. So, it is easily applied to the nonlinear system.

3.2 Fixed domain method

SCM can not be applied directly to free boundary problems due to the unknown shape of the domain. To avoid this difficulty, we use the fixed domain method[4, 8, 9]. Mapping functions are introduced for mapping the unknown domain to the fixed rectangular domain.

We use the following variable transformation : $(x, t) \rightarrow (\xi, \tilde{t})$ such that

$$\begin{aligned} t &= t(\tilde{t}) = \tilde{t}, & 0 \leq \tilde{t}, \\ x &= x(\xi, \tilde{t}) = \begin{cases} \frac{\tilde{s}(\tilde{t}) + 1}{2}(\xi + 1) - 1, & 0 \leq \tilde{t}, \quad -1 \leq x \leq s(\tilde{t}), \\ \frac{1 - \tilde{s}(\tilde{t})}{2}(\xi - 1) + 1, & 0 \leq \tilde{t}, \quad s(\tilde{t}) \leq x \leq 1. \end{cases} \end{aligned}$$

Using these mapping functions, we define

$$\tilde{s}(\tilde{t}) = s(t(\tilde{t})), \quad \tilde{u}^+(\xi, \tilde{t}) = u^+(x(\xi, \tilde{t}), t(\tilde{t})), \quad \tilde{u}^-(\xi, \tilde{t}) = u^-(x(\xi, \tilde{t}), t(\tilde{t})).$$

Then, Problem 1 is transformed in the following fixed boundary problem.

Problem 2. Find $\tilde{u}^\pm(\xi, \tilde{t})$ and $\tilde{s}(\tilde{t})$ such that

$$\begin{aligned} \tilde{u}_t^+(\xi, \tilde{t}) = & -k^+(\tilde{t}) \frac{2(\xi+1)}{\{\tilde{s}(\tilde{t})+1\}^2} \tilde{u}_\xi^+(1, \tilde{t}) \tilde{u}_\xi^+(\xi, \tilde{t}) \\ & -k^-(\tilde{t}) \frac{2(\xi+1)}{\{\tilde{s}(\tilde{t})\}^2-1} \tilde{u}_\xi^+(-1, \tilde{t}) \tilde{u}_\xi^+(\xi, \tilde{t}) + \frac{4}{\{\tilde{s}(\tilde{t})+1\}^2} \tilde{u}_{\xi\xi}^+(\xi, \tilde{t}) \\ & +q \left\{ \frac{(\beta-\alpha^+) \cos \tilde{t}}{(1+\beta \sin \tilde{t})^2} \left(\frac{\tilde{s}(\tilde{t})+1}{2} (\xi+1) - 1 - \beta \sin \tilde{t} \right) \right. \\ & \left. + \frac{(1+\alpha^+ \sin \tilde{t}) \beta \cos \tilde{t}}{1+\beta \sin \tilde{t}} \right\}, \quad 0 < \tilde{t}, \quad -1 < \xi < 1, \end{aligned}$$

$$\tilde{u}^+(-1, \tilde{t}) = 1 + \alpha^+ \sin(\omega^+ \tilde{t}), \quad 0 \leq \tilde{t},$$

$$\tilde{u}^+(1, \tilde{t}) = 0, \quad 0 \leq \tilde{t},$$

$$\tilde{u}^+(\xi, 0) = \left(\frac{a}{4} (s_0+1)(\xi+1) - \frac{1}{2(s_0+1)} \right) (s_0+1)(\xi-1), \quad -1 < \xi < 1,$$

$$\begin{aligned} \tilde{u}_t^-(\xi, \tilde{t}) = & -k^+(\tilde{t}) \frac{2(\xi-1)}{\{\tilde{s}(\tilde{t})\}^2-1} \tilde{u}_\xi^+(1, \tilde{t}) \tilde{u}_\xi^-(\xi, \tilde{t}) \\ & -k^-(\tilde{t}) \frac{2(\xi-1)}{\{\tilde{s}(\tilde{t})-1\}^2} \tilde{u}_\xi^-(-1, \tilde{t}) \tilde{u}_\xi^-(\xi, \tilde{t}) + \frac{4}{\{\tilde{s}(\tilde{t})-1\}^2} \tilde{u}_{\xi\xi}^-(\xi, \tilde{t}) \\ & +q \left\{ -\frac{(\beta-\alpha^-) \cos \tilde{t}}{(1-\beta \sin \tilde{t})^2} \left(\frac{1-\tilde{s}(\tilde{t})}{2} (\xi-1) + 1 - \beta \sin \tilde{t} \right) \right. \\ & \left. + \frac{(1-\alpha^- \sin \tilde{t}) \beta \cos \tilde{t}}{1-\beta \sin \tilde{t}} \right\}, \quad 0 < \tilde{t}, \quad -1 < \xi < 1, \end{aligned}$$

$$\tilde{u}^-(-1, \tilde{t}) = 0, \quad 0 \leq \tilde{t},$$

$$\tilde{u}^-(1, \tilde{t}) = -1 + \alpha^- \sin(\omega^- \tilde{t}), \quad 0 \leq \tilde{t},$$

$$\tilde{u}^-(\xi, 0) = \left(\frac{b}{4} (s_0-1)(\xi-1) - \frac{1}{2(s_0-1)} \right) (s_0-1)(\xi+1), \quad -1 < \xi < 1,$$

$$\frac{d}{d\tilde{t}} \tilde{s}(\tilde{t}) = -k^+(\tilde{t}) \frac{2}{\tilde{s}(\tilde{t})+1} \tilde{u}_\xi^+(1, \tilde{t}) - k^-(\tilde{t}) \frac{2}{\tilde{s}(\tilde{t})-1} \tilde{u}_\xi^-(-1, \tilde{t}), \quad 0 < \tilde{t},$$

$$\tilde{s}(0) = s_0.$$

3.3 ODE system

Numerical computation of attractors can be carried out by the applicaiton of SCM in space and time[4] to Problem 2. However, this procedure is not proper for numerical

computation of Lyapunov exponents. The derivation of the ODE system is necessary. The ODE system is very important not only in numerical computation of Lyapunov exponents but also in theoretical analysis. For its derivation SCM not in time but in space is applied.

In the paper the order of the approximation in space N_x is fixed to be 2. Of course, it is very easy to increase N_x . This means original attractors of the PDE system can be approximated arbitrarily by the method. So, the method is very important from the theoretical view point. After the application of SCM in space with $N_x = 2$ the ODE system for parameters $q = 0$, $r = 1$, $\alpha^\pm = \beta = 0.5$ is derived as follows.

Problem 3. Find $u^\pm(t)$ and $s(t)$ such that

$$\begin{aligned} \frac{d}{dt}u^+(t) = & -\frac{1}{8(s(t)+1)^2} (8u^+(t) - \sin(\omega^+t) - 2) (\sin(\omega^+t) + 2) \\ & + \frac{1}{8(s(t)^2 - 1)} (8u^-(t) - \sin(\omega^-t) + 2) (\sin(\omega^+t) + 2) \\ & - \frac{2}{(s(t)+1)^2} (4u^+(t) - \sin(\omega^+t) - 2), \quad t > 0, \end{aligned}$$

$$\begin{aligned} \frac{d}{dt}u^-(t) = & -\frac{1}{8(s(t)^2 - 1)} (8u^+(t) - \sin(\omega^+t) - 2) (\sin(\omega^-t) - 2) \\ & - \frac{1}{8(s(t) - 1)^2} (8u^-(t) - \sin(\omega^-t) + 2) (\sin(\omega^-t) - 2) \\ & - \frac{2}{(s(t) - 1)^2} (4u^-(t) - \sin(\omega^-t) + 2), \quad t > 0, \end{aligned}$$

$$\begin{aligned} \frac{d}{dt}s(t) = & -\frac{1}{2(s(t)+1)} (8u^+(t) - \sin(\omega^+t) - 2) \\ & - \frac{1}{2(s(t)-1)} (8u^-(t) - \sin(\omega^-t) + 2), \quad t > 0, \end{aligned}$$

$$u^+(0) = u_0^+, \quad u^-(0) = u_0^-, \quad s(0) = s_0.$$

Here $u^+(t)$ and $u^-(t)$ represent $u^+(\frac{s(t)-1}{2}, t)$ and $u^-(\frac{1-s(t)}{2}, t)$, respectively. For the other parameters the derivation of the ODE system is same.

3.4 Transformation into the autonomous system

The ODE system in Problem 3 is not autonomous. So, transformation into the autonomous system is necessary for numerical computation of Lyapunov exponents. It can be done by introducing a new parameter θ [2]. Then, Problem 3 is transformed into the following problem.

Problem 4. Find $u^\pm(t)$, $s(t)$ and $\theta(t)$ such that

$$\begin{aligned} \frac{d}{dt}u^+(t) = & -\frac{1}{8(s(t)+1)^2} (8u^+(t) - \sin(\omega^+\theta(t)) - 2) (\sin(\omega^+\theta(t)) + 2) \\ & + \frac{1}{8(s(t)^2 - 1)} (8u^-(t) - \sin(\omega^-\theta(t)) + 2) (\sin(\omega^+\theta(t)) + 2) \end{aligned}$$

$$\begin{aligned}
& -\frac{2}{(s(t)+1)^2} (4u^+(t) - \sin(\omega^+\theta(t)) - 2), \quad t > 0, \\
\frac{d}{dt}u^-(t) &= -\frac{1}{8(s(t)^2-1)} (8u^+(t) - \sin(\omega^+\theta(t)) - 2) (\sin(\omega^-\theta(t)) - 2) \\
& -\frac{1}{8(s(t)-1)^2} (8u^-(t) - \sin(\omega^-\theta(t)) + 2) (\sin(\omega^-\theta(t)) - 2) \\
& -\frac{2}{(s(t)-1)^2} (4u^-(t) - \sin(\omega^-\theta(t)) + 2), \quad t > 0, \\
\frac{d}{dt}s(t) &= -\frac{1}{2(s(t)+1)} (8u^+(t) - \sin(\omega^+\theta(t)) - 2) \\
& -\frac{1}{2(s(t)-1)} (8u^-(t) - \sin(\omega^-\theta(t)) + 2), \quad t > 0, \\
\frac{d}{dt}\theta(t) &= 1 \\
\theta(0) &= 0. \\
u^+(0) &= u_0^+, \quad u^-(0) = u_0^-, \quad s(0) = s_0.
\end{aligned}$$

4 Numerical results

In this section, numerical results are shown.

Fig. 1 shows numerical results for $q = 1$, $r = 0$, $\alpha^\pm = \beta = 0.5$, $a = b = 0$, $\omega^\pm = 1$. For $s_0 = 0$ exact solutions are known as in Remark and they are periodic. Fig.1 (a) shows numerical solutions are very satisfactory in accuracy. Unfortunately, Fig.1 (b) shows these solutions are not attractors.

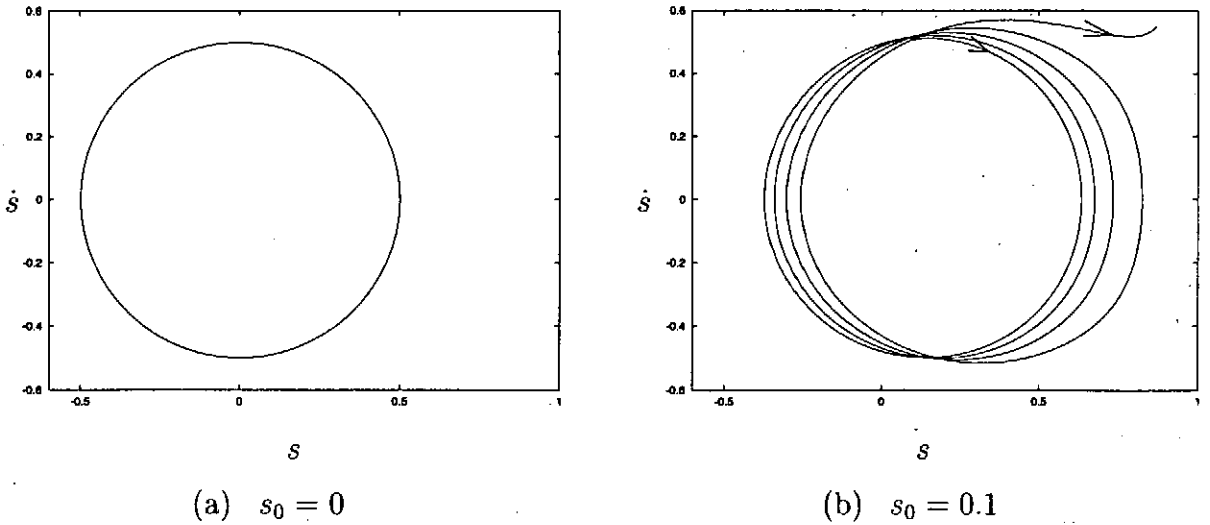


Fig.1. Numerical results in the (s, \dot{s}) plane for $q = 1$, $r = 0$, $\alpha^\pm = \beta = 0.5$, $a = b = 0$, $\omega^\pm = 1$.

Fig.2 shows attractors in the (s, \dot{s}) plane for $q = 1$, $r = 1$, $\omega^\pm = 1$. In these cases there are no exact solutions. Numerical solutions converge to the attractors. Fig.2 (a) shows in this case the attractor is a closed curve. This means periodic solutions are stable. Fig.2 (b) shows in this case the attractor is a fixed point. This means the steady state is stable.

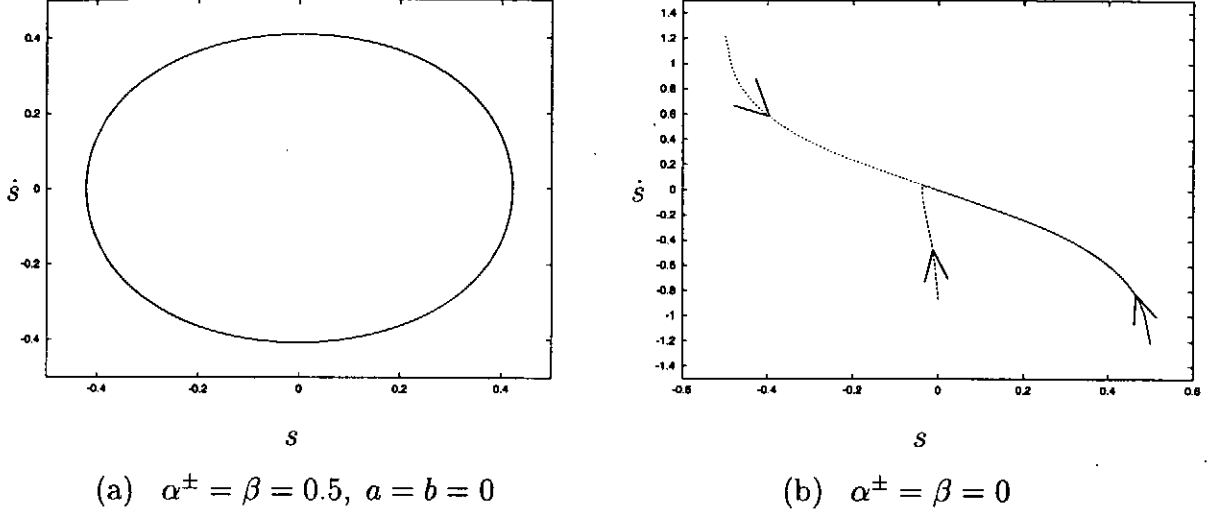


Fig.2. Attractors in the (s, \dot{s}) plane for $q = 1$, $r = 1$, $\omega^\pm = 1$.

Fig.3 shows the attractors in the solution space (u^+, u^-, s) . Fig.3 (a) shows the same attractor in Fig.2 (a). Fig.3 (b) shows in this case the attractor is a torus.

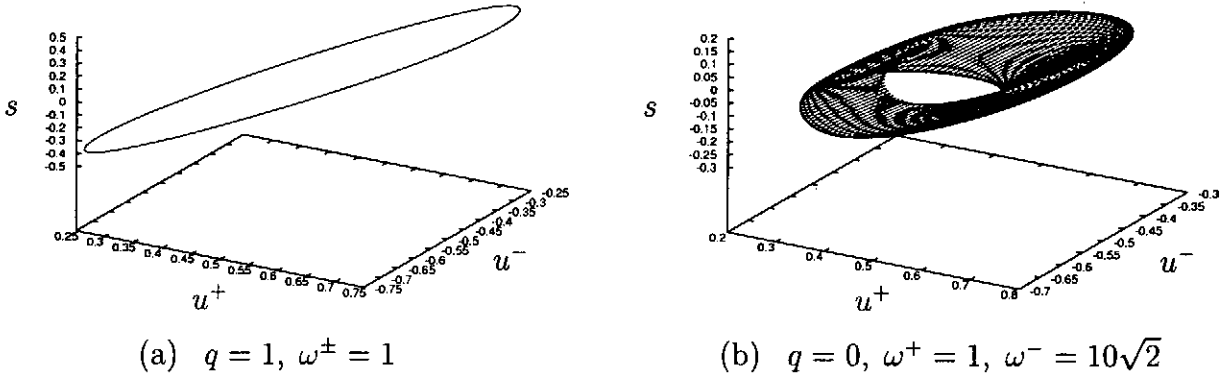


Fig.3. Attractors in the solution space for $r = 1$, $\alpha^\pm = \beta = 0.5$, $a = b = 0$.

Figs. 4 and 5 shows attractors and Lyapunov exponents. Attractors are computed from Problem 3. The exponents are computed from both Problem 4 and its linearized problem.

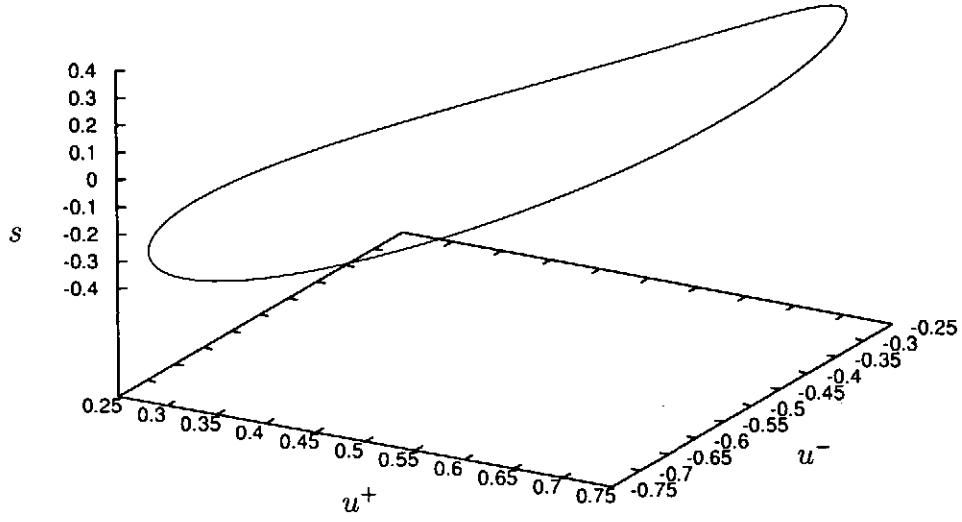


Fig.4. Attractor in the solution space for $q = 0$, $r = 1$, $\alpha^\pm = \beta = 0.5$, $a = b = 0$, $\omega^\pm = 1$.
Lyapunov exponents : $\lambda_1 = -1.360$, $\lambda_2 = -6.712$, $\lambda_3 = -19.13$, $\lambda_4 = 0.000$

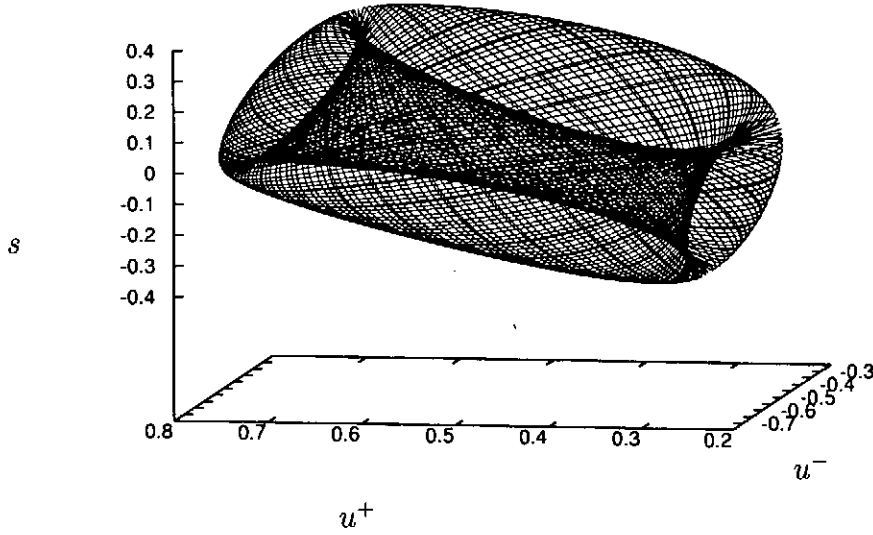


Fig.5. Attractor in the solution space for $q = 0$, $r = 1$, $\alpha^\pm = \beta = 0.5$, $a = b = 0$,
 $\omega^+ = 1$, $\omega^- = \sqrt{2}$. Lyapunov exponents : $\lambda_1 = -1.289$, $\lambda_2 = -7.228$,
 $\lambda_3 = -15.75$, $\lambda_4 = 0.000$

$\lambda_4 = 0.000$ is due to the artificial parameter θ which is introduced in the transformation into the autonomous system.

5 Conclusion

In the paper a method for numerical computation of attractors in free boundary problems and their Lyapunov exponents is presented. The method consists of SCM(Spectral Collocation Method) and the fixed domain method. To see the procedure of the method it is applied to a free boundary problem with some parameters which is of the type of a two-phase Stefan problem. Various attractors are found numerically and their Lyapunov exponents are computed.

For one-dimensional free boudary problems the method facilitate the derivation of ODE systems which approximate PDE system describing free boundary problems. SCM is used in the methos, so original attractors of the PDE system can be approximated arbitrarily. This means the method plays a very important role in theoretical analysis.

References

- [1] T. Aiki, Global Attractors for Two-Phase Stefan Problems in One-Dimensional Space, *Abstract and Applied Analysis*, **2**(1-2), pp.47-66(1997).
- [2] G.L. Baker and J.P. Gollub, *Chaotic Dynamics, an introduction*, Cambridge Univ. Press, 1990.
- [3] C. Canuto, et al., *Spectral Methods in Fluid Dynamics*, Springer-Verlag, New York, 1988.
- [4] H. Imai, Y. Shinohara and T. Miyakoda, Application of Spectral Collocation Methods in Space and Time to Free Boundary Problems, "Hellenic European Research on Mathematic and Informatics '94 (E.A. Lipitakis, ed.)," Hellenic Mathematical Society, **2**, pp.781-786(1994).
- [5] H. Imai et al., On numerical simulation of partial differential equations in arbitrary precision, *RIMS Kokyuroku*, Kyoto University, **1040**, pp.92-99(1998). (in Japanese)
- [6] H. IMAI, T. TAKEUCHI and M. KUSHIDA, On Numerical Simulation of Partial Differential Equations in Infinite Precision, *Advances in Mathematical Sciences and Applications*, **9**(2), pp.1007-1016(1999).
- [7] H. Imai, N. Ishimura and M. Nakamura, Convergence of Attractors for the Simplified Magnetic Bénard Equations, *European Journal of Applied Mathematics*, **7**, pp.53-62(1996).
- [8] Y. Katano, T. Kawamura and H. Takami, Numerical Study of Drop Formation from a Capillary Jet Using a General Coordinate System, "Theoretical and Applied Mechanics," Univ. Tokyo Press, pp.3-14(1986).
- [9] Zhou W., H. Imai and M. Natori, Numerical Study of Convection with a Free Surface by a Spectral Method, *GAKUTO Internat. Ser. Math. Sci. Appl.*, **1**, pp.49-60(1993).

MHD Stability Analysis of Helical System Plasmas

Yuji Nakamura

Graduate School of Energy Science

Kyoto University

Gokasho, Uji, Kyoto 611-0011, Japan

Abstract

Several topics of the MHD stability studies in helical system plasmas are reviewed with respect to the linear and ideal mode mainly. Difference of the method of the MHD stability analysis in helical system plasmas from that in tokamak plasmas is emphasized. Lack of the cyclic (symmetric) coordinate makes an analysis more difficult. Recent topic about TAE modes in a helical system is also described briefly.

Keywords

MHD stability, helical system, non-axisymmetric torus, energy principle, reduced MHD equation, ballooning mode, TAE mode

1. Introduction

MHD 安定性を議論する上で、まず最初に考えなければならないのは MHD 平衡である。トラスプラズマの MHD 平衡を考えると、軸対称系かそうでないかが重要となる。トカマクを代表とする軸対称プラズマでは（トカマクでも、トロイダルコイルの離散性を考えると厳密には軸対称でないという議論があるが）、トロイダル角 ϕ がサイクリック座標（または ignorable coordinate）となり、平衡量はトロイダル角に依存しない。ここでポロイダル磁束関数、トロイダル角、ポロイダル角と円柱座標 (r, ϕ, z) は図 1 のように定義する。したがって、軸対称平衡は通常 Grad-Shafranov 方程式で計算され、二次元実座標 (r, z) もしくは磁気座標 (ψ, θ) で解析することができる。

これに対して非軸対称系では平衡量がトロイダル方向の依存性を持つため、三次元 (r, ϕ, z) または (ψ, θ, ϕ) 座標系で計算する必要がある。このことは単に次元数が増えるという量的な違いだけでなく、対称性がなくなることによりサイクリック座標を持たなくなるため質的な違いが現れ、複

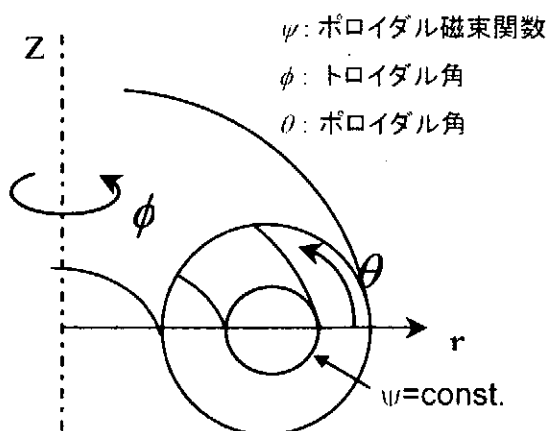


図 1 座標系の定義

雑さが増すことを意味している。このような非軸対称トーラス系の代表がヘリカル系トーラスプラズマである。日本ではLHD、CHS、Heliotron J などの高温プラズマ閉じ込め装置が挙げられる。例として、Heliotron J のコイル系とプラズマを図2に示す。Heliotron J は $L=1$ ヘリカル軸ヘリオトロン装置であり、プラズマは主に $L=1$ ヘリカルコイルの作る磁場で閉じ込められるが、プラズマ自身もヘリカル状にねじれている。

トーラスプラズマのMHD安定性の線形解析を行う場合、磁気座標上で摂動ベクトルを導入するのが一般的である。摂動ベクトルをトロイダル角でフーリエ級数展開し

$$\vec{\xi}(\psi, \theta, \phi) = \sum \vec{\xi}_n \cos(n\phi)$$

と表すと、軸対称系では平衡量にトロイダル角依存性がないためトロイダルモード数 (n) ごとに線形解析ができる。これに対し、非軸対称系では平衡量にトロイダル依存性があるため、平衡量を通じて異なったトロイダルモード数を持つ摂動モード間でモード結合が起こり、トロイダルモード数ごとの解析はできない。

以下の節では具体例を出して、これまでに行われてきたヘリカル系プラズマに対するMHD安定性の解析手法について簡単に説明する。

2. Energy Principle

理想MHD方程式に摂動ベクトルを用いて、二次形式で表すと MHD 安定性の線形解析は Lagrangian

$$L = \omega^2 K - \delta W$$

$$\begin{cases} K = \frac{1}{2} \int d\tau [\rho |\vec{\xi}|^2] \\ \delta W = \frac{1}{2} \int d\tau [\vec{Q}^2 + \vec{J} \times \vec{\xi} \cdot \vec{Q} + (\vec{\xi} \cdot \nabla p)(\nabla \cdot \vec{\xi}) + \mu p(\nabla \cdot \vec{\xi})] \end{cases}$$

に対する極値問題(固有値問題)となる[1]。ここで

$$\vec{Q} = \nabla \times (\vec{\xi} \times \vec{B})$$

は摂動磁場ベクトルを表す。その他の記号は一般的なものを使い、ここでは説明しない。また、ポテンシャルエネルギー δW については簡単のためプラズマ内部だけを考えている。良く知られているように、理想MHDにおいてLagrangianは自己随伴性を持っているため固

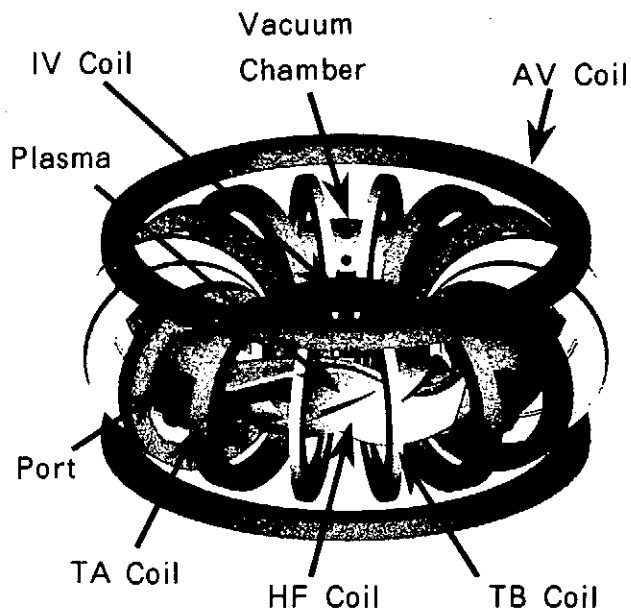


図2 Heliotron J のコイル系とプラズマ形状

有値 ω^2 は実数であり、正ならば安定（振動解）、負ならば不安定（指数関数的に成長）である。

トカマクプラズマは軸対称系なので前節で述べた通り、異なったトロイダルモード数を持つモードごとに解析し、固有値を求めることができる。したがって二次元的に解析できる。通常、Lagrangian の極値問題は、数値的には有限要素法を用いて行列の固有値問題に帰着させて解かれる。有名なコードとしては ERATO と PEST が挙げられる。ERATO では (ψ, θ) の二次元で有限要素法を用いている。PEST ではポロイダル方向にはスペクトル法（フーリエ展開）を用い、径方向一次元で有限要素法を適用している。

ヘリカル系プラズマでは、その三次元性のため直接 Lagrangian の極値問題を数値的に解くことは困難であった。このため、ステラレータ展開法と呼ばれる近似が用いられた[2]。ステラレータ展開法では平衡磁場を

$$\mathbf{B} = B_0 \mathbf{e}_\phi + \underbrace{\mathbf{B}_\delta(R, \phi, Z)}_{O(\delta)} + \underbrace{\mathbf{B}_\beta(R, Z) + \mathbf{B}_o(R, Z) + \mathbf{B}_\kappa(R, Z)}_{O(\delta^2)} + O(\delta^3)$$

のようにオーダリングし摂動展開する。ここで、 \mathbf{B}_δ はヘリカルコイルの作る磁場のうちトロイダル方向に振動する成分、 \mathbf{B}_β 、 \mathbf{B}_o 、 \mathbf{B}_κ はそれぞれプラズマ圧力による反磁性トロイダル磁場成分、磁力線に平行な平衡電流によるポロイダル磁場成分、トーラス効果によるトロイダル磁場成分である。摂動ベクトルはヘリカルコイルのトロイダル周期数 M のオーダーを持つ短波長（高調波）摂動と長波長の摂動からなると仮定し、

$$\tilde{\xi} = \sum \tilde{\xi}_{k,n} \exp[-i(kM + n)\phi] \quad n/kM = O(\delta^2)$$

とする。これらを用いて、 δW をオーダリングし最も不安定な摂動を考えると、最低次から

$$\tilde{\xi}^{(0)} = \sum \tilde{\xi}_{0,n}^{(0)} \exp(-in\phi)$$

が、二次のオーダーから

$$\tilde{\xi}^{(1)} = -(R_0/B_0) \nabla \times [\tilde{\xi}_\perp^{(0)} \times \int \tilde{\mathbf{B}}_\delta d\phi]$$

が得られる。これより、一次の摂動量は短波長摂動であるが、最低次の長波長摂動ベクトルを用いて書き表されることがわかる。これらを用いると、不安定性は四次のオーダーのポテンシャルエネルギー

$$\delta W_n^{(4)} = \frac{1}{2} \int [\bar{\mathbf{Q}}_n|^2 + p'(\tilde{\xi}_n \cdot \nabla \psi)(\tilde{\xi}_n^* \cdot \nabla \Omega) - \bar{\mathbf{J}}_\parallel \cdot \bar{\mathbf{Q}}_n \times \tilde{\xi}_n^*] d\tau + c.c.$$

$$\bar{\mathbf{Q}}_n = -in(B_0/R_0)\tilde{\xi}_n + (1/2\pi)\nabla \times [(\tilde{\xi}_n \cdot \nabla \psi)\nabla \phi]$$

$$\Omega = 2(R - R_0)/R_0 + \langle B_\delta^2 \rangle / B_0^2$$

$$\tilde{\xi}_n \equiv \tilde{\xi}_\perp^{(0)}(\psi, \theta)$$

から現れる。ここで平衡量はオーダリングに矛盾がないように、ステラレータ展開法で求められた（トロイダル方向に依存性のない）最低次の平衡量を用いなければならない。この式において、ゼロ次の摂動ベクトルは

$$\nabla \cdot \bar{\xi}^{(0)} = 0$$

の非圧縮条件を満足している。また $\xi' = \xi - f\mathbf{B}$ と変数変換することにより $\xi_{||}^{(0)} = 0$ とすることができる。これより、速い磁気音波と音波は取り除かれるとともに摂動ベクトルを

$$\bar{\xi}^{(0)} = \bar{\xi}_{\perp}^{(0)} = \nabla\phi \times \nabla\eta$$

のように、一つの流れ関数 η だけで表すことができる。したがってこの計算はトカマクに対して PEST2 コードが行っているのと同様に行える。そこで、この流れ関数を用いて、

$$\delta W = \pi \sum_{\ell, m} \int_0^{2\pi} d\psi \int_0^{2\pi} e^{i(\ell-m)\theta} d\theta (\eta_m^* \quad \eta_{m,\psi}^*) \begin{pmatrix} W & Y^* \\ Y & Z \end{pmatrix} \begin{pmatrix} \eta_{\ell} \\ \eta_{\ell,\psi} \end{pmatrix}$$

と書き、 K についても同様の二次形式で表す。この固有値問題を解くコード STEP が PEST2 をベースに開発された。PEST2 では運動エネルギーの評価は正確でなく固有値は物理的な成長率を表さず、その正負が重要であるのに対し、ステラレータ展開法に基づく STEP では近似の範囲内で運動エネルギーは正しく評価されており、物理的な成長率が得られる。ステラレータ展開法では、ある意味で平均的な平衡量と摂動を用いて二次元的に安定性解析が行われているが、摂動の短波長成分 $\xi^{(1)}$ を考慮しており（ゼロ次の摂動量を用いて表されるので陽には式に現れていない）三次元性を無視しているのではないことに注意する必要がある。同様の手法としては、ステラレータ近似法的一种である平均化法に基づいた H-ERATO や TWIST コードなどがある。ただし、これらの手法は全てステラレータ近似に依存しているため、ヘリカルコイルのトロイダル周期数 M が小さく短波長摂動と長波長摂動を分離できない場合には適用できない欠点を持っている。

一方、近年のコンピュータの発展により演算速度と主記憶メモリが飛躍的に増大したため、Lagrangian をステラレータ近似をせず三次元的に評価する計算コード TERPSICHOE と CAS3D が開発された。これらは、三次元平衡コード VMEC で得られた平衡量を Boozer 座標系と呼ばれる一種の磁気座標系で表し取り扱う。数値計算で扱いやすいように摂動ベクトルは

$$\bar{\xi} = \sqrt{g} \xi^s \nabla\theta \times \nabla\phi + \eta \frac{\bar{\mathbf{B}} \times \nabla s}{B^2} + \left(\frac{J(s)}{B^2 \psi'} \eta - \mu \right) \bar{\mathbf{B}}$$

のように表す。ここで、最も危険なモードを扱うため非圧縮条件を使うと遅い磁気音波は落とすことができる。式の上では μ を消去することができ、摂動を (ξ^s, η) のみで表すことができる。さらに、物理的な固有値には興味なく安定・不安定のみ議論するときには、PEST2 と同様に速い磁気音波を落とし、 η を ξ^s から評価することができる。これらのコードでは、ポロイダル角とトロイダル角の両方に対してスペクトル法を採用し、摂動は

$$\xi^s = \sum \xi_{m,n}^s \exp[-i(m\theta + n\phi)]$$

のようにフーリエ表示している。トカマクにおける解析との違いは、平衡量がトロイダル依存性を持つため、異なったトロイダルモード数を持つ摂動モード同士がモード結合し、

ポロイダルモード数だけでなくトロイダルモード数に対しても総和をとる必要があることである。ただし、通常平衡量はトロイダル方向に周期数 M の周期性を持つため、 $n=N$ モードは $n=N \pm jM$ のモードとしか結合しない。そこで、これらを $n=N$ モードファミリーと呼び、モードファミリーごとに安定性解析を行うことができる。

ステラレータ近似に基づく計算コードと、三次元安定性解析コードのベンチマークテストが $M=10$ の LHD プラズマに対して行われた[3]。その結果、安定性のベータ限界において非常によい一致が見られた。また、成長率も概ね一致している。三次元コードの結果によれば、交換型不安定性の固有ベクトルにおいて、高トロイダルモード数を持つモード（短波長モード）は振幅もポテンシャルエネルギーへの寄与も小さく、低トロイダルモード数を持つモード（長波長モード）が支配的である。そこで、CAS3D コードでトロイダルモード結合を無視し長波長モードのみ考慮する計算（トロイダルモード数がゼロの平衡量、すなわちトロイダル方向に単純に平均した平衡量を使った計算）を行ったが、異なる成長率が得られた。したがって、結果として得られる固有ベクトルにおいては短波長モードの寄与は小さいが、長波長モードの短波長モードとのトロイダルモード結合は重要であると考えられる。また、トロイダルモード結合を考慮した計算の方がステラレータ近似に基づく計算と良く一致することは、ステラレータ近似がトロイダルモード結合の主要な効果をうまく取り入れていることを示していると考えられる。ただし、最近の CAS3D を用いたヘリカル系におけるパルーニングモードの研究では、短波長モードが支配的な固有ベクトルが得られている[4]。このような不安定性に対しては、ステラレータ近似は妥当でない。

3. Initial Value Code

エネルギー原理に基づき、Lagrangian の極値問題を解き線形成長率を求める方法に対して、MHD 方程式を初期値問題として解く方法もある。この方法をヘリカル系プラズマに用いる場合、MHD 方程式系にステラレータ展開法や平均化法といったステラレータ近似を適用した簡約化 MHD 方程式系を使うのが一般的である。簡約化 MHD 方程式系は

$$\begin{cases} \frac{\partial \psi}{\partial t} = -\bar{\mathbf{B}} \cdot \nabla \Phi + \eta \Delta_{\perp} \psi, \\ \rho \frac{\partial}{\partial t} \Delta_{\perp} \Phi = \nabla \Phi \times \nabla (\Delta_{\perp} \Phi) \cdot \nabla \phi - \bar{\mathbf{B}} \cdot \nabla (\Delta_{\perp} \psi) + R_0^2 \nabla \Omega \times \nabla p \cdot \nabla \phi, \\ \frac{\partial p}{\partial t} = \nabla \Phi \times \nabla p \cdot \nabla \phi, \end{cases}$$

$$\bar{\mathbf{B}} \cdot \nabla = \frac{B_0}{R_0} \frac{\partial}{\partial \phi} - \nabla \psi \times \nabla \phi \cdot \nabla$$

$$\bar{\mathbf{v}}_{\perp} = \nabla \Phi \times \nabla \phi$$

と書ける[5]。最初の式は磁場の拡散方程式で右辺第二項が電気抵抗による磁場拡散を示す。抵抗をゼロとするとこの式は凍り付きの条件を与える。二番目の式は運動方程式に対応し、速度の流れ関数である静電ポテンシャル Φ のラプラシアン、すなわち渦度の方程式となつて

いる。最後の式は状態方程式に対応している。このヘリカル系プラズマに対する簡約化方程式はトカマクに対するものとほとんど同じであり、磁力線の曲率がヘリカル系における有効曲率 $\nabla\Omega$ に変わっているだけである。

この簡約化方程式系を用いる利点としては、抵抗性不安定性のような非理想モードの解析ができることであり、項を加えることで一部の運動論的效果を取り入れることも可能である。また、上記の簡約化方程式は非線型方程式であり、非線型計算が可能である。ただし、平衡量が複雑な幾何学的依存性を持つと計算が困難なため、非線型計算を行う場合には多くの場合簡単な解析的モデル平衡を用いている。

簡約化方程式系の短所としては、自由境界モードの解析は容易でないことが挙げられる（電気抵抗が非常に大きい冷たい偽プラズマを用いれば可能だと考えられる）。また、安定固有値を求めることができないので、中立安定に近い場合には問題となることがある。さらに、エネルギー原理を用いた場合も同様であるが、ステラレータ近似の妥当性に依存していることも欠点である。

線形計算を行う場合、上記の簡約化方程式をさらに線形化して用いる。線形計算ではトロイダルモード結合はないので通常、径方向には有限差分、ポロイダル方向にはスペクトル法を用いる。プラズマの幾何学形状を考慮して（円柱近似はしない）線形計算を行うコードとしてはFAR（ステラレータ版）やRESORMなどが挙げられる。

一方、非線型計算では一般に平衡に関しては円柱近似をし、径方向には有限差分を用いるが、モード間に非線型モード結合があるので、ポロイダルとトロイダル方向の両方にスペクトル法を用いモードの convolution 計算を行う。

4. Ballooning Mode Equation

無電流平衡が可能なヘリカル系プラズマにおいて、圧力駆動型モードは最も重要な不安定性と考えられる。この圧力駆動型モードの局所安定性条件としては Mercier 条件が有名であり、平衡量の磁気面平均から比較的容易に計算できるのでヘリカル形プラズマの安定性解析では良く用いられている。しかし、Mercier 条件は摂動が磁気面上で広がっている交換型モードの安定性条件であり、連結長が短くなり摂動が磁気面上の不安定な場所に局在するバルーニングモードと呼ばれる不安定性には適用できない。そこで、このモードを解析するためにバルーニングモード方程式が導かれた。

磁力線を曲げるにはエネルギーが必要なため、最も危険なモードは磁力線をほとんど曲げず、磁力線に垂直方向には短波長のフルート（縦溝）型 $k_{\parallel}/k_{\perp} \ll 1$ の摂動（図3）と考えられる。そこで、このことを利用し、WKB 理論による解析を行う。アイコナル近似を行い、摂動を

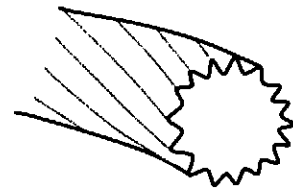


図3 フルート型摂動

$$\tilde{\xi} = \tilde{\xi}(\vec{r}, t) \exp(i\epsilon^{-1}S(\vec{r}))$$

と表す。ここで、 ε は微小パラメータで、アイコナル S は磁力線に垂直方向の速い振動を、エンベロープ ξ は磁力線方向のゆっくりした変化を表す。波数ベクトルはアイコナルを用いて

$$\bar{\mathbf{k}} \equiv \nabla S$$

となり、フルート近似より

$$\bar{\mathbf{B}} \cdot \nabla S = 0$$

である。これらを用いて理想 MHD に対する Lagrangian を ε でオーダリングすると、最低次の Euler-Lagrange 方程式から、バルーニングモード方程式

$$\bar{\mathbf{B}} \cdot \nabla \left(\frac{k_{\perp}^2}{B^2} \bar{\mathbf{B}} \cdot \nabla \xi \right) + 2 \left(\bar{\mathbf{B}} \times \bar{\mathbf{k}}_{\perp} \cdot \nabla p \right) \left(\frac{\bar{\mathbf{B}} \times \bar{\mathbf{k}}_{\perp} \cdot \bar{\mathbf{k}}}{B^4} \right) \xi + \rho_m \omega^2 \left(\frac{k_{\perp}^2}{B^2} \right) \xi = 0$$

$$\bar{\mathbf{B}} = \nabla s \times \nabla (\psi' \theta - \chi' \phi) = \chi' \nabla \alpha \times \nabla s$$

$$\alpha \equiv \phi - q \theta$$

$$\bar{\mathbf{k}}_{\perp} / k_a = \nabla \alpha + \theta_k \nabla q = (\nabla \phi - q \nabla \theta) - (\theta - \theta_k) \nabla q$$

$$\theta_k \equiv k_q / k_a$$

が得られる。ここで、 α は磁気面上での磁力線のラベルである。この方程式における微分演算子は磁力線方向の勾配だけであるので、磁力線方向の座標を導入すると二階の常微分方程式となる。したがって、適当な境界条件を与えると固有値問題となる。波数ベクトルの式の最後の項は永年項であり、波数ベクトルは θ とともに絶対値が増大し物理的な周期性を満たさない。この永年項はフルート近似に起因して現れている。これを模式的に示したのが図 4 である。径方向に「隣り合った」磁気面を考え、それぞれの磁気面上の点を通る磁力線から波面 ($S = \text{一定面}$) をつくる。アイコナル S の勾配が波数ベクトルであるので、2枚の近接した波面を考えれば波数ベクトルが決まる。ところが、有限の磁気シア (∇q) があると磁力線方向に進むにつれ、同一波面上にある2つの磁気面上の磁力線は互いに離れていき、2つの波面は振れるようにして近接しアイコナルの勾配は線形的に増大する。

これにともない波数ベクトルの絶対値も増大する。このように、シアのある系でフルート近似を適用すると常に周期性の問題が生じる。この問題を克服するために θ の定義域を無限遠方まで拡張した covering space と呼ばれる仮想

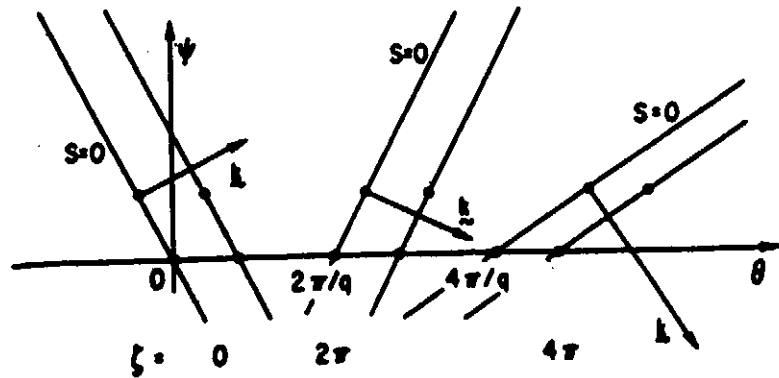


図 4 アイコナルと波数ベクトル

的な空間が考えられた。この空間でバルーニングモード方程式を解いて得られた固有モードは準モードと呼ばれる。この準モードは、それ自身は周期境界条件を満足しない非物理的なモードであるが、重ね合わせると周期境界条件を満足する物理的な固有モードが構築できることが示される。したがってこの準モードを解析することで安定性の議論ができる。

非軸対称系を含めた一般的なトロイダル系におけるバルーニングモードスペクトルについて詳細に議論したのは R.L.Dewar と A.H.Glasser である[6]。最近のヘリカル系プラズマに対するバルーニングモード解析の理論的バックグラウンドは彼らの研究にある。そこで、彼らの議論を簡単に紹介する（なお、図4も彼らの論文から引用した）。

上述のバルーニングモード方程式は磁力線に沿った微分方程式であるので、解く場合には磁力線のラベル (s, α) を指定する必要がある。また、このオーダーでは波数ベクトルは決まらないのでパラメータ θ_k を与える必要もある。すなわちパラメータ (s, α, θ_k) に対して、磁力線方向に分布を持つ固有関数と対応する固有値が得られる。言い換えると分散関係 $\omega^2 = \lambda(s, \alpha, \theta_k)$ が求められる。バルーニングモード方程式を解く上で非軸対称系が軸対称系と異なるのは平衡量が三次元であることと、軸対称系では磁気面上のどの磁力線も等価なため α 依存性はないが、非軸対称系では α もパラメータとなる点である。ほとんどのバルーニングモード解析では、このように準モードと対応する固有値から局所的に安定性を議論している。

パラメータ空間 (s, α, θ_k) における λ の等高面のトポロジ的な分類を試みる。軸対称系では α 依存性はないため、 (s, θ_k) 平面で閉曲線となればトポロジ的に α 方向を軸とする円柱となる。これに対し、非軸対称系では円柱に加え、 α 依存性が強くなると球面となる等高面が現れる。

分散関係はアイコナルの一階偏微分方程式とみなすことができる。したがって特性曲線法で解くことができ、ray 方程式が得られる。これを解いて得られる ray の軌跡は、軸対称系の円柱等高面上では、ergodic に面を覆うか、 α に周期的に螺旋運動するかである。ところが非軸対称系ではこれらに加えて、円柱等高面上で安定固定点へと attracting する軌跡と球面等高面上で不安定固定点から安定固定点へ向かう軌跡が存在する。

軌跡が円柱等高面上を周期的に螺旋運動する場合は、準モードを重ね合わせるときの振幅に対する方程式（次のオーダーまで考えて求められる）、周期性条件、caustics の条件からトロイダルモード数と節点数に対する量子化条件が得られ、これを満足する固有値は離散固有値となる。しかし、非軸対称系で固定点を持つ場合、固定点（特異点）に近づくとつれ θ_k が一定のまま波数ベクトルは発散していくと考えられ、不安定連続固有値を持っている。しかし、このように強い α 依存性をもつ場合に現れる不安定連続固有値についてはあまり良くわかっておらず、WKB 近似を用いない解析で今後明らかにされる必要がある。

5. TAE Mode (Toroidicity-induced shear Alfvén Eigenmode)

近年、大型トカマク装置での D-T 核融合反応実験や核融合反応炉 ITER の設計活動の観点から D-T 反応で生成されるアルファ粒子に関連する物理に興味が集まっており、そのひとつが TAE モードである。

磁気シアまたは密度勾配のある円柱プラズマにおいて、理想 MHD ではよく知られているように、周波数 $\omega^2 > 0$ (振動解) の領域にねじれアルヴェンスペクトルと呼ばれる連続固有値が存在する。ところが、トーラスプラズマではプラズマがトーラス状に曲がっている効果 (トロイダル効果) により、この連続スペクトルの間にギャップが生じ、そこに離散固有値が得られることがある。この離散固有値に対応する固有モードが TAE モードと呼ばれており、通常プラズマの径方向に広がった構造を持つ。

TAE モード自身は振動解であり安定であるが、その周波数はアルヴェン周波数のオーダーである。この周波数は D-T 核融合反応で生成されるアルファ粒子の周回周波数と同程度であるため、逆ランダウダンピングのような波と粒子の相互作用 (運動論的效果) により TAE モードが成長し不安定となりうる。また、アルファ粒子の軌道損失を誘起するとの指摘もある。このため、とくにトカマク装置において多くの研究がなされてきた。

TAE モードにとって本質的なスペクトルギャップはトロイダル効果だけではなく、異なるフーリエモード数を持つ振動モード間にモード結合が起これば生じる。軸対称トカマクではポロイダルモード結合がギャップを作る。トカマクでは主要なポロイダルモード結合がプラズマ柱をトーラスに曲げた効果 (Toroidicity) によるため、これにより生じた離散固有モードを TAE と呼んでいる。しかし、どんなポロイダルモード結合も連続スペクトルにギャップを開け、そこに離散固有モードを生じさせる可能性を持つ。たとえばプラズマ断面の非円形性が引き起こす “Elongation-induced shear Alfvén Eigenmode (EAE)” や “Non-circularity-induced shear Alfvén Eigenmode (NAE)” がその例である。

同様に、平衡量がトロイダル方向に変化している非軸対称トーラスプラズマにおいては、トロイダルモードカップリングによって連続スペクトルギャップが開く可能性がある。したがって一般的な非軸対称トーラスプラズマでは、ポロイダルモードカップリングもトロイダルモードカップリングも考慮する必要がある。ただし 3 節でも述べた通り、通常の三次元 MHD 平衡では、トロイダル方向に周期数 M の周期性があるため、モードファミリーごとに解析すればよいことになる。

ヘリカル系プラズマにおいては平衡量の主要なフーリエ成分は、ヘリカルコイルの巻き線則に対応したポロイダルモード数とトロイダルモード数を持ったヘリカル成分である。このヘリカル成分によるヘリカルモード結合も $\omega/\omega_A \sim qM/2$ 程度の周波数帯にスペクトルギャップを作り、このギャップ内に離散固有モード “Helicity-induced shear Alfvén Eigenmode (HAE)” が現れると考えられる。N.Nakajima らは $L=2$ ヘリオトロンのにおいて、高モード数 HAE が存在することを示した [7]。 $L=2$ ヘリオトロンのの典型的な M は 10 程度である。これらのプラズマでは平衡量のヘリカル成分はかなり大きいので、連続スペクトルに

広いギャップが現れる。しかし、このギャップ周波数はアルヴェン周波数と比べると 10 倍程度大きいので、非軸対称性の強いこれらのプラズマにおいても、周波数がアルヴェン周波数に近い TAE の方が HAE より危険であると予測される。

ヘリカル系プラズマにおいて、長波長の線形理想 TAE モードはステラレータ展開法コードや三次元安定性解析コードによって求められている[8]が、これに対する運動論的効果やその非線型発展については今後の課題である。

6. Summary

ここでは、ヘリカル系プラズマにおける MHD 安定性解析についてのいくつかの話題を紹介した。ヘリカル系プラズマは軸対称性がないため、その解析は容易でない。このため、実際の三次元 MHD 平衡の複雑な構造をできるだけ忠実に考慮し安定性を議論しようとするならば、非常に多くの労力と計算機資源を必要とするため、理想 MHD モードの線形解析のようなトカマクプラズマの研究においてはどちらかといえば基本的な解析も簡単ではない。逆に抵抗性モードの非線型発展のような複雑な問題を考える場合には、平衡に対してスラブ近似や円柱近似、直線ヘリカル近似などの近似を行い単純化するため、平衡の三次元効果を考慮するのは難しい。したがって今後も、両方の立場からさらに研究を進め、できる限り現実的な数値実験を目指すことが重要だと思われる。

References

- [1] J.P.Freidberg, “*Ideal Magnetohydrodynamics*”, Plenum Press, New York (1987).
- [2] J.M.Greene and J.L.Johnson, *Phys. Fluids* **4** (1961) 875.
- [3] Y.Nakamura, T.Matsumoto, M.Wakatani, *et. al.*, *J. Comput. Phys.* **128** (1996) 43.
- [4] N.Nakajima, private communications.
- [5] H.R.Strauss, *Plasma Phys.* **22** (1980) 733.
- [6] R.L.Dewar and A.H.Glasser, *Phys. Fluids* **26** (1983) 3038.
- [7] N.Nakajima, C.Z.Chang and M.Okamoto, *Phys. Fluids B* **4** (1992) 1115.
- [8] N.Nakajima and Y.Nakamura, *J. Plasma and Fusion Research* **75** (1999) 556.

New Applications of Neural Networks for Computational Sciences

Tatsuoki TAKEDA, Xiao Feng MA, Ali LIAQAT, Makoto FUKUHARA

Department of Computer Science

The University of Electrocommunications

1-5-1 Chofu-ga-oka, Chofu, Tokyo 182-8585

Abstract

New applications of multi-layer neural networks for numerical solution methods were studied. It is quite in the nature of things that developing numerical methods with higher efficiency and higher accuracy for solving large-scale problems in the physics and the engineering fields is most important, nevertheless it is also very important that numerical formulation of the problems can be carried out easily or complicated constraining conditions often encountered in the real world can be imposed easily. As a multi-layer neural network is a flexible mapping device representing a continuous function, the learning process of the network can be regarded as a solution process of partial differential equations or integral equations which satisfies the above requirements.

Keywords: Neural Network, Differential Equation, Integral Equation, Collocation Method, Computer Tomography

1. Introduction

Researches of artificial neural networks (hereafter neural networks) revived in the 1980s and since then various kinds of problems are being studied intensively [1-3]. Research themes of the neural networks are categorized as (1) the basic theory of the neural network and problems relating to the biological neural network, (2) development of new learning algorithms with high speed and high accuracy, and (3) applications of the neural networks to real world problems.

As for the application to the scientific diagnostics and relating numerical simulation requirement for high speed and nonlinear analysis methods for data processing is increasing [4]. In relation with it we are aiming at development of new applications of the multi-layer neural network to the field of numerical computation.

2. Neural network collocation method

Learning process of the multi-layer neural network(Fig.1) is to determine the weights assigned to connections between neurons belonging to two adjacent layers

so that the quantity representing the error of the output value from the target value (the object function) is minimized. There are, therefore, various possibilities to apply the neural network to different kinds of problems by choosing the object function in accordance with the problems to be solved. In the usual applications of the multi-layer neural networks a supervising dataset composed of many sets of input data and corresponding output data is first prepared and the network is trained so that the difference between the network output data and the supervising output data is minimized. For this kind of training (learning) process the sum of squared error of the network output data from the supervising output data is employed as the object function to be minimized.

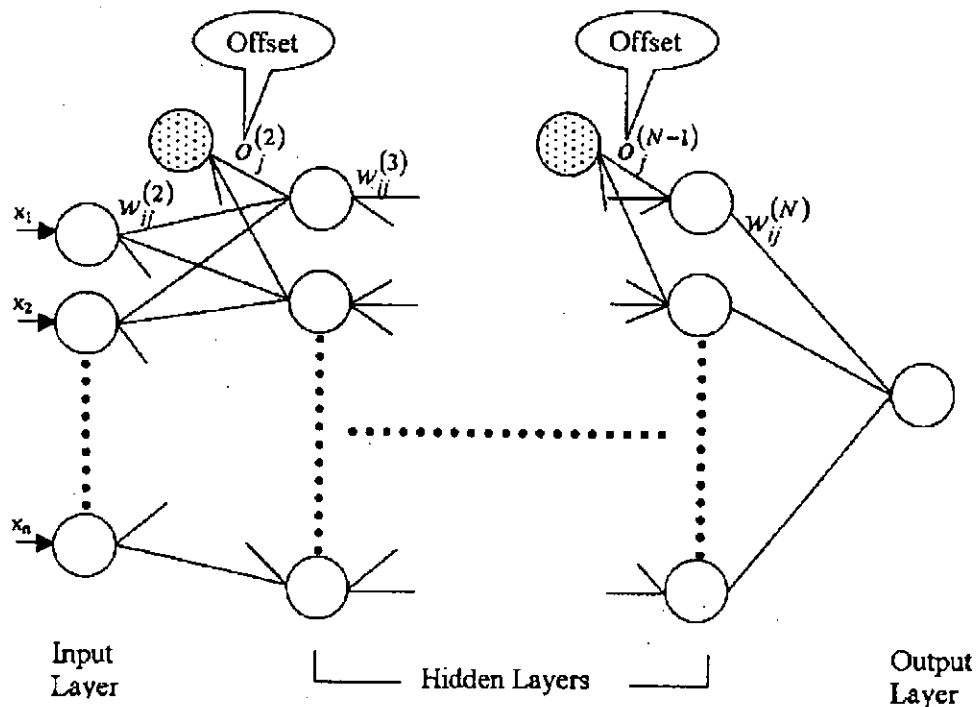


Fig.1 Structure of a multi-layer neural network

When we use the multi-layer neural network for solving partial differential equations independent variables and the unknown variables are employed as the input variables and the output variables of the network, respectively. In this case, as a matter of course, there are no supervising data for the unknown variables. The object function of the network is, however, constructed as described in the following. First, it should be noted that the output variables of the multi-layer neural network can be expressed as analytical functions of the input variables, and, therefore, derivatives of the functions with respect to the independent variables can be expressed analytically. On the basis of the above fact the sum of the squared residuals of the differential equations for collocation points chosen beforehand can be derived instead of the sum of the squared errors of the unknown functions. After the

completion of the learning process a mapping device is constructed, whose input data and output data are the dependent variables and the unknown functions for the present differential equations, respectively. For simplicity we consider a three-layered neural network. The output variables y_k ($k=1,\dots,K$) are expressed analytically as functions of the dependent variables x_i ($i=1,\dots,I$) as follows.

$$y_k = \sum_{j=1}^J w_{kj}^{(2)} \sigma \left(\sum_{i=1}^I w_{ji}^{(1)} x_i + w_{j0}^{(1)} \right) \quad (1)$$

where x , y , w , and σ are the input variables, the output variables, the weights, and the activation function (sigmoid function), in the respective order.

As described in the above this solution method is regarded as a kind of the collocation methods. Two methods for imposing boundary conditions are considered. Milligen, et al. imposed boundary conditions by using an object function with penalty terms representing the conditions [5], and Lagaris, et al. adopted a method where the solution of the differential equations is composed of the output of the network multiplied by appropriately prepared form factors and additional terms satisfying the boundary conditions [6].

There are many unique features in this solution method which are not seen in the conventional solution methods. The most important feature is that the obtained solution is, virtually, not a numerical solution but an analytical solution. Therefore, the solution is differentiable infinite times in the computational domain. If one express a solution by using series of some orthogonal functions the solution has the similar feature, but the solution by the neural network collocation method is considered to be superior in expressing a function by a small set of variable parameters. Secondly this method is essentially an element-free method, and it is very easy to control locally the computational accuracy. Another important feature is that a solution can be obtained easily even when initial conditions and/or boundary conditions are not given on regular mesh points. This feature may be utilized efficiently for a data assimilation problem. A weak point of this method is that it requires, generally, a lot of computational time because a single solution process corresponds to a single learning process of the neural network. Generally speaking the computational cost of the learning by the error back-propagation algorithm carried out on a conventional computer is considerably high and, therefore, the solution method based on the neural network is disadvantageous. However, for problems which require the above features of solution methods there is a possibility that the neural network collocation method may be advantageously used in comparison with the conventional solution methods. Moreover, there is also a possibility that the computational cost may be reduced considerably by employing higher order optimization algorithms instead of the error

back-propagation method of the first order convergence.

2.1 Neural network collocation method

First, the differential equation to be solved is given as

$$D\bar{y} = \bar{g}(\bar{x}), \quad x \in \Omega \quad (2)$$

As the analytical expression of the output variables is given in Eq.(1) for a three-layered neural network, the derivatives of the output variables with respect to the input variables are given as

$$\frac{\partial y_k}{\partial x_l} = \sum_{j=1}^l w_{kj}^{(2)} w_{jl}^{(1)} \sigma' \left(\sum_{i=1}^l w_{ji}^{(1)} x_i + w_{j0}^{(1)} \right) \quad (3)$$

$$\frac{\partial^2 y_k}{\partial x_l \partial x_m} = \sum_{j=1}^l w_{kj}^{(2)} w_{jl}^{(1)} w_{jm}^{(1)} \sigma' \left(\sum_{i=1}^l w_{ji}^{(1)} x_i + w_{j0}^{(1)} \right) \quad (4)$$

By using these expressions the residuals of the differential equations can be expressed analytically, and the object function of the neural network for solving the differential equation (Eq.(2)) is given as

$$\begin{aligned} \bar{y} &\Rightarrow \bar{f}(\bar{x}, \bar{w}) \\ E &= \int \left\{ D\bar{f}(\bar{x}, \bar{w}) - \bar{g}(\bar{x}) \right\}^2 d\bar{x} \end{aligned} \quad (5)$$

To solve the equation we then discretize the above integral and the following equations are obtained.

$$\begin{aligned} E &= \sum_{\text{pattern}} F(\bar{f}(\bar{x}_{\text{pattern}}, \bar{w})) \\ F(\bar{f}(\bar{x}_{\text{pattern}}, \bar{w})) &= \left\{ D\bar{f}(\bar{x}_{\text{pattern}}, \bar{w}) - \bar{g}(\bar{x}_{\text{pattern}}) \right\}^2 \\ \bar{x}_{\text{pattern}} &\in \Omega \end{aligned} \quad (6)$$

where pattern denotes each collocation point.

2.2 Treatment of boundary conditions

For simplicity we consider Dirichlet type boundary conditions given as

$$\bar{y}(\bar{x}_b) = \bar{y}_b, \quad \bar{x}_b \in \Gamma \quad (7)$$

where b denotes the boundary. As described previously the object function for the penalty method is given as

$$\begin{aligned} \hat{E} &= E + \lambda E_b \\ E_b &= \sum_i \left(\bar{y}(\hat{x}_{bi}) - \hat{y}_{bi} \right)^2 \end{aligned} \quad (8)$$

On the other hand, for the method using form factors the solution of the differential

equations f is given by using the form factors and the output of the neural network f_{NN} and an additional term A as

$$\vec{f}(\vec{x}, \vec{w}) = \vec{A}(\vec{x}) + \vec{H}(\vec{x}, \vec{f}_{NN}(\vec{x}, \vec{w})) \quad (9)$$

$$\vec{A}(\vec{x}_b) = \vec{y}_b \quad (10)$$

$$\vec{H}(\vec{x}_b, \vec{f}_{NN}(\vec{x}_b, \vec{w})) = 0 \quad (11)$$

2.3 Numerical experiments

To investigate the applicability of the method several problems are solved by the neural network collocation method. In the following we show two examples among them where the Navier-Stokes equations are solved under different boundary conditions.

The Navier-Stokes equations are given as

$$u \frac{\partial u}{\partial x} + v \frac{\partial u}{\partial y} + \frac{\partial P}{\partial x} - \mu \left(\frac{\partial^2 u}{\partial x^2} + \frac{\partial^2 u}{\partial y^2} \right) = 0 \quad \text{in } \Omega \quad (12a)$$

$$u \frac{\partial v}{\partial x} + v \frac{\partial v}{\partial y} + \frac{\partial P}{\partial y} - \mu \left(\frac{\partial^2 v}{\partial x^2} + \frac{\partial^2 v}{\partial y^2} \right) = 0 \quad \text{in } \Omega \quad (12b)$$

$$\frac{\partial u}{\partial x} + \frac{\partial v}{\partial y} = 0 \quad \text{in } \Omega \quad (12c)$$

(1) Flow of sigmoidal stream lines in a square domain

Flow in a box with the following boundary conditions (Fig.2) is solved.

$$\Omega = \{(x, y) \mid (x, y) \in [-1, 1] \times [-1, 1]\}$$

$$(u, v) = \begin{cases} (A_1 \sin^2 \pi y, 0) & x = -1 \cap y \in [0, 1] \\ (A_1 \sin^2 \pi y, 0) & x = -1 \cap y \in [-1, 0] \\ (0, 0) & \text{elsewhere} \end{cases} \quad (13)$$

$$P(1, 1) = 0 \quad (14)$$

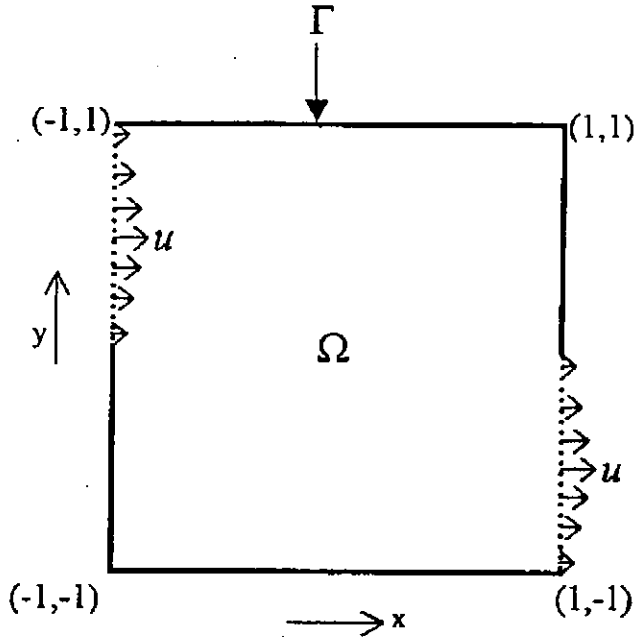


Fig.2 Computational domain

The boundary conditions were imposed by the method of form factors and two numerical experiments by using different training algorithms, i.e., the conventional error back-propagation method and the Gauss-Newton method (one of nonlinear least square method) were carried out (Figs.3 and 4). The computational times and accuracies are summarized in Table 1 for the above two numerical experiments.

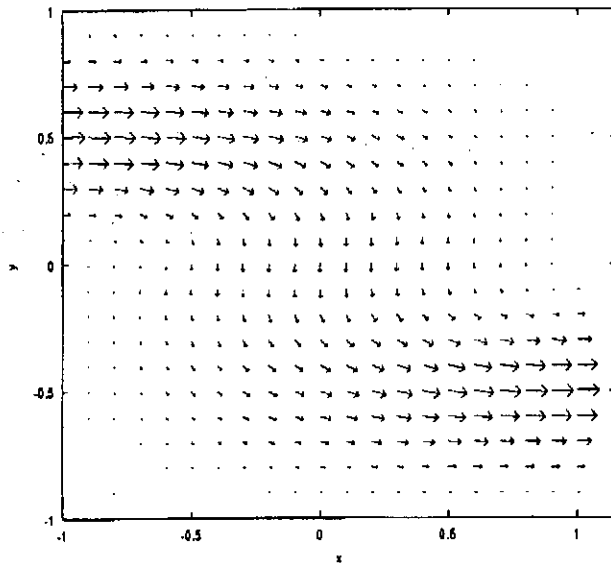


Fig.3 Flow pattern obtained by the error back-propagation method.

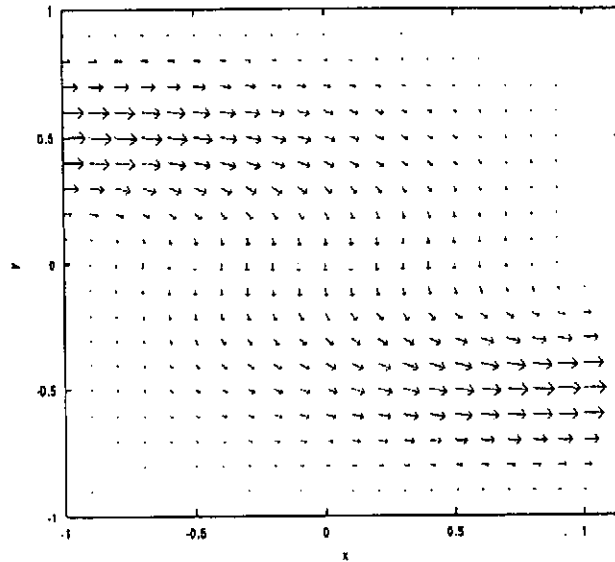


Fig.4 Flow pattern obtained by the Gauss-Newton method.

Table 1 Computational time and accuracy

Algorithm	Structure	No. of training patterns	No. of executing patterns	Iterations	Average residual error	CPU time h:m:s
Error back prop	1-12-1	121	441	10000	8.90×10^{-3}	00:02:08
Gauss Newton	1-12-1	121	441	3	6.53×10^{-3}	00:00:11

(2) Problem of calculating the wall rule

To investigate if the neural network collocation method is applicable to the problem where the behavior of the solution changes abruptly within the computational domain we solved the Navie-Stokes equations in a flow channel with a wavy wall (Fig.5).

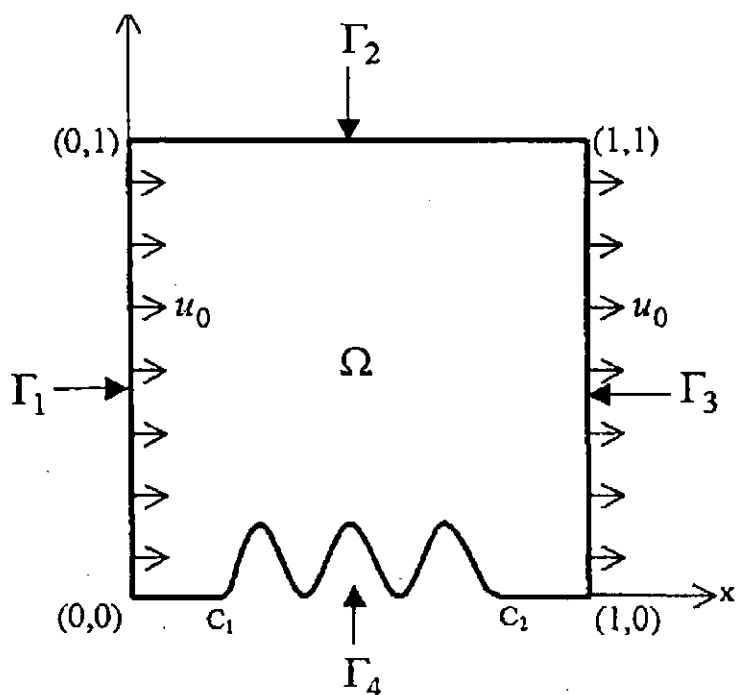


Fig.5 Computational domain for the wall rule problem.

In this computation the boundary conditions were imposed by the penalty method for the wavy wall and by the method of form factors for the other boundaries. An example of the result of the numerical experiment is shown in Figs.6 and 7.

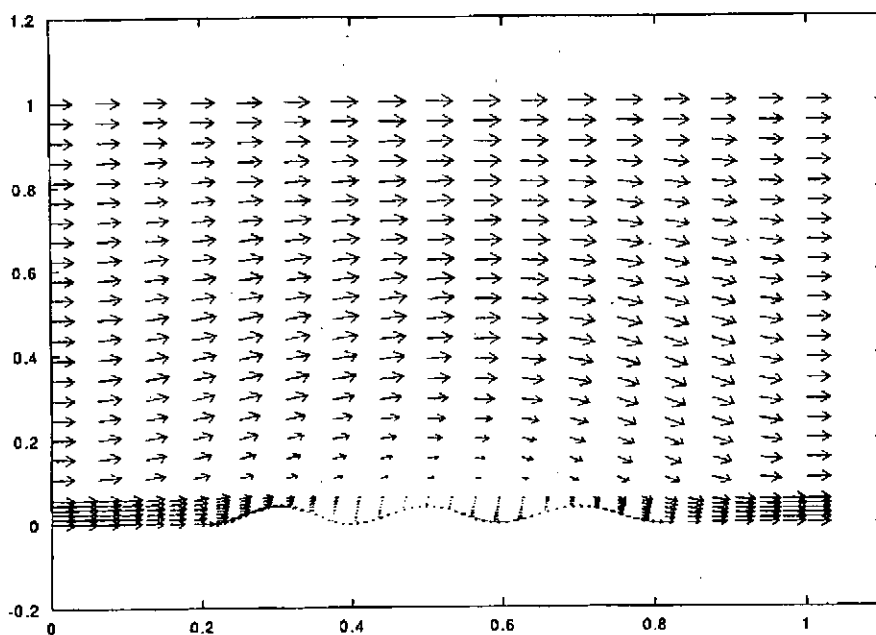


Fig.6 An example of the result of the computation of wall rule (flow pattern).

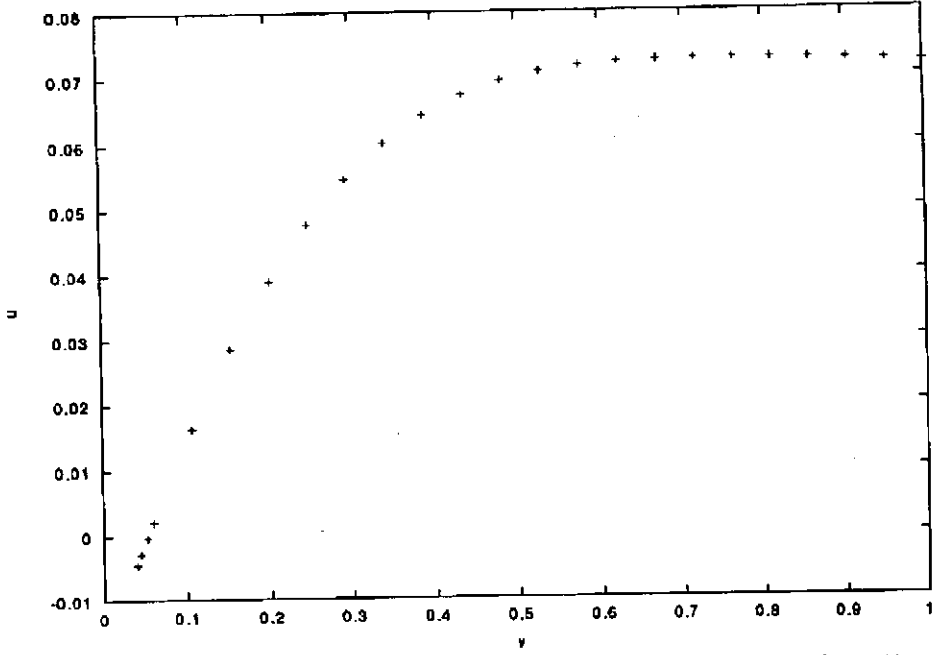


Fig.7 An example of the result of the computation of wall rule (horizontal velocity profile at $x=0.5$)

3. CT image reconstruction by using a multi-layer neural network

Similarly as the previously described differential equation solver a multi-layer neural network can be applicable for solving an integral equation by employing the sum of the squared residuals of the integral equation as the object function [7]. As a practical example we applied the method to the CT image reconstruction from a small amount of projection data. This kind of CT image reconstruction method is especially useful for data analyses in laboratory experiments or in field observations because in these applications the number of projection paths and their distribution are strongly limited the experimental or the observational conditions in comparison with the medical applications where the CT image reconstruction technique is extremely well-developed.

3.1 Formulation

We consider CT image reconstruction for the geometry given in Fig.8. Within the 2 dimensional domain distribution of some quantity is given as $f(x,y)$ and line integrals of the quantity f along a path k is observed as

$$g(r_k, \theta_k) = \int_{(k)} f(x,y) ds + n(r_k, \theta_k) \quad (15)$$

where n is noise with zero average value.

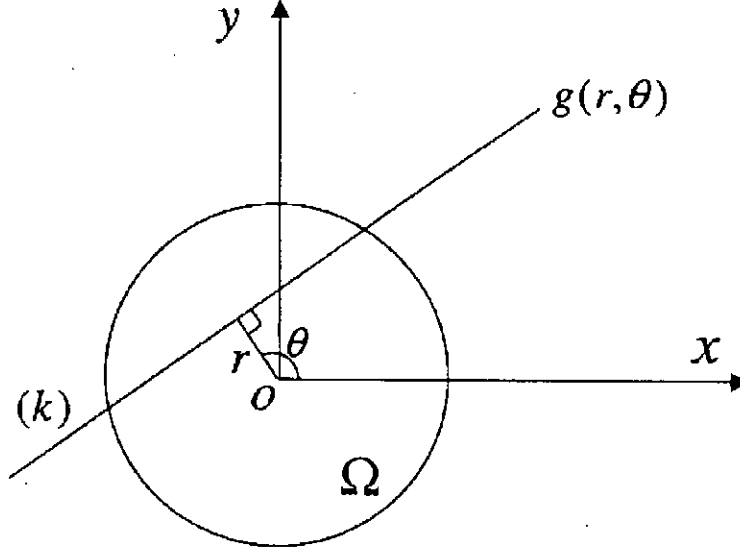


Fig.8 Two dimensional domain where image is reconstructed.

3.2 Object function and training

The object function to be minimized is given as

$$E = \sum_k (g^{NN}(r_k, \theta_k) - g_k^{meas})^2 \quad (16)$$

where the line integral $g^{NN}(r_k, \theta_k)$ is evaluated by trapezoidal formula as

$$g^{NN}(r_k, \theta_k) = \int_k f(x, y) ds \approx \sum_i \alpha_i^{(k)} f(x_i, y_i) \quad (17)$$

By using the above object function updating of the weights of the neural network is carried out as

$$\begin{aligned} \Delta w_{mn} &= -\gamma \frac{\partial E}{\partial w_{mn}} \\ &= -2\gamma \sum_{k=1}^K \sum_{i=1}^I (g^{NN}(r_k, \theta_k) - g_k^{meas}) \frac{\partial g^{NN}(r_k, \theta_k)}{\partial f_i^{NN}} \frac{\partial f_i^{NN}}{\partial w_{mn}} \\ &\approx -2\gamma \sum_{k=1}^K \sum_{i=1}^I (g^{NN}(r_k, \theta_k) - g_k^{meas}) \alpha_i^{(k)} \frac{\partial f_i^{NN}}{\partial w_{mn}} \end{aligned} \quad (18)$$

where γ is the learning rate, and the training is carried out by semi-online mode.

3.3 Numerical experiments

As a test problem we tried to reconstruct the following double-peak Gaussian distribution (Fig.9).

$$f(x,y) = 7 \exp\left[-(x-18.5)^2 / 7 - (y-13)^2 / 22\right] + 2.5 \exp\left[-(x-12)^2 / 12 - (y-13)^2 / 22\right] \quad (19)$$

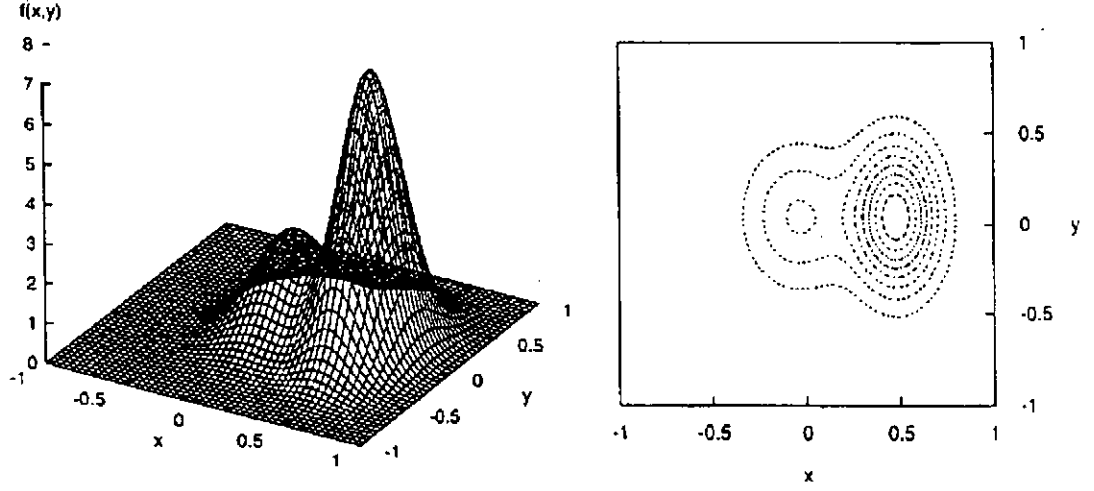


Fig.9 Bird's eye view and contour plot of the function to be reconstructed

Two kinds of projection paths, i.e., the fan-beam projection paths and the parallel-beam projection paths are adopted. The error of projection (line integral) data E_p and the average function error E_s are defined as

$$E_p = \sqrt{\frac{\sum_{k=1}^K (g^{NN}(r_k, \theta_k) - g_k^{meas})^2}{K}} \quad (20)$$

$$E_s = \frac{\sum_{i=1}^N |f^{NN}(x_i, y_i) - f(x, y)|}{N} \quad (21)$$

The neural network consisting of four layers with the structure, 2-12-12-1, is chosen experimentally. Numerical experiments for the following cases were carried out, i.e., (1) fan-beam projection paths of $30 \times 30 = 900$ without noise, (2) fan-beam projection paths of $30 \times 30 = 900$ with 5 % noise, (3) asymmetric fan-beam projection paths of $15 \times 30 = 450$ without noise, and (4) parallel-beam projection paths of $30 \times 30 = 900$ without noise. The last case was carried out to compare our result with (5) the result by the widely used filtered back-projection (FBP) method. The contour plots, and the correlation diagrams between the reconstructed and the original distributions, corresponding to the above experimental cases, (1), (4), and (5) are shown in Figs. 10-12. The errors of reconstructions are summarized in Table 2. From Figs. 11 and 12 the method by the neural network is superior to the FBP method for the image reconstruction of small amount of projection data.

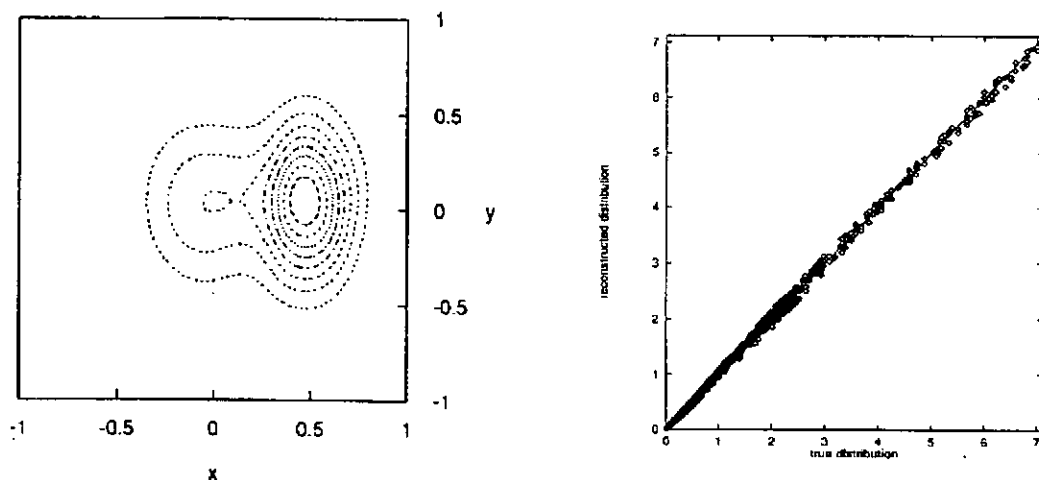


Fig.10 Contour plot of the reconstructed image, and the correlation diagram for the case of (1).

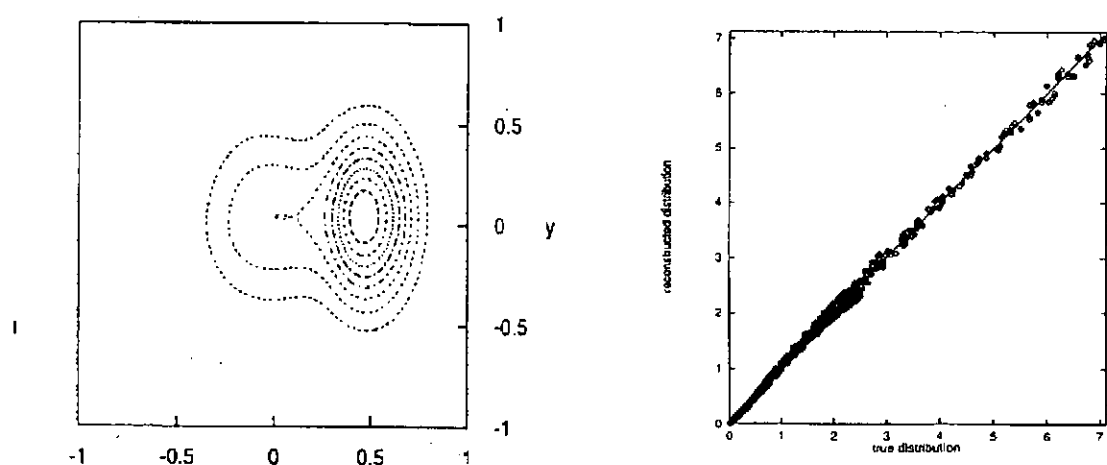


Fig.11 Bird's eye view and contour plot of the reconstructed image, and the correlation diagram for the case of (4).

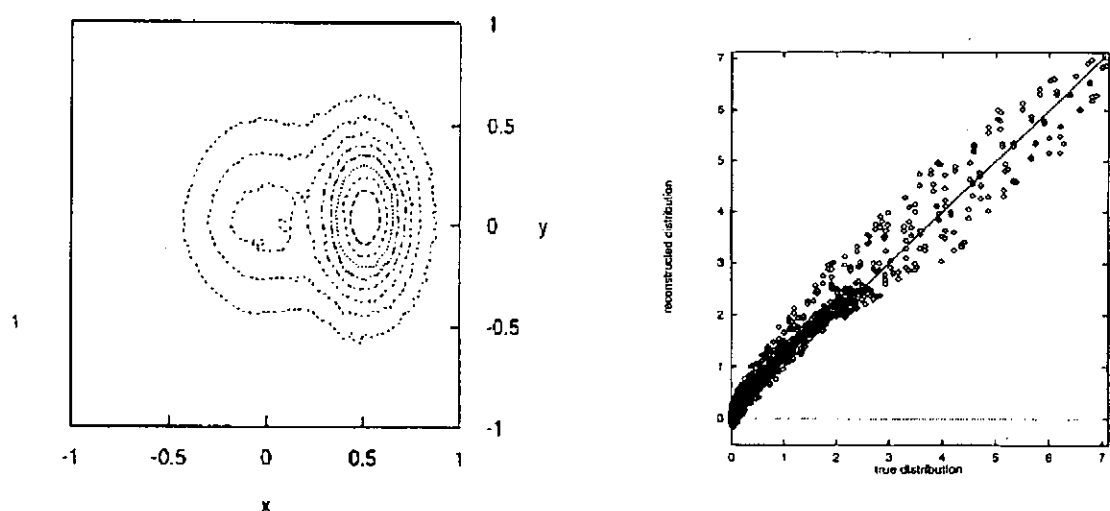


Fig.12 Bird's eye view and contour plot of the reconstructed image, and the correlation diagram for the case of (5).

Table 2 Errors of image reconstructions corresponding to the above cases.

Method	Projection paths	Noise	Error of projection data (E_p)	Average function error (E_f)
Neural network	Fan: 30 x 30	0 %	0.0167	0.0191 (0.26 %)
Neural network	Fan: 30 x 30	5 %	0.0578	0.0341 (0.47 %)
Neural network	Fan: 15 x 30	0 %	0.0226	0.0267 (0.37 %)
Neural network	Parallel: 30 x 30	0 %	0.0192	0.0219 (0.3 %)
FBP	Parallel: 30 x 30	0 %	—	0.143 (1.9 %)

By taking advantage of our method it can be applied to a large-scale image reconstruction such as determination of the plasma density in the ionosphere or the moisture density distribution in the air detected by the radio wave from satellite. Conceptual diagram of the projection paths and an example of image reconstruction is shown in Figs.13 and 14.

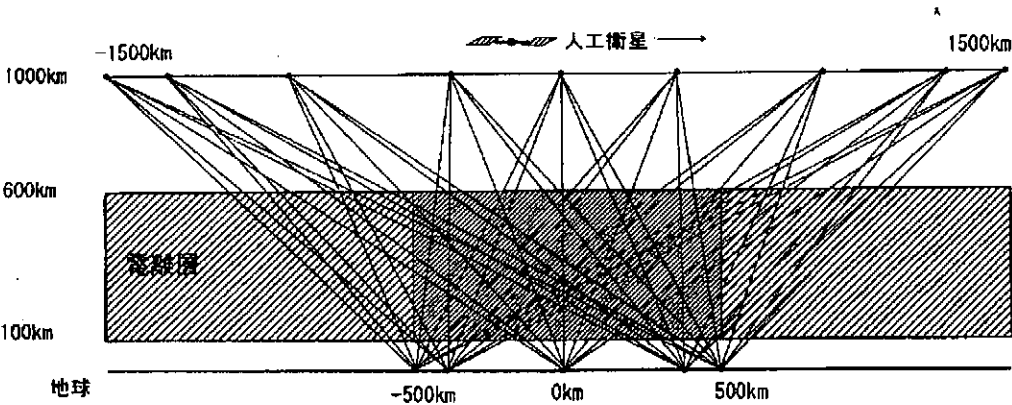


Fig.13 Conceptual diagram of the projection paths.

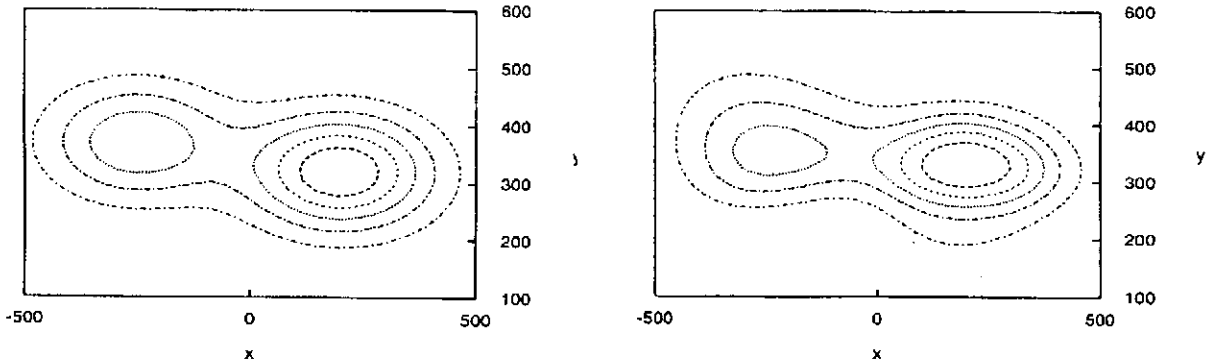


Fig.14 An example of image reconstruction. Projection paths: 10 x 50. Left: Original, right: reconstructed. Average error: 3.0 %.

4. Summary and conclusion

The results of our studies on the neural network collocation method are summarized as

- (1) We carried out numerical experiments for several problems and attained promising results.
- (2) Because of the good generalization (smoothing and interpolation) functions of the neural network this method will be effectively applied to various kinds of problems.

As for the CT image reconstruction method our studies are summarized as

- (3) We carried out numerical experiments for several problems and attained promising results.
- (4) Because the numerical formulation of our method is very simple it can be applied to problems of geometrically complicated objects.
- (5) This method is effective for problems where only a small amount of projection data or projection data from asymmetrically positioned paths is available.
- (6) As long as the error-back-propagation is used as the learning algorithm the computational cost is necessarily expensive and it is desirable that more efficient learning algorithm is implemented.

References

1. R. Beale, T. Jackson, *Neural Computing: An Introduction* (Bristol, IOP Publishing, 1990).
2. Raul Rojas, *Neural Network: A Systematic Introduction* (Berlin, Springer, 1996).
3. Kelvin Swingler, *Applying Neural Networks: A Practical Guide* (London, Academic Press, 1996).
4. Chris M. Bishop, *Neural networks and their applications*, *Review of Scientific Instruments* 65 (1994) 1803 - 1833.
5. B.Ph. van Milligen, et al., *Phys. Rev. Letters* 75 (1995) 3594.
6. I.E. Lagaris, et al., *Artificial neural network for solving ordinary and partial differential equations*, Preprint 15-96, Department of Computer Science, Univ. of Ioannia (1996).
7. X.F. Ma, M. Fukuhara, T. Takeda, *Neural network CT image reconstruction method for small amount of projection data*, *Nuclear Instruments and Methods for Physics Research A*, to be published (2000).

A New Scheme for MHD Stability Analysis

S. Tokuda, T. Watanabe, A. Ishizawa

Naka Fusion Research Establishment

Japan Atomic Energy Research Institute

Naka-machi, Naka-gun, Ibaraki, 311-0193, JAPAN

Abstract

A new scheme is presented to solve numerically inner layer equations that arise in the asymptotic matching theory on MagnetoHydroDynamic (MHD) stability of magnetically confined plasmas. The new scheme solves the inner layer equations as an initial value problem. The full implicit finite difference approximation for time yields the differential equations only with the radial variable. The differential equations thus derived are to be solved with the given asymptotic conditions at infinity. This asymptotic matching problem is transformed into a boundary value problem for which finite difference methods are well established. The present method allows for simulation of the inner layer dynamics, such as the evolution of magnetic islands, without solving the equations of motion in the whole plasma region.

Keywords: resistive MHD stability, asymptotic matching, inner layer equation, evolution equation, finite difference method, tokamak

1 序論

電気抵抗の効果で発生するプラズマの磁気流体力学的 (MHD) 不安定性は実験室プラズマ及び宇宙プラズマにおいて、良く知られた、また、重要な不安定性である。この抵抗性 MHD 不安定性はプラズマ中における磁力線の位相幾何学 (トポロジー) 的な変化 (磁気島の形成) を引き起こし得る。トカマクのような熱核融合開発研究における磁場閉じ込めプラズマに対して、抵抗性 MHD 不安定性は、しばしば、閉じ込め性能を制限し、さらには、プラズマ閉じ込めを破壊する [1]。Furth-Killeen-Rosenbluth [2] による古典的な研究以来、漸近接続法 [3, 4] に基づいた、抵抗性 MHD 安定性解析の理論的枠組 (内部層理論あるいは境界層理論と呼ばれる) はよく確立されている。この手法は線形安定性解析だけでなく、有限な幅を持つ磁気島の発展を研究する非線形解析にも有効である [5]。

漸近接続法では、抵抗性 MHD モードの特徴的な時間スケールが理想 MHD 運動の特徴的な時間 (Alfvén 時間) スケールより十分に長いことを利用する。二つの時間スケールがかけ離れていることから、プラズマを二つの領域、理想 MHD 的な外部領域と有理化のまわりの薄い内部層、とに分離することができる。外部領域では、プラズマは慣性を無視した理想 MHD 方程式、Newcomb 方程式と呼ばれる [6, 7]、で記述される。内部層におけるプラズマ・ダイナミクスを記述する方程式 (内部層方程式) は、引き伸ばされた、時間 t 及び径座標 z を独立変数とする発展方程式である [8]。そして、Newcomb 方程式の解と各有理面での内部層方程式の解を漸近的に接続することにより、抵抗性 MHD モードの運動が決定される。線形安定性解析では、この発展方程式を線形成長率を固有値とする固有値問題に置き換えることができる。

しかしながら、トカマクにおける抵抗性 MHD 安定性を解析する、漸近接続法に基づいた、実際の解析ツールはこれまで開発されていない。その大きな理由として、二次元 Newcomb 方程式及び内部層方程式の数値解法が未開発であったことがあげられる。Newcomb 方程式については、ここ 10 年の研究の結果、二次元 Newcomb 方程式の数値解法が確立された [9, 10, 11, 12]。一方、内部層方程式の固有値問題には、射撃法 (及び、その亜種) が用いられてきたけれども、内部層方程式の数値計算法に関する研究はほとんどない。その数値的な収束特性や精度を論じないとしても、我々は射撃法を論外であるとみなす。射撃法によって一枚有理面に対する固有値問題を解くことはできても、それを複数有理面問題に適用することは、ほとんど不可能であろう。また、射撃法では内部層方程式を初期値問題 (発展方程式) の形式で解くことができない。

漸近接続理論が確立されているのにも拘らず、内部層方程式を発展方程式の形式で数値的に解くことができなかったため、内部層におけるプラズマ・ダイナミックスのシミュレーションにおいては、抵抗性 MHD 方程式を全プラズマ領域で解くことが一般的であった。したがって、固有値問題の形式のみならず、発展方程式の形式で内部層方程式を解く数値計算法が確立されれば、それはトカマクにおける抵抗性 MHD 安定性の解析研究に大きく資すると期待できる。

本研究は抵抗性 MHD 安定性解析で現れる内部層方程式を発展方程式の形式で解く新しい数値計算法を報告する。基本的な考え方を明確にするためと解析解が利用できることから、最も簡単な内部層方程式の一枚有理面問題を解くことを目標とする。しかしながら、新しいスキームは、より精密な内部層方程式を複数有理面について解く場合にも拡張可能である。数値計算法の観点から見た場合、内部層問題は差分法等の数値計算法の確立している発展方程式の枠組 [13, 14] に入っていないことが大きな特徴である。そこで、我々は、内部層問題を標準的な初期値・境界値問題に変換する。このために、Newcomb 方程式の数値解法で利用された、応答問題法 [9] と Green の定理を利用し、また、時間に関しては完全陰解有限差分近似を用いる。

2 内部層問題

最も簡単な線形の内部層方程式は

$$\partial_t \frac{d^2 \Phi}{dz^2} = z \frac{d^2 \Psi}{dz^2} \quad (1)$$

$$\partial_t \Psi = -z \Phi + \frac{d^2 \Psi}{dz^2} \quad (2)$$

で与えられる [8]。ここで未知関数 $\Phi(z, t)$, $\Psi(z, t)$ は、それぞれ、静電ポテンシャル、磁気ポテンシャルであり、 z は引き伸ばされた径座標で、その区間は $(-\infty, \infty)$ である。この方程式に対して、パリティ保存が成立し、以下、

$$\Phi(-z, t) = -\Phi(z, t), \quad \Psi(-z, t) = \Psi(z, t) \quad (3)$$

の奇パリティ (ティアリングパリティ) の解を考える。

一枚有理面に対する内部層問題とは方程式 (1,2) の解で $z \rightarrow +\infty$ での漸近条件

$$\Phi(z, t) \sim \phi_{\infty}(t)(1 + \frac{c}{z}) \quad (4)$$

$$\partial_t \Psi(z, t) + z\Phi(z, t) \sim 0 \quad (5)$$

を満たすものを求めることである。ただし、 c は外部領域問題から決まる、与えられた定数（以下、接続データと呼ぶ）、 $\phi_{\infty}(t)$ は未知定数（時間に依存する）である。未知関数の時間微分を含む漸近条件 (5) は扱いが難しいので、新しい未知関数を

$$\Xi(z, t) = \partial_t \Psi + z\Phi \quad (6)$$

で定義する。関数 Φ, Ξ に対する発展方程式として

$$\partial_t \frac{d^2 \Phi}{dz^2} = z\Xi \quad (7)$$

$$\partial_t \Xi = -\frac{d^2}{dz^2}(z\Phi) + \frac{d^2 \Xi}{dz^2} \quad (8)$$

および、 $z \rightarrow +\infty$ での漸近条件として

$$\Phi(z, t) \sim \phi_{\infty}(t)(1 + \frac{c}{z}), \quad \Xi(z, t) \sim 0 \quad (9)$$

を得る。物理的には $\Xi(z, t)$ は平衡磁場に平行な電場を表し、漸近条件 (9) は、無限遠で平行電場が短絡（ショート）した理想 MHD 解に接続される解を選ぶ条件になっている。

固有値問題は、時間微分 ∂_t を線形成長率 γ に置き換えることにより

$$\gamma \frac{d^2 \Phi}{dz^2} = z\Xi \quad (10)$$

$$\gamma \Xi = -\frac{d^2}{dz^2}(z\Phi) + \frac{d^2 \Xi}{dz^2} \quad (11)$$

となる。そして、 $z \rightarrow +\infty$ での漸近条件は

$$\Phi(z) \sim \phi_{\infty}(1 + \frac{c}{z}), \quad \Xi(z) \sim 0 \quad (12)$$

である。なお、方程式 (10,11) の同次性より、漸近条件 (12) において

$$\phi_{\infty} = 1 \quad (13)$$

と置くことができる。

漸近条件 (9,12) から、内部層問題が、数値解法の確立している、従来の初期値・境界値問題の枠組 [13, 14] に入っていないことが理解される。まず、漸近条件 (12) から、方程式 (10,11) の解に対して、たとえば、

$$\|Y\| \equiv \left[\int_{-\infty}^{+\infty} (|\Phi(z)|^2 + |\Xi(z)|^2) dz \right]^{1/2}, \quad Y(z) \equiv (\Phi(z), \Xi(z))^t \quad (14)$$

で定義されるノルムは有限でない。そのため、近似解の収束を論じることができない。さらに、より一般的な内部層問題については、漸近条件は

$$\Phi(z) \sim z^{-1/2+\mu} + c z^{-1/2-\mu}, \quad \mu > 0 \quad (15)$$

となる (μ は Mercier-Suydam 指数と呼ばれる正数である)。したがって、この状況は、一般的な内部層問題においては、さらに悪くなる。次に、発展方程式に対しては、未知数 $\phi_\infty(t)$ が漸近条件 (9) に含まれている。すなわち、各時刻において、条件 (9) を満足するように $\phi_\infty(t)$ を決めなければならない。このように、内部層問題は、ノルムが有限であることを保証する、既知の境界条件が課せられる従来の初期値・境界値問題とは、著しく異なる問題となっている。このことが、これまで内部層問題を初期値問題として解けなかった理由と考えられる。

しかしながら、我々は、すでに、外部領域に対する Newcomb 方程式において、方程式 (10,11) に類似の問題に出会っている。Newcomb 問題においては、ノルムが無限大の大きい解に対する応答問題に置き換えた。この手法が内部層問題についても適用できる。これによって、方程式 (10,11) に対する漸近問題を解くことができれば、初期値問題にも適用できる。

そこで、(11) 式を使って、(10) 式を理想 MHD 方程式との関係が明確であるように表そう。これは、圧力効果を取り入れる場合にも有効である。結果は

$$\gamma^2 \frac{d^2 \Phi}{dz^2} = -z \frac{d^2}{dz^2} (z\Phi) + z \frac{d^2 \Xi}{dz^2} \quad (16)$$

である。次に、Newcomb 問題において重要な役割を果たした Grenn の定理を内部層方程式についても導いておく。この定理から漸近条件 (12) における定数 c を求める積分関係式が導かれる。今、 γ を「正の実数」とし、作用素 \mathcal{A} を

$$\mathcal{A} \begin{pmatrix} \Phi \\ \Xi \end{pmatrix} := \begin{pmatrix} -\gamma^2 \frac{d^2 \Phi}{dz^2} - z \frac{d^2}{dz^2} (z\Phi) + z \frac{d^2 \Xi}{dz^2} \\ \gamma \Xi - \frac{d^2 \Xi}{dz^2} + \frac{d^2}{dz^2} (z\Phi) \end{pmatrix} \quad (17)$$

で定義し、ベクトル関数 X, Y を

$$X := (\Phi_1, \Psi_1)^t, \quad Y := (\Phi_2, \Psi_2)^t$$

とする。 Y と $\mathcal{A}X$ との通常の内積を $(Y, \mathcal{A}X)$ とするとき、

$$\begin{aligned} (Y, \mathcal{A}X) - (X, \mathcal{A}Y) = & \gamma^2 \frac{d}{dz} \left[\Phi_1 \frac{d\Phi_2}{dz} - \Phi_2 \frac{d\Phi_1}{dz} \right] + \frac{d}{dz} \left[z\Phi_1 \frac{d}{dz} (z\Phi_2) - z\Phi_2 \frac{d}{dz} (z\Phi_1) \right] \\ & + \frac{d}{dz} \left[\Xi_2 \frac{d}{dz} (z\Phi_1) - z\Phi_1 \frac{d\Xi_1}{dz} \right] + \frac{d}{dz} \left[z\Phi_2 \frac{d\Xi_1}{dz} - \Xi_1 \frac{d}{dz} (z\Phi_2) \right] \\ & + \frac{d}{dz} \left[\Xi_1 \frac{d\Xi_2}{dz} - \Xi_2 \frac{d\Xi_1}{dz} \right] \end{aligned} \quad (18)$$

を得る。今、 $z \rightarrow +\infty$ で

$$\Phi_1(z) \sim \frac{c}{z}, \quad \Xi_1(z) \rightarrow 0 \quad (19)$$

及び

$$\Phi_2(z) \sim \frac{c_2}{z}, \quad \Xi_2(z) \rightarrow 0 \quad (20)$$

としよう (c_2 は別の定数)。このとき、境界項はすべてゼロになって

$$\mathcal{P}[X, Y] := \int_{-\infty}^{\infty} [(Y, \mathcal{A}X) - (X, \mathcal{A}Y)] dz = 0 \quad (21)$$

を得る。すなわち、作用素 \mathcal{A} は自己共役である (これは、使っているモデル方程式独特の性質と考えられる)。次に、 $\Phi_2(z), \Xi_2(z)$ が $z \rightarrow \infty$ で境界条件

$$\Phi_2(z) \equiv 1, \quad \Xi_2(z) \equiv 0 \quad (22)$$

を満たすとする。このとき、(18) 式右辺第 2 項以外はゼロになり

$$\lim_{z \rightarrow \infty} \left[z \Phi_1 \frac{d}{dz} (z \Phi_2) \right] = c, \quad \lim_{z \rightarrow \infty} \left[z \Phi_2 \frac{d}{dz} (z \Phi_1) \right] = 0$$

であるので、定数 c を与える「積分公式」

$$\mathcal{P}[X, Y] = 2c \quad (23)$$

を得る。ここで、被積分関数は偶関数であることを用いた。

3 境界値問題への変換

ここでは、文献 [9] で Newcomb 問題に対して用いられた応答問題法を内部層方程式の境界値問題に適用する。まず、作用素 \mathcal{L} を

$$\mathcal{L} \begin{pmatrix} \Phi \\ \Psi \end{pmatrix} := \begin{pmatrix} -\gamma \frac{d^2 \Phi}{dz^2} + z \Xi \\ \gamma \Xi - \frac{d^2 \Xi}{dz^2} + \frac{d^2}{dz^2} (z \Phi) \end{pmatrix} \quad (24)$$

で定義する。

$$Y := (\Phi_2, \Psi_2)^t \quad (25)$$

を $z \rightarrow \infty$ で境界条件

$$\Phi_2(z) \equiv 1, \quad \Xi_2(z) \equiv 0 \quad (26)$$

を満たす「局所的な」関数とする。たとえば

$$Y(z) \equiv 0, \quad \text{for } |z| < \epsilon$$

とする。ここで、 ϵ は与えられた正数である。このとき、関数 Y は $z \rightarrow \infty$ で

$$\mathcal{L}Y = 0 \quad (27)$$

を満たす。さて、固有値問題

$$\mathcal{L} \begin{pmatrix} \Phi \\ \Psi \end{pmatrix} = 0 \quad (28)$$

の解を

$$(\Phi, \Psi)^t = X + Y \quad (29)$$

とおくと、 X に対する非同次な方程式

$$\mathcal{L}X = -\mathcal{L}Y \quad (30)$$

を得る。 X の漸近条件

$$\Phi_1(z) \sim \frac{c(\gamma)}{z}, \quad \Xi_1(z) \rightarrow 0 \quad (31)$$

から、非同次な方程式 (30) の解として、「ノルム有限」の解を求めれば良い。

漸近条件 (31) には、まだ、未知定数 $c(\gamma)$ が含まれている。しかし、条件 (31) は $c(\gamma)$ を「含まない」同次な境界条件

$$\frac{d\Phi_1}{dz}(z_R) = -\frac{1}{z_R}\Phi_1(z_R), \quad \Xi_1(z_R) = 0 \quad (32)$$

に置き換えることができる。ここで、 $(-z_R, z_R)$ は方程式 (30) を解く区間である。

したがって、 γ を固有値の「推測値」として既知とすれば、方程式 (30) 及び境界条件 (32) は差分解法等の適用できる、古典的な境界値問題である。そして、(31) 式における定数 $c(\gamma)$ は、境界値問題の解を得てから求めることができ、それは公式 (23) を適用することによって得られる。また、この方法によって、発展方程式の差分近似解法が可能となる。

4 発展方程式の解法

発展方程式に対して完全陰解法を適用する（この利点は以下で明らかになる）。時間ステップを $1/\Delta t$ として、パラメータ γ_t を

$$\gamma_t := \frac{1}{\Delta t} \quad (33)$$

で定義する。完全陰解法より

$$\begin{aligned} \gamma_t \left(\frac{d^2 \Phi^{n+1}}{dz^2} - \frac{d^2 \Phi^n}{dz^2} \right) &= z \Xi^{n+1} \\ \gamma_t (\Xi^{n+1} - \Xi^n) &= -\frac{d^2}{dz^2}(z \Phi^{n+1}) + \frac{d^2}{dz^2} \Xi^{n+1} \end{aligned}$$

すなわち、次の非同次な方程式

$$\mathcal{L}Z^{n+1} = H(Z^n) \quad (34)$$

を得る。ここで、作用素 \mathcal{L} は (24) 式で γ を γ_t に置き換えた作用素であり

$$Z^{n+1} = (\Phi^{n+1}, \Xi^{n+1})^t \quad (35)$$

$$H(Z^n) = \gamma_t \left(-\frac{d^2 \Phi^n}{dz^2}, \Xi^n \right)^t \quad (36)$$

である。また、漸近条件 (9) は

$$\Phi(z)^{n+1} \sim \phi_\infty^{n+1} \left(1 + \frac{c}{z}\right), \quad \Xi(z)^{n+1} \rightarrow 0 \quad (37)$$

となる。

問題は、定数 c が与えられたとして、 ϕ_∞^n を求めることである。これは、境界値問題の方法を使って解くことができる。

まず、方程式 (34) の両辺を未知定数 $\phi_\infty^{n+1} \neq 0$ で割る。

$$\mathcal{L}\hat{Z}^{n+1} = \frac{1}{\phi_\infty^{n+1}} H(Z^n), \quad \hat{Z}^{n+1} := (\hat{\Phi}^{n+1}, \hat{\Xi}^{n+1})^t \quad (38)$$

したがって、未知ベクトル関数 Z^{n+1} の漸近条件は

$$\hat{\Phi}^{n+1}(z) \sim \left(1 + \frac{c}{z}\right), \quad \hat{\Xi}^{n+1}(z) \rightarrow 0 \quad (39)$$

である。そこで、ベクトル関数 Y を (25) 式で与えられる既知のベクトル関数とし、解 \hat{Z}^{n+1} を

$$\hat{Z}^{n+1} = X^{n+1} + Y, \quad X^{n+1} := (\Phi_1^{n+1}, \Xi_1^{n+1})^t \quad (40)$$

と表す。これより、 X^{n+1} に対する非同次な方程式

$$\mathcal{L}X^{n+1} = -\mathcal{L}Y + \frac{1}{\phi_\infty^{n+1}} H \quad (41)$$

を得る。そして、方程式 (41) に対する漸近条件は

$$\Phi_1^{n+1}(z) \sim \frac{c}{z}, \quad \Xi_1^{n+1}(z) \rightarrow 0 \quad (42)$$

である。

ここで、非同次な線形方程式に関する重ね合わせの原理を使う。ベクトル関数 X 及び V を、それぞれ、方程式

$$\mathcal{L}X = -\mathcal{L}Y, \quad \mathcal{L}V = H \quad (43)$$

に対する解で、(42) 式と同じタイプの漸近条件を満たすとする。

$$X \sim c_0(1/z, 0)^t, \quad V \sim c_h(1/z, 0)^t \quad (44)$$

このとき、方程式 (41) の解は

$$X^{n+1} = X + \frac{1}{\phi_\infty^{n+1}} V \quad (45)$$

と表される。これから、求めるべき ϕ_∞^{n+1} に対する方程式

$$\phi_\infty^{n+1} = \frac{c_h}{c - c_0} \quad (46)$$

を得る。なお、定数 c_0, c_h は積分公式 (23) から計算できる。我々の求めたい、方程式 (41) の解 Z^{n+1} は

$$Z^{n+1} = \begin{pmatrix} \Phi^{n+1} \\ \Xi^{n+1} \end{pmatrix} = \phi_\infty^{n+1} \left\{ \begin{pmatrix} \Phi_1^{n+1} \\ \Xi_1^{n+1} \end{pmatrix} + \begin{pmatrix} \Phi_2 \\ \Xi_2 \end{pmatrix} \right\} \quad (47)$$

と表される。得られた Z^{n+1} を (36) 式に代入して $H(Z^{n+1})$ を計算すれば、次の時間ステップに進む。

5 数値計算例

まず、方程式 (30) を境界条件 (32) のもとで解いた。区間 $[-z_R, z_R]$ において一様グリッドを生成し、式 (30,32) に対して 2 次の差分近似を用いた。また、台関数

$$H(x) = \begin{cases} \exp \left[\frac{4 \left((|x| - \epsilon_H) / (\delta_H - \epsilon_H) \right)^4}{\left((|x| - \epsilon_H) / (\delta_H - \epsilon_H) \right)^4 - 1} \right], & \epsilon_H < |x| < \delta_H \\ 1, & |x| \leq \epsilon_H \\ 0, & \delta_H \leq |x| \end{cases}$$

を導入し、

$$\Xi_2 \equiv 0, \Phi_2(z) = \text{sgn}(z)H(x), x = z_R - z$$

とした (ϵ_H, δ_H は与えられた正数)。

図 1.(a) は $\gamma = 0.2$ 及び $\gamma = 0.8$ の場合の境界値問題 (30,32) の差分近似解に対して、積分公式 (23) から求めた、漸近条件 (31) における接続データ c を示している (N_z : グリッド数)。なお、 c に対する解析表現 (分散関係式) は

$$c(\gamma) = \frac{1}{\Delta_o(\gamma)}; \quad \Delta_o(\gamma) = -\frac{\pi \gamma^{5/4} \Gamma(1/4(Q-1))}{2 \cdot 8 \Gamma(1/4(Q+5))}, \quad Q = \gamma^{3/2} \quad (48)$$

で与えられ [8], 図の縦軸に \times 印で示されている。図では、 $z_R = 160$, $\epsilon_H = 120$, $\delta_H = 40$ である。また、公式 (23) における積数値分には台形則を用いた (この例では、積分区間は有限区間 $[40, 120]$ である)。さらに、図 1.(b) に近似解 ($N_z = 8000$) から求めた $c(\gamma)$ (\circ 印) とその解析値 (\times 印) を示す。図のスケールでは、これら二つは重なっている。

図 1 は、 z_R を固定した場合、グリッド数 N_z に対する接続データ c の収束特性は逆二乗収束であり、解析値に収束することを確認する。また、 γ が小さい場合、近似解の収束は悪くなる。

次に、 $c = 6.538$ (式 (48) で $\gamma = 0.2$ に対応) の場合について、発展方程式 (7,8,9) を完全陰解法で解いて得られた $\phi_\infty(t)$ を図 2.(a) に、また、 $t = 6$ での解 $\Phi(z), \Xi(z)$ ($-10 \leq z \leq 10$) を図 2.(b) に示す。この場合、

$$z_R = 800, N_z = 16000, \epsilon_H = 200, \delta_H = 800, \Delta t = 0.02$$

である。なお、図 2.(b) では、 $\Phi(z), \Xi(z)$ は $\Phi(z)$ の最大値で規格化されている。 $\phi_\infty(t)$ は線形成長し、図 2.(a) より求めた、その成長率は $\gamma = 0.2101$ である。また、発展方程式の数値解は $\gamma = 0.2$ の固有値問題の数値解と一致している。

6 まとめと今後の課題

本報告では、抵抗性 MHD 安定性解析で現れる内部層問題を発展方程式の形式で解く新しい数値計算法を提案した。完全陰解法により発展方程式を各時間ステップにおける漸近接続問題に置き換え、Newcomb 問題に対して考案された応答問題法を適用して、この接続問題を境界値問題 (固有値問題) に変換した。これによって、内部層問題を数値計算法の確立している、古典的な初期値・境界値問題の枠組で捉えることができた。

数値実験の結果、境界値問題に変換された漸近接続問題について2次の差分近似を用いる方法では、計算領域 $[-z_R, z_R]$ を固定した場合、接続データ c はグリッド数に対して二乗収束することが確認された。発展方程式の数値計算結果も満足できるものであるが、その収束特性については、現在、研究中である。それに関しては、以下の項目が今後の課題である。ひとつは、境界値問題において計算領域を拡大させたときの接続データの収束特性である。もうひとつは、時間ステップを小さくした場合（したがって、 γ_t を大きくした場合）の発展方程式の収束特性である。特に、式(24)から分かるように、 γ が小さい場合、作用素 \mathcal{L} は最高階の常微分作用素に小さい係数の掛けられた特異作用素になることに注意することが必要である。これが、図1.(a)で示された、接続データ c の収束特性に γ 依存性が現れる原因の一つと考えられる。また、作用素 \mathcal{L} の時間ステップに対する収束特性が従来の発展方程式とは異なることが予想される。

参考文献

- [1] D. Biskamp, *Nonlinear Magnetohydrodynamics*, (Cambridge, Cambridge, 1997).
- [2] H. P. Furth, J. Killeen and M. N. Rosenbluth, *Phys. Fluids* **6**, 459 (1963).
- [3] C. M. Bender and S. A. Orszag, *Advanced Mathematical Methods for Scientists and Engineers* (McGraw-Hill, New York, 1978).
- [4] R. D. Hazeltine and J. D. Meiss, *Plasma Confinement* (Addison-Wesley, New York, 1992).
- [5] P. H. Rutherford, *Phys. Fluids* **16**, 1903 (1973).
- [6] W. A. Newcomb, *Annals of Phys.* **10**, 232 (1960).
- [7] R. L. Dewar and A. Pletzer, *J. Plasma Phys.* **43**, 291 (1990).
- [8] G. Ara, B. Basu, B. Coppi, G. Laval, M.N. Rosenbluth and B. V. Waddell, *Annals of Phys.* **112**, 443 (1978). ,
- [9] A. Pletzer and R. L. Dewar, *J. Plasma Phys.* **45**, 427 (1991).
- [10] A. Pletzer, A. Bondeson and R. L. Dewar, *J. Comput. Phys.* **115**, 530 (1994).
- [11] S. Tokuda and T. Watanabe, *J. Plasma and Fusion Res.* **73**, 1141 (1997).
- [12] S. Tokuda and T. Watanabe, *Physics of Plasmas* **6**, 3012 (1999).
- [13] R. D. Richtmyer and K. W. Morton, *Difference Methods for Initial-Value Problems*, (John Wiley, New York, 1967).
- [14] K. Yoshida, *Functional Analysis*, (Springer Verlag, Berlin, 1965).

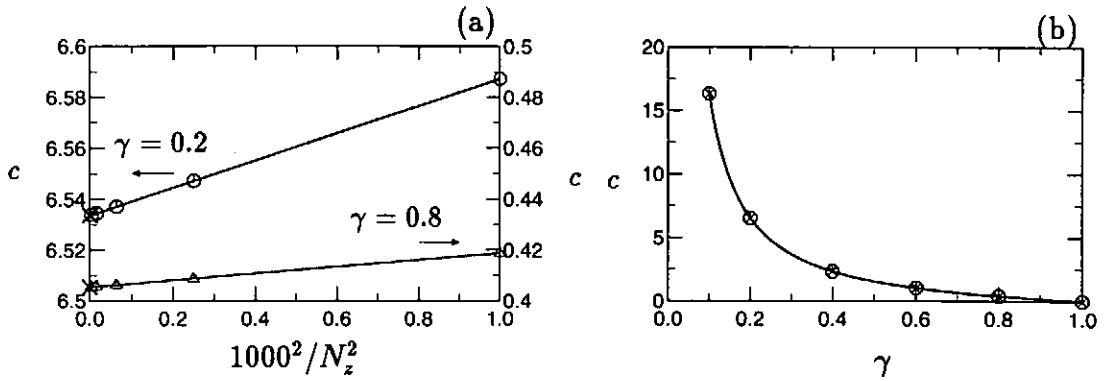


図 1: 境界値問題として解いた場合の (a) 接続データ c のグリッド数 N_z に対する収束特性, および, (b) 接続データ c の γ 依存性 ($N_z = 8000$)。× 印は解析値を示す ($z_R = 160$, $\epsilon_H = 120$, $\delta_H = 40$)。

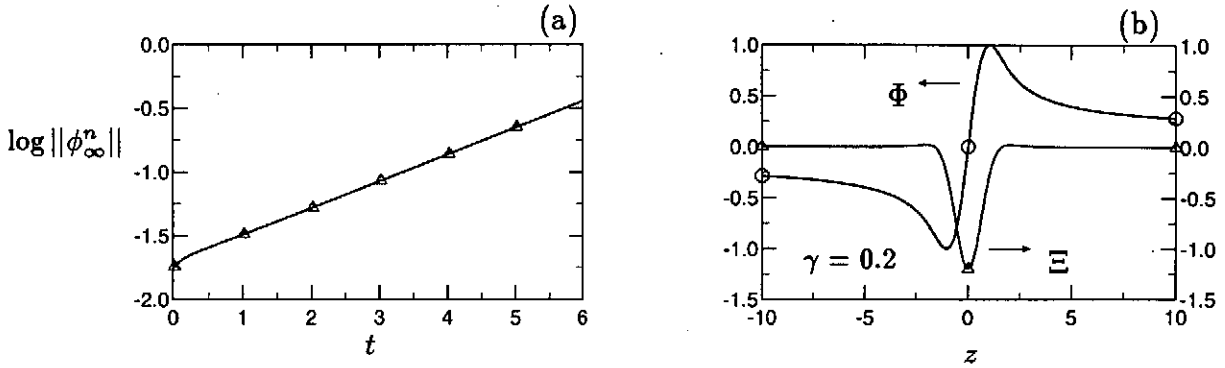


図 2: (a) $c = 6.538$ ($\gamma = 0.2$ に対応) に対する $\phi_\infty(t)$, および, (b) $t = 6$ での解 $\Phi(z), \Xi(z)$ ($z_R = 800$, $N_z = 16000$, $\epsilon_H = 200$, $\delta_H = 800$, $\Delta t = 0.02$)。発展方程式から得られた線形成長率は $\gamma = 0.2101$ である。また, 解は境界値問題として解いた解と一致する。

Influence of Numerical Integration on Convergence of Eigenvalues in the MHD Stability Analysis

IDA Akihiro, TODOROKI Jiro¹⁾ and SANUKI Heiji¹⁾

Department of Energy Engineering and Science,

Graduate School of Engineering,

Nagoya University, Nagoya 464-01, Japan

¹⁾*National Institute for Fusion Science, Toki 509-5292, Japan*

Keywords : MHD stability, eigenvalue problem, finite element method, numerical integration, convergence property, ERATO, CAS3D

Abstract

When the eigenvalue problem of the linearized MHD equation is solved by using finite element methods, whether energy integrals are exactly carried out or not affects the convergence properties of eigenvalues. If the energy integrals are exactly carried out, the eigenvalue of the most violent instability (the lowest eigenvalue) is approximated from "above", i.e., the approximated eigenvalue decreases towards the true eigenvalue as the number of elements increases. If the energy integrals are estimated by Gaussian quadrature formulas of which errors are the same order as the errors by the finite element method, the lowest eigenvalue is approximated from "below".

1 Introduction

The study of MHD stability is one of the most significant subjects in the magnetic confinement fusion research. The ideal linearized MHD equation has been extensively studied by many authors because the most violent instabilities are described by this equation; lots of codes have been constructed [1, 2, 3, 4, 5]. In these codes, finite element methods have been applied.

Most of the MHD spectrum analyzing codes utilize numerical integrations, e.g., Gaussian quadrature formulas, to evaluate energy integrals. There are a number of several reasons for this. One may be that coefficients in the integrand of the energy integrals are not constant in most cases. Another reason may be that the physical quantities derived by equilibrium codes are numerically given in actual stability calculations. The use of such a quadrature formula is a kind of variational crimes; most of theories of finite element methods depend on an assumption that energy integrals are carried out exactly.

The use of quadrature formulas brings errors into the approximated eigenvalue in addition to primary errors by the finite element method. When the errors caused by the quadrature formulas are much smaller than the primary errors by the finite element method, the effects of the numerical integrations are not substantial; the lowest eigenvalue is approximated from above [6], i.e., the approximated eigenvalue decreases towards the true eigenvalue as the number of elements increases. When the errors by the quadrature formulas are of the same order of the errors by the finite element method, the convergence properties of eigenvalues would be much affected, and the lowest eigenvalue is not always approximated from above. In most calculations by ERATO code [1, 2, 7] or CAS3D code [5] code, the lowest eigenvalue is approximated from below, i.e., the approximated eigenvalue increases towards the true eigenvalue as the number of elements increases. This may be explained by the feature of the Gaussian quadrature formulas used by these codes.

In this article, we shall investigate the effects of the Gaussian quadrature formulas, of which errors are of the same order of the primary errors by the finite element method, to the convergence property of the lowest eigenvalue.

2 Eigenvalue Problem of Ideal Linearized MHD Equation

We consider torus plasma configurations with magnetic surfaces which do not intersect each other. The magnetic surfaces are labeled by ψ , $\psi = 0$ being the magnetic axis, and $\psi = 1$ plasma surface. Let \mathbf{X} be the vector concerned with the plasma displacement vector normal to the magnetic surface, and \mathbf{Y} the vector in the magnetic surface; the combined vector \mathbf{Z} is defined by $\mathbf{Z} = (\mathbf{X}, \mathbf{Y})$. When the vector \mathbf{Z} is expanded into Fourier series with respect to poloidal and toroidal angles, the Lagrangian for the eigenvalue problem of the ideal linearized MHD equation is written in the following quadratic form [8]

$$a[\mathbf{Z}] = \lambda b[\mathbf{Z}], \quad (1)$$

where

$$a[\mathbf{Z}] = \int_0^1 \begin{pmatrix} \mathbf{X}'^H & \mathbf{X}^H & \mathbf{Y}^H \end{pmatrix} \begin{pmatrix} D & C_1^H & C_2^H \\ C_1 & A_{11} & A_{21}^H \\ C_2 & A_{21} & A_{22} \end{pmatrix} \begin{pmatrix} \mathbf{X}' \\ \mathbf{X} \\ \mathbf{Y} \end{pmatrix} d\psi, \quad (2)$$

and

$$b[\mathbf{Z}] = \int_0^1 (\mathbf{X}^H \cdot \mathbf{B}_1 \cdot \mathbf{X} + \mathbf{Y}^H \cdot \mathbf{B}_2 \cdot \mathbf{Y}) d\psi. \quad (3)$$

Here the prime in eq.(2) indicates the derivative with respect to ψ and the superscript H refers the Hermitian conjugate. The coefficients D, A_{22}, B_1 and B_2 are Hermitian and positive definite matrices; A_{11} is a Hermitian matrix. It is assumed that coefficients in eqs.(2) and (3) are sufficiently smooth. The quadratic form $a[\mathbf{Z}]$ is continuous and coercive; $b[\mathbf{Z}]$ is continuous and positive definite, so that the eigenvalue λ is real and bounded to below. The plasma is bounded by a conducting shell, so that the boundary conditions are expressed by $\mathbf{X}(0) = 0$ and $\mathbf{X}(1) = 0$. Whether the plasma is stable or unstable depends on the sign of the lowest eigenvalue of eq.(1). If there are no negative eigenvalues, the

plasma is stable; If the lowest eigenvalue is a negative value, the plasma becomes unstable. In this paper we deal with the situation that the lowest eigenvalue is negative and discrete.

3 Approximation of Function Spaces

We apply a finite element method to eq.(1). The integral region $[0,1]$ is divided into N intervals, and the i -th interval is written as (ψ_{i-1}, ψ_i) with $N + 1$ points $\psi_0 = 0 < \psi_1 < \dots < \psi_N = 1$. The maximum width of interval is expressed as h . In the following discussions, we assume $\psi_i \equiv i/N \equiv ih$, for simplicity. For a given integer l , we introduce the following finite dimensional function space K_h^l ;

$$K_h^l = \{f \mid f \text{ is a polynomial of degree } \leq l \text{ on } (\psi_{i-1}, \psi_i) \ i = 1, 2, \dots, N\}. \quad (4)$$

Furthermore the following two kinds of finite dimensional function spaces S_h^l and T_h^l are defined;

$$S_h^l = \{f \mid f \in K_h^l \cap \mathcal{H}^l, f(0) = f(1) = 0\}, \quad (5)$$

$$T_h^l = \{f \mid f \in K_h^{l-1} \cap \mathcal{H}^{l-1}\}, \quad (6)$$

where \mathcal{H}^m denotes the Sobolev space of the order of m . We choose the function spaces S_h^l and T_h^l as the finite element subspaces of \mathbf{X} and \mathbf{Y} , respectively [8]. Then the errors in eigenvalues scale as

$$|\lambda - \lambda_h| \leq Ch^{2l}, \quad (7)$$

where λ_h denotes the approximated eigenvalue, and according to the minimax principle, the lowest eigenvalue is approximated from above.

4 Numerical Integrations

The integrations in eqs.(2) and (3) are numerically carried out by using a quadrature formula over each element. When we use $k(> l)$ -point quadrature formulas, the errors in integrations are $O(h^{2k})$ and they are much smaller than the errors by finite elements $O(h^{2l})$, so that the estimation of the errors in eigenvalues (7) would be not changed; the lowest eigenvalue is still approximated from above. When we employ the just l -point quadrature formula, the errors in integrations and the errors by finite elements are both $O(h^{2l})$; the convergence properties of eigenvalues are affected by the errors of the numerical integration. An example of such a change of convergence properties is shown in Fig.1. The profile functions are here given as $p(r) = 0.05(1 - r^2)^2$ and $q(r) = 0.8 + r^2(1.82 - 1.92r^2)/(1.21 - r^2)$. The internal kink mode of $m = 1$ and $n = -1$ becomes unstable in this equilibrium. The piecewise linear function and the step function are employed as the base functions in hybrid($l = 1$). The symbols \square represent the approximated eigenvalues of the lowest eigenvalue in case of $k > l$ points Gaussian quadrature formula, and the symbols \circ in case of one point Gaussian quadrature formula($k = l$). These values are plotted with the fitting line versus N^{-2} . The number of intervals used are 64, 100, 128 and 200. In both cases the approximated eigenvalues converge towards the same value but from opposite

sides, i.e., the lowest eigenvalue is approximated from above in case of $k > l$, and from below in case of $k = l$.

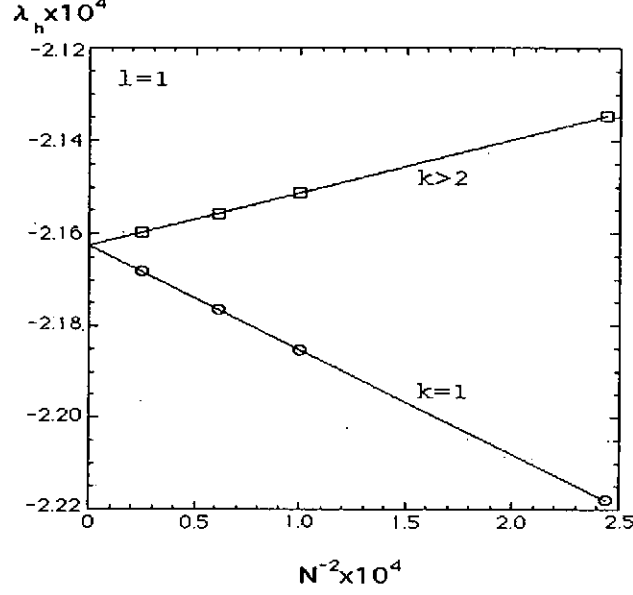


Fig. 1 : Example of a change of a convergence line when Gaussian quadrature formulas are used. The parameter for the base functions is $l = 1$. The symbols \square are the approximation of the lowest eigenvalue in case of $k = 2, 3, 4$ and $5 (> l)$ points Gaussian formulas; the lowest eigenvalue is approximated from above. The symbols \circ represent the approximation of the lowest eigenvalue in case of one point Gaussian formula ($k = l (= 1)$); the eigenvalues converge from below.

5 Evaluation of Errors Caused by Quadrature Formulas

The lowest eigenvalue is defined by

$$\lambda = \min_Z \frac{a[Z]}{b[Z]} = \frac{a[Z_0]}{b[Z_0]}, \quad (8)$$

where Z_0 is the eigenfunction of the lowest eigenvalue. The approximated eigenfunction of the lowest eigenvalue Z_h is introduced as $Z_h = (X_h, Y_h)$ where $X_h \in S_h^l$ and $Y_h \in T_h^l$. The value of $a[Z_h]$ estimated by using the just l -point quadrature formulas is denoted by $a^*[Z_h]$, and the error caused by the numerical integration is written as $\delta a[Z_h]$, i.e., $a[Z_h] = a^*[Z_h] + \delta a[Z_h]$. Similarly, we put $b[Z_h] = b^*[Z_h] + \delta b[Z_h]$. The approximated eigenvalue λ_h^* is defined by

$$\lambda_h^* = \min_{Z_h} \frac{a^*[Z_h]}{b^*[Z_h]} = \frac{a^*[Z_{h0}^*]}{b^*[Z_{h0}^*]}, \quad (9)$$

where Z_{h0}^* is the function which minimizes the quotient $\frac{a^*[Z_h]}{b^*[Z_h]}$. We express the relation between Z_{h0}^* and Z_0 as $Z_0 = Z_{h0}^* + \delta Z_{h0}^*$. We can estimate the errors in the eigenvalue by the quadrature formula up to $O(h^{2l})$ as follow

$$\lambda_h^* - \lambda = \frac{b^*[\delta Z_{h0}^*]}{b[Z_0]} \left(\lambda_h^* - \frac{a^*[\delta Z_{h0}^*]}{b^*[\delta Z_{h0}^*]} \right) + \frac{\delta b[Z_0]}{b[Z_0]} \left(\lambda_h^* - \frac{\delta a[Z_0]}{\delta b[Z_0]} \right)$$

$$\leq \frac{b^*[Z_0]}{b[Z_0]} \mu_h[Z_0], \quad \mu_h[Z] \equiv \frac{\delta b[Z]}{b^*[Z]} (\lambda_h^* - \frac{\delta a[Z]}{\delta b[Z]}). \quad (10)$$

We note that the value $\frac{b^*[Z_0]}{b[Z_0]}$ is almost unity. If $\mu_h[Z_0]$ is negative, we obtain $\lambda_h^* \leq \lambda$, i.e., the lowest eigenvalue is approximated from below.

We investigate the sign of the value $\mu_h[Z_0]$. In evaluating the value $\mu_h[Z_0]$, we shall use the approximated eigenfunction Z_{h0}^* instead of the eigenfunction Z_0 which is unknown. In the following discussions, we choose Gaussian quadrature formula as the quadrature formula and use the lowest order finite elements ($l = 1$). On the i -th interval, the abscissa of the integral point locates the middle point of the interval $\xi_i = (\psi_{i-1} + \psi_i)/2$, and the components of eigenfunction can be written in the following forms,

$$X_{h0}^* = X_0^{*i} + (\psi - \xi_i) X_1^{*i}, \quad Y_{h0}^* = Y_0^{*i}, \quad (11)$$

i.e., the function Y_{h0}^* is a constant value Y_0^{*i} , and the function X_{h0}^* is a linear function. Then the errors $\delta a[Z_{h0}^*]$ and $\delta b[Z_{h0}^*]$ are estimated up to the order of errors $O(h^2)$ as

$$\begin{aligned} \delta a[Z_{h0}^*] \simeq & \frac{h^2}{12} \sum_i^N X_1^{*iH} \cdot A_{11}(\xi_i) \cdot X_1^{*i} \\ & + \frac{h^2}{6} \sum_i^N X_1^{*iH} \cdot (C_1'(\xi_i) \cdot X_1^{*i} + A_{11}'(\xi_i) \cdot X_0^{*i} + A_{21}'(\xi_i) \cdot Y_0^{*i}) \\ & + \frac{h^2}{24} \sum_i^N (X_1^{*iH} X_0^{*iH} Y_0^{*iH}) \begin{pmatrix} D''(\xi_i) C_1''(\xi_i)^H C_2''(\xi_i)^H \\ C_1''(\xi_i) A_{11}''(\xi_i) A_{21}''(\xi_i)^H \\ C_2''(\xi_i) A_{21}''(\xi_i) A_{22}''(\xi_i) \end{pmatrix} \begin{pmatrix} X_1^{*i} \\ X_0^{*i} \\ Y_0^{*i} \end{pmatrix}, \quad (12) \end{aligned}$$

and

$$\begin{aligned} \delta b[Z_{h0}^*] \simeq & \frac{h^2}{12} \sum_i^N X_1^{*iH} \cdot B_1(\xi_i) \cdot X_1^{*i} + \frac{h^2}{6} \sum_i^N X_1^{*iH} \cdot B_1'(\xi_i) \cdot X_0^{*i} \\ & + \frac{h^2}{24} \sum_i^N (X_0^{*iH} \cdot B_1''(\xi_i) \cdot X_0^{*i} + Y_0^{*iH} \cdot B_2''(\xi_i) \cdot Y_0^{*i}). \quad (13) \end{aligned}$$

We here regard eqs.(12) and (13) as approximations of some integrals. Then the integral for $\delta b[Z_{h0}^*]$, for instance, is written as

$$\begin{aligned} \delta b[Z_{h0}^*] \simeq & \frac{h^2}{12} \int_0^1 X_{h0}^{*H} \cdot B_1(\xi_i) \cdot X_{h0}^{*'} d\psi \\ & + \frac{h^2}{24} \int_0^1 (-X_{h0}^{*H} \cdot B_1''(\xi_i) \cdot X_{h0}^* + Y_0^{*H} \cdot B_2''(\xi_i) \cdot Y_0^*) d\psi. \quad (14) \end{aligned}$$

Here we use the integration by parts. The error $\delta b[Z_{h0}^*]$ consists of the terms concerning the variation of the eigenfunction(the first term) and of the coefficients(the second term). If we assume the variation of the eigenfunction is much larger than the variation of the coefficients, we get

$$\delta b[Z_{h0}^*] \simeq \frac{h^2}{12} \int_0^1 X_{h0}^{*H} \cdot B_{11} \cdot X_{h0}^{*'} d\psi = \frac{h^2}{12} b^*[DZ_{h0}^*], \quad (15)$$

where $D^t Z_{h0}^* = (\frac{1}{h}(\frac{d}{d\psi})^t X_{h0}^*, 0)$. We can obtain the form for $\delta a[Z_{h0}^*]$ in the same way,

$$\delta a[Z_{h0}^*] \simeq \frac{h^2}{12} \int_0^1 X_{h0}^{*H} \cdot A_{11} \cdot X_{h0}^{*'} d\psi = \frac{h^2}{12} a^*[DZ_{h0}^*]. \quad (16)$$

Then the value μ_h is reduced to the following form

$$\mu_h[Z_{h0}^*] \simeq \frac{h^2}{12} \frac{b^*[DZ_{h0}^*]}{b^*[Z_{h0}^*]} (\lambda_h^* - \frac{a^*[DZ_{h0}^*]}{b^*[DZ_{h0}^*]}). \quad (17)$$

If we use the higher order finite elements, instead of eq.(17) we obtain

$$\mu_h[Z_{h0}^*] \simeq \frac{(l!)^4 h^{2l}}{(2l+1)[(2l)!]^3} \frac{b^*[D^l Z_{h0}^*]}{b^*[Z_{h0}^*]} (\lambda_h^* - \frac{a^*[D^l Z_{h0}^*]}{b^*[D^l Z_{h0}^*]}). \quad (18)$$

From this expression, we can conclude that $\mu \leq 0$, since λ_h^* is the lowest eigenvalue.

6 Numerical Examples

We shall examine numerical examples in cylindrical plasmas. The one-point Gaussian quadrature formula is here used ($k = 1$), and the piecewise linear function and the step function are employed as the base functions in hybrid ($l = 1$).

First, we give the the same profile functions in Fig.1, so that the lowest eigenvalue is concerned with the internal kink mode of $m = 1$ and $n = -1$. In Fig.2, the symbols \circ and \diamond represent the calculated lowest eigenvalues λ_h^* in eq.(9) and the values μ_h in eq.(18), respectively. These values are plotted with the fitting line versus N^{-2} . The number of intervals used are 64, 100, 128 and 200. The calculated eigenvalues λ_h^* quadratically converge towards -2.16×10^{-4} from below, and the errors μ_h towards -9.40×10^{-16} . The slopes of two fitting lines in Fig.2 agree up to three significant figures.

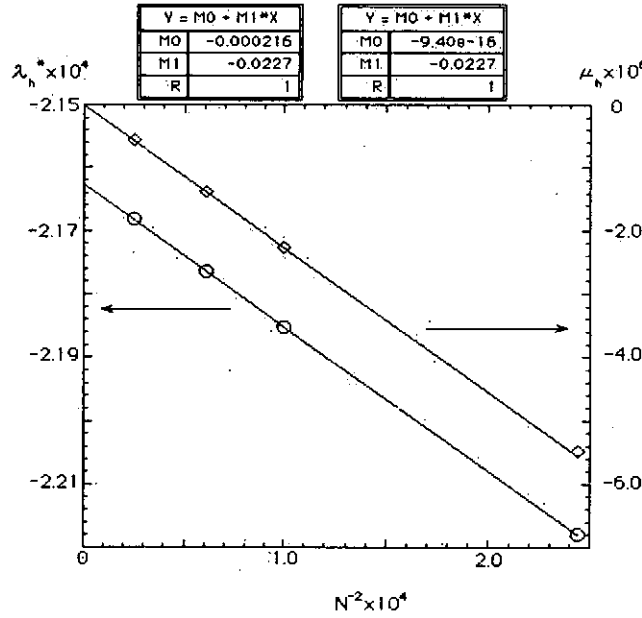


Fig. 2 : The approximated eigenvalues λ_h^* for the internal kink mode and the estimated errors in eigenvalue μ_h are plotted as a function of the number of intervals N^{-2} . Both values converge from below with the $O(h^{2l})$ rate. Convergence lines are written in a form $Y=M0+M1*X$, where M0 represents the converged value when $N \rightarrow \infty$, M1 the slope of the convergence line and $X = N^{-2} \times 10^4$. The slopes of two convergence lines agree up to three significant figures.

Next, we consider the case that profile functions are $p(r) = 0.0015(1 - r^2)^2$ and $q(r) = 1.45 + 0.2r^2$. When we choose the poloidal mode number $m = 3$ and the toroidal mode number $n = -2$, the interchange mode becomes unstable. In Fig.3, the calculated eigenvalues λ_h^* and the values μ_h are plotted with the fitting line versus N^{-2} . The number of intervals used are 64, 100, 128, 200 and 220. The calculated eigenvalues λ_h^* and the errors μ_h converge from below towards -1.18×10^{-6} and 2.32×10^{-14} , respectively. In this case, the slopes of two fitting lines agree fairly well. The relative errors is about 30%.

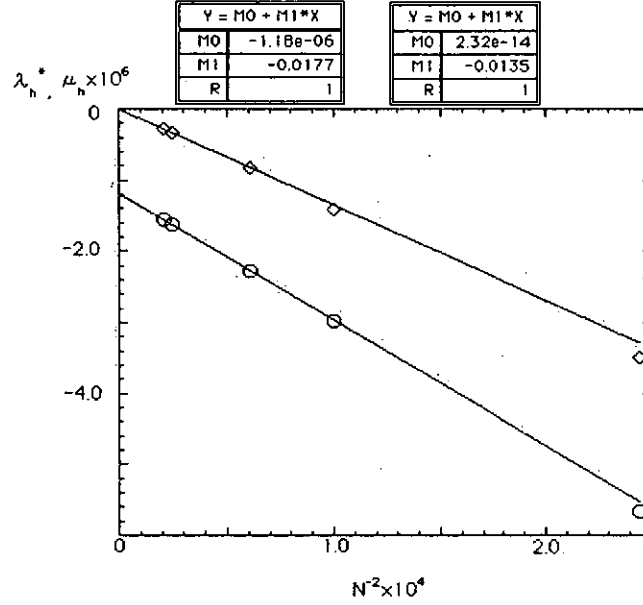


Fig. 3 : The approximated eigenvalues λ_h^* and the errors μ_h are plotted as a function of the number of intervals N^{-2} in case of the interchange mode. The meanings of M0, M1, and X are the same as in Fig.2. Quadratic convergences from below are observed in both values.

7 Conclusion

As is shown in this article, the lowest eigenvalue is approximated from below when Gaussian quadrature formulas, of which errors are of the same order of the errors by the finite element method, are employed. We note whether the lowest eigenvalue is approximated from above or below depends on quadrature formulas. For example, the sign of remainder in Lobatto's quadrature formulas is opposite to those in Gaussian formulas, so that the use of such a formula reverses the sign of the value μ_h , i.e., the lowest eigenvalue would be approximated from above.

References

- [1] R.Gruber, F.Troyon and D.Berger: Comput. Phys. Commun. **21**(1981)323.
- [2] R.Gruber, S. Semenzato, F.Troyon and T. Tsunematsu: Comput. Phys. Commun. **24**(1981)363.
- [3] R.C.Grimm, R.L.Dewar and J.Manickam: J.Comput.Phys. **49**(1983)94.
- [4] D.V.Anderson, W.A.Cooper, R.Gruber, S.Merazzi and U.Schwenn: Int. J. Supercomput. Appl. **4**(1990)3.
- [5] C.Schwab: Phys.Fluids **B5**(1993)9.
- [6] G.Strang and J.Fix: *An Analysis of the Finite Element Method*, (Prentice-Hall, New Jersey, 1973) §4.3.
- [7] R.Gruber and J.Rappaz: *FiniteElement Methods in Linear Ideal Magnetohydrodynamics*, (Springer-Verlag, 1985).
- [8] A.Ida, J.Todoroki and H.Sanuki: J.Plasma and Fusion Res.**75**(1999)572.

Effect of linear shear flow on interchange modes

T. Tatsuno*, F. Volponi, and Z. Yoshida

Graduate School of Frontier Sciences, The University of Tokyo

Feb., 2000

Abstract

Effect of the linear shear flow on linear interchange modes in incompressible neutral fluid, and linear two-dimensional electromagnetic interchange instabilities in incompressible plasmas are investigated. Although the transient growth may occur in a short period, background shear flow overcomes the interchange instability and makes it damped away in a long term due to phase mixing.

Key Words: MHD, poloidal shear flow, interchange modes, Alfvén wave, non-modal approach, spatial Fourier harmonics, phase mixing damping

1 Introduction

Since old times the instability problem for stationarily flowing MHD plasmas has been calculated and discussed in various ways [1, 2, 3, 4]. But it is remarkably difficult to estimate the exact linear stability of the system with stationary shear flow, because the spatial operator becomes nonselfadjoint for differentially flowing plasmas and the spectral resolution is not guaranteed for nonselfadjoint operators [5], and the perturbations might show the faster growth than the simple exponential dependence for such operators.

Recently, Kelvin's spatially-inhomogeneous Galilean transform method [6] is applied for some linear shear flow problems [7, 8, 9, 10, 11, 12]. For neutral fluids, the following fascinating phenomena are shown; the ability of the shear-modified waves to extract energy from the background flows [8], shear flow induced coupling between sound waves and internal waves and the excitation of beat wave [9], and the asymptotic persistence for two dimensional shear flows [10].

It is also shown the occurrence of the emission of the magnetosonic wave by the stationary vortex perturbations even in the linear regime for plasmas [11]. The authors have also applied this method [12] to investigate the basic properties of kink-type instabilities under the existence of background shear flow

*tatsuno@k.u-tokyo.ac.jp

and obtained the result that the shear flow mixing always overcomes the kink driving in a long term.

In this paper, we will show by following Kelvin's method again that the interchange mode is also damped away in a long term due to the background shear flow in the same way as kink-type mode. In Sec. 2 we will work on the neutral fluid, and extend it to treat plasmas in Sec. 3. In these sections we will show that the governing equations can be reduced to a single second order ordinary differential equation with respect to time for each, and that they show the damping behavior of the perturbations in terms of the analogy of the Newton's equation. We will summarize the result in Sec. 4.

2 Interchange instability of neutral fluid

We assume an incompressible, ideal neutral fluid. Adding gravitational term, we obtain the following basic equations:

$$\rho \frac{d\mathbf{v}}{dt} = -\nabla p + \rho \mathbf{g}, \quad (1)$$

$$\frac{d\rho}{dt} + \rho \nabla \cdot \mathbf{v} = 0, \quad (2)$$

$$\frac{dp}{dt} + \gamma p \nabla \cdot \mathbf{v} = 0. \quad (3)$$

Here we have chosen the adiabatic variation as an equation of state and d/dt denotes the convective derivative.

Considering a stationary shear flow with $\mathbf{v}_0 = (0, \sigma x, 0)$ in Cartesian coordinate and gravitational force acting in $+x$ direction, the equilibrium condition becomes

$$\rho_0 \mathbf{v}_0 \cdot \nabla \mathbf{v}_0 = -\nabla p_0 + \rho_0 \mathbf{g}, \quad (4)$$

which can be reduced under this stationary flow as

$$\nabla p_0 = \rho_0 \mathbf{g}, \quad (5)$$

where the subscript 0 denotes that the quantities are equilibrium ones. This equilibrium equation denotes that the pressure gradient is produced by the gravitational force in x direction, which is the same as the static case; i.e. a diver feels more pressure who dives deeper.

On linearizing eqs. (1)-(3), we denote the perturbed flow as $\mathbf{v}_1 = (u, v, w)$, and formulate these equations following Criminale and Drazin [7], where the subscript 1 denotes the perturbed quantities. We carry out an inhomogeneous Galilean transform $(t, x, y, z) \mapsto (T, \xi, \eta, \zeta)$ expressed as

$$\begin{aligned} T &= t, \\ \xi &= x, \\ \eta &= y - \sigma t x, \\ \zeta &= z. \end{aligned} \quad (6)$$

Under these coordinate transforms, the differential operators are written as

$$\begin{aligned}\partial_t &= \partial_T - \sigma x \partial_\eta, \\ \partial_x &= \partial_\xi - \sigma T \partial_\eta, \\ \partial_y &= \partial_\eta, \\ \partial_z &= \partial_\zeta,\end{aligned}\tag{7}$$

therefore the convective derivative can be reduced as

$$\partial_t + \sigma x \partial_y = \partial_T.\tag{8}$$

By carrying out a Fourier transform on perturbed quantities with respect to the transformed spatial variables (ξ, η, ζ) as

$$\hat{u}(k_\xi, k_\eta, k_\zeta; T) = \iiint_{-\infty}^{+\infty} u(\xi, \eta, \zeta; T) e^{i(k_\xi \xi + k_\eta \eta + k_\zeta \zeta)} d\xi d\eta d\zeta,\tag{9}$$

we obtain the following ordinary differential equations with respect to transformed time T for perturbed components.

$$\begin{aligned}\rho_0 \frac{d\hat{u}}{dT} &= i(k_\xi - \sigma T k_\eta) \hat{p}_1 + \hat{\rho}_1 g, \\ \rho_0 \frac{d\hat{v}}{dT} + \rho_0 \sigma \hat{u} &= i k_\eta \hat{p}_1, \\ \rho_0 \frac{d\hat{w}}{dT} &= i k_\zeta \hat{p}_1, \\ \frac{d\hat{\rho}_1}{dT} + \rho'_0 \hat{u} &= 0, \\ (k_\xi - \sigma T k_\eta) \hat{u} + k_\eta \hat{v} + k_\zeta \hat{w} &= 0,\end{aligned}\tag{10}$$

where the prime denotes the derivative with respect to the original coordinate x , and the local approximation is also assumed for ρ_0 . The last equation expresses the incompressibility condition for the perturbed velocity \mathbf{v}_1 . Note that $\rho_1 \mathbf{v}_0 \cdot \nabla \mathbf{v}_0 = 0$ since we have assumed the equilibrium flow as $\mathbf{v}_0 = (0, \sigma x, 0)$. This formulation (Fourier transform with respect to Galilean transformed spatial coordinate) is formally equivalent to the following ansatz,

$$\begin{aligned}f &\mapsto \hat{f}, \\ \partial_t + \sigma x \partial_y &\mapsto \partial_T, \\ \partial_x &\mapsto -i k_x(T) \equiv -i(k_\xi - \sigma T k_\eta), \\ \partial_y &\mapsto -i k_y \equiv -i k_\eta, \\ \partial_z &\mapsto -i k_z \equiv -i k_\zeta,\end{aligned}\tag{11}$$

where f denotes the representative of the perturbed quantities. This ansatz means that the wave number for x in the original coordinate system is time dependent due to x dependent shear flow directed along y axis. In other words, the wave numbers k_y, k_z are constants but k_x is transformed to be time dependent;

the flow shear mixes the plasma and induces the time-varying wave number $k_x(T)$. If we consider the compressible fluids, we can observe the coupling of sound wave and internal gravity wave due to this coefficient [9].

Substituting and reducing dependent variables in these equations, we obtain the following single second order ordinary differential equation with dependent variable \hat{u} and independent variable T ,

$$\frac{d^2}{dT^2}(\kappa^2 \hat{u}) = -\alpha^2 \frac{\rho'_0}{\rho_0} g \hat{u}, \quad (12)$$

where $\kappa^2 = k_x(T)^2 + k_y^2 + k_z^2$ and $\alpha^2 = k_y^2 + k_z^2$. Here we have used the Boussinesq approximation in which the spatial variation of the equilibrium density is neglected in the inertial term, but not in conservation of mass density since it is the driving term for interchange instability [13]. This is justified when the spatial scale of the variation of equilibrium density is much larger than that of the perturbation.

When no equilibrium shear flow exists ($\sigma = 0$), the wave number k_x becomes independent of T and eq. (12) is reduced to the usual interchange instability equation for static equilibrium. In this case dividing both sides by κ^2 , we obtain

$$\frac{d^2 \hat{u}}{dT^2} = -\frac{\alpha^2}{\kappa^2} \frac{\rho'_0}{\rho_0} g \hat{u}. \quad (13)$$

If $\rho'_0 > 0$, we have an purely oscillating solution in time as $e^{i\omega t}$, where the frequency is locally expressed as

$$\omega = \frac{\alpha}{\kappa} \sqrt{\frac{\rho'_0}{\rho_0} g}, \quad (14)$$

which expresses the internal gravity wave. Instability results when $\rho'_0 < 0$, and the growth rate γ leads to

$$\gamma = \frac{\alpha}{\kappa} \sqrt{-\frac{\rho'_0}{\rho_0} g}, \quad (15)$$

which grows in time scale of gravitational interchange mode $\tau_g = \sqrt{-\rho_0/\rho'_0 g}$. Note here that k_x has an stabilizing effect in the meaning of reducing the growth rate, though it unchanges the stability condition $\rho'_0 \geq 0$. As we can see from eq. (11), k_x is also constant in time when $k_y \equiv k_\eta = 0$, and shear flow mixing is not seen.

Now we will consider how the interchange instability is affected by inducing shear flow. We assume $\rho'_0 < 0$ hereafter. Before operating numerical calculation, we will carry out the following normalization for variables in the Galilean transform:

$$T = \frac{t}{\tau_g},$$

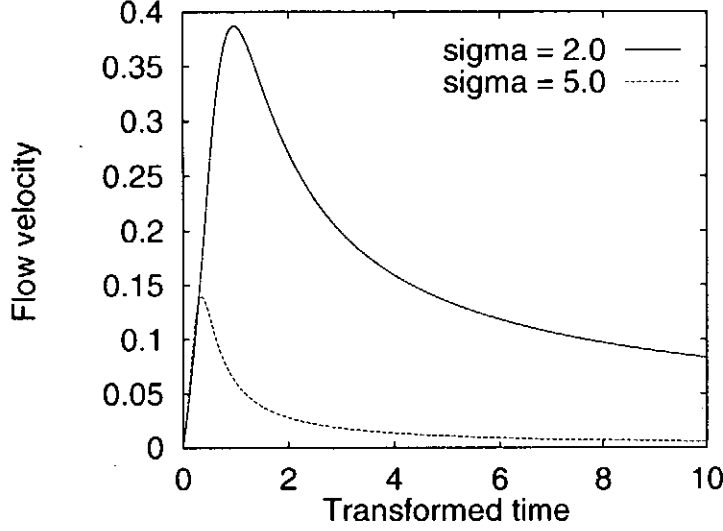


Figure 1: Solution for the initial value problem. The parameters are follows: $k_\xi = k_\eta = k_\zeta = 1.0$, and initial perturbations $\hat{u} = 0$ and $d\hat{u}/dT = 1.0$ at $T = 0$.

$$\begin{aligned}
 \xi &= \frac{x}{a}, \\
 \eta &= \frac{y}{a} - \frac{\bar{\sigma}}{\tau_g} \cdot \tau_g T \cdot \frac{x}{a}, \\
 &= \frac{1}{a}(y - \sigma t x), \\
 \zeta &= \frac{z}{a},
 \end{aligned} \tag{16}$$

where $\tau_g = \sqrt{-\rho_0/\rho'_0 g}$ is previously defined characteristic time for the growth of interchange mode, a is the characteristic length of the system, and $\bar{\sigma} = \tau_g \sigma$ denotes the normalized shear parameter. In the same way we normalize the dependent variables by a in space and τ_g in time; i.e. the velocity is normalized by a/τ_g and the wave number is normalized by a^{-1} . Then the normalized ODE is written as

$$\frac{d^2}{dT^2}(\kappa^2 \hat{u}) = \alpha^2 \hat{u}. \tag{17}$$

We can rewrite it to the following form,

$$\frac{d^2 \hat{u}}{dT^2} - \frac{4k_\eta \sigma k_x(T)}{\kappa^2} \frac{d\hat{u}}{dT} + \frac{2k_\eta^2 \sigma^2 - \alpha^2}{\kappa^2} \hat{u} = 0. \tag{18}$$

In the analogy of the Newton's equation, we notice that the coefficient of the second term represents the damping or forced oscillation as pointed out in Ref. [12]. As $T \rightarrow \infty$, $\mu_n(T) = -4k_y \sigma k_x(T)/\kappa^2$ becomes positive and large, and all initial perturbations are damped away due to the phase mixing effect of the background shear flow. A numerical result is shown in Fig. 1. As shown in eq. (18),

it is also seen in the numerical calculation that the gravitational instabilities in the case of static equilibria are stabilized due to shear flow.

3 Interchange instability of plasma with constant magnetic field

We will investigate an effect of the shear flow on interchange instability of plasma under the influence of homogeneous magnetic field. In case of treating plasmas, we must add $\mathbf{j} \times \mathbf{B}$ force in the rhs of the equation of motion (1) and also include induction equation,

$$\frac{\partial \mathbf{B}}{\partial t} - \nabla \times (\mathbf{v} \times \mathbf{B}) = 0. \quad (19)$$

We assume that there applied an strong toroidal field in z direction such as tokamaks with adding weak shearless poloidal field in y direction. The plasma is assumed to be incompressible following the previous analysis. The perturbed magnetic and velocity fields are assumed to be 2 dimensional in x - y direction, and thus we introduce the following poloidal flux function and stream function;

$$\begin{aligned} \mathbf{B}_{1\perp} &= \nabla \psi \times \mathbf{e}_z, \\ \mathbf{v}_{1\perp} &= \nabla \phi \times \mathbf{e}_z, \end{aligned} \quad (20)$$

where the subscript 1 denotes again the perturbed quantities, \perp expresses the direction with respect to the dominant magnetic field; i.e. z direction, and \mathbf{e}_z denotes the unit vector. Using these notations, we can eliminate the pressure from governing equations.

Here taking dot product with \mathbf{e}_z after taking the curl of the equation of motion leads to

$$\mu_0 \rho_0 [(\partial_t + v_{0y} \partial_y) \nabla_{\perp}^2 \phi - v_{0y}'' \partial_y \phi] = \mathbf{B}_0 \cdot \nabla (\nabla_{\perp}^2 \psi) + \mu_0 \partial_y \rho_1 g, \quad (21)$$

under the assumption of the shear flow as $\mathbf{v}_0 = (0, v_{0y}(x), 0)$ and constant magnetic field $\mathbf{B}_0 = (0, B_y, B_z)$. The component of the flow perpendicular to the ambient magnetic field can be considered to be produced by the $\mathbf{E} \times \mathbf{B}$ drift, taking account of the ideal Ohm's law, and it doesn't make any contradiction. Here we have also assumed that the gravitational force is acting in the x direction. The zeroth order stationary momentum balance is given by eq. (5) same as in the neutral fluid case, due to the straight and homogeneous magnetic field. It is noted that we recover the Rayleigh's equation [14] if we neglect the effect of the magnetic field ($B = 0$) and consider a constant density plasma. Induction equation is the same as ordinary RMHD which can include poloidal shear flow as

$$(\partial_t + v_{0y} \partial_y) \psi = \mathbf{B}_0 \cdot \nabla \phi. \quad (22)$$

Conservation of the mass density is same as that in the previous section eq. (2).

On assuming the linearity of the spatial dependence of the shear flow as $v_0 = (0, \sigma x, 0)$ again, and combining eqs. (21), (22), and (2) with the ansatz (11), we obtain

$$\begin{aligned}\mu_0 \rho_0 \frac{d}{dT} [(k_x(T)^2 + k_y^2) \hat{\phi}] &= -iF(k_x(T)^2 + k_y^2) \hat{\psi} + ik_y \mu_0 \hat{\rho}_1 g, \\ \frac{d}{dT} \hat{\psi} &= -iF \hat{\phi}, \\ \frac{d}{dT} \hat{\rho}_1 &= ik_y \rho'_0 \hat{\phi},\end{aligned}\tag{23}$$

where $F = \mathbf{k} \cdot \mathbf{B}_0 = k_y B_{0y} + k_z B_{0z}$. Thus these equations are reduced to

$$\frac{d}{dT} \left[(k_x(T)^2 + k_y^2) \frac{d\hat{\psi}}{dT} \right] = -\frac{F^2}{\mu_0 \rho_0} (k_x(T)^2 + k_y^2) \hat{\psi} - k_y^2 \frac{\rho'_0 g}{\rho_0} \hat{\psi}.\tag{24}$$

Considering the case with no shear flow ($\sigma = 0$), we find that the usual interchange instability equation can be obtained for static equilibrium. The first term on the rhs expresses the stabilizing effect due to the tension of the magnetic field, therefore the most unstable mode can be obtained in case of $\mathbf{k} \cdot \mathbf{B} = 0$ for $\rho'_0 < 0$. When we normalize time by $\tau_A = a\sqrt{\mu_0 \rho_0}/F$, we can rewrite this equation in dimensionless form as

$$\frac{d}{dT} \left[(k_x(T)^2 + k_y^2) \frac{d\hat{\psi}}{dT} \right] = -(k_x(T)^2 + k_y^2) \hat{\psi} + k_y^2 \frac{\tau_A^2}{\tau_g^2} \hat{\psi},\tag{25}$$

where the wave vectors are normalized by characteristic spatial scale length a .

We can rewrite this equation just the same way as in the previous section,

$$\frac{d^2 \hat{\psi}}{dT^2} - \mu(T) \frac{d\hat{\psi}}{dT} + [1 - S(T)] \hat{\psi} = 0,\tag{26}$$

where

$$\begin{aligned}\mu(T) &= \frac{2\sigma k_\eta k_x(T)}{k_x(T)^2 + k_y^2}, \\ S(T) &= k_y^2 \frac{\tau_A^2 / \tau_g^2}{k_x(T)^2 + k_y^2}.\end{aligned}$$

Here $\mu(T)$ represents the forced oscillation/damping term and $S(T)$ is the interchange drive term in analogy with the Newton's equation again. With neither density gradient nor shear flow, $\mu(T) = S(T) = 0$ and we have a pure oscillation representing the Alfvén wave. Including the density gradient, $S(T) \neq 0$, we obtain the interchange mode; when ρ'_0 becomes larger, the Alfvén wave represents an electromagnetic interchange instability. Further including shear flow, $k_x(T) = k_\xi - \sigma T k_\eta$ becomes larger with proportional to T , and finally, interchange drive term $S(T)$ becomes negligible compared to 1. In any case of the sign of given parameters σ , k_ξ , and k_η , the numerator of $\mu(T)$ becomes negatively large; this means forced damping. These behaviors of the instability are

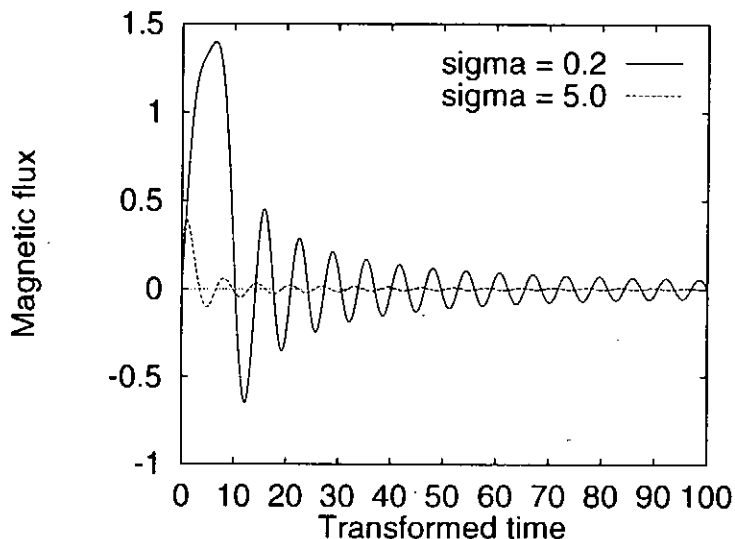


Figure 2: Solution for the initial value problem. The parameters are follows: $k_\xi = k_\eta = 1.0$, $G = 1.0$, and initial perturbations $\hat{\psi} = 0$ and $d\hat{\psi}/dT = 1.0$ at $T = 0$.

just the same as that of the kink-type mode. See eq. (32) and the following analysis in Ref. [12]. Shear flow mixing effect always overcomes the interchange drive and makes the oscillation damped away in a long term.

We will show the results for the numerical calculation. In Fig. 2 we have solved the initial value problem for the same initial condition and wave numbers on the different flow shear parameter σ . Now the ratio of the time scale $G \equiv \tau_A/\tau_g = 1$. Here we see that the shear flow mixing effect is stronger for larger shear parameter σ . It is different from the previous case that the time evolution in this case involves the oscillation. Since there is no branch included in the equation for neutral fluid in case of $\rho'_0 = 0$, the interchange mode is the only physical mechanism to perturb the system, but here we also have the Alfvén wave in a plasma which propagates stably in the static case, therefore, we have an oscillatory damping behavior when included the shear flow.

4 discussion

Applying the Kelvin’s non-modal approach, we have shown that the interchange modes are always damped away in a long term due to the phase mixing by the background shear flows. Note that we don’t have Kelvin-Helmholtz type instability which comes from the second spatial derivative of the background shear flow [?, 14]. Another point is that shear flow stretches the perturbation field and continuously varies the wavenumber component with the flow shear as can be seen in Fig. 3, which is extremely similar to the nonlinear effect.

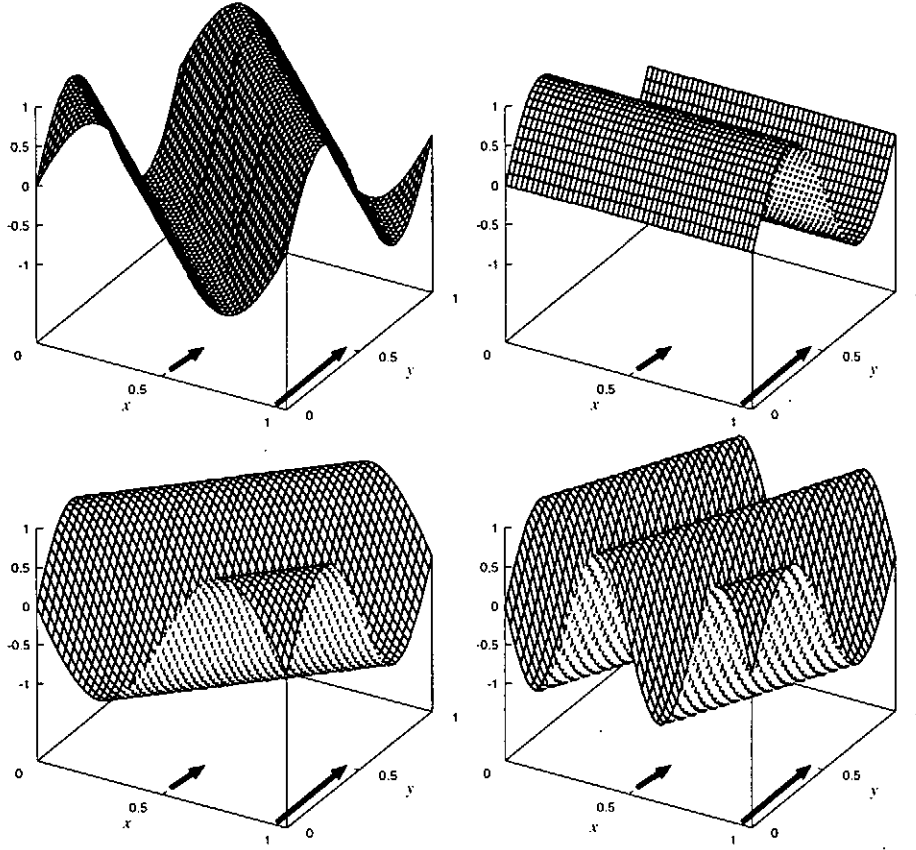


Figure 3: Mixing effect seen by the spatially inhomogeneous Galilean transform. The isophase surface is drifted and stretched in the stationary shear flows from upper left figure to the upper right, lower left, and begins to be stretched in the final lower right figure.

It should be noted that the form of the equation for the interchange instability (26) and that for kink-type instability (32) in Ref. [12] are exactly the same way in their time evolution. Of course these two modes may have spatially different structures, at least so they are for the static equilibria. But the fact means that they have no difference in time evolution, and we can say that these terms have the same effect to make the spectrum shift to more unstable side. Since we have dropped all spatial inhomogeneity in our calculus, we have get to the same equation for both modes.

Finally, this method is restricted only for spatially linear shear flow and for local perturbations. Thus we have considered the infinite plasma with homogeneous magnetic field, and assumed a spatially linear shear flow without including the boundary effect. In a linear shear flow case we have the partial differential operator ∂_x as in eq. (8) in terms of our spatially inhomogeneous

Galilean transform (7). Therefore, we have the ansatz (11) and the x dependence as $\propto \sin(k_\xi - k_\eta \sigma t)x$, i.e. we could have carried out our analysis only in the framework of a single sinusoidal function, although the wave number is shifted continuously to a larger value. If the flow profile is not linear, e.g. parabolic as $v_{0y}(x) = \sigma x^2/2$, then we'll have the partial differential operator ∂_x as

$$\partial_x = \partial_\xi - \sigma \xi T \partial_\eta,$$

by modifying our Galilean transform as $\eta = y - \sigma x^2 t/2$. Thus we have the following x dependence,

$$\propto \sin(k_\xi - k_\eta \sigma t x)x,$$

which is no longer a simple sinusoidal function with respect to x . Of course this expression is not rigorous, but it might explain why the non-modal approach is restricted only to the linear spatial dependence for stationary shear flows. Although the inhomogeneity of the magnetic field might be treated in some modification, we must be careful to extend to flows with spatially nonlinear dependence. This will be left as our future study.

References

- [1] E. Frieman and M. Rotenberg: Rev. Mod. Phys. **32**, 898 (1960).
- [2] E. Hameiri: Phys. Fluids **26**, 230 (1983).
- [3] A. Bondeson, R. Iacono, and A. Battacharjee: Phys. Fluids **30**, 2167 (1987).
- [4] E. Hameiri: Phys. Plasmas **5**, 3270 (1998).
- [5] K. Yosida: *Functional Analysis*, Springer-Verlag (Berlin, 1995).
- [6] Lord Kelvin (W. Thomson): Philos. Mag., Ser. 5, **24**, 188 (1887).
- [7] W. O. Criminale and P. G. Drazin: Stud. Appl. Math. **83**, 123 (1990).
- [8] G. D. Chagelishvili, A. D. Rogava, and I. N. Segal: Phys. Rev. E **50**, 4283 (1994).
- [9] A. D. Rogava and S. M. Mahajan: Phys. Rev. E **55**, 1185 (1997).
- [10] S. M. Mahajan and A. D. Rogava: Astrophys. J. **518**, 814 (1999).
- [11] A. G. Tevzadze: Phys. Plasmas **5**, 1557 (1998).
- [12] F. Volponi, Z. Yoshida, and T. Tatsuno: to be published in Phys. Plasmas.
- [13] S. Chandrasekhar: *Hydrodynamic and hydromagnetic stability*, Clarendon Press (Oxford, 1961) Chap. XI.
- [14] P. G. Drazin and W. H. Reid: *Hydrodynamic stability*, Cambridge Univ. Press (Cambridge, 1981) p. 131.

Comparison of shear flow formation between resonant and non-resonant resistive interchange type modes

Takeshi Unemura, Satoshi Hamaguchi and Masahiro Wakatani

Graduate School of Energy Science, Kyoto University, Gokasho, Uji, Japan 611-0011

Abstract

With a numerical code, time evolution of nonlinear resistive interchange type modes are studied numerically. Formation of poloidal shear flow due to mode coupling is seen for both the resonant and non-resonant case. There are some differences in the formation of shear flow and effect on density evolution between these two modes.

Keywords: poloidal shear flow, resistive interchange mode, resonant mode, non-resonant mode, non-linear simulation

1 Introduction

It is observed that a poloidal flow with velocity shear is generated according to the L to H transition. The flow shear destroys a global mode structure of vortex and suppresses a radial transport across magnetic field lines. Thus the shear flow may improve the plasma confinement.

Our concern is in the nonlinear model that the poloidal shear flow is created from the mode coupling of nonlinear resistive interchange type modes[1][2]. The model includes an average unfavorable curvature and finite plasma resistivity for destabilizing pressure-driven modes. The rotational transform, $\iota(r)$ is assumed non-monotonic, which is seen in currentless finite beta plasmas such as in Heliotron E and LHD[3]. Fluctuations are assumed as single helicity in a cylindrical model plasma. The helical mode with $(m, n) = (3, 2)$ and its 15 higher harmonic modes are included numerical calculations. There are two resonant surfaces at the $\iota = 2/3$ surface for our typical non-monotonic ι profile. We can change the absolute value with keeping the ι profile, and non-resonant cases are possible.

From simulation results, it is shown that a shearing rate exceeding the linear growth rate suppress a convective diffusion, and the decay of density becomes weaker than the case without the shear flow component.

In section 2, model equations used in our simulation code are described. In section 3, numerical methods to solve the model equations are explained. Numerical results are given in section 4, and in section 5 main results are discussed.

2 Model equations

The reduced two fluid equations for describing electrostatic fluctuations in a cylindrical geometry are

$$\rho^2 \frac{d}{dt} \nabla_{\perp}^2 \phi = \frac{\epsilon^2}{\nu} \nabla_{\parallel}^2 (n - \phi) + \nabla n \times \nabla \Omega \cdot \hat{z} + \mu \nabla_{\perp}^4 \phi, \quad (1)$$

$$\frac{d}{dt} (n + \bar{n}) = \frac{\epsilon^2}{\nu} \nabla_{\parallel}^2 (n - \phi) + \nabla (n - \phi) \times \nabla \Omega \cdot \hat{z} + D_{\perp} \nabla_{\perp}^2 n, \quad (2)$$

with normalized quantities[4][5]. These reduced equations are useful for numerical calculations to study physics of electrostatic turbulence.

In model equations, ϕ is a perturbation of electrostatic potential, n is a perturbation of density, ν is an electron-ion collision frequency, \bar{n} is a background density and ρ is a Larmor radius measured with an electron temperature. Also

$$\nabla_{\parallel} \equiv \frac{\partial}{\partial z} + \nabla\psi \times \hat{z} \cdot \nabla, \quad (3)$$

$$\psi = - \int_0^r r l(r) dr, \quad (4)$$

$$\Omega \equiv \frac{N\epsilon^2}{l} \left(r^2 l(r) + 2 \int_0^r r l(r) dr \right) \quad (5)$$

are used in eqs(1) and (2). Here N is a helical pitch number and l is a pole number.

The dissipative terms are added to the model equations to obtain a saturation of linear instability. These terms should be small in order to change the behavior of turbulence. In eqs.(1) and (2) μ is a viscosity and D_{\perp} is a diffusivity. These terms have also the effect to suppress the numerical instability.

The model equations (1), (2) are normalized with,

$$\begin{aligned} \frac{r}{a} = r, \quad \frac{z}{R} = z, \quad \omega_{ci} \left(\frac{\rho_s}{a} \right)^2 t = t, \\ \frac{e}{T_e} \phi_e = \phi, \quad \frac{n_1}{n_0} = n, \\ \frac{D_{\perp}}{\omega_{ci} \rho_s^2} = D_{\perp}, \quad \frac{\mu}{\omega_{ci} \rho_s^2} = \mu. \end{aligned} \quad (6)$$

Here, $\rho_s = \sqrt{T_e m_i / e B_0}$, ω_{ci} is ion cyclotron frequency and ω_{ce} is electron cyclotron frequency.

When \mathbf{v}_{\perp} is equal to the $\mathbf{E} \times \mathbf{B}$ drift velocity, the vorticity, ω is given by

$$\omega \equiv \nabla_{\perp}^2 \phi. \quad (7)$$

3 Numerical method

Here, the numerical methods used in our simulation code are explained.

Numerical instabilities from the advection terms can be suppressed when numerical dissipations are included to the numerical scheme. However, the time step is limited with the CFL criterion when the explicit scheme is used. If the diffusion term and the viscosity term are solved with the explicit scheme, these terms might produce a numerical instability when the time step does not satisfy the CFL criterion. In the code we use the implicit scheme for the diffusion term and the viscosity term to avoid the numerical instability and a severe limitation for the time step. Thus, the model equations are solved with the semi-implicit scheme, or the dissipation terms are solved implicitly and other terms are solved explicitly.

The model equations, (1), (2) are the partial differential equations with respect to r, θ, z and t . These equations are expanded with the Fourier series in the poloidal direction (θ direction) and the toroidal direction (z direction) as follows :

$$\begin{aligned} \phi(r, \theta, z, t) &= \sum_{m,n=-\infty}^{\infty} \phi_{(m,n)}(r, t) \exp(im\theta - inz), \\ \omega(r, \theta, z, t) &= \sum_{m,n=-\infty}^{\infty} \omega_{(m,n)}(r, t) \exp(im\theta - inz), \end{aligned} \quad (8)$$

$$n(r, \theta, z, t) = \sum_{m,n=-\infty}^{\infty} n_{(m,n)}(r, t) \exp(im\theta - inz)$$

In the numerical calculations, however, summations are limited within finite number terms.

For the radial derivatives, we use a finite difference method. For the time evolution, the two-step method is used to keep the second order accuracy of the time steps.

For the boundary conditions, it is assumed that there is a completely conductive wall at $r = a$. Thus,

$$n_{(m,n)}|_{r=a} = 0, \phi_{(m,n)}|_{r=a} = 0, \omega_{(m,n)}|_{r=a} = 0. \quad (9)$$

At $r = 0$, for $(m \neq 0, n)$ modes,

$$n_{(m,n)}|_{r=0} = 0, \phi_{(m,n)}|_{r=0} = 0, \omega_{(m,n)}|_{r=0} = 0. \quad (10)$$

And for $(0, 0)$ mode and $(m = 0, n)$ modes,

$$\frac{\partial n_{(0,n)}}{\partial r}\bigg|_{r=0} = 0, \frac{\partial \phi_{(0,n)}}{\partial r}\bigg|_{r=0} = 0, \frac{\partial \omega_{(0,n)}}{\partial r}\bigg|_{r=0} = 0. \quad (11)$$

In the following numerical simulations we assume, $\nu = 1.0 \times 10^{-4}$, $\mu = 5.0 \times 10^{-3}$, $D_{\perp} = 5.0 \times 10^{-3}$, $n_0(r) = \exp(-2.0r^2) - \exp(-2.0)$, $\rho = 0.02$, $\epsilon = 0.1$, $N = 19$, $l = 2$. Here, ν is the normalized collision frequency with $\nu = \nu_{ci}/\omega_{ce}$. μ is the viscosity coefficient normalized with $\mu = \mu/(\omega_{ci}\rho_s^2)$. D_{\perp} is the diffusion coefficient normalized with $D_{\perp} = D_{\perp}/(\omega_{ci}\rho_s^2)$, also. $\rho = \rho_s/a$. The spatial meshes are assumed 200. Although our code can treat multi-helicity cases, $(m, n) = (3, 2)$ single helicity mode is studied in the following, where $m(n)$ is a poloidal (toroidal) mode number. In this case, the mode resonance surface is located at the $\iota = 2/3$ surface, where ι is a rotational transform.

A small fluctuation is necessary as a seed of turbulence at $t = 0$. Here, the following fluctuation is assumed initially,,

$$\phi_{(3,2)}(r, t = 0) = 1.0 \times 10^{-3}(1 - r^2)^4 r^4 \quad (12)$$

for the $(m, n) = (3, 2)$ mode.

The rotational transform profile is assumed as in Fig. 1. Each solid line is the ι profile assumed in each simulation. To label each ι profile, the value $\Delta\iota$ is defined as $\Delta\iota \equiv n/m - \iota_{\min}$.

4 Numerical results

At first, the generated poloidal flow velocity profiles are shown. Fig. 2 (a)–(f) correspond to $\Delta\iota = -0.07, -0.04, -0.02, 0.00, 0.02, 0.04$, respectively. And, the case of monotonic rotational transform is shown in Fig. 2 (g) as a reference.

When the two resonance surfaces are separated, the case of $\Delta\iota = -0.07$, the poloidal flow is formed in the $-\theta$ direction at the region near the inner resonance surface, and the $+\theta$ direction flow is formed between the two resonance surfaces. The property near the inner resonant surface is similar to the case of Fig. 2 (g), showing that the $-\theta$ direction flow are formed near the single resonant surface. When the two resonant surfaces become close each other, or $\Delta\iota$ becomes small, the $-\theta$ direction poloidal flow is formed over a broad region and has a peak near the minimum ι surface. And the magnitude of flow velocity becomes larger than the case of $\Delta\iota = -0.07$. When the mode becomes non-resonant, the $-\theta$ direction poloidal flow is also formed near the minimum ι surface.

Next, the behavior of fluctuations in the presence of the poloidal shear flow are shown. Here, in order to clarify the effect of the poloidal shear flow, we also tried the numerical simulations in which the poloidal flow component is removed.

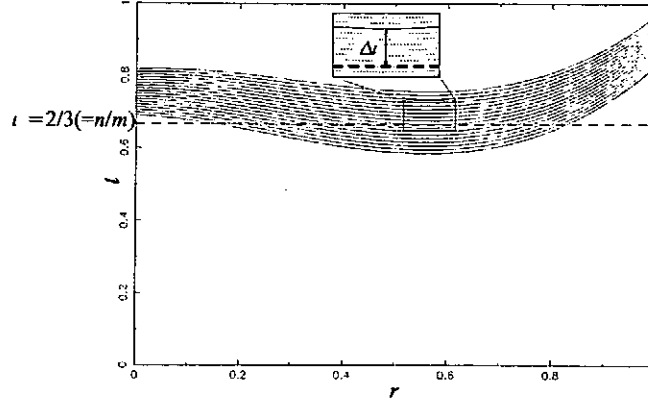


Figure 1: Rotational transform, $\iota(r)$, profiles. The broken line is $\iota = 2/3$, and the mode resonant surface corresponds to the $\iota = 2/3$ surface. Here, $\Delta\iota$ is defined as a difference between the minimum value of ι and $2/3$.

Fig. 3(a)—(f) show time evolution of the kinetic energy of the fluctuations with $(m, n) = (3, 2), (6, 4), (9, 6)$ modes for the cases of $\Delta\iota = -0.07$ — $+0.04$, respectively. The solid lines denote the cases including the poloidal flow component. On the other hand, the broken lines denote the cases removing flow component.

For the cases of $\Delta\iota = -0.07$ and $\Delta\iota = 0.04$, the suppression of the fluctuations are observed clearly when the poloidal flow component is included. However, for the cases with $\Delta\iota \simeq 0$, the suppression is not clear.

Fig. 4(a)—(f) show time evolution of the shearing rate of the poloidal flow and density at several radial positions. The shearing rate is normalized with the linear growth rate of the $(m, n) = (3, 2)$ mode. The solid line denotes the cases including the poloidal flow component. The broken line denotes the case removing the poloidal flow component.

The normalized shearing rate becomes small as $\Delta\iota$ becomes close to 0. For the cases with $\Delta\iota = -0.07$ and $\Delta\iota = -0.04$, the normalized shearing rate are larger than the cases with $\Delta\iota = -0.02$ or $\Delta\iota = 0.0$.

In the time evolution of the density, there is a difference between the solid line and the broken line. At the inner region with $r = 0.04[m]$, the density shown by the solid line becomes higher than that shown by the broken line. At the outer region with $r = 0.08[m]$, the density shown by the solid line becomes close to that shown by the broken line. This result suggests the suppression of the particle transport from the inner region to the outer region with the poloidal shear flow.

When the mode becomes non-resonant, the normalized shearing rate becomes large. Thus the density keeps a higher value when the poloidal flow is included. This means that suppression of transport may be more effective in the case of non-resonant mode than the case of $\Delta\iota = 0$.

5 Discussion

When the two resonance surfaces are separated, for the case of $\Delta\iota = -0.07$, the generated poloidal flow is localized near the inner resonant surface and the velocity shear becomes large. This poloidal shear flow has an effect to reduce the radial particle transport.

When the modes becomes non-resonant and is still linearly unstable, it generates a similar poloidal flow. This poloidal flow has a larger shearing rate than that in the case $\Delta\iota = 0.0$, and is effective to reduce the radial particle confinement.

When $\Delta\iota$ is close to 0, the velocity of the generated poloidal flow becomes large. The linear growth

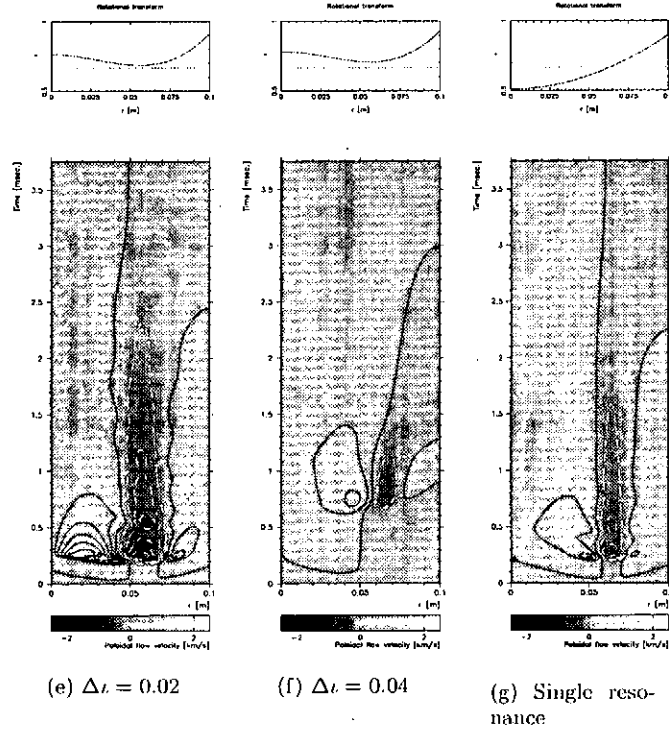
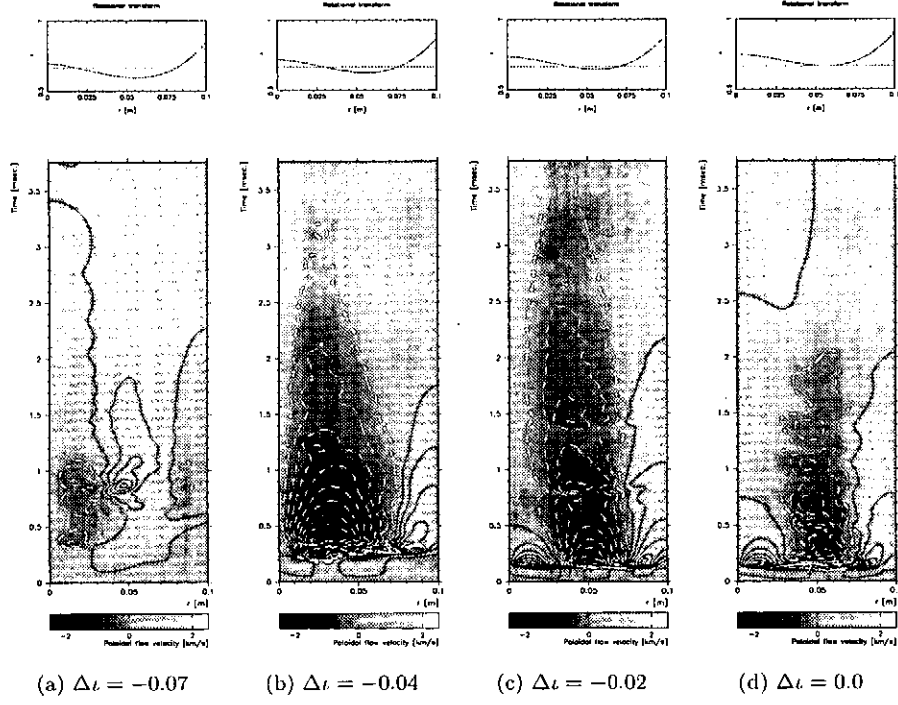


Figure 2: Time evolution of the radial profile of the poloidal flow velocity. The solid line contour denotes positive value describing the $+\theta$ direction poloidal flow, and the broken line contour denotes negative value describing the $-\theta$ direction poloidal flow.

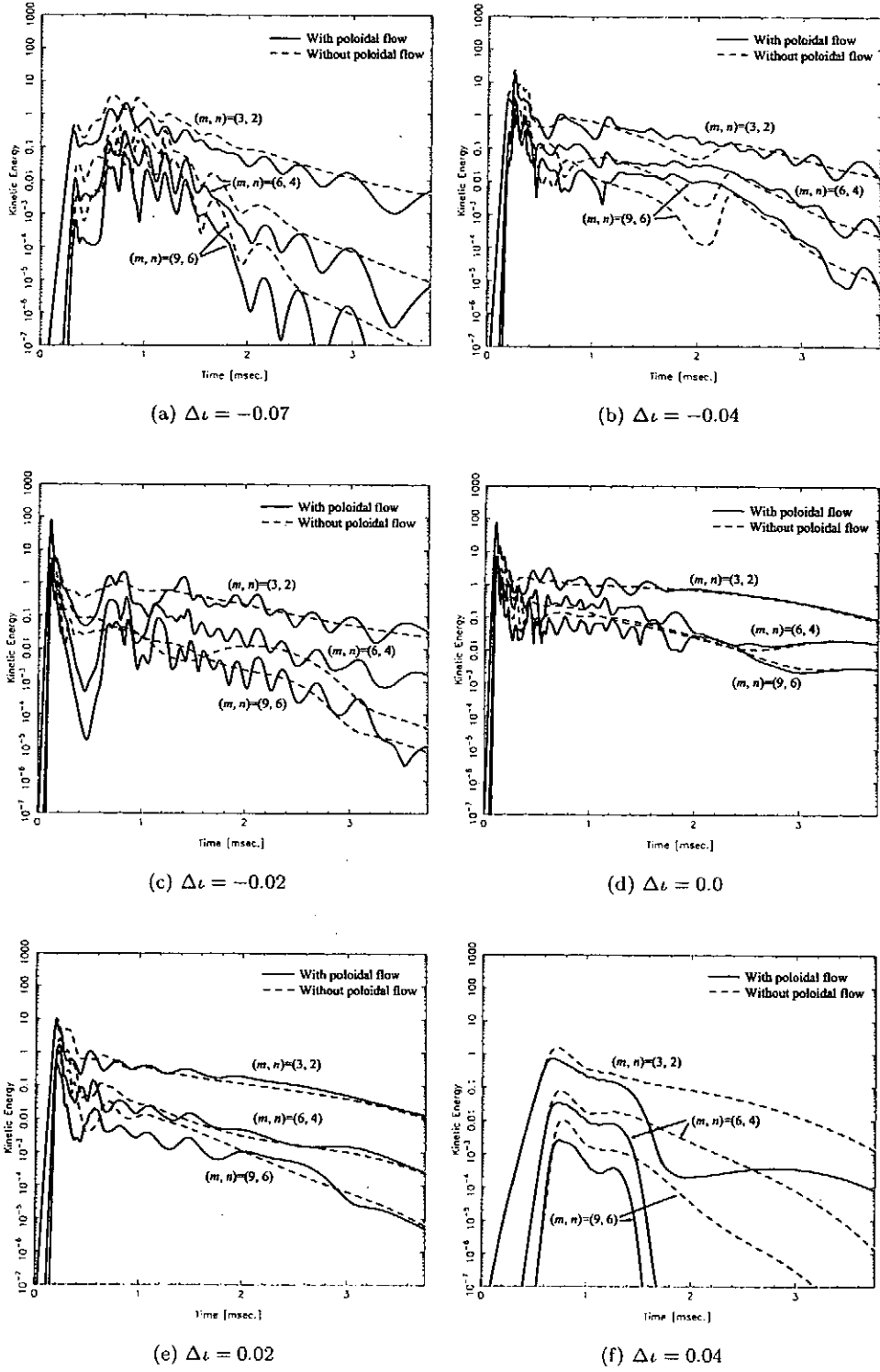


Figure 3: Time evolution of the kinetic energy of the fluctuations with $(m, n) = (3, 2), (m, n) = (6, 4), (m, n) = (9, 6)$. The solid lines denote the cases including the poloidal flow component. The broken lines denote the cases removing the poloidal flow component.

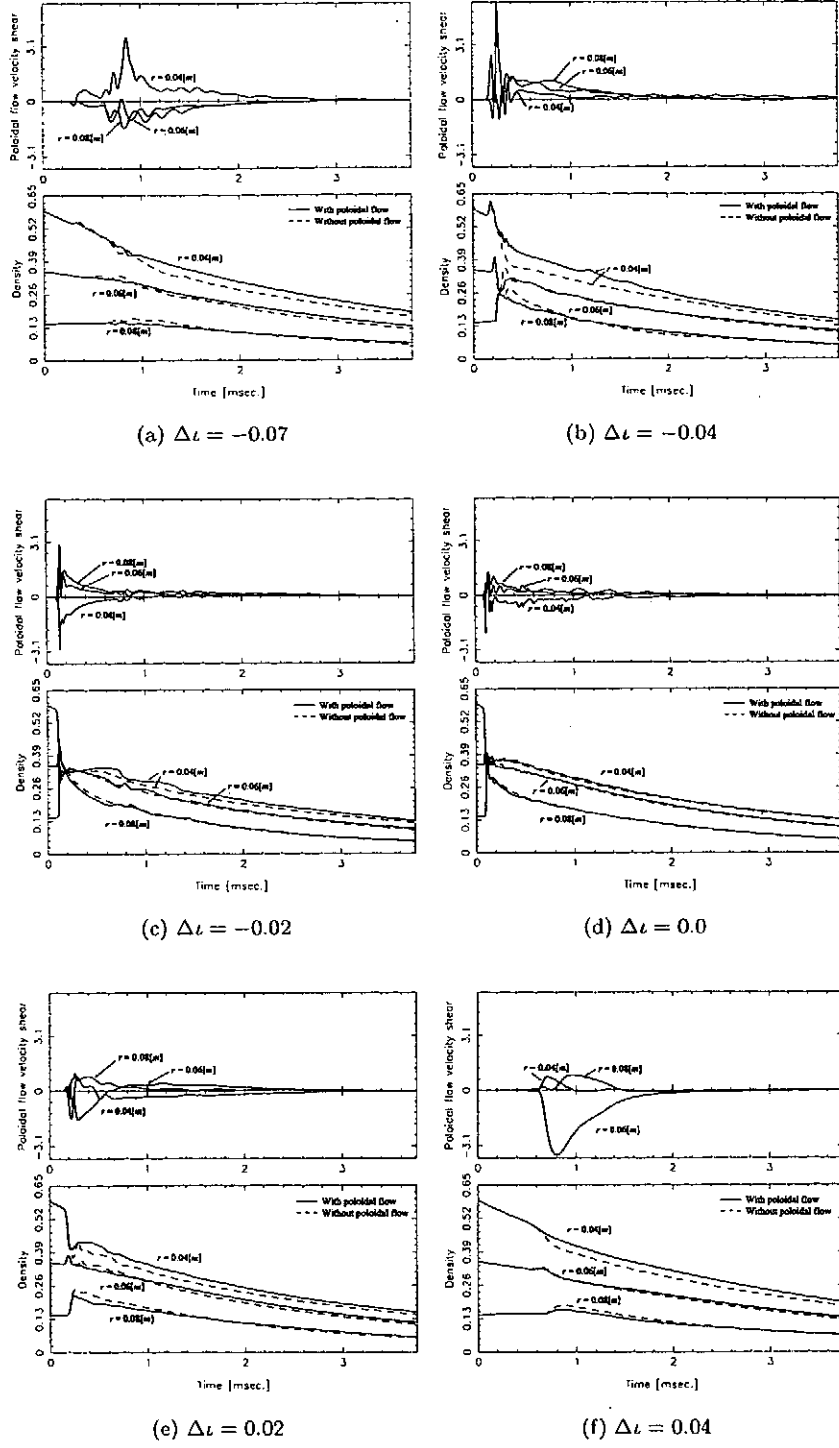


Figure 4: Time evolution of the shearing rate of the poloidal flow and the density at $r = 0.04, 0.06$ and $0.08[m]$. The shearing rate is normalized with the linear growth rate of the $(n, n) = (3, 2)$ mode.

rate also becomes large in this case because the magnetic shear vanishes at the resonant surface. However, the shearing rate normalized by the linear growth rate is not large compared to the case of $\Delta\iota = -0.07$ or $\Delta\iota = 0.04$. Thus, in the case of $\Delta\iota = 0.0$ the obtained poloidal flow may have less effect on the radial particle transport.

As a next step we will study a multi-helicity case to understand a relation between the poloidal shear flow generation and the radial particle transport in a edge region.

References

- [1] A. Hasegawa and M. Wakatani, Phys. Rev. Lett. **59** 1581 (1987).
- [2] B. A. Carreras and V. E. Lynch, Phys. Fluids **B5** 1795 (1993).
- [3] K. Ichiguchi, Y. Nakamura and M. Wakatani, Nucl. Fusion **31** 2073 (1991).
- [4] H. Sugama, M. Wakatani and A. Hasegawa, Phys. Fluids **31**, 1601 (1988).
- [5] M. Wakatani, K. Watanabe, H. Sugama and A. Hasegawa, Phys. Fluids **B4** 1754 (1992).

Gyro-kinetic Simulation of Self-generated Radial Electric Field induced by Kinetic $m=1$ Internal Kink Mode

T.MATSUMOTO, S.TOKUDA, Y.KISHIMOTO

Naka Fusion Research Establishment, Japan Atomic Energy Research Institute,
801-1, Naka-machi, Naka-gun, Ibaraki Pref. 311-0193, Japan
E-mail : tmatsumo@naka.jaeri.go.jp

H.NAITOU

Department of Electrical and Electronic Engineering, Yamaguchi University,
Ube city 755-8611, Japan

Abstract

Effects of density gradient on the kinetic $m=1$ ($m/n=1/1$) internal kink mode in a cylindrical tokamak plasma are studied by the gyro-kinetic particle simulations. When the density gradient is not large enough to change the full reconnection process, the phenomena after the full reconnection, such as the secondary reconnection and the evolution of the safety factor profile, are changed considerably due to the self-generated radial electric field, i.e. the $m/n=0/0$ mode. The growing mechanism is explained by the difference of \mathbf{ExB} drift motion between ions and electrons, which is caused by the fast parallel motion of electron. Once the radial electric field is triggered by the symmetrical flow induced by the $1/1$ mode, the $0/0$ mode grows up to the same level as the $1/1$ mode, and drives an \mathbf{ExB} plasma rotation in the ion diamagnetic direction, which breaks the symmetrical plasma flow induced by the $1/1$ mode. The density and current distributions, and therefore minimum safety factor q_{\min} after the full reconnection, are found to be affected by the asymmetrical flow driven by the $1/1$ and $0/0$ modes.

Keywords

fusion, tokamak, internal collapse, $m=1$ mode, magnetic reconnection, gyro-kinetic model, particle simulation, radial electric field, density gradient, diamagnetic effect

1. Introduction

In fusion plasma research, the tokamak type device has a great advantage for a candidate of commercial fusion reactor. However, there are still several physical problems to be clarified until the construction and operation of tokamak reactor. Then, it is necessary to clarify this problem experimentally in support of theoretical and numerical results.

In tokamak plasma with the safety factor q at the magnetic axis less than unity, a magnetohydrodynamic (MHD) mode with $m/n=1/1$ becomes unstable. Here m and n are the poloidal and the toroidal mode numbers, respectively. The $m=1$ mode has attracted much interest, since it is accompanied by fast magnetic reconnection and triggers a subsequent internal collapse, and this process would be repeated (sawtooth oscillations) in a steady-state operation.

In the early period of plasma research, the internal collapse by the $m=1$ mode has been explained with the resistive MHD model[1]. However, as the plasma temperature is getting higher, the behavior of the $m=1$ mode in many tokamak experiments [2,3] (in particular, the magnetic reconnection time and the behavior of the safety factor after the collapse) are not well explained using only the resistive MHD model, suggesting the importance

of some other effects.

It is also found that the $m=1$ mode can be influenced by kinetic effects of the plasma, such as the electron inertia, density and temperature gradients, finite ion Larmor radius and high energy trapped ions. Because the kinetic effects are crucial in the linear and nonlinear development of the $m=1$ mode, a model including the kinetic effects is required to simulate the collisionless nature of the mode.

Wesson pointed out the importance of electron inertia to explain the fast collisionless reconnection[4]. In his theory, the width of the current layer is of the order of the collisionless electron skin depth. Naitou et.al. performed a nonlinear gyro-kinetic particle simulation of the $m=1$ mode in a cylindrical geometry with an uniform plasma pressure[5,6]. They showed that the magnetic reconnection is triggered by the electron inertia in a much faster time scale than that caused by the resistivity, and the magnetic configuration with $q_{min}<1$ can be reconstructed after the full reconnection. This two step model was firstly proposed by Biskamp et.al. [7] with the two fluid MHD model. In the first step, the full reconnection process due to the electron inertia is completed, and the $m=1$ mode of the electrostatic potential retains after the full reconnection. In the second step, a secondary reconnection is observed due to the current reconcentration which is caused by strong $\mathbf{E} \times \mathbf{B}$ motion.

In this paper, in order to study effects of density gradient on the kinetic $m=1$ mode, we extend the previous gyro-kinetic simulation to the non-uniform plasma with a density gradient. In Section 2, we present a gyrokinetic simulation model where the density gradient is taken into account, and describe the model configuration and parameters. In Section 3, the simulation results with a non-uniform density profile are shown and are compared with those obtained with the uniform density profile. The diamagnetic effect and the density gradient effect are shown in the full reconnection process. The mechanism of the charge separation is also shown by the fast parallel motion of electrons. In Section 4, the nonlinear kinetic effect due to the density gradient are shown. In particular, the growth of the radial electric field is found to change the behavior of the plasma such as the density and current profiles. The energy history is also explained with the above results. Finally, a summary is given in Section 5.

2. Simulation Model

In our study, we employ a gyrokinetic model[8] to simulate the $m/n=1/1$ mode, because it is efficient compared with the full kinetic model from a view point of the computation. In the gyrokinetic model, the characteristic time scale is larger than the ion cyclotron period. Hence, the time step can be chosen much larger than the standard particle simulation model in which time step is of the order of electron plasma period.

We adopt a δf method to reduce the statistical noise drastically. In order to include the effect of density gradient in the formulation of the gyro-kinetic equations, we modify the perturbation part of Ampere's law and the time evolution of the weight function obtained in Ref.5. These formulations are given in Ref.9.

The dynamics of the δf are computed in a three dimensional rectangular box with the Cartesian coordinate (x,y,z) . Toroidal effects are ignored for simplicity. A periodic boundary condition is adopted in the z direction, and a perfect conducting wall is imposed on the x - y boundary surfaces. We assume a uniform temperature profile.

The length and velocity used in this simulation are normalized with the ion Larmor radius ρ_i and the Alfvén velocity L_z/V_A , and the main parameters are listed on Table 1. In the present simulation, we choose the skin depth ($\delta_e = c/\omega_{pe}$) as $\delta_e = 4\rho_i$, and the grid size in the z -direction as 1000 times larger than that in x or y -direction.

3. Internal Collapse

3.1. Diamagnetic Effect

It is well known that the behavior of the $m/n=1/1$ mode is affected by the pressure gradient due to the

diamagnetic effect. The linear growth rate of the 1/1 mode is restricted with the dependency of a square of the diamagnetic frequency, as been evaluated by the resistive and kinetic models [10]. In the two fluid simulation, it is also shown that the 1/1 mode could be saturated nonlinearly, and result in a new equilibrium with $m=1$ magnetic island[11].

In our simulation model, the diamagnetic effect is induced only by the density gradient, since the temperature profile is assumed to be uniform. Figure 2 shows the linear growth rate of the $n=1$ mode in the presence of the density gradient. The ω_* stabilization is found to have a parabolic dependence which is similar to that obtained in Ref.10

However, the purpose of our research is to clarify the nonlinear kinetic effect of the density gradient on the sawtooth crash rather than the ω_* stabilization effect. Then, for the case of the non-uniform density profile, we mainly choose $\omega_* = 0.196V_A/L_Z$, which is much less than the growth rate for the uniform density ($\gamma_0 \sim 0.87V_A/L_Z$), and has an adequate density gradient as shown in Fig.1(b). Therefore, the ω_* stabilization is negligible, and the nonlinear kinetic effect of the density gradient becomes clear as mentioned in the next section.

3.2. Full Reconnection

Next, the simulation results of the non-uniform density case are compared with those obtained for the uniform density case. Figure 3 shows the Poincare plots of the magnetic field lines before and after the full reconnection in the simulations with (I) non-uniform and (II) uniform density profiles. As shown in Fig.3(I-a) before the full reconnection, the core plasma has concentric flux surfaces and the $m=1$ magnetic island has a crescent shape. The core plasma is swept out from the central region due to the \mathbf{ExB} motion induced by the $m=1$ mode of the electrostatic potential which grows inside the $q=1$ rational surface.

As a result of the full reconnection, the magnetic configuration has nested flux surfaces as shown in Fig.3(I-b). The process of the full reconnection with the density gradient is almost the same as that obtained with the uniform density profile as shown in Fig.3(II-a,b). Figure 3(I-c) and (II-c) are the magnetic configurations from which we find the discrepancy between them. For the uniform density case (II-c), the secondary reconnection occurs, while for the non-uniform density case (I-c), the secondary reconnection is unclearly seen.

Figure 4 shows the electrostatic potential energy decomposed in the longitudinal mode numbers n in (I) the non-uniform and (II) the uniform density cases. After the full reconnection is completed [$t = 34 \sim 35(V_A/L_Z)$, near the arrows of (I-b) and (II-b)], the $n=1$ mode is dominant in both cases. Figure 5 shows the electrostatic potential contours at $z=0$. In the poloidal direction, the $m=1$ mode is obviously dominant in both cases, as seen in Fig.5(I-b) and (II-b). Then, the $m/n=1/1$ mode is dominant through the full reconnection process.

3.3. Charge Separation

From the above results, it seems that the behavior of the magnetic configuration and the 1/1 mode is not affected so much by the density gradient during the full reconnection. However, as the core plasma is swept out due to the \mathbf{ExB} flow, the 0/0 mode grows with negative sign at the central region. Figure 6 shows the difference of the $n=0$ mode energy between the non-uniform and the uniform density cases, which means the charge separation with the increase of the plasma shift until the end of the full reconnection ($t \sim 32.5V_A/L_Z$).

The elementary process causing the charge separation is explained by the difference of motion between ions and electrons. The parallel velocity of electrons is much faster than that of ions by $(m_i/m_e)^{1/2}$ if $T_e \sim T_i$. Then, in the process of \mathbf{ExB} motion, the electrons are obedient to the electric field averaged along the magnetic field line, while the ions faithfully submit to the local electric field. As a result, the electron \mathbf{ExB} motion delays compared with the ion motion. In the presence of the density gradient, the charge separation can be induced by this process. Therefore, the radial electric field is closely relevant to the motion of high density plasma region.

4. Nonlinear Effects

4.1. Nonlinear Evolution of Radial Electric Field

After the full reconnection, on the contrary, the density gradient is found to affect considerably the nonlinear behavior of plasma. In the presence of the density gradient, the $n=0$ mode grows exponentially to be the same level as that of the $n=1$ mode, as shown in Fig.4(I) ($t = 35 \sim 38 V_A/L_z$). At the same time, we found that the $m=0$ component of the electrostatic potential, i.e. the radial electric field, grows up as shown in Fig.5(I-d). Then, it is found that the $0/0$ mode grows nonlinearly with positive sign at the central region.

On the other hand, the radial electric field is not observed in the uniform density case. In the poloidal direction, the $m=1$ mode is still dominant, although the electrostatic potential has a reversed structure radially. Then, the $m/n=1/1$ mode is dominant at $t = 38.45 (V_A/L_z)$, as can be seen in Fig.5(II-d) and Fig.4(II).

The evolution of the density profile in the nonlinear phase is affected by the \mathbf{ExB} rotation due to the self-generated radial electric field. The black region in Fig.7 represents the high density region in the non-uniform density case. The high density region of the initial equilibrium (I-a) is swept out from the central region because of the full reconnection, as shown in Fig.7(I-b). After the full reconnection, the high density plasma rotates in the ion diamagnetic direction, and comes into the central region spirally as shown in Fig.7(I-c) and (I-d).

The formation of the vortex structure is found to be closely related with the radial electric field. The mechanism of the nonlinear growth of the $0/0$ mode and the vortex density is shown prior to this.

4.2. Physical Mechanism

The \mathbf{ExB} motion just after the full reconnection is sustained by the $m=1$ mode, as shown in Fig.5(I-b). The high dense plasma comes into the central region again by the symmetrical flow induced by the $m=1$ mode. At that moment, the ion comes inside faster than the electron due to the electron delay process mentioned in the previous section. Then, the weak charge separation makes the seed radial electric field, i.e., the $m=0$ mode which changes the symmetrical flow pattern into the asymmetrical one, as shown in Fig.7(I-b).

Once the seed field is generated, the \mathbf{ExB} rotation is induced, and more dense plasma enters into the central region. Then, the charge separation is facilitated due to the electron delay. As a result, the radial electric field is self-generated by this positive feedback mechanism.

4.3. Break of Symmetry

Such a radial electric field ($0/0$ mode) is found to play an important role on the nonlinear behavior of the current and density profiles and on the stage after the full reconnection such as the secondary reconnection and the density redistribution. The growth of the radial electric field means the destruction of the symmetrical flow produced by the $m/n=1/1$ mode. Then, in the presence of the density gradient, the plasma behavior after the full reconnection is characterized by the resultant asymmetrical flow induced by the $0/0$ and $1/1$ modes.

As seen in Fig.5(I-d), the sign of the radial electric field is positive at the central region. Therefore, the \mathbf{ExB} rotation induced by the radial electric field is in the ion diamagnetic direction. Figure 8 shows the deviation of the longitudinal current from the equilibrium distribution $\delta J_z = J_z - J_{z0}$ for (I) the non-uniform and (II) uniform density cases. The dashed line represents the symmetry line of the \mathbf{ExB} motion produced by the $m=1$ mode, as shown in Fig.5(I-b) and (II-b). After the full reconnection the current which is swept out from the central region is equally divided into two parts, as shown in Fig.8(I-b) and (II-b).

In the uniform density case, both parts of δJ_z move around symmetrically along the same potential contour and concentrate again after a half poloidal rotation. As seen in Fig.8(II-b'), the current concentration induces a negative peaked current which causes the secondary magnetic reconnection in Fig.3(II-c). At the same time, the positive longitudinal current comes into the central region again[8]. However, in the non-uniform density case, the self-generated radial electric field breaks the symmetrical motion of δJ observed in the uniform density case.

Then, as shown in Fig.8(I-c), only a part of the longitudinal current can contribute to the induction of the secondary reconnection, and the amount of longitudinal current coming into the central region is less than that of the uniform density case. Therefore, the radial field is found to weaken the reconcentration of the longitudinal current and to restrict the secondary reconnection as seen in Fig.3(I-c).

The magnetic configuration depends on the behavior of the current density profile. Figure 9 shows the minimum safety factor value (q_{\min}) for the non-uniform and the uniform density cases. The rapid increase of q_{\min} observed at $t \sim 33 (V_A / L_z)$ is caused by the full reconnection. After the reconnection, the safety factor increases above unity in the whole plasma region. For the uniform density case, the q_{\min} decreases due to the concentration of the longitudinal current and the secondary reconnection. The q_{\min} becomes less than unity again at $t \sim 38 (V_A / L_z)$. However, for the non-uniform density case, the radial electric field restricts the secondary reconnection, as discussed above. Then, the reduction of the q_{\min} is observed but is weaker than that observed for the uniform density case.

4.4. Energy History

In the process of the internal collapse, the density gradient effect is also presented on the energy history. Figure 10 shows the time evolution of the energy deviation from the initial value for (I) non-uniform and (II) uniform density cases.

Until the end of the full reconnection, the energy history is almost the same in both cases. The poloidal magnetic energy produced by the parallel current is consumed into the electrostatic potential energy of the 1/1 mode. In the process of the magnetic reconnection, the electron is accelerated by the electric field near the resonant ($q=1$) surface, so that the kinetic energy is also increased. The deviation of the total energy is relatively small even at the end of the simulation ($\Delta E_T / E_T < 0.02 \%$, where $E_T \sim 5.34 \times 10^3$), so that the total energy is well conserved.

However, after the full reconnection, the electrostatic potential energy is not reduced because the 0/0 mode grows up due to the density gradient effect. On the other hand, in the uniform density case, the parallel current is reconcentrated in the central region due to the ExB flow induced by the 1/1 mode. Then the electrostatic potential energy is returned to the poloidal magnetic energy again so as to increase the parallel current density which induces the secondary reconnection shown in Fig.3(II-c).

5. Summary

The density gradient effect is taken into account in a gyro-kinetic nonlinear simulation of the kinetic $m=1$ internal kink mode in a cylindrical plasma. The simulation results of the non-uniform density case are compared with those of the uniform density case. The core plasma is swept out by the ExB motion due to the $m=1$ electric field produced by the unstable kinetic internal kink mode. The process of the full reconnection is completed without saturation, and is almost the same as the one obtained for the uniform density simulation.

It is found that even when the ω_* is not large enough to change the linear growth rate of the 1/1 mode, the nonlinear phenomena after the full reconnection are considerably changed due to the self generated radial electric field, i.e. 0/0 mode. This mode is induced by the electron delay process during the ExB motion in the presence of the density gradient, and grows to the same level as the 1/1 mode. It should be noted that a radial electric field with positive central charge is experimentally obtained in the JIPP T-IIU tokamak just after the internal collapse of the sawtooth oscillations[12].

The self-generated radial electric field drives an ExB plasma rotation in the ion diamagnetic direction, which breaks the symmetrical plasma flow induced by the 1/1 mode. It is found that the density profile becomes a vortex structure due to this plasma rotation. The formation of the vortex is closely related with the growth of the radial electric field. It is also found that the concentration of the parallel current after the full reconnection is weakened by the nonlinear growth of the radial electric field. As a result, the minimum safety factor does not

recover the value enough smaller than unity after the full reconnection in the presence of density gradient.

In high temperature plasmas, the effect of FLR (Finite Larmor Radius) becomes important. In the case of large FLR compared with electron skin depth, the reduction of the linear growth rate can be expected from the two-fluid theory[10] and the results of the gyro-fluid simulation[13]. However, it is not easy to estimate the effect of large FLR on the nonlinear phase of internal collapse, especially on the nonlinear growth of radial electric field. The large FLR effect, and the mechanism of the nonlinear growth of the radial electric field are being analyzed now, and will be shown in the near future.

References

- [1] B.B.Kadomtsev, Sov. J. Plasma Phys. **1** 153 (1975).
- [2] D.J.Campbell, R.D.Jill, C.W.Gowers, et. al., Nuclear Fusion **26** 1085 (1986).
- [3] W.P.West, D.M.Thomas and J.S. de Grassie, Phys. Rev. Lett. **58** 2758 (1987).
- [4] J.A.Wesson, Nuclear Fusion **30** 2545 (1990).
- [5] H.Naitou, K.Tsuda, W.W.Lee and R.D.Sydora, Phys. Plasma **2** 4257 (1995).
- [6] H.Naitou, T.Sonoda, S.Tokuda and V.K.Decyk, J. Plasma and Fusion Research **72** 259 (1996).
- [7] D.Biskamp and J.F.Drake, Phys. Rev. Lett. **73** 971 (1994).
- [8] W.W.Lee, Phys. Fluids **26** 556 (1983).
- [9] T.Matsumoto, S.Tokuda, Y.Kishimoto, T.Takizuka and H.Naitou, J. Plasma and Fusion Research **75**, 1188 (1999).
- [10] L. Zakharov and B. Rogers, Phys. Fluids , **B4** 3285 (1992).
- [11] A.Y.Aydemir, Phys. Fluids , **B4** 3496 (1992).
- [12] Y.Hamada, A.Nishizawa, Y.Kawasumi, et. al., Nuclear Fusion **36** 515 (1996).
- [13] H.Naitou, et. al., "Stabilization of Kinetic Internal Kink Mode by Electron Diamagnetic Effect", 9th Toki Conference, P-II-9, Toki, Japan, 7-11, December 1998 : to be published in JPFR Series Vol.2.

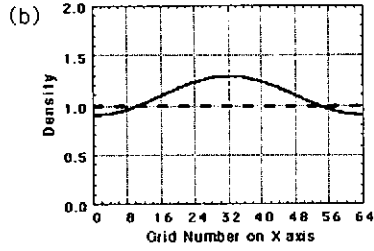
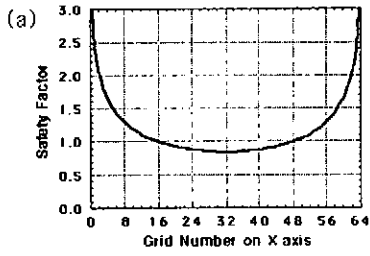


Figure 1
The equilibrium profiles of (a) the safety factor and (b) the particle density on the $y=32$ line. The solid line and the dashed line indicate the uniform profile and the non-uniform profile, respectively.

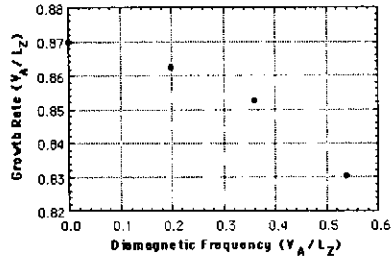


Figure 2
The dependence of the linear growth rate of the $m=1$ mode on the diamagnetic frequency.

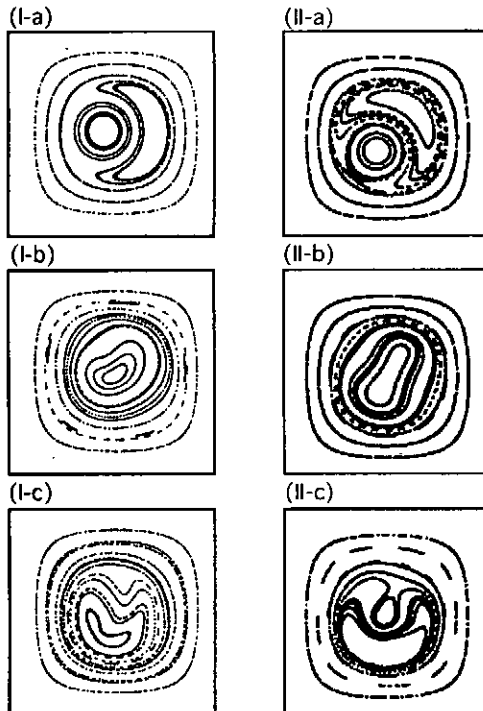


Figure 3
Poincaré Plots of the non-uniform density simulation at (I-a) $t=30.11$, (I-b) $t=34.54$, (I-c) $t=37.34$ and the uniform density simulation at (II-a) $t=29.81$, (II-b) $t=33.79$, (II-c) $t=37.28$. (I-a) and (II-a) show the shifted magnetic surfaces due to the $1/1$ mode. (I-b) and (II-b) show the nested surfaces just after the full reconnection. (I-c) and (II-c) show the secondary reconnection process.

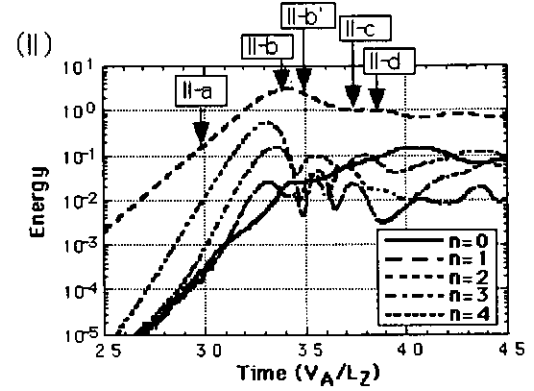
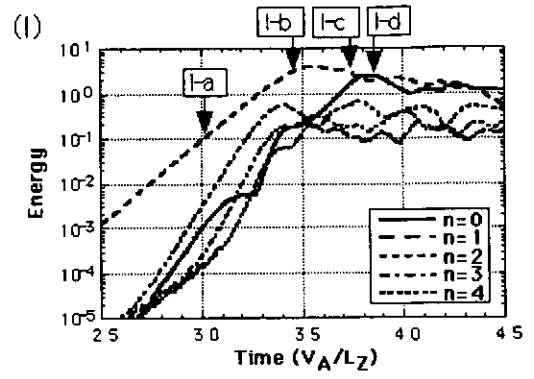


Figure 4
The time evolution of the electrostatic potential energy decomposed in the longitudinal mode numbers for (I) the non-uniform density simulation and (II) the uniform density simulation.

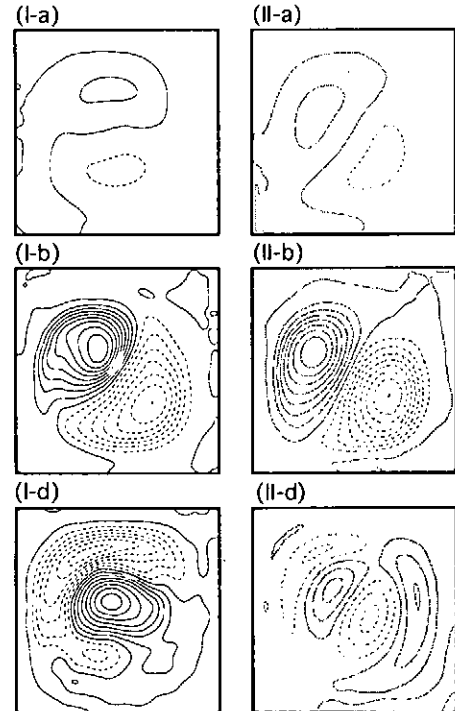


Figure 5
The contours of the electrostatic potential in the non-uniform density simulation at (I-a) $t=30.11$, (I-b) $t=34.54$, (I-d) $t=38.51$ and the uniform density simulation at (II-a) $t=29.81$, (II-b) $t=33.79$, (II-d) $t=38.45$. The solid and dashed lines indicate the plus and minus contour lines, respectively. (I-b) and (II-b) show the $1/1$ mode just after the full reconnection. (I-c) and (II-c) show the secondary reconnection process.

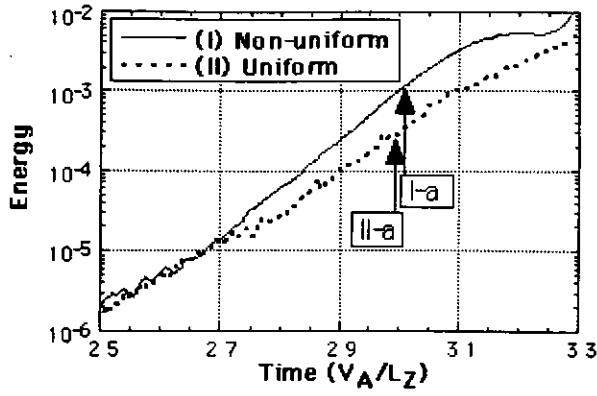


Figure 6
The time evolution of the $n=0$ electrostatic potential energy with the increase of the plasma shift for (I) the non-uniform and (II) the uniform density cases.

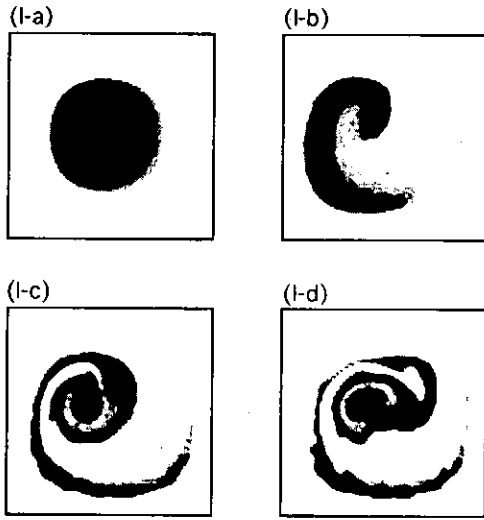


Figure 7
The high density regions of electrons in the peaked density simulation at (I-a) $t=30.11$, (I-b) $t=34.54$, (I-c) $t=37.34$, and (I-d) $t=38.51$.

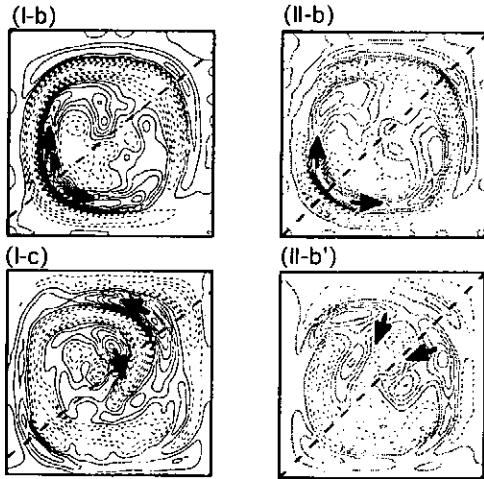


Figure 8
The contours of the perturbation of the parallel current in the non-uniform density simulation at (I-b) $t=34.54$, (I-c) $t=37.34$ and the uniform density simulation at (II-b) $t=33.79$, (II-b') $t=34.95$. The solid and dashed lines indicates the plus and minus contour lines, respectively. The thick dashed line show the symmetrical plane described by the electrostatic potential just after the full reconnection. The arrows indicate the direction of motion of the peak.

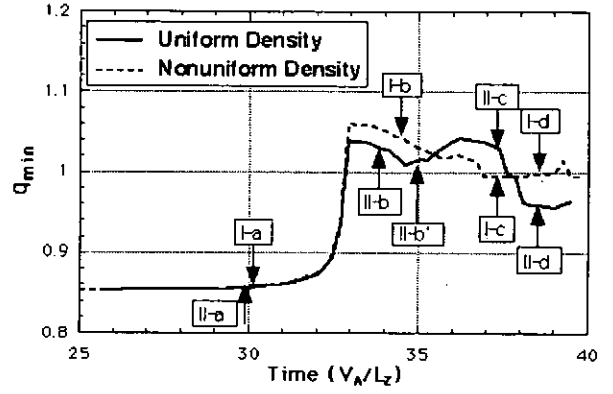


Figure 9
The variation of the minimum safety factor in both of the non-uniform and uniform density simulations.

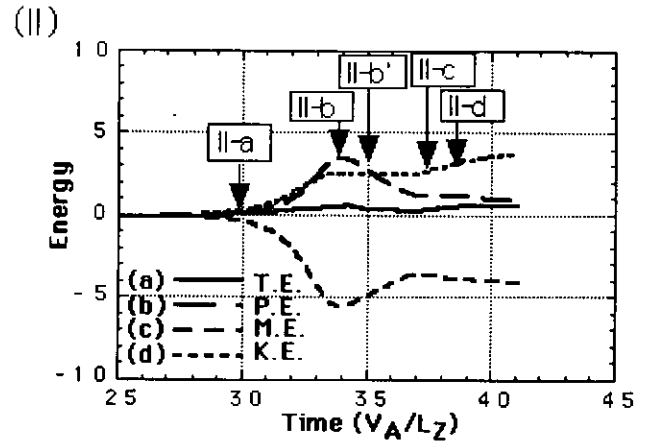
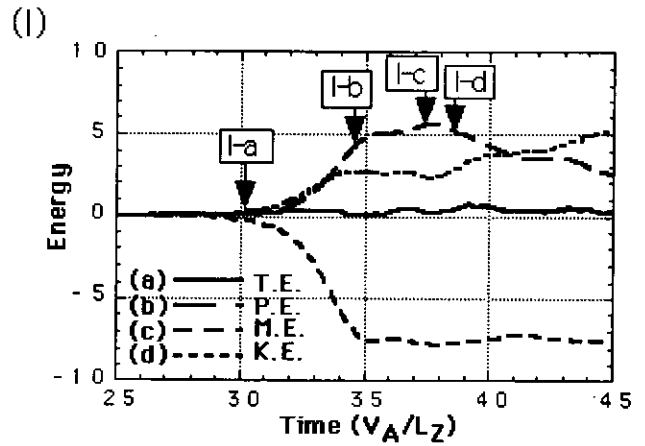


Figure 10
The time evolution of (a) the total energy, (b) the electrostatic potential energy, (c) the magnetic energy, and (d) the kinetic energy for (I) the non-uniform and (II) the uniform density cases. Only the deviation from the initial condition is drawn.

MHD Simulation Study of Compact Toroid Injection into Magnetized Plasmas

Yoshio SUZUKI ¹⁾, Takaya HAYASHI ²⁾ and Yasuaki KISHIMOTO ¹⁾

1) *Plasma Theory Laboratory, Department of Fusion Plasma Research,*

Naka Fusion Research Establishment, Japan Atomic Energy Research Institute, Naka 311-0193, Japan

2) *Theory and Computer Simulation Center,*

National Institute for Fusion Science, Toki 509-5292, Japan

Abstract:

To understand the fuelling process in a fusion device by a compact toroid (CT) plasmoid injection method, we have carried out MHD numerical simulations where a spheromak-like CT (SCT) is injected into a magnetized target plasma region. So far, we revealed that the penetration depth of the SCT plasma becomes shorter than that estimated from the conducting sphere (CS) model, because in the simulation the Lorentz force of the target magnetic field sequentially decelerates the injected SCT while in the CS model only the magnetic pressure force acts as the deceleration mechanism. In this study, we represent the new theoretical model where the injected SCT is decelerated by both the magnetic pressure force and the magnetic tension force (we call it the non-slipping sphere (NS) model) and investigate in detail the deceleration mechanism of the SCT by comparison with simulation results. As a result, it is found that the decrease of the SCT kinetic energy in the simulation coincides with that in the NS model more than in the CS model. It means that not only the magnetic pressure force but also the magnetic tension force acts as the deceleration mechanism of the SCT. Furthermore, it is revealed that magnetic reconnection between the SCT magnetic field and the target magnetic field plays a role to relax the SCT deceleration.

Keywords: fuelling, compact toroid, MHD simulation, magnetic reconnection

1. Introduction

In recent year, the compact toroid (CT) plasmoid injection has been considered as one of the advanced methods for deep fueling in a fusion reactor. This method is expected to supply the high density plasma deeply, since the injection velocity of fuel by this scheme is much faster than that by any of the other schemes. So far, the CT injection method has been discussed in relation to several experimental [1-7] and theoretical [8-11] studies. Since 1997, in Japan Atomic Energy Research Institute, the CT injection experiment into JFT-2M tokamak has been carried out in cooperation with Himeji Institute of Technology [12-14]. Also in National Institute for Fusion Science, the CT injection experiment into LHD has been planning [15]. Although these studies have shown the possibility of fuelling by this method, the CT dynamics in the fuelling process as well as the penetration depth of the CT has not been well understood. To reveal this, we have carried out MHD numerical simulations where a spheromak-like CT (SCT) is injected into a magnetized target plasma region [16-20].

In our previous paper [19,20], it is revealed that 1) the magnetic configuration of the injected SCT is disrupted by magnetic reconnection between the SCT magnetic field and the target magnetic field, which leads to supply of the SCT high density plasma, 2) the penetration depth of the SCT plasma into the target region becomes shorter than that estimated from the conducting sphere (CS) model, because the Lorentz force of the target magnetic field sequentially decelerates the SCT while in the CS model only the magnetic pressure force decelerates it. In this study, we represent the new theoretical model where the injected SCT is decelerated by both the magnetic pressure force and the magnetic tension force and investigate in detail the deceleration mechanism of the injected SCT by comparison with simulation results.

2. Theoretical model

So far, the CS model has been widely employed to estimate the penetration depth of the injected CT [2,5,13]. This model indicates that the CT, for which an incompressible, perfectly conducting sphere is substituted, penetrates with slipping the target magnetic field, that is, the CT can penetrate until its initial kinetic energy is exceeded by the magnetic energy required to exclude the magnetic field from its volume:

$$\frac{d}{dt} \int_{CT} \frac{1}{2} \rho V^2 dv = - \frac{d}{dt} \int_{CT} \frac{1}{2\mu_0} B^2 dv \quad (1)$$

where ρ , V and B are the CT density, the CT velocity and the strength of the target magnetic field at the point where the CT is penetrating, respectively. Taking $V = V_{CT}$, $B = 0$ for the initial condition and $V = 0$, $B = B_{target}$ for the final condition when the CT stops, we can lead

$$\frac{1}{2} \rho V_{CT}^2 v_{CT} = \frac{1}{2\mu_0} B_{target}^2 v_{CT} \quad (2)$$

where v_{CT} is the CT volume. Thus, the CT can penetrate until the point where the strength of the target magnetic field is

$$B_{target} = \sqrt{\mu_0 \rho V_{CT}} \quad (3)$$

Furthermore, taking a z -axis for the injection direction, we can lead the equation of motion from eq. (1) as follows:

$$\frac{d}{dt} \int_{CT} \frac{1}{2} \rho V_z^2 dv = \int_{CT} - \frac{\partial z}{\partial t} \frac{\partial}{\partial z} \frac{1}{2\mu_0} B^2 dv \quad (4)$$

$$\int_{CT} V_z \frac{\partial}{\partial t} \rho V_z dv = \int_{CT} - V_z \frac{\partial}{\partial z} \frac{1}{2\mu_0} B^2 dv \quad (5)$$

$$\frac{\partial}{\partial t} \rho V_z = F - \frac{\partial}{\partial z} \frac{B^2}{2\mu_0} \quad (6)$$

where F is the CT acceleration force. Therefore, in this model only the magnetic pressure force acts as the deceleration mechanism of the CT. However, the CT actually has the finite resistivity, which could inhibit the CT from slipping the target magnetic field. It is confirmed from the simulation with the finite resistivity that the injected SCT does not slip the target magnetic field but bent it with the SCT penetration. In addition, it is revealed that the Lorentz force of the target magnetic field sequentially decelerates the SCT through the penetration process. The Lorentz force consists of the magnetic pressure force and the magnetic tension force:

$$\mathbf{J} \times \mathbf{B} = -\nabla \left(\frac{B^2}{2\mu_0} \right) + (\mathbf{B} \cdot \nabla) \mathbf{B} \quad (7)$$

Therefore, the magnetic tension force could also decelerate the SCT. If we approximate the bent target magnetic field with a cosine function, the z component of the magnetic tension force is lead as follows:

$$z = \frac{L_p + L_{SCT}}{2} \cos\left(\frac{\pi y}{R}\right) + \frac{L_p + L_{SCT}}{2} \quad (8)$$

$$\frac{dz}{dy} = \frac{B_z}{B_y} = -\frac{\pi(L_p + L_{SCT})}{2R} \sin\left(\frac{\pi y}{R}\right) \quad (9)$$

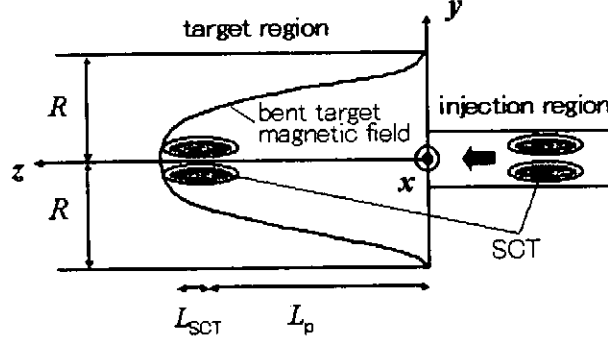


Fig.1: The schematic diagram of the bent target magnetic field.

$$\mathbf{B} = B_0 \left[-\frac{\pi(L_p + L_{SCT})}{2R} \sin\left(\frac{\pi y}{R}\right) \mathbf{z} + y \right] \quad (12)$$

$$[\mathbf{B} \cdot \nabla \mathbf{B}_z]_{y=0} = -\frac{B_0^2}{\mu_0} \frac{\pi^2 (L_p + L_{SCT})}{2R^2} \quad (11)$$

where L_{SCT} , L_p and R are the half size of the SCT, the SCT penetration depth and the radius of a target region, respectively (Fig. 1).

The equation of motion for the SCT is given by adding the term (11) to eq. (6):

$$\frac{\partial}{\partial t} \rho V_z = F - \frac{\partial}{\partial z} \frac{B^2}{2\mu_0} - \frac{B^2 \pi^2 (L_p + L_{SCT})}{2\mu_0 R^2} \quad (12)$$

Neglecting the convection term, we call it the non-slipping (NS) model. Thus, we respectively represent

CS model:

$$\rho \frac{\partial V_z}{\partial t} = F - \frac{\partial}{\partial z} \frac{B^2}{2\mu_0} \quad (13)$$

NS model:

$$\rho \frac{\partial V_z}{\partial t} = F - \frac{\partial}{\partial z} \frac{B^2}{2\mu_0} - \frac{B^2 \pi^2 (L_p + L_{SCT})}{2\mu_0 R^2} \quad (14)$$

where the magnetic pressure force and the magnetic tension force are averaged over the SCT volume. Furthermore, from the simulation result, we approximate the decrease of the SCT density with

$$\rho = -\frac{0.3}{v_{init}} t + \rho^{init} \quad (15)$$

(Fig. 2: approximate line), where ρ^{init} and v_{init} are the initial SCT density and the initial SCT volume, respectively. The SCT penetration depth is determined by solving simultaneously

$$\frac{dL_p}{dt} = V_z \quad (16)$$

In addition, each model in the following section is calculated based on the case with null target magnetic field ($B_{target} = 0$).

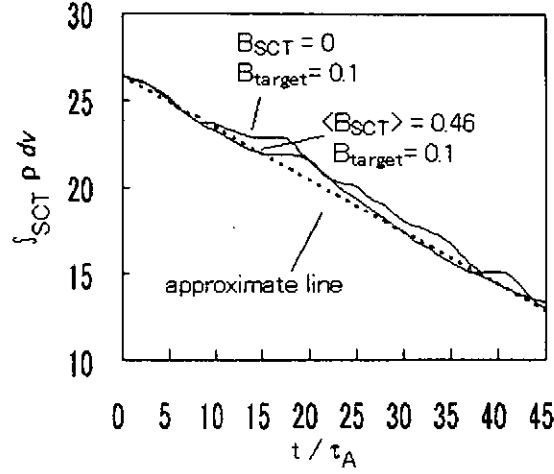


Fig2: The time evolution of the SCT (the bare plasmoid) density. The broken line is approximated by the equation: $-0.3t + \rho^{init} v^{init}$.

3. Comparison with simulation results

Figure 3 shows the SCT penetration depth given by the NS model, the CS model and the simulation with $\langle B_{SCT} \rangle = 0.46$ and $B_{target} = 0.1$ [19,20]. It can be seen that the SCT penetration depth in the NS model well coincides with that in the simulation while it in the CS model is longer. It means that the magnetic tension force effectively acts as the deceleration mechanism of the SCT. However, the SCT penetration depth in the NS model is a little shorter than that in the simulation with time. Figure 4 shows the time evolution of the SCT kinetic energy both in the NS model and the simulation by subtracting them from the null target magnetic field case. It can be seen that the SCT kinetic energy in the NS model well coincides with that in the simulation until about $30 \tau_A$. After that, however, the SCT kinetic energy in the NS model continues to decrease while it in the simulation begins to increase. It means that in the SCT penetration process the deceleration force is a little relaxed by some mechanism.

4. Effect of magnetic reconnection

As indicated in § 1, it is observed that magnetic reconnection between the SCT magnetic field and the target magnetic field takes place, which leads to supply of the SCT high density plasma in the target region [19,20]. Magnetic reconnection could also relax the SCT deceleration, since it can dynamically change the topology of the magnetic field. Thus, to examine the effect of magnetic reconnection, we carried out the simulation in which the bare plasmoid, that is, the SCT with null magnetic field is injected ($B_{SCT} = 0$). All parameters except the SCT magnetic field in this case are the same as those in the previous paper [19,20].

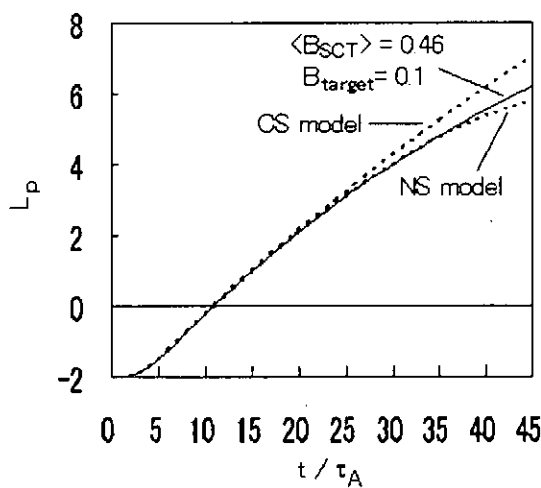


Fig3: The time evolution of the SCT penetration depth in the CS model, the NS model and the simulation with $\langle B_{SCT} \rangle = 0.46$ and $B_{target} = 0.1$. The target region corresponds to $0 < L_p < 8$.

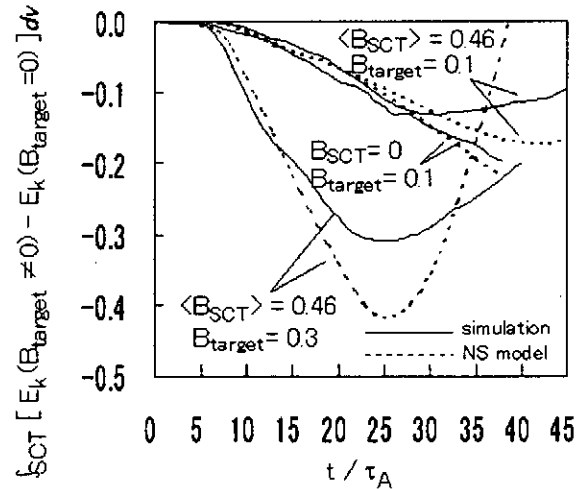


Fig4: The time evolution of the SCT kinetic energy in the NS model and simulation, which is shown by subtracting the case with the null target magnetic field.

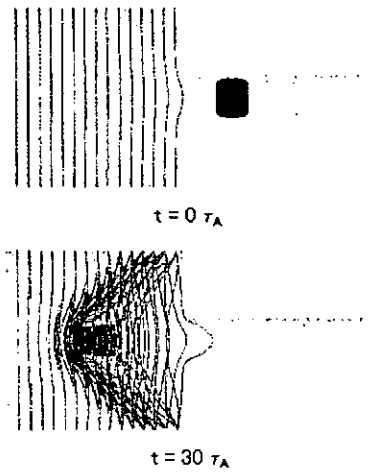


Fig5: The spatial structure of the high density plasma and the magnetic field lines at $t = 0$ and $30 \tau_A$ in the case without the SCT magnetic field.

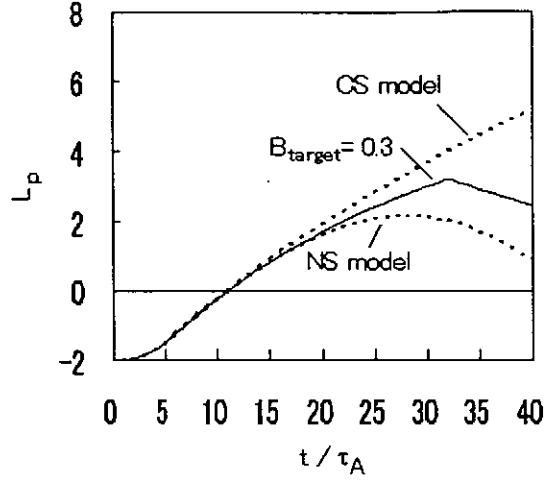


Fig6: The time evolution of the SCT penetration depth. The target magnetic field $B_{\text{target}} = 0.3$, which is three times larger than the previous simulation.

Figure 5 shows the spatial structure of the high density plasma (dark region) and target magnetic field lines at $t = 0$ and $30 \tau_A$. It is found that the high density plasma penetrates into the target region as shown in the SCT injection [19,20]. Since the initial pressure profile is spatially constant and the heat conductive time is longer than the Alfvén time, the diffusion of the high density plasma is not so different from that in the SCT injection (Fig. 2). In addition, it is obvious that such a magnetic reconnection as observed in the SCT injection does not occur. In figure 4, the time evolution of the bare plasmoid kinetic energy is also shown. It is found that this time evolution coincides with that in the NS model more than that of the SCT kinetic energy does. These results mean that magnetic reconnection between the SCT magnetic field and the target magnetic field relaxes the SCT deceleration. Magnetic reconnection could give the SCT penetration the same effect as the slipping indicated in the CS model, since it takes place between the SCT magnetic field and the bent target magnetic field. Therefore, it is considered that the relaxation of the magnetic tension force by magnetic reconnection causes that of the SCT deceleration.

5. Dependence on the target magnetic field strength

Figure 6 shows the SCT penetration depth in the case with $B_{\text{target}} = 0.3$. It is found that in this case also the SCT penetration depth in the CS model is longer than that in the simulation. On the other hand, it in the NS model becomes shorter. In figure 4, the time evolution of the SCT kinetic energy in this case is also shown. The difference of the SCT kinetic energy between the NS model and the simulation is larger when the target magnetic field is stronger, which causes the larger difference of the SCT penetration depth between them. We have not yet examined the dependence of the time scale when the relaxation is triggered as well as how long it continues on the strength of the target magnetic field. It would be reported in a future work.

6. Summary

We investigate the deceleration mechanism of the SCT injected into the magnetized target plasma region. It is revealed that in the SCT penetration process both the magnetic pressure force and the magnetic tension force effectively decelerate the SCT. In addition, it is found that magnetic reconnection between the SCT magnetic field and the target magnetic field relaxes the SCT deceleration. However the dependence of the time scale when the relaxation is triggered as well as how long it continues on the strength of the target magnetic field has not been examined yet. Furthermore, in the current simulation the target magnetic field is fixed on the boundary wall, which would cause the over estimate of the magnetic tension force. These would be reported in a future work.

References

- [1] Brown, M.R., Bellan, P.M., Nucl. Fusion **32** (1992) 1125.
- [2] Raman, R., et al., Phys. Rev. Lett. **73** (1994) 3101.
- [3] Raman, R., et al., Nucl. Fusion **37** (1997) 967.
- [4] Raman, R., et al., in Controlled Fusion and Plasma Physics (Proc. 24th Eur. Conf. Berchtesgaden, 1997), Vol. 21A, Part I, European Physical Society, Geneva (1999) 293.
- [5] Gouge, M.J., et al., in Fusion Energy 1996 (Proc. 16th Int. Conf. Montreal, 1996), Vol. 3, IAEA, Vienna (1997) 481.
- [6] Slough, J.T., Hoffman, A.L., in Fusion Energy 1996 (Proc. 16th Int. Conf. Montreal, 1996), Vol. 2, IAEA, Vienna (1997) 237.
- [7] Yee, J., Bellan, P.M., Nucl. Fusion **38** (1998) 711.
- [8] Parks, P.B., Phys. Rev. Lett. **61** (1988) 1364.
- [9] Perkins, L.J., Ho, S.K., Hammer, J.H., Nucl. Fusion **28** (1988) 1365.
- [10] Newcomb, W.A., Phys. Fluids B **3** (1991) 1818.
- [11] Hwang, D.Q., Ryutova, M., McLean, H., Phys. Plasmas **6** (1999) 1515.
- [12] Fukumoto, N., et al., Bull. Am. Phys. Soc. **42** (1997) 1961.
- [13] Ogawa, T. et al., Nucl. Fusion **39** (1999) 1911.
- [14] Uyama, T., Nagata, M., Journal of Plasma and Fusion Research **74** (1998) 200.
- [15] Miyazawa, J., Yamada, H., Motojima, O., Jpn. J. Appl. Phys. **37** (1998) 6620.
- [16] Suzuki, Y. et al., in Plasma Physics and Controlled Nuclear Fusion, JPFR Series (Proc. Joint Conf. 11th Int. Stellarator Conf. & 8th Int. Toki Conf. Toki, 1998), Vol. 1, The Japan Society of Plasma Science and Nuclear Fusion Research, Nagoya (1998) 518.
- [17] Suzuki, Y. et al., to be published in Chinese Physics Letters (2000).
- [18] Suzuki, Y. et al., in Plasma Physics and Controlled Nuclear Fusion, JPFR Series (Proc. 9th Int. Toki Conf. Toki, 1998), Vol. 2, The Japan Society of Plasma Science and Nuclear Fusion Research, Nagoya (2000) 271.
- [19] Suzuki, Y. et al., Journal of Plasma and Fusion Research **75**, (1999) 10_CD.
- [20] Suzuki, Y. et al., to be published in Nucl. Fusion (2000).

Nonlinear Density Wave Theory for the Spiral Structure of Galaxies

Shigeo Kondoh, Reiji Teramoto, and Zensho Yoshida*

*Graduate School of Engineering, University of Tokyo,
7-3-1 Hongo, Bunkyo-ku, Tokyo 113-8656*

Graduate School of Frontier Science, University of Tokyo,
7-3-1 Hongo, Bunkyo-ku, Tokyo 113-8656*

Abstract

The theory of nonlinear waves for plasmas has been applied to the analysis of the density wave theory of galaxies which are many-body systems of gravity. A nonlinear Schrödinger equation has been derived by applying the reductive perturbation method on the fluid equations that describe the behavior of infinitesimally thin disk galaxies. Their spiral arms are characterized by a soliton and explained as a pattern of a propagating nonlinear density wave.

Keywords: density wave, galaxy, nonlinear wave, soliton, reductive perturbation method, nonlinear Schrödinger equation.

1 Introduction

A galaxy is a many-body system composed of stars interacting with each other through a long range force, gravity[1]. There are a lot of common characteristics between the physics of galaxies and plasmas, which are systems of charged particles interacting through the Lorentz force. Macroscopic description of these systems can be casted in a fluid model including internal forces which bring about collective behavior such as waves or instabilities[1, 2].

The spiral of a galaxy has been explained by the density wave theory[1, 3, 4] as a pattern of a rotating density wave on a disk. This theory resolves the winding, i.e. the spiral arms must be wound up far beyond the observed structure in normal ages of galaxies if we assume a simple rotational deformation ansatz[1]. Lin and Shu[3] treated galaxies as compressible fluids and showed that the linearized fluid equations for an infinitesimally thin disk galaxy have a spiral wave solution that is proportional to $\exp(\omega t - m\theta + \lambda f(r))$, where ω is the frequency of the wave, m is the azimuthal wave number (which is also the number of arms of the galaxy), λ is a constant ($\lambda \gg 1$), $f(r)$ is the phase factor of the wave in the radial direction (Fig. 1). They obtained the dispersion relation

$$\lambda |f'(r)| = \frac{\kappa^2 - (\omega - m\Omega)^2}{2\pi G n_0}, \quad (1)$$

where ϵ is the sign of $f'(r)$, $\Omega(r)$ is the angular frequency of the rotation of the disk, $n_0(r)$ is the equilibrium surface mass density, G is the gravitational constant, and κ is the epicyclic frequency defined by

$$\kappa^2(r) = 4\Omega^2 \left(1 + \frac{r}{2\Omega} \frac{d\Omega}{dr} \right). \quad (2)$$

The physical meaning of the epicyclic frequency is explained as follows: Orbits of stars in a galaxy are usually not exact circles and always have a certain amount of randomness. If one of the perturbed orbits is observed on a framework rotating with the mean angular velocity around the center of the galaxy, it is known to be

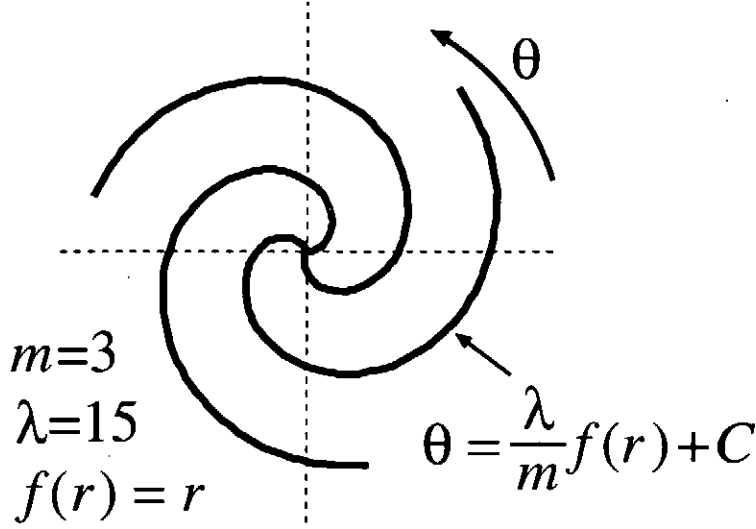


Figure 1: An example of curves on which the phase of $\exp(\omega t - m\theta + \lambda f(r))$ is constant. These curves are explained as the arms of the galaxy in the linear density wave theory.

a small circle[1]. The frequency of such small cyclic motions that originate from randomness is called the epicyclic frequency.

In this report, we extend Lin and Shu's analysis to the nonlinear regime and characterize the spiral structure as an asymptotic soliton-like nonlinear wave. Using the reductive perturbation theory[5], we derive a nonlinear equation for the envelope wave, which resembles a Schrödinger equation.

Within the framework of linear approximation, the pattern of galaxies is still undetermined, because any linear combination of spiral waves solves the linear equations. A specific structure stems from the nonlinear effect that yields coupling among linear modes and selects a special pattern which can sustain for a long term.

2 Nonlinear Density Wave Theory and Soliton Structure

We consider a galaxy whose mass density is concentrated on an infinitesimally thin disk. The set of the fluid equations (the mass conservation, the momentum equations, and Poisson's equation) reads, in the cylindrical polar coordinates (r, θ, z) ,

$$\frac{\partial n}{\partial t} + \frac{1}{r} \left[\frac{\partial}{\partial r}(rnu) + \frac{\partial}{\partial \theta}(nv) \right] = 0, \quad (3)$$

$$\frac{\partial u}{\partial t} + u \frac{\partial u}{\partial r} + \frac{v}{r} \frac{\partial u}{\partial \theta} - \frac{v^2}{r} = \frac{\partial \phi}{\partial r}, \quad (4)$$

$$\frac{\partial v}{\partial t} + u \frac{\partial v}{\partial r} + \frac{v}{r} \frac{\partial v}{\partial \theta} + \frac{uv}{r} = \frac{1}{r} \frac{\partial \phi}{\partial \theta}, \quad (5)$$

$$\frac{\partial^2 \phi}{\partial r^2} + \frac{1}{r} \frac{\partial \phi}{\partial r} + \frac{1}{r^2} \frac{\partial^2 \phi}{\partial \theta^2} + \frac{\partial^2 \phi}{\partial z^2} = -4\pi G n(r, \theta) \delta(z), \quad (6)$$

where n is the surface mass density, u and v are the r -component and the θ -component of the fluid velocity, respectively, and ϕ is the negative of the gravitational potential. Mean fields are given by $n = n_0(r)$, $u = 0$, $v = r\Omega(r) > 0$. Here we normalize r and z by the mean wave length of the carrier wave in the radial direction $2\pi R/\lambda$, where R is the radial size of the galaxy and $\lambda \gg 1$ is a dimensionless constant, t by the period of the carrier wave $2\pi/\omega$, n by $n_0(0)$, u and v by the phase velocity $\omega R/\lambda$, ϕ by $\omega^2 R^2/\lambda^2$, and G by $\omega^2 R/2n_0(0)\lambda$.

Using a small parameter ε , we transform the independent variables (r, θ, z) into stretched variables (ξ, η, τ) as

$$\xi = \varepsilon(r - Vt),$$

$$\eta = \epsilon^2 \theta, \quad (7)$$

$$\tau = \epsilon^2 t,$$

where V is a constant. The partial derivatives translates as

$$\frac{\partial}{\partial r} = \epsilon \frac{\partial}{\partial \xi},$$

$$\frac{\partial}{\partial \theta} = \epsilon^2 \frac{\partial}{\partial \eta}, \quad (8)$$

$$\frac{\partial}{\partial t} = -\epsilon V \frac{\partial}{\partial \xi} + \epsilon^2 \frac{\partial}{\partial \tau}.$$

We expand the dependent variables around their mean values as

$$n = n_0 + \sum_{n=1}^{\infty} \epsilon^n \sum_{l=-\infty}^{\infty} n_l^{(n)}(\xi, \eta, \tau) \exp[i l(\omega t - m\theta + \lambda f(r))], \quad (9)$$

$$u = \sum_{n=1}^{\infty} \epsilon^n \sum_{l=-\infty}^{\infty} u_l^{(n)}(\xi, \eta, \tau) \exp[i l(\omega t - m\theta + \lambda f(r))], \quad (10)$$

$$v = r\Omega + \sum_{n=1}^{\infty} \epsilon^n \sum_{l=-\infty}^{\infty} v_l^{(n)}(\xi, \eta, \tau) \exp[i l(\omega t - m\theta + \lambda f(r))], \quad (11)$$

where, we assume, $n_l^{(n)}$, $u_l^{(n)}$, and $v_l^{(n)}$ vary much slower than $\exp\{il(\omega t - m\theta + \lambda f(r))\}$. The reality conditions on physical quantities demand

$$n_l^{(n)*} = n_{-l}^{(n)}, \quad (12)$$

$$u_l^{(n)*} = u_{-l}^{(n)}, \quad (13)$$

$$v_l^{(n)*} = v_{-l}^{(n)}, \quad (14)$$

where asterisks (*) denote the complex conjugate.

We approximate the potential gradient as

$$\frac{\partial \phi}{\partial r} \simeq -r\Omega^2 + 2\pi G\epsilon \sum_{n=1}^{\infty} \epsilon^n \sum_{l=1}^{\infty} \text{Re} \left[2in_l^{(n)} \exp[i l(\omega t - m\theta + \lambda f(r))] \right], \quad (15)$$

$$\frac{\partial \phi}{\partial \theta} \simeq 0, \quad (16)$$

which means that the phases of $\partial \phi / \partial r$ and $n^{(n)}$ are shifted by $\pi/2$. Equations (15) and (16) are in principle the same as Eq. (11) of Ref. [3], where the phase shift is given by the complex expression $\partial \phi / \partial r \propto in^{(n)}$. Note that the first term on the right-hand side of Eq.(15) is equivalent to the zeroth-order gravitational field.

Substituting Eqs.(7)-(16) into the fluid equations (3)-(5) gives

$$\begin{aligned} & \sum_{l=-\infty}^{\infty} \exp\{il(\omega t - m\theta + \lambda f(r))\} \left[\left(i l \omega - \epsilon V \frac{\partial}{\partial \xi} + \epsilon^2 \frac{\partial}{\partial \tau} \right) \sum_{n=1}^{\infty} \epsilon^n n_l^{(n)} \right. \\ & + \frac{\epsilon^2}{V\tau} \left(1 - \frac{\xi}{V\tau} \epsilon \right) \left(n_0 \sum_{n=1}^{\infty} \epsilon^n u_l^{(n)} + \sum_{l'=-\infty}^{\infty} \sum_{n=1}^{\infty} \sum_{n'=1}^{\infty} \epsilon^{n+n'} n_{l-l'}^{(n)} u_{l'}^{(n')} \right) + \left(i l \lambda f'(r) + \epsilon \frac{\partial}{\partial \xi} \right) \left(n_0 \sum_{n=1}^{\infty} \epsilon^n u_l^{(n)} \right) \\ & + \sum_{l'=-\infty}^{\infty} \left(i l \lambda f'(r) + \epsilon \frac{\partial}{\partial \xi} \right) \sum_{n=1}^{\infty} \sum_{n'=1}^{\infty} \epsilon^{n+n'} n_{l-l'}^{(n)} u_{l'}^{(n')} + \frac{\epsilon^2}{V\tau} \left(1 - \frac{\xi}{V\tau} \epsilon \right) n_0 \left(-ilm + \epsilon^2 \frac{\partial}{\partial \eta} \right) \sum_{n=1}^{\infty} \epsilon^n v_l^{(n)} \\ & + \Omega \left(-ilm + \epsilon^2 \frac{\partial}{\partial \eta} \right) \sum_{n=1}^{\infty} \epsilon^n n_l^{(n)} + \frac{\epsilon^2}{V\tau} \left(1 - \frac{\xi}{V\tau} \epsilon \right) \sum_{l'=-\infty}^{\infty} \left\{ \left(-ilm + \epsilon^2 \frac{\partial}{\partial \eta} \right) \sum_{n=1}^{\infty} \sum_{n'=1}^{\infty} \epsilon^{n+n'} n_{l-l'}^{(n)} v_{l'}^{(n')} \right\} \Big] \\ & = 0, \end{aligned} \quad (17)$$

$$\begin{aligned}
& \sum_{l=-\infty}^{\infty} \exp \{il(\omega t - m\theta + \lambda f(r))\} \left[\left(i\omega - \varepsilon V \frac{\partial}{\partial \xi} + \varepsilon^2 \frac{\partial}{\partial \tau} \right) \sum_{n=1}^{\infty} \varepsilon^n u_l^{(n)} \right. \\
& + \sum_{l'=-\infty}^{\infty} \sum_{n=1}^{\infty} \sum_{n'=1}^{\infty} \varepsilon^{n+n'} u_{l-l'}^{(n)} \left(il' \lambda f'(r) + \varepsilon \frac{\partial}{\partial \xi} \right) u_{l'}^{(n')} + \Omega \left(-ilm + \varepsilon^2 \frac{\partial}{\partial \eta} \right) \sum_{n=1}^{\infty} \varepsilon^n u_l^{(n)} \\
& + \frac{\varepsilon^2}{V\tau} \left(1 - \frac{\xi}{V\tau} \varepsilon \right) \sum_{l'=-\infty}^{\infty} \sum_{n=1}^{\infty} \sum_{n'=1}^{\infty} \varepsilon^{n+n'} v_{l-l'}^{(n)} \left(-il'm + \varepsilon^2 \frac{\partial}{\partial \eta} \right) u_{l'}^{(n')} - 2\Omega \sum_{n=1}^{\infty} \varepsilon^n v_l^{(n)} \\
& \left. - \frac{\varepsilon^2}{V\tau} \left(1 - \frac{\xi}{V\tau} \varepsilon \right) \sum_{l'=-\infty}^{\infty} \sum_{n=1}^{\infty} \sum_{n'=1}^{\infty} \varepsilon^{n+n'} v_{l-l'}^{(n)} v_{l'}^{(n')} \right] \\
& = 2\pi G \varepsilon \sum_{n=1}^{\infty} \varepsilon^n \sum_{l=1}^{\infty} \text{Re} \left[2in_l^{(n)} \exp[il(\omega t - m\theta + \lambda f(r))] \right], \tag{18}
\end{aligned}$$

$$\begin{aligned}
& \sum_{l=-\infty}^{\infty} \exp \{il(\omega t - m\theta + \lambda f(r))\} \left[\left(i\omega - \varepsilon V \frac{\partial}{\partial \xi} + \varepsilon^2 \frac{\partial}{\partial \tau} \right) \sum_{n=1}^{\infty} \varepsilon^n v_l^{(n)} + \frac{\kappa^2}{2\Omega} \sum_{n=1}^{\infty} \varepsilon^n u_l^{(n)} \right. \\
& + \sum_{l'=-\infty}^{\infty} \sum_{n=1}^{\infty} \sum_{n'=1}^{\infty} \varepsilon^{n+n'} u_{l-l'}^{(n)} \left(il' \lambda f'(r) + \varepsilon \frac{\partial}{\partial \xi} \right) v_{l'}^{(n')} + \Omega \left(-ilm + \varepsilon^2 \frac{\partial}{\partial \eta} \right) \sum_{n=1}^{\infty} \varepsilon^n v_l^{(n)} \\
& + \frac{\varepsilon^2}{V\tau} \left(1 - \frac{\xi}{V\tau} \varepsilon \right) \sum_{l'=-\infty}^{\infty} \sum_{n=1}^{\infty} \sum_{n'=1}^{\infty} \varepsilon^{n+n'} v_{l-l'}^{(n)} \left(-il'm + \varepsilon^2 \frac{\partial}{\partial \eta} \right) v_{l'}^{(n')} \\
& \left. + \frac{\varepsilon^2}{V\tau} \left(1 - \frac{\xi}{V\tau} \varepsilon \right) \sum_{l'=-\infty}^{\infty} \sum_{n=1}^{\infty} \sum_{n'=1}^{\infty} \varepsilon^{n+n'} u_{l-l'}^{(n)} v_{l'}^{(n')} \right] \\
& = 0, \tag{19}
\end{aligned}$$

Here we used a relation

$$\frac{1}{r} = \frac{1}{\varepsilon^{-1}\xi + \varepsilon^{-2}V\tau} = \frac{\varepsilon^2}{V\tau} \frac{1}{1 + \varepsilon\xi/(V\tau)} \simeq \frac{\varepsilon^2}{V\tau} \left(1 - \varepsilon \frac{\xi}{V\tau} \right). \tag{20}$$

Because the coefficients in Eqs (17)-(19) are slow functions of t , r , and θ in comparison with the “carrier” $\exp \{il(\omega t - m\theta + \lambda f(r))\}$, we can assume that each Fourier component is linearly independent, and hence, Eqs.(17)-(19) demand vanishing of every Fourier coefficients separately.

Now we separate terms in Eqs. (17)-(19) into each order of ε . The coefficients of the order of ε^1 read (see Appendix)

$$il\omega n_l^{(1)} + il\lambda f'(r)n_0 u_l^{(1)} - ilm\Omega n_l^{(1)} = 0, \tag{21}$$

$$il\omega u_l^{(1)} - ilm\Omega u_l^{(1)} - 2\Omega v_l^{(1)} = 2\pi i G \varepsilon n_l^{(1)} \text{sgn } l, \tag{22}$$

$$il\omega v_l^{(1)} + \frac{\kappa^2}{2\Omega} u_l^{(1)} - ilm\Omega v_l^{(1)} = 0, \tag{23}$$

for each Fourier component l . Equations (21)-(23) immediately yield the linear dispersion relation Eq. (1) and

$$u_{\pm 1}^{(1)} = -pn_{\pm 1}^{(1)}, \tag{24}$$

$$v_{\pm 1}^{(1)} = \mp iqn_{\pm 1}^{(1)}, \tag{25}$$

where

$$p = \frac{\omega - m\Omega}{\lambda f'(r)n_0}, \tag{26}$$

$$q = \frac{\kappa^2}{2\Omega \lambda f'(r)n_0}. \tag{27}$$

Note that we have assumed

$$u_l^{(1)} = v_l^{(1)} = n_l^{(1)} = 0 \tag{28}$$

for $l \neq \pm 1$, which means that the “carrier wave” is sinusoidal.

The coefficients of ϵ^2 in Eqs.(17)-(19) yield relations

$$il(\omega - m\Omega)n_l^{(2)} - V\frac{\partial n_l^{(1)}}{\partial \xi} + il\lambda f'(r)n_0 u_l^{(2)} + \frac{\partial}{\partial \xi}(n_0 u_l^{(1)}) + il\lambda f'(r) \sum_{l'=-\infty}^{\infty} n_{l'}^{(1)} u_{l-l'}^{(1)} = 0, \quad (29)$$

$$il(\omega - m\Omega)u_l^{(2)} - V\frac{\partial u_l^{(1)}}{\partial \xi} - 2\Omega v_l^{(2)} + \sum_{l'=-\infty}^{\infty} il'\lambda f'(r)u_{l-l'}^{(1)}u_{l'}^{(1)} = 2\pi i G \epsilon n_l^{(2)} \text{sgn } l, \quad (30)$$

$$il(\omega - m\Omega)v_l^{(2)} - V\frac{\partial v_l^{(1)}}{\partial \xi} + \frac{\kappa^2}{2\Omega}u_l^{(2)} + \sum_{l'=-\infty}^{\infty} il'\lambda f'(r)u_{l-l'}^{(1)}v_{l'}^{(1)} = 0, \quad (31)$$

for each l . Substituting Eqs. (24)-(28) and $l=2$ into Eqs. (29)-(31) gives

$$u_2^{(2)} = b_1 n_1^{(1)2}, \quad (32)$$

$$v_2^{(2)} = ib_2 n_1^{(1)2}, \quad (33)$$

$$n_2^{(2)} = b_3 n_1^{(1)2}, \quad (34)$$

where

$$b_1 = \frac{(\omega - m\Omega)(-\kappa^2 + 4\pi G \epsilon \lambda f'(r)n_0)}{\lambda f'(r)n_0^2 [4(\omega - m\Omega)^2 - \kappa^2 + 4\pi G \epsilon \lambda f'(r)n_0]}, \quad (35)$$

$$b_2 = -\frac{\kappa^2(\omega - m\Omega)^2}{\lambda f'(r)\Omega n_0^2 [4(\omega - m\Omega)^2 - \kappa^2 + 4\pi G \epsilon \lambda f'(r)n_0]}, \quad (36)$$

$$b_3 = \frac{4(\omega - m\Omega)^2}{n_0 [4(\omega - m\Omega)^2 - \kappa^2 + 4\pi G \epsilon \lambda f'(r)n_0]}. \quad (37)$$

Similarly substituting Eqs. (24)-(28) and $l=1$ into Eqs. (29) and (31) yield

$$\begin{bmatrix} i(\omega - m\Omega) & i\lambda f'(r)n_0 & 0 \\ -2\pi i G \epsilon & i(\omega - m\Omega) & -2\Omega \\ 0 & \frac{\kappa^2}{2\Omega} & i(\omega - m\Omega) \end{bmatrix} \begin{bmatrix} n_1^{(2)} \\ u_1^{(2)} \\ v_1^{(2)} \end{bmatrix} = \begin{bmatrix} (V + n_0 p) \frac{\partial n_1^{(1)}}{\partial \xi} \\ -pV \frac{\partial n_1^{(1)}}{\partial \xi} \\ -iqV \frac{\partial n_1^{(1)}}{\partial \xi} \end{bmatrix}. \quad (38)$$

Since the determinant of the matrix in Eq. (38) is zero due to Eqs. (21)-(23), there are no solutions to Eq. (38) unless

$$V = \frac{\pi G n_0 \epsilon}{\omega - m\Omega}. \quad (39)$$

Equation (39) determines the group velocity of the nonlinear wave. It might seem a contradiction that the right-hand side of Eq. (39) is a function of r , while V is a constant. However, Eq. (39) is locally justified by the fact that the mean fields are slow functions of r .

Under the condition (39), solutions to Eq. (38) cannot be determined uniformly, because the determinant of the matrix in the left-hand side is zero. Hence we assume

$$n_1^{(2)} = 0. \quad (40)$$

Equations (38) and (40) yield

$$u_1^{(2)} = \frac{1}{i\lambda f'(r)n_0} \frac{\partial}{\partial \xi} \left[(V + n_0 p) n_1^{(1)} \right] - \frac{\omega - m\Omega}{\lambda f'(r)n_0} n_1^{(2)}, \quad (41)$$

$$v_1^{(2)} = \frac{1}{\omega - m\Omega} \left[\left(-V \frac{\partial q}{\partial \xi} + q \frac{\partial}{\partial \xi} (n_0 p) \right) n_1^{(1)} + n_0 p q \frac{\partial n_1^{(1)}}{\partial \xi} \right] - iq n_1^{(2)}. \quad (42)$$

Furthermore, we substitute $l = 0$ into Eqs. (30) and (31) and use Eqs.(12) and (24)-(28). Then the following equations are obtained:

$$u_0^{(2)} = \frac{2p}{n_0} \left| n_1^{(1)} \right|^2, \quad (43)$$

$$v_0^{(2)} = 0. \quad (44)$$

The coefficients of ϵ^3 in Eqs.(17)-(19) read

$$\begin{aligned} & il(\omega - ilm\Omega)n_l^{(3)} - V \frac{\partial n_l^{(2)}}{\partial \xi} + \frac{\partial n_l^{(1)}}{\partial \tau} + \frac{1}{V\tau} n_0 u_l^{(1)} + il\lambda f'(r) n_0 u_l^{(3)} + \frac{\partial}{\partial \xi} (n_0 u_l^{(2)}) \\ & + \sum_{l'=-\infty}^{\infty} \left\{ il\lambda f'(r) (n_{l-l'}^{(1)} u_{l'}^{(2)} + n_{l'}^{(2)} u_{l-l'}^{(1)}) + \frac{\partial}{\partial \xi} (n_{l'}^{(1)} u_{l-l'}^{(1)}) \right\} - \frac{ilmn_0}{V\tau} v_l^{(1)} + \Omega \frac{\partial n_l^{(1)}}{\partial \eta} \\ & = 0, \end{aligned} \quad (45)$$

$$\begin{aligned} & il(\omega - m\Omega)u_l^{(3)} - V \frac{\partial u_l^{(2)}}{\partial \xi} + \frac{\partial u_l^{(1)}}{\partial \tau} \\ & + \sum_{l'=-\infty}^{\infty} \left\{ il'\lambda f'(r) (u_{l-l'}^{(1)} u_{l'}^{(2)} + u_{l-l'}^{(2)} u_{l'}^{(1)}) + u_{l-l'}^{(1)} \frac{\partial u_{l'}^{(1)}}{\partial \xi} \right\} + \Omega \frac{\partial u_l^{(1)}}{\partial \eta} - 2\Omega v_l^{(3)} \\ & = 2\pi i G \epsilon n_l^{(3)}, \end{aligned} \quad (46)$$

$$\begin{aligned} & il(\omega - m\Omega)v_l^{(3)} - V \frac{\partial v_l^{(2)}}{\partial \xi} + \frac{\partial v_l^{(1)}}{\partial \tau} + \frac{\kappa^2}{2\Omega} u_l^{(3)} \\ & + \sum_{l'=-\infty}^{\infty} \left\{ il'\lambda f'(r) (u_{l-l'}^{(1)} v_{l'}^{(2)} + u_{l-l'}^{(2)} v_{l'}^{(1)}) + u_{l-l'}^{(1)} \frac{\partial v_{l'}^{(1)}}{\partial \xi} \right\} + \Omega \frac{\partial v_l^{(1)}}{\partial \eta} \\ & = 0, \end{aligned} \quad (47)$$

for each l . Substituting $l = 0$ into Eq.(45) and using Eqs.(12) and (24) give

$$\frac{\partial}{\partial \xi} \left(-V n_0^{(2)} + n_0 u_0^{(2)} - 2p \left| n_1^{(1)} \right|^2 \right) = 0. \quad (48)$$

Substituting Eq. (43) into Eq. (48) gives

$$\frac{\partial n_0^{(2)}}{\partial \xi} = 0, \quad (49)$$

which can be immediately integrated as

$$n_0^{(2)} = \psi(\eta, \tau), \quad (50)$$

where $\psi(\eta, \tau)$ is an arbitrary function of η and τ . Here we assume $\psi \equiv 0$ to obtain

$$n_0^{(2)} = 0. \quad (51)$$

For $l=1$, Eqs. (45)-(47) yield

$$i(\omega - m\Omega)n_1^{(3)} + i\lambda f'(r)n_0 u_1^{(3)} + g_1 = 0, \quad (52)$$

$$i(\omega - m\Omega)u_1^{(3)} - 2\Omega v_1^{(3)} - 2\pi i G \epsilon n_1^{(3)} + g_2 = 0, \quad (53)$$

$$i(\omega - m\Omega)v_1^{(3)} + \frac{\kappa^2}{2\Omega} u_1^{(3)} + g_3 = 0, \quad (54)$$

where

$$\begin{aligned} g_1 &= -V \frac{\partial u_1^{(2)}}{\partial \xi} + \frac{\partial n_1^{(1)}}{\partial \tau} + \frac{n_0}{V\tau} u_1^{(1)} + \frac{\partial}{\partial \xi} (n_0 u_1^{(2)}) - \frac{in_0 m}{V\tau} v_1^{(1)} + \Omega \frac{\partial n_1^{(1)}}{\partial \eta} \\ &+ i\lambda f'(r) (n_1^{(1)} u_0^{(2)} + n_0^{(2)} u_1^{(1)} + n_{-1}^{(1)} u_2^{(2)} + n_2^{(2)} u_{-1}^{(1)}), \end{aligned} \quad (55)$$

$$g_2 = -V \frac{\partial u_1^{(2)}}{\partial \xi} + \frac{\partial u_1^{(1)}}{\partial \tau} + \Omega \frac{\partial u_1^{(1)}}{\partial \eta} + i\lambda f'(r) (u_{-1}^{(1)} u_2^{(2)} + u_0^{(2)} u_1^{(1)}), \quad (56)$$

$$g_3 = -V \frac{\partial v_1^{(2)}}{\partial \xi} + \frac{\partial v_1^{(1)}}{\partial \tau} + \Omega \frac{\partial v_1^{(1)}}{\partial \eta} + i\lambda f'(r) (2u_{-1}^{(1)} v_2^{(2)} + u_0^{(2)} v_1^{(1)} - u_2^{(2)} v_{-1}^{(1)}). \quad (57)$$

Under the condition given by Eq.(1), Eqs. (52)-(54) are not independent with respect to $n_1^{(3)}$, $u_1^{(3)}$, and $v_1^{(3)}$. Equation (54) times $2i\Omega/(\omega - m\Omega)$ minus Eq. (52) times $2\pi G\epsilon/(\omega - m\Omega)$ becomes

$$i(\omega - m\Omega)u_1^{(3)} - 2\Omega v_1^{(3)} - 2\pi i G\epsilon n_1^{(3)} + \frac{2i\Omega g_3 - 2\pi G\epsilon g_1}{\omega - m\Omega} = 0, \quad (58)$$

where the dispersion relation Eq.(1) has been used. Comparing Eqs. (53) and (58), we obtain

$$(\omega - m\Omega)g_2 = -2\pi G\epsilon g_1 + 2i\Omega g_3. \quad (59)$$

Finally, we substitute Eqs. (24)-(28), (32)-(34), (40)-(44), (51), and (55)-(57) into Eq. (59) and assume that p , q , $f'(r)$, Ω , and n_0 vary much slower than $n_1^{(1)}$. Then, we obtain

$$i\left(\frac{\partial}{\partial\tau} + \Omega\frac{\partial}{\partial\eta}\right)n_1^{(1)} + d_1\frac{\partial^2 n_1^{(1)}}{\partial\xi^2} + \frac{id_2}{\tau}n_1^{(1)} + d_3\left|n_1^{(1)}\right|^2 n_1^{(1)} = 0, \quad (60)$$

where

$$d_1 = \frac{2V(\omega - m\Omega) - 2\pi G\epsilon n_0 + V^2\lambda f'(\tau)}{2(\omega - m\Omega)\lambda f'(\tau)}, \quad (61)$$

$$d_2 = \frac{\pi G\epsilon n_0^2 \lambda f'(\tau)(mq + p)}{(\omega - m\Omega)^2 V}, \quad (62)$$

$$d_3 = -\frac{3(\omega - m\Omega)\kappa^2}{[\kappa^2 + 2(\omega - m\Omega)^2]n_0^2}. \quad (63)$$

Taking the limit of $\tau \rightarrow \infty$, Eq. (60) reduces into the nonlinear Schrödinger equation, which describes envelope solitons[6]. We thus see that the spiral structure of galaxies approaches to a soliton-like state.

Note that $\exp\{il(\omega t - m\theta + \lambda f(\tau))\}$ does not express an observable wave pattern any longer. In other words, the variable m is not a number of arms of a galaxy any longer (which used to be in the linear theory by Lin and Shu[3]). Instead, $\exp\{il(\omega t - m\theta + \lambda f(\tau))\}$ expresses the carrier of the nonlinear wave here.

3 Numerical solutions

Although Eq. (60) reduces into the nonlinear Schrödinger equation in the limit of $\tau \rightarrow \infty$, no exact solutions to Eq. (60) have been found for $d_2 \neq 0$. In this section, we study the solutions for finite τ numerically.

If $d_2 = 0$, the analytic solution to Eq. (60) is well-known to be

$$n_1^{(1)} = A \operatorname{sech}\left[A\sqrt{\frac{d_3}{2d_1}}(\xi + V_1\tau + \xi_0)\right] \exp\left[i\left(\frac{d_3 A^2}{2} - \frac{V_1^2}{4d_1}\right)\tau - i\frac{V_1}{2d_1}(\xi + \xi_1)\right] \quad (64)$$

for $d_1 d_3 > 0$ or

$$n_1^{(1)} = A \tanh\left[A\sqrt{-\frac{d_3}{2d_1}}(\xi + V_1\tau + \xi_0)\right] \exp\left[i\left(d_3 A^2 - \frac{V_1^2}{4d_1}\right)\tau - i\frac{V_1}{2d_1}(\xi + \xi_1)\right] \quad (65)$$

for $d_1 d_3 < 0$, where A , V_1 , ξ_0 , and ξ_1 are arbitrary constants. The constant A determines the amplitude and the width of the soliton, V_1 (and V) determine(s) the group velocity, and ξ_0 and ξ_1 determine the initial positions of the soliton and the carrier wave, respectively. Equations (64) and (65) correspond to the bright and dark solitons, respectively.

Figure 2(a) shows an analytic solution for $d_2 = 0$ given by Eq. (64). Here $d_1 = d_3 = 1$, $A = 2$, $V_1 = -10$, $\xi_0 = 6$, $\xi_1 = 2.76$, and the initial time $\tau_0 = 1$. We can see that an envelope soliton propagates in the ξ -direction without change of its shape. On the other hand, Figs. 2(b) and 2(c) show numerical solutions to Eq. (60) for $d_2 = 1$. The initial time $\tau_0 = 0.5$ in Fig. 2(b) and $\tau_0 = 0.1$ in Fig. 2(c). The initial positions of the soliton and the carrier wave in Figs. 2(b) and 2(c) are the same as Fig. 2(a). We can see from these figures that the amplitude of the solitary waves decreases as it propagates in the ξ -direction. This result is quite natural, because the wave propagating in the ξ -direction, which corresponds to the radial direction, decreases its energy density (the $1/\tau$ term in Eq. (60) comes from the $1/r$ terms in Eqs. (3)-(5)).

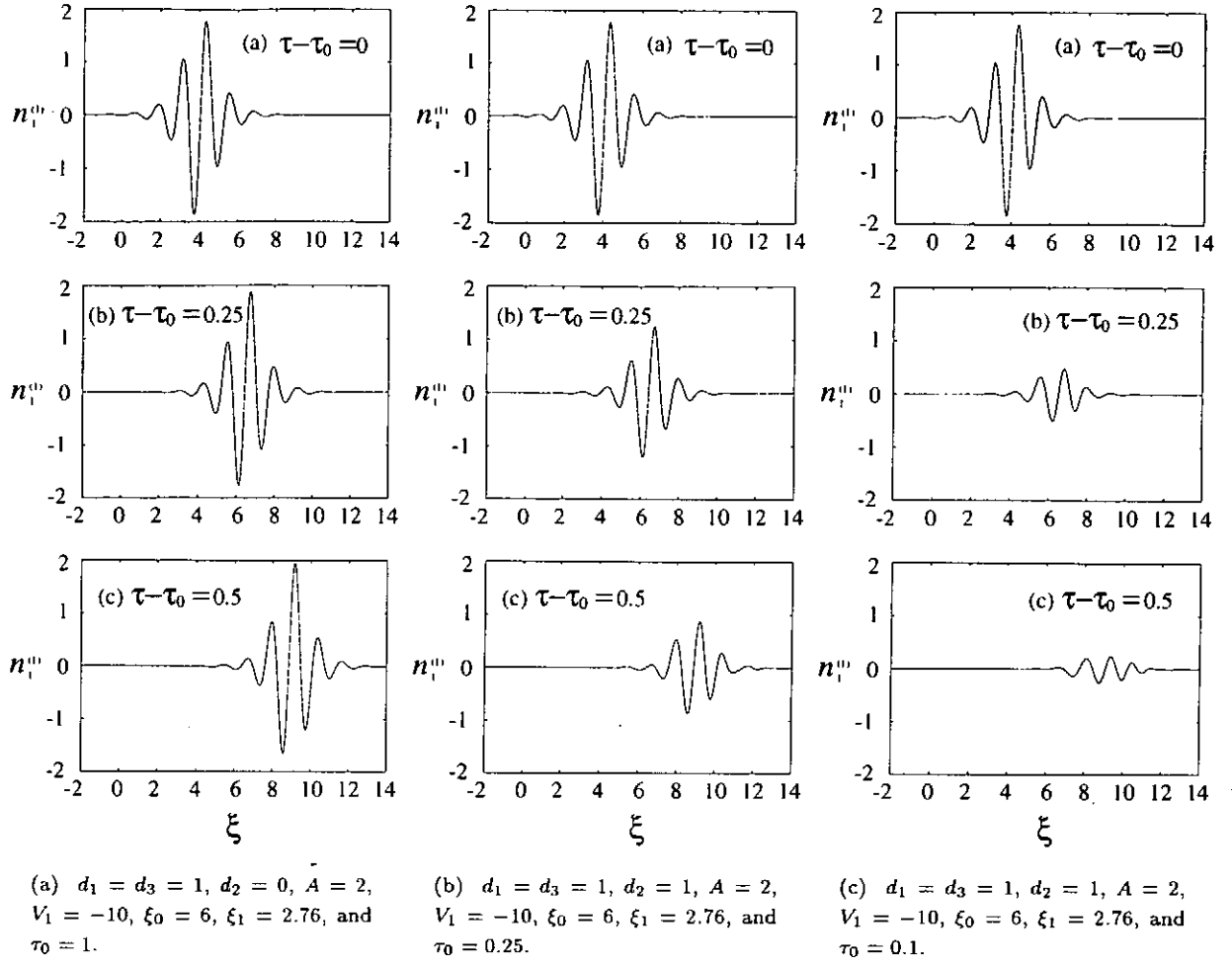


Figure 2: (a) An analytic solution for $d_2 = 0$ given by Eq. (64) and (b),(c) numerical solutions for $d_2 = 1$. Here $\tau_0 = 0.25$ in Fig. (b) and $\tau_0 = 0.1$ in Fig. (c). The initial position of the wave is the same as Fig. (a). We can see that the amplitude decreases as the solitary wave propagates in ξ -direction when $d_2 = 1$.

4 Concluding remarks

We have derived a nonlinear Schrödinger-type equation that describes a spiral structure of a galaxy. As well-known to plasma physics, the Langmuir wave, which is a density wave propagating on electrons, can generate an envelope soliton that is described by a nonlinear Schrödinger equation. A galaxy is a gravitational many-body system, while a plasma is an electromagnetic many-body system, which, in the electrostatic limit, obeys the same set of equations. Hence, the fact that the galactic density wave has a soliton-like structure can be naturally deduced. A unique feature of the present formalism is that a thin-disk geometry is considered and the soliton-like structure of a gravitational medium is obtained.

Galaxies resemble plasmas in that their components interact with each other through a long range force produced by the particles themselves. In particular, single-species non-neutral plasmas such as pure electron plasmas are quite similar to galaxies except that electrons are repulsive while stars are attractive. Because of this nature of galaxies and non-neutral plasmas, they exhibit similar collective phenomena such as vortices[7].

The behavior of single-species non-neutral plasmas is often analyzed under the assumption that they have an infinite length in the axial direction, while galaxies are often assumed to have a zero thickness. The advantage of the infinite-length analysis is that the Poisson's equation becomes two-dimensional, which makes our problem completely two-dimensional. Then the analysis is greatly simplified. It is meaningful to analyze the behavior of galaxies in such a way because of its simplicity. Such an analysis is to be published

elsewhere.

Acknowledgements

The authors are grateful to Dr. Tomoya Tatsuno for his useful discussions.

Appendix

We show that the following two equations are equivalent:

$$\sum_{l=-\infty}^{\infty} \exp(il\varphi) \left(X_l^{(n)} + iY_l^{(n)} \right) + \sum_{l=1}^{\infty} \operatorname{Re} \left[2iZ_l^{(n)} \exp(il\varphi) \right] = 0 \quad (\forall \varphi), \quad (66)$$

$$X_l^{(n)} + iY_l^{(n)} + iZ_l^{(n)} \operatorname{sgn} l = 0 \quad (\forall l), \quad (67)$$

where $X_l^{(n)}$, $Y_l^{(n)}$, and $Z_l^{(n)}$ are complex constants or slowly varying functions of φ that satisfy the reality condition

$$X_l^{(n)*} = X_{-l}^{(n)}, \quad (68)$$

$$Y_l^{(n)*} = Y_{-l}^{(n)}, \quad (69)$$

$$Z_l^{(n)*} = Z_{-l}^{(n)}. \quad (70)$$

Equation (66) can be written as

$$\begin{aligned} & \sum_{l=-\infty}^{\infty} \left[\left(X_{lr}^{(n)} - iY_{li}^{(n)} \right) \cos(l\varphi) - \left(X_{li}^{(n)} + iY_{lr}^{(n)} \right) \sin(l\varphi) \right] \\ & + i \sum_{l=-\infty}^{\infty} \left[\left(X_{li}^{(n)} + iY_{lr}^{(n)} \right) \cos(l\varphi) + \left(X_{lr}^{(n)} - iY_{li}^{(n)} \right) \sin(l\varphi) \right] \\ & - \sum_{l=1}^{\infty} \left[2Z_{li}^{(n)} \cos(l\varphi) + 2Z_{lr}^{(n)} \sin(l\varphi) \right] = 0, \end{aligned} \quad (71)$$

where subscripts r and i denote the real part and imaginary part, respectively. The second term of the left-hand side of Eq. (71) vanishes because of the reality condition Eqs. (68)-(70). Then Eq. (71) becomes

$$\sum_{l=0}^{\infty} \left[2 \left(X_{lr}^{(n)} - iY_{li}^{(n)} - Z_{li}^{(n)} \right) \cos(l\varphi) - 2 \left(X_{li}^{(n)} + iY_{lr}^{(n)} + Z_{lr}^{(n)} \right) \sin(l\varphi) \right] = 0. \quad (72)$$

Thus,

$$X_{lr}^{(n)} - iY_{li}^{(n)} - Z_{li}^{(n)} = 0, \quad (73)$$

$$X_{li}^{(n)} + iY_{lr}^{(n)} + Z_{lr}^{(n)} = 0, \quad (74)$$

for each $l > 0$. Equations (73) and (74) are identical to

$$X_l^{(n)} + iY_l^{(n)} + iZ_l^{(n)} = 0 \quad (l > 0). \quad (75)$$

Taking complex conjugate on Eq. (75) gives

$$\begin{aligned} & X_{-l}^{(n)} - iY_{-l}^{(n)} - iZ_{-l}^{(n)} = 0 \quad (l > 0) \\ \iff & X_l^{(n)} + iY_l^{(n)} - iZ_l^{(n)} = 0 \quad (l < 0). \end{aligned} \quad (76)$$

Equations (75) and (76) are written as

$$X_l^{(n)} + iY_l^{(n)} + iZ_l^{(n)} \operatorname{sgn} l = 0 \quad (\forall l). \quad (77)$$

References

- [1] G. Bertin and C.C.Lin, *Spiral Structure in Galaxies : A Density Wave Theory* (The MIT Press, Massachusetts, 1996).
- [2] S.Chandrasekhar, *Principles of Stellar Dynamics* (Dover, New York, 1960), p.184
- [3] C.C.Lin and F.H.Shu, *Astrophys. J.* **140**, 646 (1964).
- [4] C.C.Lin and F.H.Shu, *Proc. Nat. Acad. Sci.* **55**, 229 (1966).
- [5] A.Jeffrey and T.Kawahara, *Asymptotic Methods in Nonlinear Wave Theory* (Pitman, London, 1982), p. 70.
- [6] A.Jeffrey and T.Taniuti, *Non-linear Wave Propagation: with Applications to Physics and Magnetohydrodynamics* (Academic Press, 1964).
- [7] C.F.Driscoll and K.S.Fine, *Phys. Fluids B* **2**, 1359 (1990)

Investigations on Application of Multigrid Method to MHD Equilibrium Analysis

Soichiro Ikuno

Faculty of Engineering Science, School of Engineering, Tokyo University of Technology
Hachioji, Tokyo 192-0982, Japan

Abstract

The potentiality of application for Multigrid method to MHD equilibrium analysis is investigated. The nonlinear eigenvalue problem often appears when the MHD equilibria are determined by solving the Grad-Shafranov equation numerically. After linearization of the equation, the problem is solved by use of the iterative method. Although the Red-Black SOR method or Gauss-Seidel method is often used for the solution of the linearized equation, it takes much CPU time to solve the problem. The Multigrid method is compared with the SOR method for the Poisson problem. The results of computations show that the CPU time required for the Multigrid method is about 1000 times as small as that for the SOR method.

Keywords: MHD equilibrium, Multigrid method, Red-Black SOR method.

§ 1. はじめに

核融合炉内の低アスペクト比トロイダル・プラズマのMHD平衡を数値的に求める場合、2階の楕円型偏微分方程式である、Grad-Shafranov方程式の境界値問題に帰着される。同境界値問題は非線形固有値問題をなし、低アスペクト比トロイダル・プラズマのMHD平衡は最小固有値に属する固有関数を求めることにより決定される。しかしながら、同問題は非線形であるため解析的に解くのは困難である。この困難を克服するため、非線形方程式に線形化を施しプラズマ電流が一定、もしくは、固有関数の最大値（最小値）が一定となる反復法を用いて固有関数を決定する。一般に、SOR法等を用いて線形化方程式を解くが、計算時間が掛かりすぎるという欠点をもつ[1]。

本研究の目的は、Poisson方程式を例にとりRed-Black Gauss-Seidel法とRed-Black SOR法との比較を行い、Multigrid法(Multigrid Method, MGM)の特徴を数値的に評価することである。さらに、Multigrid法(Multigrid Method, MGM)のMHD平衡解析に対する適用を検討する。

§ 2. Multigrid 法

偏微分方程式の境界値問題を数値的に解く場合、解析領域を格子に分割し差分法を用いて離散化する。得られた離散方程式は、Jacobi法、Gauss-Seidel法やSOR法等の反復法を用いて解くのが一般的である。しかしながら、前述の解法の収束速度は長波長成分の誤差の収束に依存していることがわかっている[2]。そのため、長波長成分を解にもつ問題に対しては、計算に時間が掛かってしまうという難点をもつ。

Multigrid法の基本的な考え方は、Coarse-Grid Correction Schemeと呼ばれる方法による。Fig. 2.1に示すように細かい格子(fine grid)で分割された領域 Ω^h と粗い格子(coarse grid)で分割された Ω^H を考える。 Ω^h 上の波数 $n=2$ の波動を Ω^H 上に写像したとすると、同じ波動でも Ω^h 上では長波長成分と扱っていたものが、 Ω^H 上では短波長成分と扱うことができる。即ち、fine grid上で収束しづらい長波長成分の誤差は、coarse grid上に写像することによって短波長成分の誤差に変換され、coarse grid上で反復計算を行うことにより容易に誤差を収束させることができる。上述のように二つ

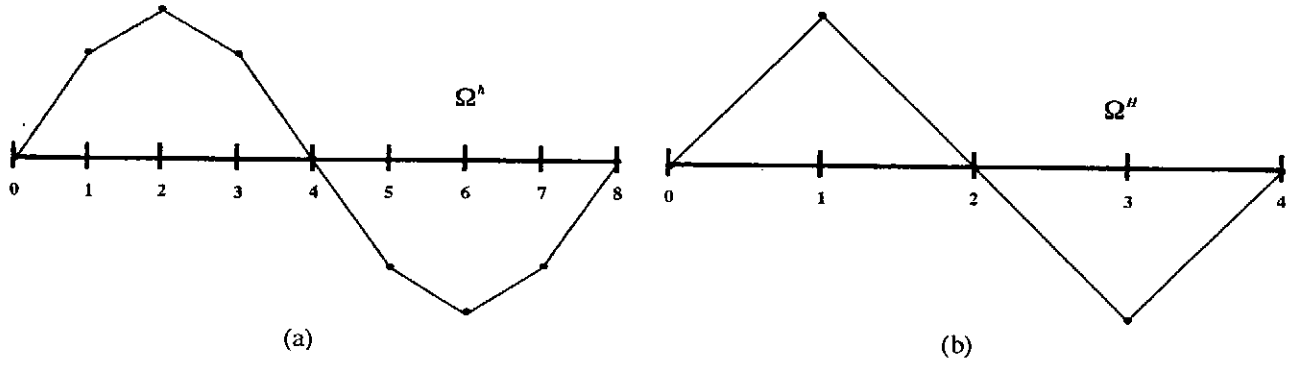


Fig. 2.1 The wave with wavenumber $k = 2$ on (a) Ω^h and (b) Ω^H .

の離散空間を準備し、それぞれの空間で誤差を収束させる手法を Coarse-Grid Correction Scheme と呼ぶ[2-4]. 次節では、Coarse-Grid Correction の詳細について述べる.

2.1 Coarse-Grid Correction Scheme

本説では2次元平面内の楕円型偏微分方程式の境界値問題を例に挙げ、Coarse-Grid Correction Scheme について述べる. 支配方程式:

$$\hat{L}u = f, \quad (2.1)$$

の境界値問題を考える. 但し, \hat{L} は線形の楕円型偏微分演算子を示し, f は既知関数である. 解析領域を刻み幅 h の格子 (fine grid) で分割し, 同領域内で (2.1) に離散化を施すと,

$$L_h u_h = f_h, \quad (2.2)$$

で示される離散化方程式を得る. 但し, L_h は離散化された偏微分演算子であり, f_h は離散化された既知関数 f を示す. また, u_h は (2.2) の厳密解を示す. ここで, (2.2) に対する近似解を \tilde{u}_h とすると (2.2) を数値的に解いたときの誤差は

$$v_h = |u_h - \tilde{u}_h|, \quad (2.3)$$

で与えられる. 同様に, \tilde{u}_h を用いると (2.2) の残差 d_h は

$$d_h = L_h \tilde{u}_h - f_h, \quad (2.4)$$

と表せられる. ここで, \hat{L} が線形偏微分演算子であることを用いると, 残差方程式:

$$L_h v_h = -d_h, \quad (2.5)$$

を得る. (2.5) を反復解法 (sweeper) で数値的に解き, 残差 d_h を求める. 本研究では sweeper として Red-Black Gauss-Seidel 法と Red-Black SOR 法を用いている.

前述のように, 長波長成分の誤差は反復解法の計算に於いて非常に収束しにくい. その反面, 短波長成分の誤差は数回の反復計算で消滅してしまうことがわかっている [2]. 即ち, (2.5) を数値的に解いて得られる残差 d_h の中には主に, 長波長成分の誤差が含まれていると考えられる. Coarse-Grid Correction Scheme では前述の難点を克服するため, 残差 d_h を coarse grid に写像し, 長波長成分を短波長成分として扱うことにより, 収束の速度を向上させている. 即ち, 残差 d_h を刻み幅 H ($h < H$) の coarse grid に次式を用いて写像する.

$$d_H = \hat{R} d_h. \quad (2.6)$$

但し, \hat{R} は restriction 演算子と呼ばれる演算子である. \hat{R} については次節で詳細に述べる. (2.6) で得られた d_H を用いて残差方程式:

$$L_H v_H = -d_H, \quad (2.7)$$

を得る. 但し, L_H は刻み幅 H の grid を用いて離散化した偏微分演算子である. (2.7) を sweeper により数値的に解き, coarse grid 上の誤差 v_H を得る. ここで, 誤差 v_H 内には刻み幅 H よりも短い短波長成分の誤差が混在する. しかしながら, これらの誤差は再度 fine grid 上に写像し, 同領域内で sweeper を用いることにより, 容易に収束させることが可能である. 即ち, prolongation 演算子 \hat{P} を用いて fine grid 上の誤差 v_h を次のように求める.

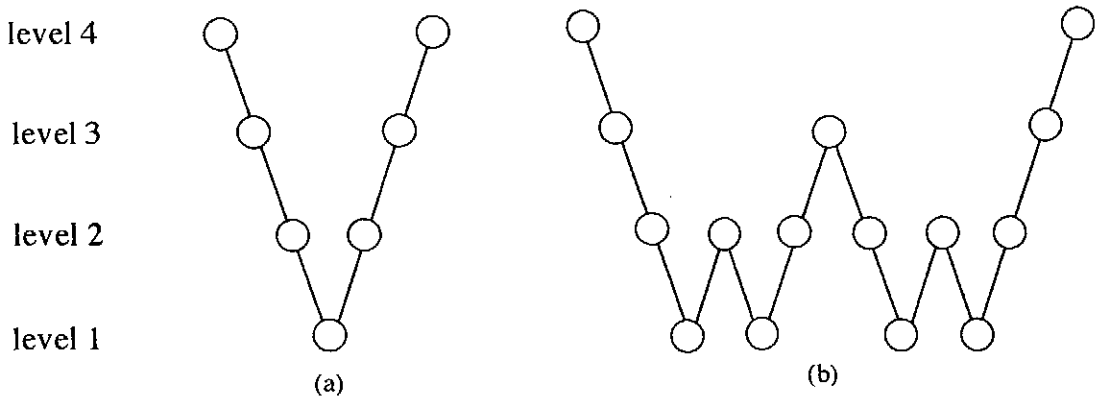


Fig. 2.2 The structure of multigrid cycles. (a) V-cycle, (b) W-cycle.

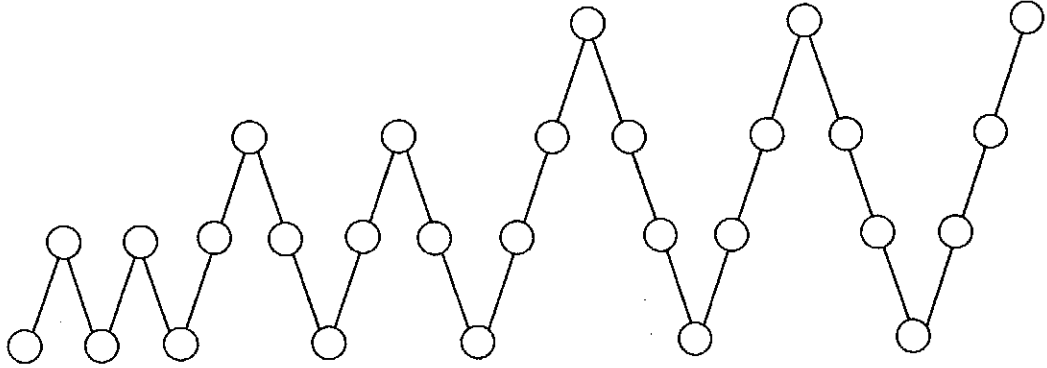


Fig. 2.3 The structure of Full Multigrid V-cycle. The number of cycle is two.

$$v_h = \hat{P} v_H. \quad (2.8)$$

\hat{P} については \hat{R} と同様に次節で詳細に述べる。(2.8)より得られた v_h を用いて \tilde{u}_h を更新し、新たな反復を開始する。上述の手続きを残差 d_h が充分小さくなるまで反復することにより、(2.2)に対する近似解を \tilde{u}_h を得る。

2.2 V-cycle と W-cycle

Coarse-Grid Correction Schemeは2種類の格子を用いて計算する手法であるが、Multigrid法はCoarse-Grid Correction Schemeを入れ子状にし、さらに長波長成分の誤差の収束速度を向上させる手法である。まず、刻み幅の異なる格子を解析領域内に生成し、最も粗い格子 (coarser grid) をレベル1とし、格子が細くなるに従い、レベル2、レベル3・・・とする。また、最も細かい格子 (finest grid) からcoarser gridまでCoarse-Grid Correction Schemeを行い、再びfinest gridまで戻ってくる手続きをcycleと呼ぶ。Fig. 2.2に示すように、レベル $k-1$ ($k > 1$)でのCoarse-Grid Correction Schemeを行う回数 γ によってサイクルの構造が決定される。 $\gamma=1$ の場合をV-cycleと呼び、 $\gamma=2$ の場合をW-cycleと呼ぶ。

2.3 Full Multigrid V-cycle (FMV)

前節で示したV-cycleとW-cycleは、finest gridから適当な初期値より計算を始め、残差が収束するまで反復する反復解法である。本節で紹介するFull Multigrid V-cycle (FMV)は、coarse gridでの計算が多いのが特徴であり、長波長成分誤差の収束速度向上がより期待できる手法である。また、Coarse-Grid Correction Schemeを行う限り、下位レベルのgridは用意しなければならないので、メモリのロスはない。さらには、coarser grid上での厳密な数値解を次のレベルでの初期値として使用しているため、各レベルで行うsweeperの反復回数はV-cycleやW-cycleに比べ減少し、高速化も期待できる。Fig. 2.3にFull Multigrid V-cycleのサイクル構造を示す。

2.4 prolongation 演算子と restriction 演算子

coarse grid 上 (レベル k) の関数値を fine grid 上 (レベル $k+1$) に写像する prolongation 演算子としては 9 点を用いた線形補間が一般的であり、次のように表される。

$$s_{x,y}^h = (\hat{P} s_H)_{(x,y)} = s_{x,y}^H + \frac{1}{2}(s_{x+H,y}^H + s_{x-H,y}^H + s_{x,y+H}^H + s_{x,y-H}^H) + \frac{1}{4}(s_{x+H,y+H}^H + s_{x-H,y-H}^H + s_{x-H,y+H}^H + s_{x+H,y-H}^H) . \quad (2.9)$$

となる。但し、 $s_{x,y}^h$, $s_{x,y}^H$ は fine grid 上, coarse grid 上の座標 (x, y) における関数値をそれぞれ示す。即ち、 \hat{P} の具体形は、

$$\hat{P} = \begin{bmatrix} 1/4 & 1/2 & 1/4 \\ 1/2 & 1 & 1/2 \\ 1/4 & 1/2 & 1/4 \end{bmatrix} , \quad (2.10)$$

となる。一方、restriction 演算子 \hat{R} は \hat{P} の随伴演算子として定義する [2]。先ず、 \hat{P} の随伴演算子 \hat{P}^\dagger を定義するために、以下の内積を定義する。

$$\langle s^h, t^h \rangle_h = h^2 \sum_{(x,y)} s_{x,y}^h t_{x,y}^h . \quad (2.11)$$

但し、 $s_{x,y}^h$ 及び $t_{x,y}^h$ は刻み幅 h の格子上的座標 (x, y) における関数値を示す。(2.11) の内積を用いることにより、随伴演算子 \hat{P}^\dagger は刻み幅 H の格子上で

$$\langle s^H, \hat{P}^\dagger t^h \rangle_H = \langle \hat{P} s^H, t^h \rangle_h , \quad (2.12)$$

と定義できる。ここで、 $H = 2h$, $\hat{P}^\dagger = \hat{R}$ とすると

$$s_{x,y}^H = (\hat{R} v_h)_{(x,y)} = \frac{1}{4} s_{x,y}^h + \frac{1}{8}(s_{x+h,y}^h + s_{x-h,y}^h + s_{x,y+h}^h + s_{x,y-h}^h) + \frac{1}{16}(s_{x+h,y+h}^h + s_{x-h,y-h}^h + s_{x-h,y+h}^h + s_{x+h,y-h}^h) \quad (2.13)$$

となり、 \hat{R} の具体形は

$$\hat{R} = \begin{bmatrix} 1/16 & 1/8 & 1/16 \\ 1/8 & 1/4 & 1/8 \\ 1/16 & 1/8 & 1/16 \end{bmatrix} , \quad (2.14)$$

と表される。

次節では、Poisson 方程式の境界値問題を例に挙げ、Multigrid 法の特徴を数値的に検討する。

§ 3. 計算結果

本章では、Poisson 方程式の境界値問題を例に挙げ、Multigrid 法の特徴を Red-Black Gauss-Seidel 法と Red-Black SOR 法と比較し数値的に検討する。解析領域は、 (x, y) 平面内の $[0, 1] \times [0, 1]$ 領域であり Ω とする。また、境界を $\partial\Omega$ とする。

解析領域 Ω 内で

$$-\Delta u = f(x, y) , \quad (3.1)$$

が成り立つとし、(3.1) の境界条件は $\partial\Omega$ 上で同次 Dirichlet 条件：

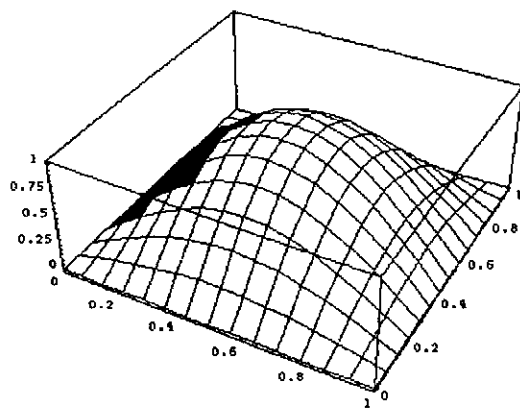
$$u = 0 , \quad (3.2)$$

を与える。但し、(3.1) の非同次項の関数 $f(x, y)$ は case1 の場合、

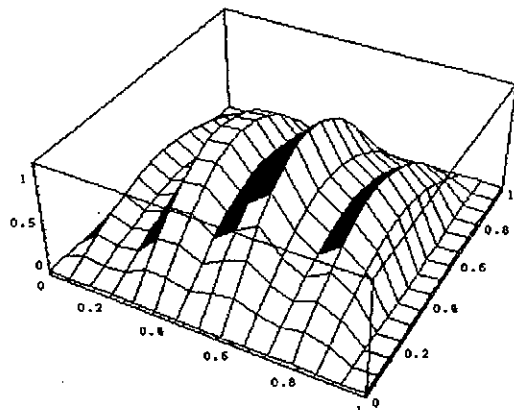
$$f(x, y) = \sin \pi x \sin \pi y , \quad (3.2)$$

で与え、case2 の場合、

$$f(x, y) = (\sin \pi x + \frac{1}{4} \sin 8\pi x) \sin \pi y , \quad (3.3)$$



(a)



(b)

Fig. 3.1 The distributions of the solution of eq. (3.1). (a) case1, (b) case2.

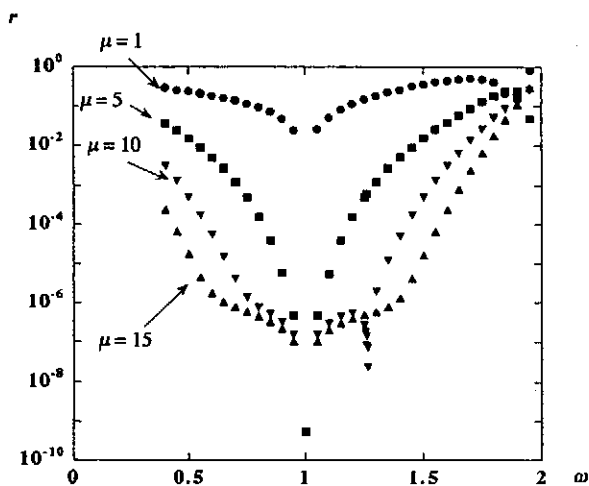


Fig. 3.2 The values of r as functions of relaxation factor ω (case 1).

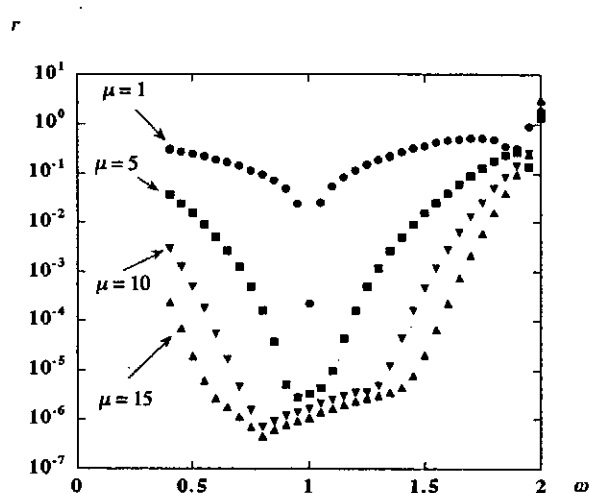


Fig. 3.3 The values of r as functions of relaxation factor ω (case 2).

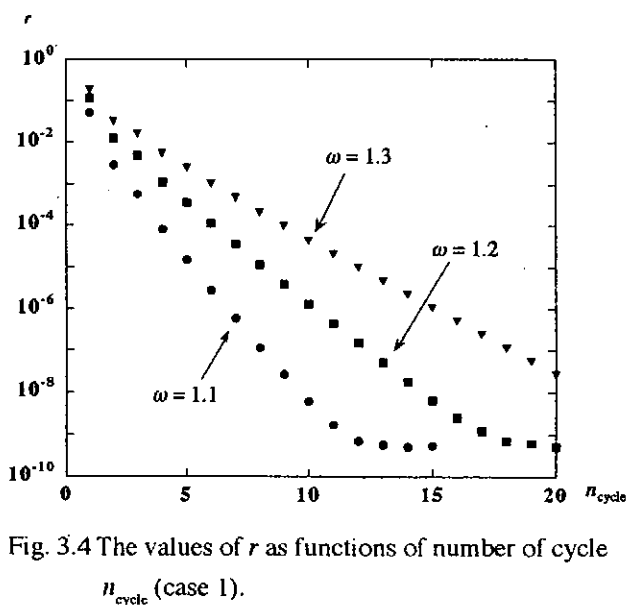


Fig. 3.4 The values of r as functions of number of cycle n_{cycle} (case 1).

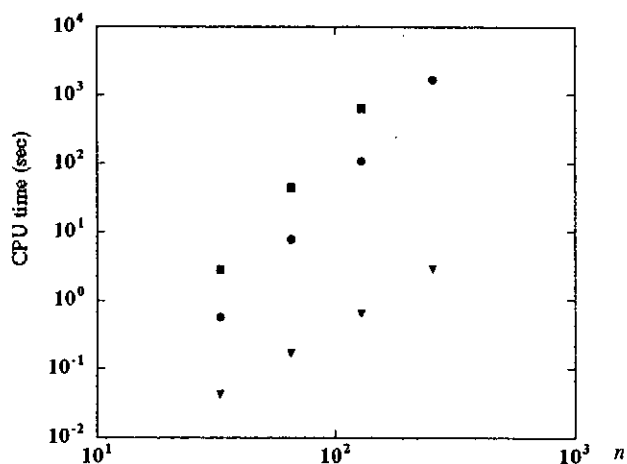


Fig. 3.5 The values of CPU time as functions of number of division number n (case 1). ■: Red-Black Gauss-Seidel method, ●: Red-Black SOR method, ▼: Multigrid method.

とした。Fig. 3.1よりわかるように case1 の場合、(3.1)の解析解は長波長成分のみをもつように与え、一方、case2 の場合は長波長成分内に短波長成分が混在する解をもつように非同次項の関数を与えている。

上記の境界値問題に対し、FMV を適用し計算を行った。但し、本研究では 256x256 の finest grid、即ち、8 階層の grid を用いている。Fig. 3.2 に case1 の場合の加速（緩和）係数 ω に対する r の変化を示す。ここで、 r は

$$r \equiv \frac{|u - u^{\text{SOR}}|}{|u^{\text{SOR}}|}$$

で定義し、 u^{SOR} は SOR 法を用いて充分収束させた解を示す。また、 μ は各レベルで行う sweeper の反復回数を示す。但し、FMV のサイクル数 n_{cycle} は $n_{\text{cycle}} = 1$ として計算を行っている。Fig. 3.2 からわかるように、 μ の値に関わらず、 $\omega = 1$ の Red-Black Gauss-Seidel 法で充分な数値解が得られていることがわかる。また、 ω の増加に伴い sweeper の反復回数を増加しないと充分な数値解が得られないこともわかる。これは、各レベルの sweeper の反復において加速（緩和）係数 ω が解の短波長成分を破壊しているためであると考えられる。Fig. 3.3 に case2 の場合の加速（緩和）係数 ω に対する r の変化を示す。case1 と比較するとわかるように sweeper の反復回数 μ をある程度増大させないと充分な数値解は得られないことがわかる。case2 の場合、短波長成分が解に内在しているため、レベルの高い位置で sweeper の反復が必要であるからである。しかしながら、 $\omega = 1$ の Red-Black Gauss-Seidel 法が sweeper としての性能が一番良く、同解法が Multigrid 法の sweeper として一番適していると考えられる。

case2 の場合、サイクル数 $n_{\text{cycle}} = 1$ では充分に解が収束しなかったため、サイクル数と r の関係について計算を行った。Fig. 3.4 に case2 の場合のサイクル数 n_{cycle} に対する r の変化を示す。但し、sweeper の反復回数 μ は $\mu = 1$ で行っている。Fig. 3.4 からわかるように $\omega = 1.1$ の場合、 $n_{\text{cycle}} = 12$ で収束した数値解が得られていることが分かる。それに対して、sweeper として Red-Black SOR 法を用いた場合、最低でも $n_{\text{cycle}} = 18$ のサイクル数が必要である。

最後に、Fig. 3.5 に finest grid の x, y 方向の分割数 n に対する CPU 時間の変化を示す。同図よりわかるように通常の SOR 法を用いた場合に比べ、Multigrid 法では最高で 1 0 0 0 倍程度の高速化が可能であることがわかる。

§ 4. 結論

本研究では、Poisson 方程式を例にとり Red-Black Gauss-Seidel 法と Red-Black SOR 法との比較を行い、Multigrid 法 (Multigrid Method, MGM) の特徴を数値的に評価を行った。得られた結果をまとめると以下ようになる。

1. Multigrid 法の sweeper として最も適しているのは Red-Black Gauss-Seidel 法であると考えられる。
2. 加速（緩和）係数 ω の増加（減少）に伴い、sweeper の反復回数を増加しないと充分収束した数値解が得られないことがわかる。これは、各レベルの sweeper の反復において加速（緩和）係数 ω が解の短波長成分を破壊しているためであると考えられる。
3. SOR 法を用いた場合に比べ、Multigrid 法では最高で 1 0 0 0 倍程度の高速化が可能である。
4. sweeper として Red-Black Gauss-Seidel 法を用いているため分散処理への対応は容易である。

本研究で用いた Multigrid 法を低アスペクト比トロイダル・プラズマの MHD 平衡解析コードに適用するのは容易であり、コードも開発済みである。しかしながら、円柱座標系内での Multigrid 法を用いた MHD 平衡解析では収束速度の劣化が激しく、また、中心対称軸上で誤差の蓄積があるとの報告がある [5]。

参考文献

- [1] Soichiro Ikuno, Atsushi Kamitani and Makoto Natori: NIFS-PROC-40(1999) 72-81.
- [2] William L. Briggs: A Multigrid Tutorial SIAM, Philadelphia, Pennsylvania (1987).
- [3] William H. Press, Saul A. Teukolsky, William T. Vetterling and Brian P. Flannery: Numerical Recipes in Fortran 77 - Second Edition-, Cambridge University Press (1992) 862-869.
- [4] Arieh Iserles: A First Course in the Numerical Analysis of Differential Equations, Cambridge University Press (1996) 227-244
- [5] Tatsuoki Takeda and Atsushi Kamitani: private communications.

ERROR ANALYSIS OF NEWMARK'S METHOD FOR THE SECOND ORDER EQUATION WITH INHOMOGENEOUS TERM

F. CHIBA and T. KAKO

*Department of Computer Science,
The University of Electro-Communications,
1-5-1 Chofugaoka, Chofu, Tokyo 182-8585, Japan.
email: chiba@im.uec.ac.jp, kako@im.uec.ac.jp*

Abstract

For the second order time evolution equation with a general dissipation term, we introduce a recurrence relation of Newmark's method. Deriving an energy inequality from this relation, we consider the stability and the convergence criteria of Newmark's method. We treat a dissipation term under the assumption that the coefficient damping matrix is constant in time and nonnegative. We can relax however the assumptions for the dissipation and the rigidity matrices to be arbitrary symmetric matrices.

Keywords: dissipation term, energy inequality, Newmark's method, recurrence relation, stability

1 Introduction of Newmark's method

We introduce the basic ideas of Newmark's method[9] for the second order time evolution equation in the d -dimensional Euclidean space \mathbf{R}^d . Let M , C and K be $d \times d$ matrices on \mathbf{R}^d which are constant in time, and let $f(t)$ be a given \mathbf{R}^d -valued function on $[0, \infty)$. Throughout this paper, we assume that M is symmetric and positive definite:

$$M \geq mI, \quad m > 0. \quad (1)$$

Here I is the identity matrix on \mathbf{R}^d . We consider the approximation method for the following initial value problem of the second order time evolution equation for an \mathbf{R}^d -valued function $u(t)$:

$$M \frac{d^2}{dt^2} u(t) + C \frac{d}{dt} u(t) + Ku(t) = f(t), \quad u(0) = u_0, \quad \frac{d}{dt} u(0) = v_0. \quad (2)$$

Let a_n , v_n and u_n be approximations of $(d^2/dt^2)u(t)$, $(d/dt)u(t)$ and $u(t)$ respectively at $t = \tau n$ with a positive time step τ and an integer n , and let $f_n = f(\tau n)$. Then Newmark's method for (2) is defined through the following relations:

$$\begin{cases} Ma_n + Cv_n + Ku_n = f_n, \\ u_{n+1} = u_n + \tau v_n + \frac{1}{2} \tau^2 a_n + \beta \tau^2 (a_{n+1} - a_n), \\ v_{n+1} = v_n + \tau a_n + \gamma \tau (a_{n+1} - a_n). \end{cases} \quad (3)$$

The first relation corresponds to the equation (2), and the second and the third relations correspond to the Taylor expansions of $u(t + \tau)$ and $v(t + \tau)$ at $t = \tau n$ respectively. Here, β and γ are positive tuning parameters of the method.

An interpretation of the parameter β related to the acceleration $(d^2/dt^2)u(t)$ can be seen in [9]: The case $\beta = 1/6$ corresponds to the approximation that the acceleration is a linear function of t in each time interval; the case $\beta = 1/4$ corresponds to the approximation of the acceleration to be a constant function during the time interval which is equal to the mean of the initial and final values of acceleration; the case $\beta = 1/8$ corresponds to the case that the acceleration is a step function with the initial value for the first half of each time interval and the final value for the second half of the interval. It is often the case that γ is equal to $1/2$.

2 Iteration scheme of Newmark's method

Based on the formulas in (3), Newmark's method generates the approximation sequence $u_n, n = 0, 1, 2, \dots, N$ by the following iteration scheme:

Step 1. For $n = 0$, compute a_0 from the initial data u_0 and v_0 :

$$a_0 = M^{-1}(f_0 - Cv_0 - Ku_0).$$

Step 2. Compute a_{n+1} from f_{n+1}, u_n, v_n and a_n solving a linear equation:

$$\begin{aligned} a_{n+1} &= (M + \gamma\tau C + \beta\tau^2 K)^{-1} \\ &\quad \times [-Ku_n - (C + \tau K)v_n + \{(\gamma - 1)\tau C + (\beta - \tfrac{1}{2})\tau^2 K\}a_n + f_{n+1}]. \end{aligned}$$

Step 3. Compute u_{n+1} from u_n, v_n, a_n and a_{n+1} :

$$u_{n+1} = u_n + \tau v_n + (\tfrac{1}{2} - \beta)\tau^2 a_n + \beta\tau^2 a_{n+1}.$$

Step 4. Compute v_{n+1} from v_n, a_n and a_{n+1} :

$$v_{n+1} = v_n + (1 - \gamma)\tau a_n + \gamma\tau a_{n+1}.$$

Step 5. Replace n by $n + 1$, and return to Step 2.

Here, Step 1 is nothing but the first relation of (3) with $n = 0$. The expression of a_{n+1} in Step 2 is obtained by eliminating u_{n+1} and v_{n+1} from the second and the third equalities in (3) together with the first equality in (3) with n replaced by $n + 1$:

$$Ma_{n+1} + Cv_{n+1} + Ku_{n+1} = f_{n+1}.$$

Step 3 and Step 4 are from the second and the third relations of (3).

3 Recurrence relation of Newmark's method

Newmark's method (3) for the second order equation (2) is reformulated as follows in the recurrence relation([1], [2], [3] and [13]). Eliminating v_n and a_n from (3) by a series of tedious manual computations, we have

$$\begin{aligned} (M + \beta\tau^2 K)D_{\tau\tau}u_n \\ + \gamma CD_{\tau}u_n + \{(1 - \gamma)C + \tau(\gamma - \tfrac{1}{2})K\}D_{\tau}u_n + Ku_n = \{I + \tau(\gamma - \tfrac{1}{2})D_{\tau} + \beta\tau^2 D_{\tau\tau}\}f_n, \end{aligned} \quad (4)$$

where

$$\begin{cases} D_\tau u_n &= (u_{n+1} - u_n)/\tau, \\ D_{\bar{\tau}} u_n &= (u_n - u_{n-1})/\tau, \\ D_{\tau\bar{\tau}} u_n &= (D_\tau u_n - D_{\bar{\tau}} u_n)/\tau. \end{cases}$$

We confirmed this result by a formula manipulation software NCAIgebra[6] on Mathematica[12]. Especially, in the case $\gamma = 1/2$, we have:

$$(M + \beta\tau^2 K)D_{\tau\bar{\tau}} u_n + \frac{1}{2}C(D_\tau + D_{\bar{\tau}})u_n + Ku_n = (I + \beta\tau^2 D_{\tau\bar{\tau}})f_n. \quad (5)$$

These recurrence relations are useful for the stability and error analyses of Newmark's method. See [8] and [10] for the case with $C \equiv 0$.

4 Derivation of an energy inequality

Taking a scalar product of (4) and $(D_\tau + D_{\bar{\tau}})u_n$, we can derive an energy inequality for Newmark's method. From this inequality, we obtain the stability conditions for Newmark's method. In the following, we use the usual Euclidean scalar product (\cdot, \cdot) and the corresponding norm $\|\cdot\|$ in \mathbf{R}^d .

From now on, let T be a fixed positive number and N be a positive integer, and define $\tau := T/N$ and $n = 0, 1, 2, \dots, N-1$. Let C be nonnegative: $C \geq 0$, let K be positive definite: $K \geq kI$, $k > 0$ and $m > 0$ is the smallest eigenvalue of M . We also assume that

$$\gamma \geq \frac{1}{2}.$$

The main result of this section is the following theorem for the energy inequality.

THEOREM 4.1 *Let $\{u_n\}_{n=0}^N$ be a sequence generated by the scheme in Section 2. Then for a positive constant τ_0 determined as below, there exists a positive constant C_0 such that the inequality:*

$$\|M^{1/2} D_\tau u_n\|^2 + \tau^2 \left\{ \beta - \frac{1}{2}(\gamma - \frac{1}{2}) - \frac{1}{2}\alpha \right\} \|K^{1/2} D_\tau u_n\|^2 + (1 - \frac{1}{2\alpha}) \|K^{1/2} u_n\|^2 \leq C_0 \quad (6)$$

holds for all $\tau \leq \tau_0$ and an arbitrary positive constant α , where τ_0 is determined either as

$$\tau_0 > 0 \text{ when } \beta \geq \frac{\gamma}{2} \quad (7)$$

or as

$$0 < \tau_0 < \sqrt{\frac{m}{(\frac{1}{2}\gamma - \beta)\|K^{1/2}\|^2}} \text{ when } 0 \leq \beta < \frac{\gamma}{2}. \quad (8)$$

REMARK 4.1 *The constant C_0 in the theorem depends primarily on the coefficient matrices M , C and K , and secondarily on the tuning parameters β and γ and it also depends on the initial values u_0 and v_0 and the inhomogeneous term f , and finally on τ_0 in the way described above.*

PROOF. Using (4), we derive an energy inequality as follows (see [1] and [2] for the case $\gamma = 1/2$). Rearranging (4), we have

$$\begin{aligned} (M + \beta\tau^2 K)D_{\tau\bar{\tau}} u_n + \frac{1}{2}C(D_\tau + D_{\bar{\tau}})u_n \\ + (\gamma - \frac{1}{2})C(D_\tau - D_{\bar{\tau}})u_n + \tau(\gamma - \frac{1}{2})KD_{\bar{\tau}} u_n + Ku_n = g_n, \end{aligned} \quad (9)$$

where

$$g_n := \{I + \tau(\gamma - \frac{1}{2})D_{\bar{\tau}} + \beta\tau^2 D_{\tau\bar{\tau}}\}f_n. \quad (10)$$

We take a scalar product of (9) and $(D_{\tau} + D_{\bar{\tau}})u_n$. Since C is nonnegative, we have

$$\begin{aligned} & ((M + \beta\tau^2 K)D_{\tau\bar{\tau}}u_n, (D_{\tau} + D_{\bar{\tau}})u_n) \\ & + (\gamma - \frac{1}{2})(C(D_{\tau} - D_{\bar{\tau}})u_n, (D_{\tau} + D_{\bar{\tau}})u_n) \\ & + \tau(\gamma - \frac{1}{2})(KD_{\bar{\tau}}u_n, (D_{\tau} + D_{\bar{\tau}})u_n) \\ & + (Ku_n, (D_{\tau} + D_{\bar{\tau}})u_n) - (g_n, (D_{\tau} + D_{\bar{\tau}})u_n) \\ & = -(\frac{1}{2}C(D_{\tau} + D_{\bar{\tau}})u_n, (D_{\tau} + D_{\bar{\tau}})u_n) \leq 0. \end{aligned} \quad (11)$$

Using the assumption for M , C and K , we obtain the following lemma:

LEMMA 4.2 *When we put*

$$\begin{aligned} w_n &:= ((M + \beta\tau^2 K)D_{\tau}u_n, D_{\tau}u_n) + (Ku_{n+1}, u_n) \\ &+ \tau(\gamma - \frac{1}{2})(CD_{\tau}u_n, D_{\tau}u_n) - \frac{1}{2}\tau^2(\gamma - \frac{1}{2})(KD_{\tau}u_n, D_{\tau}u_n), \end{aligned}$$

we have

$$w_n \leq w_{n-1} + \tau(g_n, D_{\tau}u_n + D_{\tau}u_{n-1}). \quad (12)$$

PROOF. We omit the proof. \square

Using the equality:

$$(Ku_{n+1}, u_n) = \tau(KD_{\tau}u_n, u_n) + (Ku_n, u_n),$$

we can modify the expression of w_n as

$$\begin{aligned} w_n &= \|M^{1/2}D_{\tau}u_n\|^2 + \tau^2\{\beta - \frac{1}{2}(\gamma - \frac{1}{2})\}\|K^{1/2}D_{\tau}u_n\|^2 \\ &+ \tau(KD_{\tau}u_n, u_n) + \|K^{1/2}u_n\|^2 + \tau(\gamma - \frac{1}{2})\|C^{1/2}D_{\tau}u_n\|^2, \end{aligned} \quad (13)$$

Using (12) repeatedly, we have

$$\begin{aligned} w_n &\leq w_{n-1} + \tau(g_n, D_{\tau}u_n + D_{\tau}u_{n-1}) \\ w_{n-1} &\leq w_{n-2} + \tau(g_{n-1}, D_{\tau}u_{n-1} + D_{\tau}u_{n-2}) \\ &\dots\dots\dots \\ w_{n-m} &\leq w_{n-m-1} + \tau(g_{n-m}, D_{\tau}u_{n-m} + D_{\tau}u_{n-m-1}) \\ &\dots\dots\dots \\ w_1 &\leq w_0 + \tau(g_1, D_{\tau}u_1 + D_{\tau}u_0). \end{aligned}$$

Summing up these inequalities, we obtain

$$w_n \leq w_0 + \sum_{i=1}^n \tau(g_i, D_{\tau}u_i + D_{\tau}u_{i-1}). \quad (14)$$

To modify (14), we show the next lemma.

LEMMA 4.3 *Under either the condition*

$$(7) \text{ and } 0 < \delta \leq m, \quad (15)$$

or

$$(8) \text{ and } \tau \leq \tau_0 \text{ and } 0 < \delta \leq m - \tau_0^2(\frac{1}{2}\gamma - \beta)\|K^{1/2}\|^2, \quad (16)$$

we have

$$\delta\|D_\tau u_i\|^2 \leq w_i. \quad (17)$$

PROOF. Let δ be a positive number. Using the assumption that M and K are positive definite, C is nonnegative and $\gamma \geq 1/2$, we have

$$\begin{aligned} w_i - \delta\|D_\tau u_i\|^2 &\geq \|M^{1/2}D_\tau u_i\|^2 + \tau^2(\beta - \frac{1}{2}\gamma)\|K^{1/2}D_\tau u_i\|^2 + \frac{1}{4}\|K^{1/2}(\tau D_\tau u_i + 2u_i)\|^2 - \delta\|D_\tau u_i\|^2 \\ &\geq (m - \delta)\|D_\tau u_i\|^2 + \tau^2(\beta - \frac{1}{2}\gamma)\|K^{1/2}D_\tau u_i\|^2 + \frac{1}{4}\|K^{1/2}(\tau D_\tau u_i + 2u_i)\|^2. \end{aligned}$$

If β and γ satisfies the condition (7) and $\delta \leq m$, then $w_i - \delta\|D_\tau u_i\|^2$ becomes nonnegative for any i .

On the other hand, if $\beta - \gamma/2 < 0$, then we have

$$\begin{aligned} w_i - \delta\|D_\tau u_i\|^2 &\geq m\|D_\tau u_i\|^2 - \tau^2(\frac{1}{2}\gamma - \beta)\|K^{1/2}\|^2\|D_\tau u_i\|^2 - \delta\|D_\tau u_i\|^2 \\ &= \{m - \tau^2(\frac{1}{2}\gamma - \beta)\|K^{1/2}\|^2 - \delta\}\|D_\tau u_i\|^2. \end{aligned}$$

If τ_0 satisfies the condition (8) and $\tau \leq \tau_0$ then

$$m - \tau^2(\frac{1}{2}\gamma - \beta)\|K^{1/2}\|^2 - \delta > m - \tau_0^2(\frac{1}{2}\gamma - \beta)\|K^{1/2}\|^2 - \delta.$$

Hence, if $\delta \leq m - \tau_0^2(\frac{1}{2}\gamma - \beta)\|K^{1/2}\|^2$, then $w_i - \delta\|D_\tau u_i\|^2 \geq 0$ for any i . Thus we obtain (17). \square

Using Lemma 4.3, we have the next lemma.

LEMMA 4.4 Under either the condition

$$(7) \text{ and } 0 < \delta \leq \min\{m, 2/\tau_0\}, \quad (18)$$

or

$$(8) \text{ and } \tau \leq \tau_0 \text{ and } 0 < \delta \leq \min\{m - \tau_0^2(\frac{1}{2}\gamma - \beta)\|K^{1/2}\|^2, 2/\tau_0\}, \quad (19)$$

we have, for $\tau \leq \tau_0$,

$$w_n \leq C_0, \quad n = 0, 1, 2, \dots, N-1. \quad (20)$$

PROOF. Using (17), we modify (14) as follows:

$$\begin{aligned} w_n &\leq w_0 + \tau \sum_{i=1}^n (g_i, D_\tau u_i + D_\tau u_{i-1}) \\ &\leq w_0 + \tau \sum_{i=1}^n \|g_i\|(\|D_\tau u_i\| + \|D_\tau u_{i-1}\|) \\ &\leq w_0 + \sum_{i=1}^n \left\{ \frac{\tau}{\delta^2} \|g_i\|^2 + \left(\frac{\tau\delta^2}{2} \|D_\tau u_i\|^2 + \frac{\tau\delta^2}{2} \|D_\tau u_{i-1}\|^2 \right) \right\} \\ &\leq w_0 + \frac{\delta\tau}{2} \sum_{i=1}^n (w_i + w_{i-1}) + \frac{\tau}{\delta^2} \sum_{i=1}^n \|g_i\|^2 \\ &\leq w_0 + \frac{\delta\tau}{2} w_n + \delta\tau \sum_{i=0}^{n-1} w_i + \frac{\tau}{\delta^2} \sum_{i=1}^{N-1} \|g_i\|^2. \end{aligned}$$

If $f(t)$ is bounded on $[0, T]$, then, for $i \geq 1$, we have

$$\begin{aligned}\|g_i\| &= \|(I + \tau(\gamma - \frac{1}{2})D_\tau + \beta\tau^2 D_{\tau\tau})f_i\| \\ &= \|f_i + (\gamma - \frac{1}{2})(f_i - f_{i-1}) + \beta(f_{i+1} - 2f_i + f_{i-1})\| \\ &\leq (4\beta + 2\gamma) \sup_{0 \leq t \leq T} \|f(t)\|.\end{aligned}$$

Hence we have

$$\begin{aligned}w_n &\leq w_0 + \frac{\delta\tau}{2}w_n + \delta\tau \sum_{i=0}^{n-1} w_i + \frac{\tau}{\delta^2} \sum_{i=1}^{N-1} \{(4\beta + 2\gamma) \sup_{0 \leq t \leq T} \|f(t)\|\}^2 \\ &\leq w_0 + \frac{\delta\tau_0}{2}w_n + \delta\tau \sum_{i=0}^{n-1} w_i + \frac{T}{\delta^2} \{(4\beta + 2\gamma) \sup_{0 \leq t \leq T} \|f(t)\|\}^2.\end{aligned}$$

Since $0 < 1 - \delta\tau_0/2$ from (18) or (19), we have

$$w_n \leq (1 - \frac{1}{2}\delta\tau_0)^{-1} [w_0 + \delta\tau \sum_{i=0}^{n-1} w_i + \frac{T}{\delta^2} \{(4\beta + 2\gamma) \sup_{0 \leq t \leq T} \|f(t)\|\}^2].$$

Using the Gronwall inequality, we then obtain

$$w_n \leq (1 - \frac{1}{2}\delta\tau_0)^{-1} [w_0 + \frac{T}{\delta^2} \{(4\beta + 2\gamma) \sup_{0 \leq t \leq T} \|f(t)\|\}^2] \exp(\delta(1 - \frac{1}{2}\delta\tau_0)^{-1}T),$$

where we use $N\tau = T$. Thus, we can define C_0 as follows

$$C_0 := (1 - \frac{1}{2}\delta\tau_0)^{-1} [w_0 + \frac{T}{\delta^2} \{(4\beta + 2\gamma) \sup_{0 \leq t \leq T} \|f(t)\|\}^2] \exp(\delta(1 - \frac{1}{2}\delta\tau_0)^{-1}T), \quad (21)$$

where

$$\begin{aligned}w_0 &= \|M^{1/2}D_\tau u_0\|^2 + \tau^2 \{\beta - \frac{1}{2}(\gamma - \frac{1}{2})\} \|K^{1/2}D_\tau u_0\|^2 \\ &\quad + \tau(KD_\tau u_0, u_0) + \|K^{1/2}u_0\|^2 + \tau(\gamma - \frac{1}{2}) \|C^{1/2}D_\tau u_0\|^2.\end{aligned} \quad (22)$$

□

Lastly, under either the condition (7) or (8), using the following inequality with an arbitrary α :

$$\begin{aligned}\tau(K^{1/2}D_\tau u_n, K^{1/2}u_n) &\geq -\tau \|K^{1/2}D_\tau u_n\| \times \sqrt{\alpha} \times \frac{1}{\sqrt{\alpha}} \times \|K^{1/2}u_n\| \\ &\geq -\frac{1}{2} \{\alpha\tau^2 \|K^{1/2}D_\tau u_n\|^2 + \frac{1}{\alpha} \|K^{1/2}u_n\|^2\},\end{aligned}$$

we obtain the energy inequality (6) from (20) in Lemma 4.4. From (14) we have

$$\text{If } f_n = g_n = 0, \text{ then } C_0 = w_0.$$

□

5 Stability conditions for Newmark's method

In this section, using the energy inequality (6) we derive stability conditions for Newmark's method. With respect to a parameter β , we divide the stability condition into two cases and lead to the next theorem.

THEOREM 5.1 *Let M and K be positive definite matrices and C be a nonnegative matrix. Let m and k be the smallest eigenvalues of M and K . Assume $\gamma \geq 1/2$. Then, Newmark's method for (2) in a time interval $[0, T]$ is stable in the following two cases with respect to β :*

Case 1: *If*

$$\frac{1}{2}\gamma < \beta,$$

then with $\tau_0 > 0$ and δ given in (18) we have, for $\tau < \tau_0$ and $N = T/\tau$,

$$\|u_n\| \leq \sqrt{\frac{(4\beta - 2\gamma + 1)}{(4\beta - 2\gamma)k}} C_0, \quad n = 0, 1, 2, \dots, N. \quad (23)$$

Case 2: *If*

$$0 \leq \beta \leq \frac{1}{2}\gamma,$$

then for τ_0 satisfying

$$0 < \tau_0 < \sqrt{\frac{m}{(\frac{1}{2}\gamma - \beta)\|K^{1/2}\|^2}}, \quad (24)$$

we have for $\tau \leq \tau_0$ and $N = T/\tau$

$$\|u_n\| \leq \|u_0\| + \sqrt{\frac{C_0}{m - \tau_0^2(\frac{1}{2}\gamma - \beta)\|K^{1/2}\|^2}} \tau n, \quad n = 0, 1, 2, \dots, N. \quad (25)$$

Here, in both cases, C_0 is given by (21) together with (22).

PROOF. We omit the proof. \square

REMARK 5.1 *H. Fujii investigated in [4] and [5] the stability condition for the Rayleigh damping case with $C = aK + bM$, $a, b \in \mathbf{R}$.*

6 Relaxation of restrictions on C and K

To extend the applications of the stability theorem in Section 5 and also the convergence theorem in Section 7, we consider the case with weaker assumptions for C and K as in the next lemma. (See pp. 30–33 in [11].)

LEMMA 6.1 *For the second order equation:*

$$M \frac{d^2}{dt^2} u(t) + C \frac{d}{dt} u(t) + Ku(t) = f(t), \quad (26)$$

we assume that M, C and K are symmetric and satisfy the following conditions:

$$\begin{aligned} (Mw, w) &\geq m\|w\|^2, \quad (Cw, w) \geq -c\|w\|^2, \\ (Kw, w) &\geq -c\|w\|^2 \text{ for } w \in \mathbf{R}^d, \end{aligned} \quad (27)$$

where m and c are positive constants. Then, we can transform (26) into the equation:

$$M \frac{d^2}{dt^2} v(t) + (2\lambda M + C) \frac{d}{dt} v(t) + (\lambda^2 M + \lambda C + K)v(t) = e^{-\lambda t} f(t), \quad (28)$$

where

$$v(t) = e^{-\lambda t} u(t), \quad (2\lambda M + C) \geq 0, \quad (\lambda^2 M + \lambda C + K) \geq kI, \quad (29)$$

with positive constants λ and k .

PROOF. We omit the proof. \square

So we can obtain the energy inequality based on (28).

7 Convergence of Newmark's method

Using the recurrence relation (4) and the stability theorem, we show in this section the convergence of Newmark's method together with its convergence order.

Let T be a fixed positive number and N be a positive integer, and define $\tau := T/N$. Let $u(t)$ be the solution of (2) and u_n ($n = 0, 1, 2, \dots, N$) be the solution of Newmark's method for (2). We assume that M and K are positive definite and C is nonnegative.

The discretization error e_n is defined as $e_n := u(\tau n) - u_n$. Then we have the following theorem.

THEOREM 7.1 *We assume that $f \in C^2([0, T])$, then we have the estimate $\|e_n\| = O(\tau^l)$, where*

$$\begin{cases} l = 2 & \text{for } \gamma = \frac{1}{2}, \\ l = 1 & \text{for } \gamma > \frac{1}{2}. \end{cases}$$

PROOF. To prove this theorem, we first show the following two lemmas.

LEMMA 7.2 *At the mesh points $t = \tau n$ with $n = 0, 1$, we have*

$$e_0 = 0, \quad e_1 = O(\tau^3).$$

PROOF. Since $u_0 = u(0)$, we have $e_0 = u(0) - u_0 = 0$. Next we estimate e_1 . From Step 3 in the iteration scheme in Section 2, we have

$$u_1 = u_0 + \tau v_0 + \left(\frac{1}{2} - \beta\right)\tau^2 a_0 + \beta\tau^2 a_1,$$

where

$$v_0 = \frac{d}{dt}u(0), \quad a_0 = \frac{d^2}{dt^2}u(0)$$

and

$$\begin{aligned} a_1 &= (M + \gamma\tau C + \beta\tau^2 K)^{-1} \\ &\quad \times [f_1 - (C + \tau K)v_0 - Ku_0 + \{(\gamma - 1)\tau C + (\beta - \frac{1}{2})\tau^2 K\}a_0]. \end{aligned}$$

On the other hand, by Taylor's theorem, we have

$$\begin{aligned} u(\tau) &= u_0 + \tau v_0 + \frac{1}{2}\tau^2 a_0 + O(\tau^3) \\ &= u_0 + \tau v_0 + \left(\frac{1}{2} - \beta\right)\tau^2 a_0 + \beta\tau^2 a_0 + O(\tau^3). \end{aligned}$$

So, we obtain

$$\begin{aligned} e_1 &= u(\tau) - u_1 = \beta\tau^2 a_0 + O(\tau^3) - \beta\tau^2 a_1 \\ &= \beta\tau^2(a_0 - a_1) + O(\tau^3), \end{aligned}$$

and from the relation

$$a_0 = M^{-1}(f_0 - Cv_0 - Ku_0)$$

and the above expression of a_1 , we have

$$\begin{aligned} a_1 &= (M^{-1} + O(\tau)) \times [(f_0 + O(\tau)) - (Cv_0 + O(\tau)) - Ku_0 + O(\tau)] \\ &= M^{-1}(f_0 - Cv_0 - Ku_0) + O(\tau). \end{aligned}$$

Thus we obtain $e_1 = O(\tau^3)$. \square

At the mesh points $t = \tau n$, $n = 0, 1, 2, \dots, N$, we have $u_n = u(\tau n) - e_n$ and $f_n = f(\tau n)$. Using the recurrence relation (4), we can prove the next technical lemma.

LEMMA 7.3 Define p_n as

$$\begin{aligned} p_n &:= (M + \beta\tau^2 K)D_{\tau\bar{\tau}}e_n \\ &\quad + [\{\gamma CD_\tau + (1 - \gamma)CD_{\bar{\tau}}\} + \tau(\gamma - \tfrac{1}{2})KD_{\bar{\tau}}]e_n + Ke_n. \end{aligned} \quad (30)$$

Then it is expressed as follows:

$$p_n = -\tau(\gamma - \tfrac{1}{2})M \frac{d^3}{dt^3}u(\tau n) + O(\tau^2). \quad (31)$$

PROOF. Substituting $u(\tau n) - e_n$ for u_n in the recurrence relation (4), we have

$$\begin{aligned} p_n &= (M + \beta\tau^2 K)D_{\tau\bar{\tau}}e_n \\ &\quad + [\{\gamma CD_\tau + (1 - \gamma)CD_{\bar{\tau}}\} + \tau(\gamma - \tfrac{1}{2})KD_{\bar{\tau}}]e_n + Ke_n \\ &= (M + \beta\tau^2 K)D_{\tau\bar{\tau}}u(\tau n) \\ &\quad + [\{\gamma CD_\tau + (1 - \gamma)CD_{\bar{\tau}}\} + \tau(\gamma - \tfrac{1}{2})KD_{\bar{\tau}}]u(\tau n) + Ku(\tau n) \\ &\quad - \{I + \tau(\gamma - \tfrac{1}{2})D_{\bar{\tau}} + \beta\tau^2 D_{\tau\bar{\tau}}\}f(\tau n). \end{aligned}$$

Using the expressions

$$\begin{aligned} D_\tau u(\tau n) &= \{u(\tau(n+1)) - u(\tau n)\}/\tau, \\ D_{\bar{\tau}} f(\tau n) &= \{f(\tau n) - f(\tau(n-1))\}/\tau, \\ D_{\tau\bar{\tau}} u(\tau n) &= \{u(\tau(n+1)) - 2u(\tau n) + u(\tau(n-1))\}/\tau^2, \text{ etc.,} \end{aligned}$$

we rewrite the right hand side of the above formula. Applying Taylor's theorem to $u(\tau(n+1))$, $f(\tau(n-1))$, etc. at $t = \tau n$, we have

$$\begin{aligned} p_n &= M \frac{d^2}{dt^2}u(\tau n) + C \frac{d}{dt}u(\tau n) + Ku(\tau n) - f(\tau n) \\ &\quad + \tau(\gamma - \tfrac{1}{2})(C \frac{d^2}{dt^2}u(\tau n) + K \frac{d}{dt}u(\tau n) - \frac{d}{dt}f(\tau n)) + O(\tau^2). \end{aligned}$$

Using the equalities:

$$M \frac{d^2}{dt^2}u(\tau n) + C \frac{d}{dt}u(\tau n) + Ku(\tau n) - f(\tau n) = 0$$

and

$$C \frac{d^2}{dt^2}u(\tau n) + K \frac{d}{dt}u(\tau n) - \frac{d}{dt}f(\tau n) = -M \frac{d^3}{dt^3}u(\tau n),$$

we obtain (31). \square

Proof of Theorem 7.1 (continued). Using Lemma 7.2, 7.3 and the stability theorem we can obtain the estimate of $\|e_n\|$. To apply Theorem 5.1 to (30) we consider a modification of (21). If we look the proof of Theorem 4.1 again, we can replace $(4\beta + 2\gamma) \sup_{0 \leq t \leq T} \|f(t)\|^2$ with $\sup_{1 \leq n \leq N-1} \|p_n\|^2$. Then we have in this case

$$C_0 = (1 - \tfrac{1}{2}\delta\tau_0)^{-1} \{w_0 + \frac{T}{\delta^2} \sup_{1 \leq n \leq N-1} \|p_n\|^2\} \exp(\delta(1 - \tfrac{1}{2}\delta\tau_0)^{-1}T).$$

Hence we have from (23) or (25)

$$\|e_n\| \leq C_1 \sqrt{C_0} + \|e_0\| = C_1 \sqrt{C_0},$$

where C_1 is independent of u_0 , v_0 and p_n . By Lemma 7.2 and (22), where u_0 is replaced by e_0 , we have

$$\begin{aligned} w_0 &= \|M^{1/2} D_\tau e_0\|^2 + \tau^2 \left\{ \beta - \frac{1}{2} \left(\gamma - \frac{1}{2} \right) \right\} \|K^{1/2} D_\tau e_0\|^2 \\ &\quad + \tau (K D_\tau e_0, e_0) + \|K^{1/2} e_0\|^2 + \tau \left(\gamma - \frac{1}{2} \right) \|C^{1/2} D_\tau e_0\|^2 \\ &= \|M^{1/2} \frac{1}{\tau} e_1\|^2 + \tau^2 \left\{ \beta - \frac{1}{2} \left(\gamma - \frac{1}{2} \right) \right\} \|K^{1/2} \frac{1}{\tau} e_1\|^2 \\ &\quad + \tau \left(\gamma - \frac{1}{2} \right) \|C^{1/2} \frac{1}{\tau} e_1\|^2 \\ &= O(\tau^4). \end{aligned}$$

From this we obtain with another constant C_2

$$C_0 \leq C_2 \{ O(\tau^4) + \sup_{1 \leq n \leq N-1} \|p_n\|^2 \}.$$

On the other hand, from Lemma 7.3, we have

$$\begin{cases} \sup_{1 \leq n \leq N-1} \|p_n\|^2 = O(\tau^4) & \text{for } \gamma = \frac{1}{2}, \\ \sup_{1 \leq n \leq N-1} \|p_n\|^2 = O(\tau^2) & \text{for } \gamma > \frac{1}{2}. \end{cases}$$

Thus we obtain the results. \square

REFERENCES

- [1] F. Chiba, and T. Kako., *On the stability of Newmark's β method*, RIMS Kôkyûroku 1040, Research Institute of Mathematical Sciences, Kyoto University, 1998, pp. 39–44.
- [2] F. Chiba, and T. Kako., *On the stability and convergence of Newmark's β method*, The Institute of Statistical Mathematics Cooperative Report 110 Proceedings of 1997-Workshop on MHD Computations —Numerical methods and optimization techniques in controlled thermonuclear fusion research—, 1998, pp. 196–202.
- [3] F. Chiba, and T. Kako., *Stability and error analyses by energy estimate for Newmark's method*, NIFS-PROC-40. Proceeding of 1998-Workshop on MHD Computations “Study on numerical methods related to plasma confinement”, National Institute for Fusion Science, 1999, pp. 82–91.
- [4] H. Fujii., *Finite-Element Galerkin Method for Mixed Initial-Boundary Value Problems in Elasticity Theory*, Center for Numerical Analysis, The University of Texas at Austin, October 1971.
- [5] H. Fujii., *A Note on Finite Element Approximation of Evolution Equations*, RIMS Kôkyûroku 202, Research Institute of Mathematical Sciences, Kyoto University, 1974, pp. 96–117.
- [6] J. W. Helton, and R. L. Miller., *NCAIgebra*, Department of Mathematics, University of California San Diego, 1994.
- [7] T. Kako., *Spectral and numerical analysis of resistive linearized magnetohydrodynamic operators*, Series on Applied Mathematics Vol.5, Proceedings of the First China-Japan Seminar on Numerical Mathematics, Z.-C. Shi and T. Ushijima eds., Kinokuniya, 1993, pp. 60–66.
- [8] M. Matsuki, and T. Ushijima., *Error estimation of Newmark method for conservative second order linear evolution*, Proc. Japan Acad., Vol. 69, Ser A (1993), pp. 219–223.
- [9] N. M. Newmark., *A method of computation for structural dynamics*, Proceedings of the American Society of Civil Engineers, Journal of the Engineering Mechanics Division, Vol.85, No. EM 3 (1959), pp. 67–94.
- [10] P. A. Raviart, and J. M. Thomas., *Introduction à l'Analyse Numérique des Equations aux Dérivées Partielles*, Masson, Paris, 1983.
- [11] R. E. Showalter., *Mathematical Surveys and Monographs Vol. 49 Monotone Operators in Banach Space and Nonlinear Partial Differential Equations*, AMS, 1997.
- [12] S. Wolfram., *The Mathematica Book, Third Edition*, Addison Wesley, 1998.
- [13] W. L. Wood., *A further look at Newmark, Houbolt, etc., time-stepping formulate*, International Journal for Numerical Methods in Engineering, Vol. 20 (1984), pp. 1009–1017.

Numerical Conformal Mapping by the Charge Simulation Method *

Kaname AMANO, Dai OKANO and Hidenori OGATA

Department of Computer Science, Faculty of Engineering, Ehime University

Abstract

We present a method of numerical conformal mapping of a bounded Jordan domain onto the unit disk, which is a basic problem of conformal mapping. We reduce the mapping problem to a Dirichlet problem of the Laplace equation with a pair of conjugate harmonic functions and employ the charge simulation method, where the conjugate harmonic functions are approximated by a linear combination of complex logarithmic potentials. We give some schemes of approximating mapping function which is continuous and analytic in the problem domain using the principal value of logarithmic function in computation. Numerical examples show that high accuracy is obtained if the problem domain has no reentrant corners.

Keywords: numerical conformal mapping, Riemann's mapping theorem, charge simulation method, continuity, analyticity

1 Introduction

Conformal mappings are familiar in science and engineering. However exact mapping functions are not known except for some special domains. The numerical conformal mapping has been an attractive subject in scientific computation.

Symm [29, 30, 31] proposed an integral equation method of numerical conformal mappings of interior, exterior and doubly-connected Jordan domains onto the unit disk, its exterior and a circular annulus, respectively. He expressed a pair of conjugate harmonic functions by a complex single-layer logarithmic potential and reduced the mapping problem to the singular Fredholm integral equation of the first kind. The integral equation method was improved by Hayes, Kahaner and Kellner [16] and Hough and Papamichael [18, 19]. Amano [1, 2, 3, 6], with these points as background, proposed a charge simulation method of numerical conformal mappings of the interior, exterior and doubly-connected domains. He approximated the conjugate harmonic functions by a linear combination of complex logarithmic potentials and reduced the mapping problem directly to a system of simultaneous linear equations.

See Gaier [15], Henrici [17], Trefethen [32] and Kythe [25] for surveys of numerical conformal mappings.

We here present some schemes of approximating mapping function of the numerical conformal mapping of a bounded Jordan domain onto the unit disk. The approximate mapping function is continuous and ana-

lytic in the problem domain using the principal value of logarithmic function.

2 Charge Simulation Method

The charge simulation method is a solver for potential problems. We have two schemes, i.e., the conventional scheme [26, 28] and the invariant scheme [27].

Consider the two-dimensional Dirichlet problem of the Laplace equation

$$\Delta g(z) = 0 \text{ in } D, \quad (1)$$

$$g(z) = b(z) \text{ on } C, \quad (2)$$

where D is the problem domain with the boundary C and $b(z)$ is the boundary data. We abbreviate (x, y) as (z) for $z = x + iy$.

In the conventional scheme, the solution is approximated by a linear combination of logarithmic potentials

$$G(z) = \sum_{i=1}^N Q_i \log |z - \zeta_i|, \quad (3)$$

where the points $\zeta_1, \zeta_2, \dots, \zeta_N$, called *charge points*, are placed outside D . The unknown constants Q_1, Q_2, \dots, Q_N , called *charges*, are determined to satisfy the boundary condition (2) at the same number of points z_1, z_2, \dots, z_N , called *collocation points*, placed on C . That is to say, they are solutions of the simultaneous linear equations

$$\sum_{i=1}^N Q_i \log |z_j - \zeta_i| = b(z_j) \quad (j = 1, 2, \dots, N), \quad (4)$$

*Supported by the Grant-in-Aid for Scientific Research of the Ministry of Education, Science, Sports and Culture in Japan (09440081).

which are called *collocation condition*. This simple approximation can be highly accurate, but does not remain invariant with respect to trivial affine transformations [27].

In the invariant scheme, the solution is approximated by

$$G(z) = Q_0 + \sum_{i=1}^N Q_i \log |z - \zeta_i|, \quad (5)$$

and the constant term Q_0 and the charges Q_1, Q_2, \dots, Q_N are determined under the constraint $\sum_{i=1}^N Q_i = 0$. That is to say, they are solutions of the simultaneous linear equations

$$\sum_{i=1}^N Q_i \log |z_j - \zeta_i| = b(z_j) \quad (j = 1, 2, \dots, N), \quad (6)$$

$$\sum_{i=1}^N Q_i = 0. \quad (7)$$

It is called the *invariant scheme* and satisfies mathematically nice and physically natural properties.

The approximation $G(z)$ exactly satisfies the Laplace equation. If D is bounded, the maximum principle for harmonic functions tells us that the error takes its maximum value somewhere on C and is estimated as

$$\begin{aligned} |G(z) - g(z)| &\leq \max_{z \in C} |G(z) - b(z)| \\ &\simeq \max_{1 \leq j \leq N} |G(z_{j+1/2}) - b(z_{j+1/2})|, \end{aligned} \quad (8)$$

where $z_{j+1/2}$ is an intermediate point on C between the collocation points z_j and z_{j+1} . It is known that the error decays exponentially with respect to N if C is smooth and $b(z)$ is analytic [20, 21, 22, 23, 24].

We extend the charge simulation method to the complex function and, in application to the numerical conformal mapping, approximate a pair of conjugate harmonic functions by a linear combination of complex logarithmic potentials.

3 Problem and Theorem

We are concerned here with the basic problem of conformal mapping, i.e., the mapping of a domain D bounded by a closed Jordan curve C given in the z -plane onto the unit disk $|w| < 1$ in the w -plane.

Theorem 1 (Riemann) *The mapping function $w = f(z; z_0)$ is uniquely determined by the normalization conditions $f(z_0; z_0) = 0$ and $f'(z_0; z_0) > 0$, where z_0 is an arbitrary point in D and is called the normalization point.*

We take $z_0 = 0$ and abbreviate $f(z; 0)$ as $f(z)$, which does not lose generality. Then the normalization conditions are $f(0) = 0$ and $f'(0) > 0$.

Figure 1 shows the situation of the problem.

4 Numerical Method

4.1 Conventional Scheme

The mapping function is expressed as

$$f(z) = z \exp(g(z) + ih(z)), \quad (9)$$

where $g(z)$ and $h(z)$ are conjugate harmonic functions in D . They should satisfy the boundary condition $|f(z)| = 1$ ($z \in C$) and the normalization condition $f'(0) > 0$, i.e.,

$$g(z) = -\log |z| \quad (z \in C) \quad (10)$$

and

$$h(0) = 0, \quad (11)$$

respectively. From (9), the normalization condition $f(0) = 0$ is satisfied. Conversely, if (10) and (11) are satisfied, (9) is the mapping function of the problem. The uniqueness of the solution tells us that the problem is reduced to finding the conjugate harmonic functions $g(z)$ and $h(z)$ satisfying (10) and (11).

Amano [1, 6] applied the conventional scheme of the charge simulation method (3) to $g(z) + ih(z)$ and obtained the following scheme of the numerical conformal mapping.

Scheme 1 *The approximate mapping function is expressed as*

$$F(z) = z \exp(G(z) + iH(z)), \quad (12)$$

$$\begin{aligned} G(z) + iH(z) &= \sum_{i=1}^N Q_i \log(z - \zeta_i) + i\Theta_0 \\ &= \sum_{i=1}^N Q_i \left\{ \log |z - \zeta_i| + i \arg \left(1 - \frac{z}{\zeta_i} \right) \right\}, \end{aligned} \quad (13)$$

where Θ_0 is the constant of rotation determined by the normalization condition (11). The charges Q_1, Q_2, \dots, Q_N are the solutions of the N simultaneous linear equations

$$\sum_{i=1}^N Q_i \log |z_j - \zeta_i| = -\log |z_j| \quad (j = 1, 2, \dots, N). \quad (14)$$

4.2 New Continuous Schemes

The same mapping function is also expressed as

$$f(z) = \frac{z}{r_D} \exp(g(z) + ih(z)), \quad (15)$$

where r_D is a constant to be $f'(0) = 1/r_D > 0$, i.e., the mapping radius of D at $z = 0$ (strictly speaking, at the normalization point $z = z_0$). The boundary condition $|f(z)| = 1$ ($z \in C$) and the normalization condition $f'(0) = 1/r_D$ are

$$g(z) - \log r_D = -\log |z| \quad (z \in C) \quad (16)$$

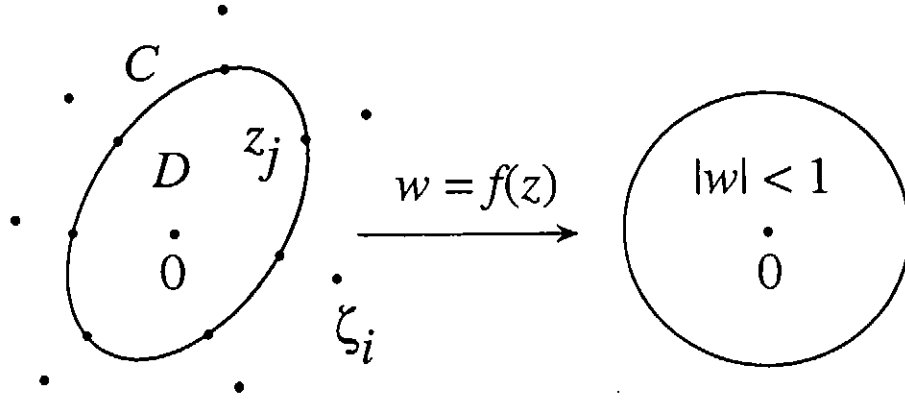


Figure 1: Conformal mapping by the charge simulation method. The normalization conditions are $f(0) = 0$ and $f'(0) > 0$, and ζ_i and z_j are the charge points and the collocation points, respectively.

and

$$g(0) + ih(0) = 0, \quad (17)$$

respectively. The problem is reduced to finding $g(z)$ and $h(z)$ satisfying (16) and (17).

We apply the invariant scheme of the charge simulation method (5) to $g(z) + ih(z)$ under the constraint

$$\sum_{i=1}^N Q_i = -1 \quad (18)$$

instead of (7) as proposed by Amano and Inoue [11], and have the approximate mapping function

$$F(z) = \frac{z}{R_D} \exp(G(z) + iH(z)), \quad (19)$$

$$G(z) + iH(z) = Q_0 + \sum_{i=1}^N Q_i \log(z - \zeta_i), \quad (20)$$

where Q_0 is a complex constant.

4.2.1 Starlike Case

Assume that C is starlike with respect to the origin. We rewrite (20) to

$$G(z) + iH(z) = Q_0 + \sum_{i=1}^N Q_i \left\{ \log \left(1 - \frac{z}{\zeta_i} \right) + \log(-\zeta_i) \right\} \quad (21)$$

for $H(z)$ to be continuous in D using the principal value of logarithmic function. Note that discontinuity of $\text{Arg}(1 - z/\zeta_i)$ appears on the radial line behind ζ_i . The normalization condition (17) requires

$$G(0) + iH(0) = Q_0 + \sum_{i=1}^N Q_i \log(-\zeta_i) = 0. \quad (22)$$

We eliminate Q_0 from (21) and (22), and obtain the following scheme of the numerical conformal mapping.

Scheme 2 If C is starlike with respect to the origin, the approximate mapping function is expressed

$$F(z) = \frac{z}{R_D} \exp(G(z) + iH(z)), \quad (23)$$

$$G(z) + iH(z) = \sum_{i=1}^N Q_i \log \left(1 - \frac{z}{\zeta_i} \right), \quad (24)$$

where the charges Q_1, Q_2, \dots, Q_N and the mapping radius r_D are the solutions of the $N + 1$ simultaneous linear equations

$$\sum_{i=1}^N Q_i \log \left| 1 - \frac{z_j}{\zeta_i} \right| - \log R_D = -\log |z_j| \quad (25)$$

$$(j = 1, 2, \dots, N),$$

$$\sum_{i=1}^N Q_i = -1. \quad (26)$$

If C is starlike with respect to a point z_s in D , which may be different from the the normalization point z_0 , we obtain the following scheme of the numerical conformal mapping in a similar way.

Scheme 3 If C is starlike with respect to z_s in D , the approximate mapping function is expressed as

$$F(z) = \frac{z}{R_D} \exp(G(z) + iH(z)), \quad (27)$$

$$G(z) + iH(z) = \sum_{i=1}^N Q_i \left\{ \log \left(1 - \frac{z - z_s}{\zeta_i - z_s} \right) - \log \left(1 - \frac{-z_s}{\zeta_i - z_s} \right) \right\}, \quad (28)$$

where the charges Q_1, Q_2, \dots, Q_N and the mapping radius r_D are the solutions of the $N + 1$ simultaneous linear equations

$$\sum_{i=1}^N Q_i \left\{ \log \left| 1 - \frac{z_j - z_s}{\zeta_i - z_s} \right| - \log \left| 1 - \frac{-z_s}{\zeta_i - z_s} \right| \right\} - \log R_D = -\log |z_j| \quad (j = 1, 2, \dots, N), \quad (29)$$

$$\sum_{i=1}^N Q_i = -1. \quad (30)$$

4.2.2 General Case

If C is not starlike, using the constraint (18), we rewrite (20) to

$$\begin{aligned} G(z) + iH(z) &= Q_0 + Q_1 \log(z - \zeta_1) \\ &+ \sum_{i=2}^N \left(\sum_{k=1}^i Q_k - \sum_{k=1}^{i-1} Q_k \right) \log(z - \zeta_i) \\ &= Q_0 + \sum_{i=1}^{N-1} \left(\sum_{k=1}^i Q_k \right) (\log(z - \zeta_i) - \log(z - \zeta_{i+1})) \\ &+ \left(\sum_{k=1}^N Q_k \right) \log(z - \zeta_N) \\ &= Q_0 + \sum_{i=1}^{N-1} \left(\sum_{k=1}^i Q_k \right) \log \left(\frac{z - \zeta_i}{z - \zeta_{i+1}} \right) \\ &- \log(z - \zeta_N) \end{aligned} \quad (31)$$

for $H(z)$ to be continuous in D using the principal value of logarithmic function. The discontinuity of $\text{Arg}((z - \zeta_i)/(z - \zeta_{i+1}))$ appears on the straight line connecting ζ_i and ζ_{i+1} . The discontinuity of $\log(z - \zeta_N)$ term is mentioned later. The normalization condition (17) requires

$$\begin{aligned} G(0) + iH(0) &= Q_0 + \sum_{i=1}^{N-1} \left(\sum_{k=1}^i Q_k \right) \log \left(\frac{\zeta_i}{\zeta_{i+1}} \right) - \log(-\zeta_N) \\ &= 0. \end{aligned} \quad (32)$$

We eliminate Q_0 from (31) and (32), and obtain the following scheme of the numerical conformal mapping.

Scheme 4 Whether C is starlike or not, the approximate mapping function is expressed as

$$F(z) = \frac{z}{R_D} \exp(G(z) + iH(z)), \quad (33)$$

$$\begin{aligned} G(z) + iH(z) &= \sum_{i=1}^{N-1} Q_i \left\{ \log \left(\frac{z - \zeta_i}{z - \zeta_{i+1}} \right) - \log \left(\frac{\zeta_i}{\zeta_{i+1}} \right) \right\} \\ &- \log \left(1 - \frac{z}{\zeta_N} \right), \end{aligned} \quad (34)$$

where the unknown constants, the partial sums of charges,

$$Q^i = \sum_{k=1}^i Q_k \quad (i = 1, 2, \dots, N-1) \quad (35)$$

and the mapping radius r_D are the solutions of the N simultaneous linear equations

$$\begin{aligned} \sum_{i=1}^{N-1} Q^i \left(\log \left| \frac{z_j - \zeta_i}{z_j - \zeta_{i+1}} \right| - \log \left| \frac{\zeta_i}{\zeta_{i+1}} \right| \right) - \log R_D \\ = \log \left| 1 - \frac{z_j}{\zeta_N} \right| - \log |z_j| \end{aligned} \quad (36)$$

$(j = 1, 2, \dots, N).$

The charge point ζ_N should be placed for discontinuity of $\text{Arg}(1 - z/\zeta_N)$ not to intersect D also in this scheme.

5 Some Remarks

1. We can obtain the mapping radius with Scheme 1 by

$$R_D = \exp \left(- \sum_{i=1}^N Q_i \log |-\zeta_i| \right). \quad (37)$$

However, it is advisable to use schemes with a constant term [11].

2. The maximum modulus theorem for analytic functions tells us that the error takes its maximum value somewhere on C and is estimated as

$$\begin{aligned} E_F(z) &= |F(z) - f(z)| \\ &\leq \max_{z \in C} |F(z) - f(z)| = E_F. \end{aligned} \quad (38)$$

The collocation condition means $|F(z_j)| = 1$ ($j = 1, 2, \dots, N$), so that

$$\begin{aligned} E_M &= \max_{z \in C} ||F(z)| - 1| \\ &\simeq \max_{1 \leq j \leq N} ||F(z_{j+1/2})| - 1|. \end{aligned} \quad (39)$$

Many examples imply

$$E_F \simeq E_M, \quad (40)$$

which is useful to estimate errors when analytical solutions are unknown.

3. A simple method of charge placement is

$$\begin{aligned} \zeta_j &= z_j + \frac{q}{2} |z_{j+1} - z_{j-1}| \\ &\cdot \exp \left\{ i \left(\arg(z_{j+1} - z_{j-1}) - \frac{\pi}{2} \right) \right\}, \end{aligned} \quad (41)$$

where $q > 0$ is a parameter called *assignment factor*. It gives numerical results of high accuracy in many problems [5].

6 Numerical Examples

We show numerical examples on typical problems.

1. an eccentric circle: $|z - x_0| < 1$ ($x_0 = 0.75$),

$$\begin{aligned} \text{(a)} \quad z_j &= x_0 + e^{i\theta_j}, \\ \text{(b)} \quad z_j &= r_j e^{i\theta_j}, \\ r_j &= x_0 \cos \theta_j + \sqrt{1 - x_0^2 \sin^2 \theta_j}, \\ \theta_j &= 2\pi(j-1)/N. \end{aligned}$$

2. an ellipse: $x^2/a^2 + y^2 < 1$ ($a = 4$),

$$\begin{aligned} \text{(a)} \quad z_j &= a \cos \theta_j + i \sin \theta_j, \\ \text{(b)} \quad z_j &= r_j e^{i\theta_j}, \\ r_j &= a / \sqrt{\cos^2 \theta_j + a^2 \sin^2 \theta_j}, \\ \theta_j &= 2\pi(j-1)/N. \end{aligned}$$

3. a Cassini's oval: $|z^2 - 1| < a^2$ ($a = 1.0219$),

$$\begin{aligned} z_j &= r_j e^{i\theta_j}, \\ r_j &= \sqrt{\cos 2\theta_j + \sqrt{\cos^2 2\theta_j + a^4 - 1}}, \\ \theta_j &= 2\pi(j-1)/N, \end{aligned}$$

4. a square: $\{|x| < 1\} \cap \{|y| < 1\}$,

$$|z_{j+1} - z_j| = 8/N, \quad z_1 = 1.$$

5. an L-shaped polygon: $\{|x-0.5| < 1\} \cap \{|y-0.5| < 1\} - \{(x \geq 0.5) \cap (y \geq 0.5)\}$,

$$|z_{j+1} - z_j| = 8/N, \quad z_1 = 0.5 + 0.5i.$$

We use (41) for charge placement, and compute

$$\begin{aligned} E_M &= \max_{1 \leq j \leq N} (|F(z_{j+1/2})| - 1), \\ E_F &= \max_{1 \leq j \leq N} \{|F(z_j) - f(z_j)|, \\ &\quad |F(z_{j+1/2}) - f(z_{j+1/2})|\} \end{aligned}$$

for error estimation.

Table 1 shows the numerical results by Scheme 1. Errors are estimated by E_F for the eccentric circle and the Cassini's oval since their analytical solutions are known, and by E_M for the others. The relation (40) holds in the former cases. They show that high accuracy is obtained if the problem domain has no reentrant corners. The error decays exponentially with respect to N in the problems 1–4. As q increases, i.e., the charges move away from the boundary, the error first increases and then decreases till the coefficient matrix of the linear equations becomes numerically singular.

We can obtain an approximate inverse mapping function $z = F^{-1}(w)$ by the same algorithm using the boundary correspondence between z_j and $F(z_j)$ established in advance [4]. Figure 2 is an example of the bidirectional numerical conformal mapping by the charge simulation method.

7 Concluding Remarks

The charge simulation method has first been applied to the numerical conformal mappings of interior, exterior and doubly-connected domains onto the unit disk, its exterior and a circular annulus, respectively [1, 2, 3, 6]; and then mappings of unbounded multiply-connected domains onto the parallel, circular and radial slit domains [7, 8, 9, 10, 12]. The latter three problems are important in the two-dimensional potential flow analysis [13].

The method presented here for the mapping of a bounded Jordan domain onto the unit disk has the following advantages.

- High accuracy by simple computation for domains with curved boundaries.
- Explicit forms of approximate mapping function continuous and analytic in the problem domain using the principal value of logarithmic function in computation.

These characteristics are important from applicational viewpoints. See Amano, Okano and Ogata [14] for details of the continuity problem of the approximate mapping function.

Numerical experiments by Schemes 2–4 should be made in future studies.

References

- [1] Amano, K.: Numerical conformal mapping based on the charge simulation method (in Japanese), Trans. Inform. Process. Soc. Japan, **28** (7), 697–704 (1987).
- [2] Amano, K.: Numerical conformal mapping of exterior domains based on the charge simulation method (in Japanese), Trans. Inform. Process. Soc. Japan, **29** (1), 62–72 (1988).
- [3] Amano, K.: Numerical conformal mapping of doubly-connected domains by the charge simulation method (in Japanese), Trans. Inform. Process. Soc. Japan, **29** (10), 914–924 (1988).
- [4] Amano, K.: A bidirectional method for numerical conformal mapping based on the charge simulation method (in Japanese), J. Inform. Process. Soc. Japan, **31** (5), 623–632 (1990).
- [5] Amano, K.: Error properties of numerical conformal mapping based on the charge simulation method (in Japanese), Trans. Inform. Process. Soc. Japan, **32** (1), 1–10 (1991).
- [6] Amano, K.: A charge simulation method for the numerical conformal mapping of interior, exterior and doubly-connected domains, J. Comput. Appl. Math., **53** (3), 353–370 (1994).

Table 1: Numerical results with $N = 64$ simulation charges.

1. an eccentric circle E_F	(a)	2.7E-05	2.6E-06	6.2E-06	7.5E-06
	(b)	4.4E-07	1.0E-10	1.3E-13	8.7E-12
q		2	4	6	8
2. an ellipse E_M	(a)	2.7E-05	1.2E-05	1.5E-05	1.5E-05
	(b)	4.5E-05	1.8E-06	1.6E-08	1.8E-09
q		2	4	6	8
3. a Cassini's oval E_F		1.3E-04	1.0E-05	1.0E-06	9.3E-05
q		1	2	3	4
4. a square E_M		1.6E-05	2.1E-07	2.4E-09	1.5E-10
q		3	6	9	12
5. an L-shaped polygon E_M		9.5E-02			
q		0.5			

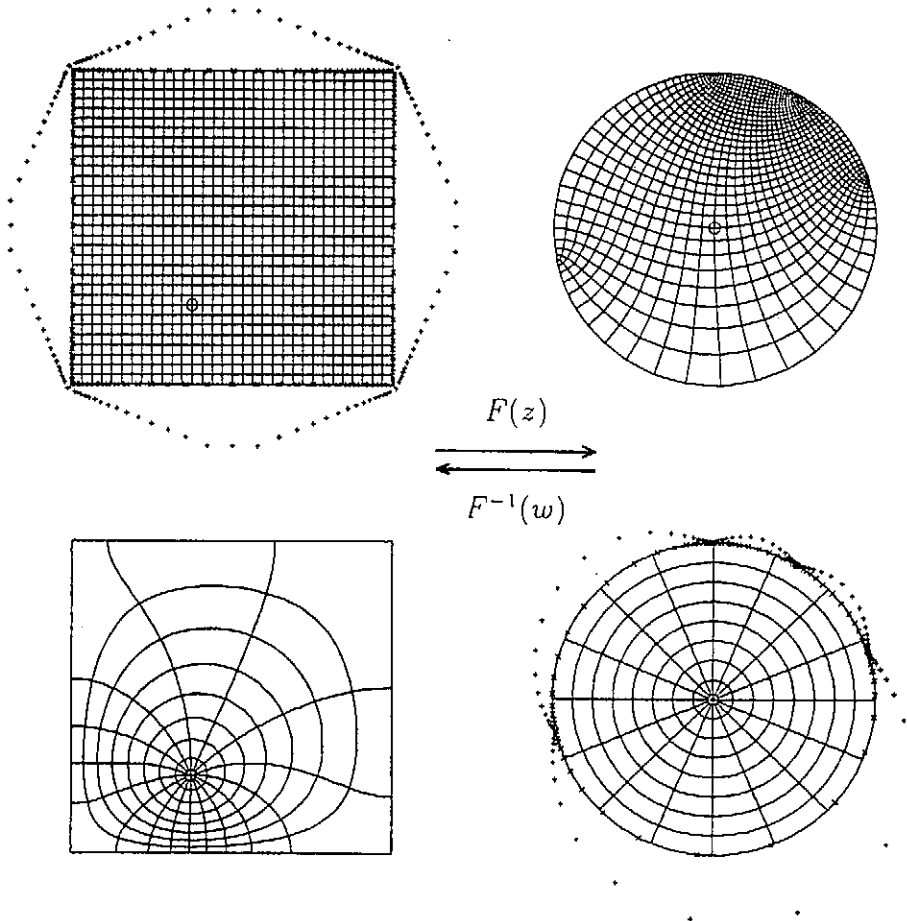


Figure 2: Bidirectional numerical conformal mapping between a square domain and the unit disk.

- [7] Amano, K.: Numerical conformal mapping onto the circular slit domains (in Japanese), Trans. Inform. Process. Soc. Japan, **36** (2), 219–225 (1995).
- [8] Amano, K.: Numerical conformal mapping onto the radial slit domains by the charge simulation method (in Japanese), Trans. Japan SIAM, **5** (3), 267–280 (1995).
- [9] Amano, K., Shibuya, Y., Tsuchie, M. and Sugihara, M.: Numerical conformal mapping onto the parallel slit domains by the charge simulation method (in Japanese), Trans. Japan SIAM, **6** (4), 353–371 (1996).
- [10] Amano, K.: A charge simulation method for numerical conformal mapping onto circular and radial slit domains, SIAM J. Sci. Comput., **19** (4), 1169–1187 (1998).
- [11] Amano, K. and Inoue, T.: Dilatation invariance of the numerical conformal mapping by the charge simulation method (in Japanese), Trans. Japan SIAM, **8** (1), 1–17 (1998).
- [12] Amano, K., Okano, D., Shimohira, H. and Sugihara, M.: Numerical conformal mapping onto parallel, circular and radial slit domains, Advances in Numerical Mathematics (Proceedings of The Fourth Japan-China Joint Seminar on Numerical Mathematics, Edited by Kawarada, H., Nakamura M. and Shi, Z.), Mathematical Sciences and Applications, **12**, 1–10 (1999).
- [13] Amano, K., Okano, D., Shimohira, H., Okamoto, T. and Igaue Y.: Potential flow analysis by the numerical conformal mapping, Information, **3** (1), 73–88 (2000, to appear).
- [14] Amano, K., Okano, D. and Ogata, H.: Numerical conformal mapping onto the unit disk with concentric circular slits by the charge simulation method (in Japanese), Trans. Inform. Process. Soc. Japan, **41** (4), (2000, to appear).
- [15] Gaier, D.: Konstruktive Methoden der konformen Abbildung, Springer-Verlag, Berlin (1964).
- [16] Hayes, J.K., Kahaner, D.K. and Kellner, R.G.: An improved method for numerical conformal mapping, Math. Comput, **26** (118), 327–334 (1972).
- [17] Henrici, P.: Applied and Computational Complex Analysis **3**, John Wiley & Sons, New York (1986).
- [18] Hough, D.M. and Papamichael, N.: The use of splines and singular functions in an integral equation method for conformal mapping, Numer. Math., **37**, 133–147 (1981).
- [19] Hough, D.M. and Papamichael, N.: An integral equation method for the numerical conformal mapping of interior, exterior and doubly-connected domains, Numer. Math, **41**, 287–307 (1983).
- [20] Katsurada, M.: A mathematical study of the charge simulation method II, J. Fac. Sci. Univ. Tokyo Sect. IA Math., **36** (1), 135–162 (1989).
- [21] Katsurada, M.: Asymptotic error analysis of the charge simulation method in a Jordan region with an analytic boundary, J. Fac. Sci. Univ. Tokyo Sect. IA Math., **37** (3), 635–657 (1990).
- [22] Katsurada, M.: Charge simulation method using exterior mapping functions, Japan J. Indust. Appl. Math., **11** (1), 47–61 (1994).
- [23] Katsurada, M. and Okamoto, H.: A mathematical study of the charge simulation method I, J. Fac. Sci. Univ. Tokyo Sect. IA Math., **35** (3), 507–518 (1988).
- [24] Katsurada, M. and Okamoto, H.: The collocation points of the fundamental solution method for the potential problem, Computers Math. Appl., **31** (1), 123–137 (1996).
- [25] Kythe, P.K.: Computational Conformal Mapping, Birkhäuser, Boston (1998).
- [26] Murashima, S.: Charge Simulation Method and Its Applications (in Japanese), Morikita, Tokyo (1983).
- [27] Murota, K.: On “invariance” of schemes in the fundamental solution method (in Japanese), Trans. Inform. Process. Soc. Japan, **34** (3), 533–535 (1993).
- [28] Okamoto, H. and Katsurada, M.: A rapid solver for the potential problems (in Japanese), Bull. Japan SIAM, **2** (3), 2–20 (1992).
- [29] Symm, G.T.: An integral equation method in conformal mapping, Numer. Math., **9**, 250–258 (1966).
- [30] Symm, G.T.: Numerical mapping of exterior domains, Numer. Math., **10**, 437–445 (1967).
- [31] Symm, G.T.: Conformal mapping of doubly-connected domains, Numer. Math., **13**, 448–457 (1969).
- [32] Trefethen, L.N. (ed.): Numerical Conformal Mapping, North-Holland, Amsterdam (1986).

Forced Magnetic Reconnection due to Boundary Perturbation

Akihiro ISHIZAWA and Shinji TOKUDA

*Department of Fusion Plasma Research, Naka Fusion Research Establishment,
Japan Atomic Energy Research Institute, Naka, Ibaraki, 311-0193, Japan
e-mail: ishizawa@fusion.naka.jaeri.go.jp*

Boundary layer analysis of forced magnetic reconnection due to an externally imposed boundary perturbation is revised. This revised analysis introduces correct asymptotic matching to take into account the effect of inertia in the inner layer precisely, and adopts a time dependent boundary perturbation which is suitable for this analysis. The revised analysis demonstrates a new reconnection process and clarifies the role of stability against the tearing modes in the process. The initial evolution of this new reconnection process is characterized by some significant features. One is that the reconnected flux increases on the same time scale as the boundary perturbation, which excludes the Sweet-Parker time scale obtained by use of the invalid constant- ψ asymptotic matching. Another is that an induced surface current on a resonant surface is in such a direction as to oppose the progress of the reconnection, because the equilibrium is stable against the tearing modes in the absence of the boundary perturbation.

Keywords: MHD, forced reconnection, boundary layer, asymptotic matching

I. INTRODUCTION

In plasma confinement, there are two kinds of magnetic reconnections: free reconnection and forced reconnection. Free reconnection is caused by spontaneous instabilities such as the tearing mode [1]. Even if a magnetic equilibrium is stable for resistive modes, an externally imposed boundary perturbation gives rise to magnetic reconnection called forced reconnection [2]. The energy source of the perturbation of the forced reconnection is the boundary perturbation, while that of the free reconnection is the equilibrium magnetic field.

The boundary perturbation is caused by resonant magnetic field errors in tokamak plasmas. The error field is the small deviation from axial symmetry of the magnetic field lines and it perturbs the plasma boundary to form the magnetic islands [2]. The boundary perturbation is also caused by, as a model, the toroidal coupling with a magnetic signal produced by another MHD event and it gives rise to the seed islands for the neo-classical tearing mode [3].

The response of the plasma to the applied boundary perturbation is described by a simple model [2]. In this model, the perturbation is caused by a deformation of the plasma boundary. This deformation yields two ideal MHD equilibria with different topologies of magnetic field lines. One magnetic equilibrium has the same topology as the original equilibrium, while it has a surface current on the resonant surface. The other has the different topology with magnetic islands on the resonant surface and no surface current. The former is called equilibrium (I), and the latter is called equilibrium (II) [2]. The existence of equilibrium (II) implies that the boundary perturbation can change the topology of the magnetic field lines and give rise to the forced reconnection to form the magnetic islands on the resonant surface.

The time evolution of the forced reconnection is represented by the superposition of these equilibria with an unknown coefficient, called the reconnected flux. The reconnected flux is calculated by use of the boundary layer theory as an initial value problem [2-7]. In the previous analysis, the time scale of the initial evolution of the forced reconnection is believed to be the Sweet-Parker time scale. We reveal that this time scale stems from the use of the matching condition which is valid only in the constant- ψ approximation; the effect of the inertia in the inner layer is neglected in this matching condition. Therefore the results in the previous works do not reflect the effect of the inertia correctly.

In this paper, we adopt the appropriate asymptotic matching and use the exact solution for the inner layer equation to take into account the effect of the inertia in the inner layer, precisely [12]. Moreover, we adopt a time dependent boundary perturbation to be suitable for elucidating the process of the forced reconnection. The corrected reconnection process exhibits the new time evolution of the magnetic islands and of the surface current induced on the resonant surface. Furthermore, the role of tearing stability in this reconnection process is clarified in terms of the tearing stability parameter.

The paper is organized as follows. We present the model and the initial value problem of the reconnected flux by use of the boundary layer theory in Sec. II. A new Laplace transformed reconnected flux based on the appropriate matching condition is presented in Sec. III. The initial evolution of the forced reconnection is calculated in Sec. IV. Finally Sec. V is devoted to the summary and discussion.

II. MODEL AND BOUNDARY LAYER THEORY

In order to investigate the process of forced reconnection due to a boundary perturbation, we consider the response of a plasma to the perturbation as an initial-value problem by adopting the boundary layer theory [1,2]. We impose a time varying boundary perturbation on a static equilibrium which has a current density gradient. By correctly taking account of the effect of the inertia in the inner layer, we deduce an asymptotic expansion of an inner-layer solution to obtain a matching condition which yields a significantly different reconnection process from the one in the previous works [2-5].

We consider the response of a slab of an incompressible plasma to an applied boundary perturbation. The magnetic field is represented by $\mathbf{B} = B_T \mathbf{e}_z + \mathbf{e}_z \times \nabla \psi$, where B_T stands for a uniform toroidal field and ψ is a magnetic potential. The plasma is supposed to be bounded by two parallel perfectly conducting walls. We assume that the xy -plane is normal to the toroidal field and the y -axis is parallel to the wall and the x -axis normal to it.

A. Outer region

In the outer region, following Hahm and Kulsrud [2], we introduce a quasi-static equilibrium as the response of a plasma to a boundary perturbation. We retain the effect of the current density gradient of the equilibrium to clarify the effect of stability of a tearing mode on the reconnection process. The outer region is governed by the ideal MHD equilibrium equation,

$$\nabla \times (\mathbf{j} \times \mathbf{B}) = 0, \quad (2.1)$$

where $\mathbf{j} = \nabla \times \mathbf{B}/4\pi$ is the current density.

In the absence of the boundary perturbation there is a static equilibrium which is represented by an even function, $\psi = \psi_0(x)$, subjected to the boundary conditions $\psi_0(\pm a) = \text{const.}$, where $x = \pm a$ expresses the boundaries of the plasma. This equilibrium is assumed to have the resonant surface at the center of the plasma, $\psi'_0(0) = 0$, and is supposed to be stable for the usual tearing mode.

Let us impose a boundary perturbation on the original static equilibrium. It is described in terms of a deformed plasma boundary as

$$\psi(x = \pm(a - \delta \cos ky)) = \text{const.},$$

where k and δ are the wave number and the amplitude of the boundary deformation, respectively. The boundary perturbation is assumed to be weak, $\delta \ll a$, such as the error fields in a tokamak. In this work, we consider the time varying boundary perturbation, $\delta = \delta(t/\tau_e)$, instead of the suddenly imposed boundary perturbation, because the time varying perturbation is suitable to clarify the reconnection process in the analysis which includes the effect of the inertia in the inner layer correctly as shown below. The time scale of the deformation τ_e is assumed to be much slower than the Alfvén time scale but much faster than the resistive time scale, $\tau_A \ll \tau_e \ll \tau_R$; τ_A and τ_R are defined below.

The magnetic potential perturbed by the boundary deformation is written as

$$\psi(x, t) = \psi_0(x) + \psi_1(x, t) \cos ky, \quad (2.2)$$

where $\psi_1(x, t)$ denotes the perturbed part due to the boundary perturbation. Since the perturbation is imposed on a time scale much slower than the Alfvén time scale, the plasma is quasi-static and obeys the ideal MHD equilibrium equation except in the vicinity of the resonant surface, where $x = 0$. The ideal MHD equilibrium equation, Eq. (2.1), for the perturbation $\psi_1(x, t)$ is reduced to

$$\psi'_0(x) \left\{ \frac{\partial^2 \psi_1(x, t)}{\partial^2 x} - k^2 \psi_1(x, t) \right\} - \psi_0'''(x) \psi_1(x, t) = 0, \quad (2.3)$$

with the boundary condition

$$\psi_1(\pm a, t) = \delta(t/\tau_e) \psi'_0(a) \equiv \psi_e(t/\tau_e).$$

The solution to this equation, $\psi_1(x, t)$, should be an even function of x , because Eq. (2.3) and the boundary condition are unchanged for $x \rightarrow -x$.

Here we consider the solution to Eq. (2.3) for Taylor's model, $\psi_0'''(x) = 0$ [2]. It has the form

$$\psi_1(x, t) = \psi_1(0, t) \left\{ \cosh kx - \frac{|\sinh kx|}{\tanh ka} \right\} + \psi_e(t/\tau_e) \frac{|\sinh kx|}{\sinh ka}, \quad (2.4)$$

where $\psi_1(0, t)$ is the magnetic potential on the resonant surface. Equilibrium (I) [2] which has the surface current and no magnetic islands corresponds to $\psi_1(0, t) = 0$ and $\psi_e(t) \neq 0$. On the other hand equilibrium (II) [2] corresponds to $\psi_1(0, t) = \psi'_0(a)\delta/\cosh ka$ and $\psi_e(t/\tau_e) = \psi'_0(a)\delta$, and it has the magnetic islands with width $2\sqrt{2a\psi_1(0)/\psi'_0(a)}$, and no surface current. Therefore the non-zero value of $\psi_1(0, t)$ implies the formation of magnetic islands by the reconnection. Moreover, $\psi_1(0, t)$ represents the amount of reconnected flux; hereafter we call it the reconnected flux.

In this paper, we consider the general form of the solution to Eq. (2.3) which includes the gradient of the current density of the static equilibrium to elucidate the effect of the stability of a tearing mode on the reconnection process. The solution is written as

$$\psi_1(x, t) = \psi_1(0, t)f(x) + \psi_e(t/\tau_e)g(x), \quad (2.5)$$

where $f(x)$ and $g(x)$ satisfy Eq. (2.3) respectively, and are subjected to the boundary conditions $f(0) = 1$, $f(\pm a) = 0$ and $g(0) = 0$, $g(\pm a) = 1$ [3, 6]. The first term is related to the tearing mode and corresponds to the first term in Eq. (2.4). Equilibrium (I) is described by $\psi_1(0, t) = 0$ and $\psi_e(t) \neq 0$. The surface current vanishes when $\psi_1(0, t)f'(0) + \psi_e(t)g'(0) = 0$, and thus it corresponds to equilibrium (II). Note that the first term and the second term in Eq. (2.5) correspond to the reconnected flux and the shielded flux for the cylindrical geometry [6, 7], respectively.

The quasi-static equilibrium, Eq. (2.5), is determined only by the reconnected flux $\psi_1(0, t)$, because $\psi_e(t/\tau_e)$ is assumed to be a given function. In order to obtain the reconnected flux we should investigate the dynamics in the vicinity of the resonant surface, i.e. the inner layer. In the analysis of the inner layer it is important to include not only the resistivity but also the inertia of the plasma correctly as shown below.

B. Inner layer

In the inner layer, we adopt the reduced MHD equations,

$$\rho \left(\frac{\partial}{\partial t} + \mathbf{v} \cdot \nabla \right) \nabla^2 \varphi = \mathbf{B} \cdot \nabla j_z, \quad (2.6)$$

$$\frac{\partial \psi}{\partial t} + \mathbf{B} \cdot \nabla \varphi = \frac{\eta}{4\pi} \nabla^2 \psi, \quad (2.7)$$

where $j_z = \nabla^2 \psi / 4\pi$ and $\mathbf{v} = \mathbf{e}_z \times \nabla \varphi$ indicate a z -component of the current density and a velocity of the plasma respectively, and φ is a static potential or a stream function, and the constants η and ρ are the magnetic diffusivity and the density of the plasma. Since the deformation of the boundary is very small, the perturbed quantities are small and the magnetic potential and the static potential can be written as Eq. (2.2) and $\varphi = \varphi_1(x, t) \sin ky$. Thus they obey the linearized reduced MHD equations. We apply the Laplace transform

$$\tilde{f}(x, s) = \int_0^\infty f(x, t) e^{-st} dt, \quad (2.8)$$

to these linearized reduced MHD equations. The initial conditions for the perturbations are $\psi_1(x, 0) = \varphi_1(x, 0) = 0$, because there is no deformation of the boundary at $t = 0$, $\psi_e(0) = 0$. By stretching the variables in the vicinity of the resonant surface according to

$$\hat{x} = \frac{x}{\epsilon a}, \quad \hat{s} = \tau_e s,$$

where

$$\epsilon = \left(\frac{\tau_A}{\tau_R k a} \right)^{1/3}, \quad \tau_e = \frac{\tau_A}{\epsilon k a},$$

the equations in the inner layer become

$$\hat{s} \frac{d^2 \tilde{\varphi}_{in}}{d\hat{x}^2} = -\hat{x} \frac{d^2 \tilde{\psi}_{in}}{d\hat{x}^2}, \quad (2.9)$$

$$\hat{s} \tilde{\psi}_{in} - \hat{x} \tilde{\varphi}_{in} = \frac{d^2 \tilde{\psi}_{in}}{d\hat{x}^2}, \quad (2.10)$$

where

$$\tilde{\psi}_{in}(\hat{x}, \hat{s}) = \frac{\tilde{\psi}_1(x, s)}{\psi_0''(0)a^2}, \quad \tilde{\varphi}_{in}(\hat{x}, \hat{s}) = \frac{\tilde{\varphi}_1(x, s)}{v_A a},$$

$\tau_A = a/v_A$, $\tau_R = 4\pi a^2/\eta$ and $v_A = \psi_0''(0)a/\sqrt{4\pi\rho}$. It follows from Eqs. (2.9) and (2.10) that the inner-layer equation is

$$\hat{s} \left(\frac{d^2\chi}{d\hat{x}^2} - \frac{2}{\hat{x}} \frac{d\chi}{d\hat{x}} \right) - (\hat{s}^2 + \hat{x}^2)\chi = -\chi_\infty \hat{x}^2, \quad (2.11)$$

where

$$\chi \equiv -\hat{s} \frac{d\tilde{\varphi}_{in}}{d\hat{x}} + \chi_\infty = \hat{x}^2 \frac{d}{d\hat{x}} \left(\frac{\tilde{\psi}_{in}}{\hat{x}} \right). \quad (2.12)$$

This inner-layer equation corresponds to the equation (III.9) in Ref. [8] by rewriting the variables $\hat{x} \rightarrow \hat{x}/\hat{s}^{1/4}$ and $\hat{s} \rightarrow \hat{\lambda}$.

In the forced reconnection process, it is important to take account of the effect of the inertia in the inner layer, because the plasma is forced to move by the externally imposed boundary perturbation. Therefore, we solve the inner-layer equation without any approximation to obtain the reconnected flux which includes the effect of the inertia correctly. The exact solution to the inner-layer equation, Eq. (2.11), is given by Ara *et al.* [8] as

$$\chi = \chi_\infty - \frac{\chi_\infty \hat{s}^{3/2}}{2^{5/2}} \int_0^1 y^{(i^{3/2}-5)/4} \sqrt{1+y} \exp\left(\frac{-\hat{x}^2}{2\hat{s}^{1/2}} \frac{1-y}{1+y}\right) dy. \quad (2.13)$$

Since the solution in the outer region has the symmetry $\psi_1(-x) = \psi_1(x)$, φ_{in} and ψ_{in} should be odd and even functions of \hat{x} , respectively. Integrating Eq. (2.12) to satisfy these parities gives the solutions for positive \hat{x} as

$$\begin{aligned} \tilde{\varphi}_{in}(\hat{x}, \hat{s}) &= \frac{-1}{\hat{s}} \int_0^{\hat{x}} (\chi - \chi_\infty) d\hat{x}, \\ \tilde{\psi}_{in}(\hat{x}, \hat{s}) &= -\chi + \hat{x} \int_0^{\hat{x}} \frac{1}{\hat{x}} \frac{d\chi}{d\hat{x}} d\hat{x} \\ &= -\chi_\infty + \chi_\infty \frac{\hat{s}^{3/2}}{2^{5/2}} \int_0^1 y^{(i^{3/2}-5)/4} \sqrt{1+y} \exp\left(\frac{-\hat{x}^2}{2\hat{s}^{1/2}} \frac{1-y}{1+y}\right) dy \\ &\quad + \chi_\infty \hat{x} \frac{\sqrt{\pi} \hat{s}^{5/4}}{8} \int_0^1 y^{(i^{3/2}-5)/4} \sqrt{1-y} \operatorname{erf}\left(\frac{\hat{x}}{\sqrt{2}\hat{s}^{1/4}} \frac{\sqrt{1-y}}{\sqrt{1+y}}\right) dy, \end{aligned} \quad (2.14)$$

where $\operatorname{erf}(x)$ indicates the Error function and the normalization factor χ_∞ is related to the magnetic potential at the origin of the stretched coordinate, $\tilde{\psi}_{in}(0, \hat{s})$, as

$$\chi_\infty = \frac{\tilde{\psi}_{in}(0, \hat{s})}{\frac{i^{3/2}}{\hat{s}^{3/2}-1} F(1, -1/2, \hat{s}^{3/2}/4 + 3/4, 1/2) - 1}, \quad (2.15)$$

where F is Gauss's Hypergeometric function [9].

C. Outer and inner expansions

We have obtained the solutions in the outer region and inner layer, Eqs. (2.5) and (2.14), respectively. Here we expand these solutions to obtain the matching condition. We derive an asymptotic expansion of the inner-layer solution without the constant- ψ approximation to reflect the effect of the inertia correctly.

We consider the time evolution of the quasi-static equilibrium as an initial-value problem, by applying the Laplace transform, Eq. (2.8), to the outer-solution, Eq. (2.5). Then we derive the expansion to the outer solution as

$$\tilde{\psi}_1(x, s) = \tilde{\psi}_1(0, s) + \tilde{\psi}_1'(0, s) \frac{\Delta'_{out}}{2} x + \cdots, \quad x \rightarrow +0, \quad (2.16)$$

where

$$\Delta'_{out}(s) = \frac{1}{\tilde{\psi}_1(0, s)} \left[\frac{d\tilde{\psi}_1(x, s)}{dx} \right]_{-0}^{+0} = \Delta'_0 + \Delta'_s \frac{\tilde{\psi}_e(s)}{\tilde{\psi}_1(0, s)}, \quad (2.17)$$

and where

$$\Delta'_0 = \left[\frac{df(x)}{dx} \right]_{-0}^{+0}, \quad \Delta'_s = \left[\frac{dg(x)}{dx} \right]_{-0}^{+0}.$$

The first term, Δ'_0 , is the tearing mode stability parameter in the absence of the boundary perturbation. Since the original static equilibrium is supposed to be stable, Δ'_0 is negative.

On the other hand the inner-layer solution, Eq. (2.14), can be expanded asymptotically as

$$\tilde{\psi}_{in}(\hat{x}, \hat{s}) \approx -\chi_\infty + \chi_\infty \frac{\pi \hat{s}^{5/4}}{8} \frac{\Gamma(\hat{s}^{3/2}/4 - 1/4)}{\Gamma(\hat{s}^{3/2}/4 + 5/4)} \hat{x} + \dots, \quad \hat{x} \rightarrow +\infty, \quad (2.18)$$

where Γ is the Gamma function.

We have obtained the expansion of the outer-solution which represents the quasi-static equilibrium due to the time dependent boundary perturbation, and we have obtained the expansion of the inner-layer solution which correctly includes the effect of the inertia in the inner layer. Asymptotic matching of these expansions yield a greatly different time evolution of the reconnected flux from the one in the previous works, as shown in the following section.

III. RECONNECTED FLUX BY EXACT ASYMPTOTIC MATCHING

Demanding that the solution to the inner-layer equation matches asymptotically with the solution in the outer region yields the exact matching condition. On the other hand the matching adopted in the previous works is available only in the constant- ψ approximation. In order to clarify this point, we rewrite the asymptotic expansion of $\tilde{\psi}_{in}$, Eq. (2.18), as

$$\tilde{\psi}_{in}(\hat{x}) \approx \psi_\infty \left\{ 1 + \frac{\Delta'_{in}}{2} \hat{x} + \dots \right\} \quad \hat{x} \rightarrow +\infty, \quad (3.1)$$

where

$$\psi_\infty \equiv -\chi_\infty, \quad (3.2)$$

$$\begin{aligned} \Delta'_{in}(s) &\equiv \frac{1}{\varepsilon a \psi_\infty} \left[\frac{d\tilde{\psi}_{in}}{d\hat{x}} \right]_{-\infty}^{\infty} \\ &= \frac{1}{\varepsilon a \psi_\infty} \int_{-\infty}^{\infty} \frac{1}{\hat{x}} \frac{d\chi}{d\hat{x}} d\hat{x} = \frac{-\pi \hat{s}^{5/4}}{8\varepsilon a} \frac{\Gamma(\hat{s}^{3/2}/4 - 1/4)}{\Gamma(\hat{s}^{3/2}/4 + 5/4)}. \end{aligned} \quad (3.3)$$

In the previous analysis [2-5], $[d\tilde{\psi}_{in}/d\hat{x}]_{-\infty}^{+\infty}$ is divided by $\tilde{\psi}_{in}(0, \hat{s})$ instead of ψ_∞ in Eq. (3.3). That is valid only in the constant- ψ approximation realized by neglecting the effect of the inertia of the plasma in the inner layer, because the effect of the inertia makes $\tilde{\psi}_{in}(0)$ deviate from $\psi_\infty = -\chi_\infty$ as shown in Eq. (2.15). Therefore the matching condition derived by the expansion, Eq. (3.1), reflects the effect of the inertia in the inner layer correctly.

Asymptotic matching of Eqs. (2.16) and (3.1) yields the matching conditions as

$$\tilde{\psi}_1(0, s) = \psi_0''(0) a^2 \psi_\infty, \quad (3.4)$$

$$\Delta'_{out}(s) = \Delta'_{in}(s). \quad (3.5)$$

Combining Eq. (2.17) and the matching condition, Eq. (3.5), we have the new Laplace-transformed reconnected flux

$$\tilde{\psi}_1(0, s) = \frac{\Delta'_s \tilde{\psi}_e(s)}{\Delta'_{in}(s) - \Delta'_0}. \quad (3.6)$$

Notice that in the absence of the boundary perturbation, $\psi_e = 0$, the initial-value problem reduces to the eigenvalue problem and Eq. (3.6) gives the dispersion relation for general resistive modes, $\Delta'_{in}(s) - \Delta'_0 = 0$ [8,10].

There are two reconnected fluxes to be precise. One is, as introduced above, the reconnected flux at $x = 0$, Eq. (3.6), and represents the temporal change of the quasi-static equilibrium, Eq. (2.5). The other is a reconnected flux at the origin of the stretched coordinate $\hat{x} = 0$, $\tilde{\psi}_{in}(0, \hat{s})$, and represents the reconnected flux in the inner layer; it is called the inner-layer reconnected flux in this paper. The inertia of the plasma affects the inner-layer reconnected flux, $\tilde{\psi}_{in}(0, \hat{s})$, to be different from the reconnected flux, $\tilde{\psi}_1(0, s)$. This difference between the inner-layer reconnected flux and the reconnected flux is given by the matching condition, Eq. (3.4), with Eqs. (2.15) and (3.2) as

$$\tilde{\psi}_{in}(0, \hat{s}) = \frac{1}{\psi''_0(0)a^2} \left\{ 1 - \frac{\hat{s}^{3/2}}{\hat{s}^{3/2} - 1} F(1, -1/2, \hat{s}^{3/2}/4 + 3/4, 1/2) \right\} \tilde{\psi}_1(0, s). \quad (3.7)$$

Notice that this difference corresponds to the one between the reconnection rate, R , and $q\hat{c}$ in Eq. (18) in Ref. [11].

The exact matching gives the Laplace-transformed reconnected fluxes, Eqs. (3.6) and (3.7). In the next section, these reconnected fluxes provide a new reconnection process.

IV. INITIAL EVOLUTION

The inverse of the Laplace transform of Eq. (3.6) yields a new time development of the reconnected flux. In this section we calculate an initial evolution of the reconnected flux by use of the theorem that the Taylor-series expansion of a function $f(t)$ at $t = 0$ corresponds to the asymptotic power expansion of the Laplace-transformed function $\tilde{f}(s)$ for $s \rightarrow \infty$ (Appendix A).

Before calculating the initial evolution, we discuss the time dependence of the boundary perturbation. The suddenly imposed boundary perturbation $\psi_e(t/\tau_e) = B_0\delta\theta(t)$, where θ is the Heaviside function, corresponds to the time dependent perturbation in the case $\tau_e \rightarrow 0$ in our analysis. However, in this case, the constraint on the time scale $\tau_A \ll \tau_e$ is not valid. Thus our analysis may not clarify the process of the forced reconnection by this perturbation (see Appendix B for the details). We consider, therefore, the time dependent boundary perturbation. In this paper, the function $\psi_e(t/\tau_e)$ is assumed to be even in t for simplicity, so it can be expanded at $t = 0$ as

$$\psi_e(t/\tau_e) = \frac{\psi''_e(0)}{2!} \frac{t^2}{\tau_e^2} + \frac{\psi_e^{(iv)}(0)}{4!} \frac{t^4}{\tau_e^4} + \frac{\psi_e^{(vi)}(0)}{6!} \frac{t^6}{\tau_e^6} + \dots, \quad (4.1)$$

because $\psi_e(0) = 0$.

Hence the Laplace-transformed reconnected flux, Eq. (3.6), can be expanded in s as

$$\begin{aligned} \tilde{\psi}_1(0, s) \approx & -\frac{\Delta'_0}{\Delta'_0} \left\{ \frac{\psi''_e(0)}{\tau_e^2 s^3} + \frac{\psi''_e(0)}{\tau_\alpha \tau_e^2 s^4} + \left(\frac{\psi''_e(0)}{\tau_e^2 \tau_\alpha^2} + \frac{\psi_e^{(iv)}(0)}{\tau_e^4} \right) \frac{1}{s^5} \right. \\ & + \left(\frac{\psi''_e(0)}{\tau_e^2 \tau_\alpha^2} + \frac{\psi_e^{(iv)}(0)}{\tau_e^4} \right) \frac{1}{\tau_\alpha s^6} \\ & \left. + \left(\frac{\psi_e^{(vi)}(0)}{\tau_e^6} + \frac{\psi''_e(0)}{\tau_e^2 \tau_\alpha^4} + \frac{\psi_e^{(iv)}(0)}{\tau_e^4 \tau_\alpha^2} + \frac{5\psi''_e(0)}{4\tau_e^2 \tau_\alpha \tau_c^3} \right) \frac{1}{s^7} + \dots \right\}, \end{aligned} \quad (4.2)$$

as $s \rightarrow \infty$, where

$$\tau_\alpha = \frac{-\Delta'_0}{\pi k} \tau_A, \quad \tau_c = \frac{\tau_A^{2/3} \tau_R^{1/3}}{(ka)^{2/3}}, \quad (4.3)$$

denote the ideal time scale and the typical time scale in the inner layer, respectively. Note that the tearing stability parameter, $\Delta'_0 < 0$, is included in the ideal time scale, τ_α . The inversion of the Laplace transform of Eq. (4.2) gives the Taylor-series expansion of the reconnected flux as

$$\psi_1(0, t) = -\frac{\Delta'_0}{\Delta'_0} \left\{ \frac{\psi''_e(0)}{\tau_e^2} \frac{t^2}{2!} + \frac{\psi''_e(0)}{\tau_\alpha \tau_e^2} \frac{t^3}{3!} + \left(\frac{\psi''_e(0)}{\tau_e^2 \tau_\alpha^2} + \frac{\psi_e^{(iv)}(0)}{\tau_e^4} \right) \frac{t^4}{4!} \right.$$

$$\begin{aligned}
& + \left(\frac{\psi_e''(0)}{\tau_e^2 \tau_\alpha^2} + \frac{\psi_e^{(iv)}(0)}{\tau_e^4} \right) \frac{t^5}{\tau_\alpha 5!} \\
& + \left(\frac{\psi_e^{(vi)}(0)}{\tau_e^6} + \frac{\psi_e''(0)}{\tau_e^2 \tau_\alpha^4} + \frac{\psi_e^{(iv)}(0)}{\tau_e^4 \tau_\alpha^2} + \frac{5\psi_e''(0)}{4\tau_e^2 \tau_\alpha \tau_c^3} \right) \frac{t^6}{6!} + \dots \Bigg\}. \quad (4.4)
\end{aligned}$$

The initial evolution of the reconnected flux is dominated by the first term, therefore its typical time scale is the same as the time scale of the boundary perturbation, τ_e , which can be faster than the Sweet-Parker time scale [2,4,5], $\tau_{sp} = \tau_A^{1/2} \tau_R^{1/2}$, and $\tau_{sp}^{2/(2+b)} \tau_e^{b/(2+b)}$ [3], where $b = 2$ in this paper, obtained by use of the constant- ψ matching (Appendix C). Hence we find that the appropriate matching leads to a different time scale of the initial evolution of the forced reconnection compared to previous works. Each term in the Taylor-series expansion, Eq. (4.4), contains t/τ_e , t/τ_A and $t/(\tau_A^{2/3} \tau_R^{1/3})$ and the resistive time scale in $\tau_c \propto \tau_A^{2/3} \tau_R^{1/3}$ appears at higher than 5th order. Notice that the stability parameter for the tearing mode, Δ'_0 , included in τ_α is important, because it makes τ_α different from the Alfvén time scale, τ_A , as shown in Eq. (4.3): for instance, large Δ'_0 makes the time scale τ_α large.

When the boundary perturbation is imposed, the surface current is induced at the resonant surface. The amount of the surface current is represented by the total current in the inner layer and is equivalent to the finite jump of the y -component of the magnetic field at the resonant surface, $x = 0$,

$$\Delta B_y(t) \equiv \left[\frac{\partial \psi_1(x, t)}{\partial x} \right]_{-0}^{+0} = \Delta'_0 \psi_1(0, t) + \Delta'_e \psi_e(t). \quad (4.5)$$

The total current increases with the increase of the amplitude of the boundary deformation, $\psi_e(t)$, while it decreases with the increase of the reconnected flux, $\psi_1(0, t)$, because $\Delta'_0 < 0$ for the stable equilibrium and $\Delta'_e > 0$. Substituting Eqs. (4.1) and (4.4) into Eq. (4.5) gives the initial evolution of the total current in the inner layer as

$$\begin{aligned}
\Delta B_y(t) = -\Delta'_e \Bigg\{ & \frac{\psi_e''(0)}{3!} \frac{t^3}{\tau_\alpha \tau_e^2} + \frac{\psi_e''(0)}{\tau_\alpha^2 \tau_e^2} \frac{t^4}{4!} + \left(\frac{\psi_e''(0)}{\tau_e^2 \tau_\alpha^2} + \frac{\psi_e^{(iv)}(0)}{\tau_e^4} \right) \frac{t^5}{\tau_\alpha 5!} \\
& + \left(\frac{\psi_e''(0)}{\tau_e^2 \tau_\alpha^4} + \frac{\psi_e^{(iv)}(0)}{\tau_e^4 \tau_\alpha^2} + \frac{5\psi_e''(0)}{4\tau_e^2 \tau_\alpha \tau_c^3} \right) \frac{t^6}{6!} + \dots \Bigg\}. \quad (4.6)
\end{aligned}$$

It grows with a negative sign and with the time scale $\tau_\alpha^{1/3} \tau_e^{2/3}$ at the initial evolution. In order to compare Eq. (4.6) with the result found in previous works [2,4,5], we consider the time evolution of the stability parameter $\Delta'(t) \equiv \Delta B_y / \psi_1(0, t)$. For the stability of usual tearing modes the stability parameter $\Delta'(t)$ often has the fixed value such as Δ'_0 , while $\Delta'(t)$ varies with time in the forced reconnection process. The stability parameter $\Delta'(t)$ is negative in the initial evolution and $\Delta'(t) = 0$ at $t = 0$, while it was claimed that $\Delta'(t) \rightarrow \infty$ with the positive sign at $t = 0$ in the previous works. The sign of $\Delta'(t)$ determines whether the surface current stabilizes or destabilizes the magnetic islands. The negative sign of $\Delta'(t)$ or $\Delta B_y(t)$ implies that the surface current is induced to hinder the growth of the magnetic islands. However the push caused by the imposed boundary deformation overcomes this hindrance to form the magnetic islands. We remark that the negative sign of $\Delta'(t)$ stems from the fact that the original static equilibrium is stable in the absence of the boundary perturbation, $\Delta'_0 < 0$, because $\tau_\alpha = -\Delta'_0 \tau_A / (\pi k) > 0$ leads to $\Delta B_y(t) < 0$ and $\Delta'(t) < 0$.

As stated in the previous section there are two reconnected fluxes. The reconnected flux derived above is defined at the origin of the outer variable $x = 0$. However the limit $x \rightarrow 0$ of the outer variable corresponds to the limit $\hat{x} \rightarrow \infty$ of the inner variable as shown in the asymptotic matching. The magnetic and dynamic structures in the inner layer make the reconnected flux at $x = 0$ deviate from the one at $\hat{x} = 0$. Therefore the exact reconnected flux in the inner layer should be defined at $\hat{x} = 0$. Although these reconnected fluxes have the same value in the constant- ψ approximation, $s \rightarrow 0$, the effect of the inertia forces these values to differ in the forced reconnection process, as shown in Eq. (3.7). The inner-layer reconnected flux is defined by the inverse of the Laplace transform of $\tilde{\psi}_{in}(0, s)$. The inverse Laplace transformation of the expansion of Eq. (3.7) for $|s| \rightarrow \infty$ with Eqs. (4.2), (C2) yields the Taylor-series expansion of the inner-layer reconnected flux:

$$\begin{aligned}
\psi_{in}(0, t) = \frac{\Delta'_e}{\Delta'_0} \Bigg\{ & \frac{2\psi_e''(0)}{\tau_e^2 \tau_c^3} \frac{t^5}{5!} + \frac{2\psi_e''(0)}{\tau_\alpha \tau_e^2 \tau_c^3} \frac{t^6}{6!} + \frac{t^7}{7! \tau_e^2 \tau_c^3} \left(\frac{\psi_e''(0)}{\tau_\alpha^2} + \frac{\psi_e^{(iv)}(0)}{\tau_e^2} \right) \\
& + \left(\frac{2\psi_e''(0)}{\tau_\alpha^3 \tau_e^2 \tau_c^3} + \frac{2\psi_e^{(iv)}(0)}{\tau_e^4 \tau_\alpha \tau_c^3} - \frac{4\psi_e''(0)}{\tau_e^2 \tau_c^6} \right) \frac{t^8}{8!} + \dots \Bigg\}. \quad (4.7)
\end{aligned}$$

Since the initial evolution is dominated by the first term, the time scale of the initial evolution is $\tau_e^{2/5} \tau_c^{3/5}$. It is close to the typical time scale of the inner layer, $\tau_c \propto \tau_A^{2/3} \tau_R^{1/3}$, compared with that of the reconnected flux, τ_e . Therefore the time scale of the inner-layer reconnected flux is also significantly different from the Sweet-Parker time scale and can be shorter than it.

We have shown that the correct asymptotic matching produces the new time scale at the initial evolution of the forced reconnection, that is affected by the time scale of the boundary perturbation and is different to the Sweet-Parker time scale: τ_e for the reconnected flux and $\tau_e^{2/5} \tau_c^{3/5}$ for the inner-layer reconnected flux. It also produces a negative increase in the surface current in the initial evolution. Moreover, it is clearly represented by Δ'_0 that the stability of the initial static equilibrium, which is supposed to be stable, affects the characteristic feature of the reconnection process such as the ideal time scale, τ_α , and the negative sign of the surface current.

V. SUMMARY AND DISCUSSION

We have corrected the asymptotic matching in the boundary layer analysis of forced reconnection due to the externally imposed boundary perturbation, because it is revealed that the asymptotic matching in the previous works [2-5] is not appropriate and is valid only in the constant- ψ approximation. The appropriate asymptotic matching yields the exact reconnection process which reflects the effect of the inertia of the plasma in the inner layer correctly, and leads to the two reconnected fluxes: the reconnected flux and the inner-layer reconnected flux. The former determines the time evolution of the quasi-static equilibrium of the outer region. The latter is newly introduced and represents the reconnection in the inner layer. The corrected analysis adopts the time dependent boundary perturbation to be suitable for clarifying the process of the reconnection. The time scale of this perturbation affects the initial growth of these reconnected fluxes.

It is shown that the characteristic time scale of the reconnection in the initial evolution is substantially different from the one in the previous works for island formation due to the error fields [2,4,5] and for seed island formation [3]. The reconnected flux initially increases on the same time scale as the boundary perturbation, τ_e . The time scale of the inner-layer reconnected flux is derived from not only the time scale of the boundary perturbation but also the typical time scale of the inner layer, $\tau_c \propto \tau_A^{2/3} \tau_R^{1/3}$. Therefore the initial evolution of the forced reconnection is strongly affected by the time scale of the boundary perturbation and can be faster than the evolution on the Sweet-Parker time scale. Moreover the role of tearing stability in the amplitude and in the time scale of the reconnected flux is elucidated in terms of the parameter Δ'_0 which deviates the ideal time scale τ_α from the Alfvén time scale, τ_A .

The correct matching also yields a new feature of the surface current induced on the resonant surface and the role of tearing stability in it. In the initial evolution, the surface current increases with $\Delta'(t) < 0$ to hinder the progress of the reconnection. In contrast, it was believed to be a typical feature of forced reconnection that $\Delta'(t) > 0$ and $\Delta'(t) \rightarrow \infty$ at $t = 0$, in the previous works [2,4,5]. The negative sign of the surface current, $\Delta'(t) < 0$, originates from the negative sign of the tearing stability parameter, $\Delta'_0 < 0$, therefore, the hindrance of the reconnection stems from the fact that the original static equilibrium is stable in the absence of the boundary perturbation.

These results imply that the previous estimation for the transition from the linear to a nonlinear stage of a forced reconnection [4] should be modified, because this estimation was carried out using an initial evolution of the reconnected flux which grows on the Sweet-Parker time scale. Such a modification of the transition is expected to have a significant effect on the time scale of the reconnection and on the decay of the surface current in the nonlinear stage of the island formation due to the error fields [4] and the seed island formation [3].

This modification is described by the subsequent evolution to the initial evolution. It will be obtained by calculating the inverse of Laplace transform of reconnected flux numerically in a following paper.

ACKNOWLEDGMENTS

The authors would like to thank Dr. A. Funahashi, Dr. M. Azumi and Dr. Y. Kishimoto at JAERI for their encouragement.

APPENDIX A: EXPANSION OF RECONNECTED FLUX

In this appendix, we expand the reconnected flux, Eq. (3.6), for $|s| \rightarrow \infty$. It follows from

$$\frac{\Gamma(\hat{s}^{3/2}/4 - 1/4)}{\Gamma(\hat{s}^{3/2}/4 + 5/4)} \approx \frac{8}{\hat{s}^{9/4}} \left\{ 1 + \frac{5}{4} \frac{1}{\hat{s}^3} + \dots \right\}, \quad |\hat{s}| \rightarrow \infty, \quad (\text{A1})$$

Eq. (3.3) and $\hat{s} = s\tau_A/(\varepsilon k a) = \tau_e s$ that the expansion

$$\frac{\Delta'_{in}(s)}{\Delta'_0} \approx \frac{1}{s\tau_\alpha} \left\{ 1 + \frac{5}{4} \frac{1}{(s\tau_e)^3} + \dots \right\}, \quad |s| \rightarrow \infty. \quad (\text{A2})$$

Substituting this into Eq. (3.6) yields

$$\tilde{\psi}_1(0, s) \approx \frac{-\Delta'_s}{\Delta'_0} \frac{\tilde{\psi}_e(s)}{1 - \frac{1}{s\tau_\alpha} \left\{ 1 + \frac{5}{4} \frac{1}{(s\tau_e)^3} + \dots \right\}}. \quad (\text{A3})$$

Using the Laplace transform of Eq. (4.1),

$$\tilde{\psi}_e(s) \approx \frac{\psi_e''(0)}{\tau_e^2 s^3} + \frac{\psi_e''''(0)}{\tau_e^4 s^5} + \frac{\psi_e''''''(0)}{\tau_e^6 s^7} + \dots, \quad (\text{A4})$$

and utilizing the relation

$$\frac{\sum_{k=0}^{\infty} b_k z^k}{\sum_{k=0}^{\infty} a_k z^k} = \frac{1}{a_0} \sum_{k=0}^{\infty} c_k z^k, \quad c_n + \frac{1}{a_0} \sum_{k=1}^n c_{n-k} a_k - b_n = 0, \quad (\text{A5})$$

Eq. (A3) is reduced to the expansion of the reconnected flux, Eq. (4.2), as $|s| \rightarrow \infty$.

APPENDIX B: SUDDENLY IMPOSED BOUNDARY PERTURBATION

Here we consider the initial evolution of the reconnected flux for the suddenly imposed boundary perturbation, $\psi_e(t/\tau_e) = \delta B_0 \theta(t)$. Substituting $\tilde{\psi}_e(s) = \delta B_0/s$ into Eq. (A3) and using Eq. (A5), we have the expansion of the Laplace-transformed reconnected flux:

$$\tilde{\psi}_1(0) \approx \frac{-\Delta'_s B_0 \delta}{\Delta'_0} \left\{ \frac{1}{s} + \frac{1}{s^2 \tau_\alpha} + \dots \right\}, \quad |s| \rightarrow \infty. \quad (\text{B1})$$

The inversion of the Laplace transform gives

$$\psi_1(0, t) = \frac{-\Delta'_s B_0 \delta}{\Delta'_0} \left\{ \theta(t) + \frac{t}{\tau_\alpha} + \dots \right\}. \quad (\text{B2})$$

This reconnected flux increases suddenly at $t = 0$ to $-\Delta'_s B_0 \delta / \Delta'_0$ which corresponds to equilibrium (II). It means a sudden increase in the width of the magnetic islands from equilibrium (I) to equilibrium (II). Therefore the reconnection process is not clarified by the suddenly imposed boundary perturbation.

APPENDIX C: CONSTANT- ψ MATCHING

Although the constant- ψ matching is valid only for $|s| \rightarrow 0$, here we adopt it and consider the initial evolution by calculating the expansion of the reconnected flux for $|s| \rightarrow \infty$. Then we have the same results as the initial evolution in Ref. [2]. For $|s| \rightarrow 0$ Eq. (2.15) reduces to $\chi_\infty = -\tilde{\psi}_{in}(0, \hat{s})$ to validate the replacement of ψ_∞ with $\tilde{\psi}_{in}(0)$ in Eq. (3.3). This replacement gives

$$\begin{aligned} \Delta'_{in}(s) &= \frac{1}{\varepsilon a \tilde{\psi}_{in}(0, \hat{s})} \left[\frac{d\tilde{\psi}_{in}}{d\hat{x}} \right]_{-\infty}^{\infty} \\ &= \frac{1}{\frac{\hat{s}^{3/2}}{\hat{s}^{3/2}-1} F(1, -1/2, \hat{s}^{3/2}/4 + 3/4, 1/2) - 1} \frac{\pi \hat{s}^{5/4} \Gamma(\hat{s}^{3/2}/4 - 1/4)}{8\varepsilon a \Gamma(\hat{s}^{3/2}/4 + 5/4)}. \end{aligned} \quad (\text{C1})$$

Substituting this Δ'_{in} into Eq. (3.5) yields the constant- ψ matching and the reconnected flux is given by Eq. (3.6). Using Eq. (A1),

$$F(1, -1/2, \hat{s}^{3/2}/4 + 3/4, 1/2) = \frac{\Gamma(\hat{s}^{3/2}/4 + 3/4)}{\Gamma(-1/2)} \sum_{n=0}^{\infty} \frac{\Gamma(-1/2 + n)}{\Gamma(\hat{s}^{3/2}/4 + 3/4 + n)} \frac{1}{2^n} \\ \approx 1 - \frac{1}{\hat{s}^{3/2}} + \frac{2}{\hat{s}^3} + \dots, \quad |\hat{s}| \rightarrow \infty, \quad (\text{C2})$$

and Eq. (A5) yields the expansion of the Laplace-transformed reconnected flux as

$$\tilde{\psi}_1(0, s) \approx \frac{2ka^2 \Delta'_s \tilde{\psi}_e(s)}{\pi} \left\{ \frac{1}{\tau_A \tau_R s^2} + \dots \right\}, \quad |s| \rightarrow \infty. \quad (\text{C3})$$

The inversion of the Laplace transform of this equation gives

$$\psi_1(0, t) = \frac{2B_0 \delta (ka)^2}{\pi \sinh ka} \left\{ \left(\frac{t}{\tau_A^{1/2} \tau_R^{1/2}} \right)^2 + \dots \right\}, \quad (\text{C4})$$

for Taylor's model [2] and the suddenly imposed boundary perturbation, $\Delta'_s = 2k/\sinh ka$ and $\tilde{\psi}_e(s) = B_0 \delta/s$. This is the same as the initial evolution given in the previous studies [2,4,5] and indicates the growth with the Sweet-Parker time scale. Therefore if we adopt the constant- ψ matching, we have the initial evolution with the Sweet-Parker time scale. However this result is wrong, because replacing ψ_∞ with $\psi_{in}(0)$ is forbidden for $|s| \rightarrow \infty$. This replacement is valid only for the limit $|s| \rightarrow 0$ as mentioned in Sec. III. For $|s| \rightarrow 0$, the constant- ψ approximation is valid and Eq. (C1) is reduced to

$$\Delta'_{in}(s) = \frac{-\pi \hat{s}^{5/4}}{8\epsilon a} \frac{\Gamma(-1/4)}{\Gamma(5/4)}.$$

Notice that replacing $B_0 \delta$ in Eq. (C4) to $\Psi_s(t/\tau_G)^\alpha$ gives the initial evolution which corresponds to the one by Hegna *et al.* [3].

- [1] H. P. Furth, J. Killeen and M. N. Rosenbluth, *Phys. Fluids* **6**, 459 (1963).
- [2] T. S. Hahm and R. M. Kulsrud, *Phys. Fluids* **28**, 2412 (1985).
- [3] C. C. Hegna, J. D. Callen and R. J. LaHaye, *Phys. Plasmas* **6**, 130 (1999).
- [4] X. Wang and A. Bhattacharjee, *Phys. Fluids B* **4**, 1795 (1992).
- [5] Z. W. Ma, X. Wang and A. Bhattacharjee, *Phys. Plasmas* **3**, 2427 (1996).
- [6] R. Fitzpatrick and T. C. Hender, *Phys. Fluids B* **3**, 644 (1991).
- [7] X. Wang and A. Bhattacharjee, *Phys. Plasmas* **4**, 748 (1997).
- [8] G. Ara, B. Basu, B. Coppi, G. Laval, M. N. Rosenbluth and B. V. Waddell, *Ann. Phys.* **112**, 443 (1978).
- [9] W. Magnus, F. Oberhettinger and R. P. Soni, *Formulas and Theorems for the Special Functions of Mathematical Physics* (Springer, New York, 1966) pp. 37-65.
- [10] A. Otto, *Phys. Fluids B* **3**, 1739 (1991).
- [11] G. T. Birk and A. Otto, *Phys. Fluids B* **3**, 1746 (1991).
- [12] A. Ishizawa and S. Tokuda, *Phys. Plasmas* **7**, 875 (2000).

Frequency Dependence of Magnetic Shielding Performance of HTS Plates in Mixed States

Atsushi Kamitani and Takafumi Yokono

Abstract—The magnetic shielding performance of the high-Tc superconducting (HTS) plate is investigated numerically. The behavior of the shielding current density in the HTS plate is expressed as the integral-differential equation with a normal component of the current vector potential as a dependent variable. The numerical code for solving the equation has been developed by using the combination of the Newton-Raphson method and the successive substitution method and, by use of the code, damping coefficients and shielding factors are evaluated for the various values of the frequency ω . The results of computations show that the HTS plate has a possibility of shielding the high-frequency magnetic field with $\omega \gtrsim 1$ kHz.

Index Terms—flux creep, flux flow, magnetic shielding, superconductor

I. INTRODUCTION

Recently, the high-Tc superconductor (HTS) has attracted great attention as a magnetic shielding material over the high-conductivity and the high-permeability materials. This is mainly because the superconducting state can be easily maintained by use of the mini-refrigerator or the liquid nitrogen. In addition, the HTS has a possibility of shielding the strong magnetic field below its upper critical one. For this reason, intensive studies on the magnetic shielding performance of the HTS have been performed experimentally [1]–[4] and numerically [5]–[7].

When the HTS is exposed to the ac magnetic field with an amplitude above the lower critical field, it becomes the mixed state in which the fluxoids penetrate into the HTS and induce the phenomena peculiar to the Type-II superconductor. In this case, the force balance between the pinning force and the Lorentz one is violated so that fluxoids move inside the HTS. In addition, fluxoids can move due to the thermal fluctuation even if the static magnetic field is applied. For this reason, both the flux flow and the flux creep should be taken into account for the evaluation of the shielding performance of the HTS against the ac magnetic field.

The purpose of the present study is to develop the numerical code for analyzing the time evolution of the

shielding current density by means of the flux flow creep model [7]–[10] and to investigate the magnetic shielding performance of the disk-shaped HTS plate by use of the code. In particular, we investigate the frequency dependence of the magnetic shielding performance.

II. MATHEMATICAL FORMULATION

The time evolution of the shielding current density is indispensable for the estimation of the magnetic shielding performance of HTS plates. Therefore, we explain the governing equation of the shielding current density in this section. First, let us assume that a disk-shaped HTS plate of radius R and of thickness D is placed in the ac homogeneous magnetic field (see Fig. 1). By taking the symmetry axis of the plate as z -axis and by choosing its center of gravity as the origin, we use the cylindrical coordinate system (r, θ, z) throughout the present paper. In terms of the coordinate system, the applied magnetic flux density B_0 is written as $B_0 = B_0^* \sin \omega t e_z$, where B_0^* and ω are constants, and e_z represents a unit vector in the z direction. As is well known, the critical current density j_c of the HTS has a strong anisotropy due to the crystallographic structure [11]. Its component along the c -axis is sufficiently small as compared with that parallel to the a - b plane so that the shielding current density can hardly flow along the c -axis. By taking this fact into account, we further assume that the HTS plate is composed of M pieces of thin layers perpendicular to the c -axis and that the spatial distribution of the shielding current density does not change through the thickness direction in each layer.

Under the above assumptions, the governing equation of the shielding current density can be written as follows [7]:

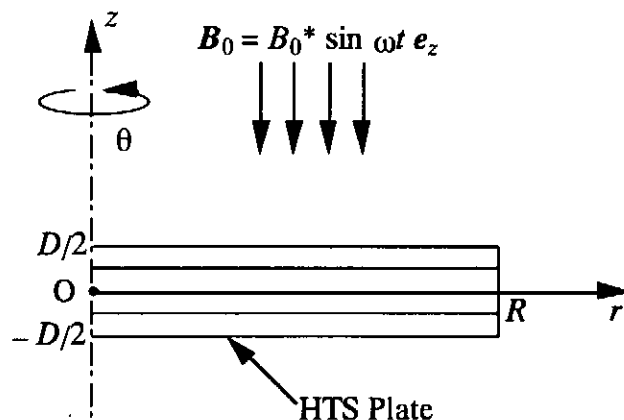


Fig. 1. Schematic view of the magnetic shielding measurements.

This work was supported in part by the Japanese Ministry of Education, Science, Sports and Culture under Grant-in-Aid for Scientific Research (C).

A. Kamitani is with the Department of Electrical and Information Engineering, Faculty of Engineering, Yamagata University, Johann 4-3-16, Yonezawa, Yamagata 992-8510, JAPAN (e-mail: kamitani@emperor.yz.yamagata-u.ac.jp).

T. Yokono is with the Institute of Information Sciences and Electronics, University of Tsukuba, Tennoudai 1-1-1, Tsukuba, Ibaraki 305-8573, JAPAN (e-mail: tyokono@is.tsukuba.ac.jp).

$$\begin{aligned} \mu_0 \frac{\partial}{\partial t} \sum_{q=1}^M \int_0^R S_q(r', t) Q_{pq}^*(r, r') r' dr' + \frac{\mu_0}{\epsilon} \frac{\partial S_p}{\partial t} \\ = - \frac{\partial}{\partial t} (B_0 \cdot e_z) - \frac{1}{r} \frac{\partial}{\partial r} (r E_{p\theta}) . \end{aligned} \quad (1)$$

Here μ_0 is a magnetic permeability of vacuum and 2ϵ denotes the thickness of the layer. The scalar function $S_p(r, t)$ is z -component of the current vector potential and is related to θ -component $j_{p\theta}$ of the shielding current density in the p th layer through the relation: $j_{p\theta} = -(1/\epsilon) \partial S_p / \partial r$. The first term in the left-hand side of (1) represents the electromagnetic coupling between the p th layer and the other ones, and the coupling function Q_{pq}^* is written as follows:

$$\begin{aligned} Q_{pq}^*(r, r') = - [4 \pi \epsilon^2 (r r')^{1/2}]^{-1} \\ \times \sum_{m=0}^{\infty} \sum_{n=0}^{\infty} (-1)^{m+n} k_{pq}^{m,n} K(k_{pq}^{m,n}) . \end{aligned} \quad (2)$$

Here, $K(x)$ denotes a complete elliptic integral of the first kind and its parameter is given by $k_{pq}^{m,n} = 4rr' [(r + r')^2 + \{[z_p + (-1)^m \epsilon] - [z_q + (-1)^n \epsilon]\}^2]^{-1/2}$. Here z_p denotes z -coordinate of the central plane of the p th layer. In addition, $E_{p\theta}$ represents θ -component of the electric field in the p th layer and is associated with $j_{p\theta}$ through the J - E constitutive relation: $E_{p\theta} = \text{sgn}(j_{p\theta}) E(|j_{p\theta}|, B)$. Here, B denotes a magnitude of the magnetic flux density and the function $E(j, B)$ represents the macroscopic characteristics of the superconductor.

Since the HTS plate in a mixed state is treated in the present study, both the flux creep and the flux flow should be included in the J - E constitutive relation. For this reason, we adopt the flux flow creep model [7]–[10] as the function $E(j, B)$. This model is written in the form,

$$\begin{aligned} E(j, B) = \\ \begin{cases} 2 \rho_c j_c(B) \sinh(\alpha j / j_c(B)) \exp(-\alpha) & ; j \leq j_c(B) \\ \rho_c j_c(B) [1 - \exp(-2\alpha)] + \rho_f (j - j_c(B)) & ; j > j_c(B) \end{cases} \end{aligned} \quad (3)$$

where ρ_c and ρ_f are the creep and the flow resistivity, respectively. The parameter α represents a strength of the flux pinning to the thermal fluctuation and is defined by $\alpha \equiv U_0 / (k_B T)$. Here, U_0 , k_B and T denote the pinning potential, the Boltzmann constant and the temperature, respectively. In addition, the B -dependence of the critical current density is included by assuming j_c as a function of the magnetic flux density. Although many kinds of models have been so far proposed as the function, we can use only the models that have enough accuracy for small B . This is because only a small amount of the magnetic flux density penetrates inside the HTS plate. For this reason, we adopt the following two models:

$$j_c(B) = j_{c0} , \quad (4)$$

$$j_c(B) = j_{c0} [B_j / (B_j + B)] , \quad (5)$$

where j_{c0} and B_j are constants. Equation (5) is known as the Kim model and it becomes the same as (4) in the limit

of $B_j \rightarrow \infty$. In order to distinguish (4) from (5), we call (4) as the constant- j_c model.

As the initial and the boundary conditions to (1), we impose $S_p(r, 0) = S_p(R, t) = 0$ as usual. By solving (1) together with the conditions, we can determine the time evolution of the shielding current density.

III. NUMERICAL METHOD

In this section, let us explain the numerical method for solving the initial-boundary-value problem of (1). By using the finite element method, (1) is discretized together with the boundary condition as follows:

$$W(S^{n+1} - S^n) = -b - \int_{t^n}^{t^{n+1}} f(S, J_c(S)) dt , \quad (6)$$

where the nodal vectors, S , b , f and J_c , correspond to the function S_p , the applied magnetic flux density B_0 , the electric field E_p and the critical current density $j_c(B)$, respectively, and the matrix W is calculated from the shape function and the coupling function Q_{pq}^* . The superscript n indicates the value at the n th time step $t^n (= n \Delta t)$. Note that the nodal vector J_c depends on S . The reason for this is explained as follows. As is apparent from the B -dependence of j_c , the critical current density depends on both the applied and the induced magnetic flux densities. In addition, the latter is calculated from the shielding current density $j_{p\theta}$ ($p=1, 2, \dots, M$) by using Biot-Savart's law. Therefore, the critical current density is a functional of S_1, S_2, \dots, S_M . This is why the nodal vector J_c becomes a function of S . Incidentally, J_c has no dependence on S for the case where the constant- j_c model is employed. By applying the θ -method [12] to the numerical integration of the second term in the right-hand side of (6), the nodal vector S^{n+1} becomes a solution of the nonlinear equation:

$$G(S, J_c(S)) \equiv WS + \theta \Delta t f(S, J_c(S)) - u = 0 , \quad (7)$$

where u is written as $u = WS^n - b - (1-\theta) \Delta t f(S^n, J_c(S^n))$ and θ is a constant such that $0 < \theta \leq 1$.

In general, either the successive substitution method or the Newton-Raphson method has been often employed to the numerical solutions of the nonlinear equation. Although the successive substitution method has been applied to the solution of (7), the scheme does not converge in most cases. It is only when both the time step and the underrelaxation factor are sufficiently small that we can obtain the converged solution. This fact implies that the successive substitution method is impracticable for the solution of (7). On the other hand, in order to apply the Newton-Raphson method to the solution of (7), the Jacobian matrix has to be calculated analytically. As mentioned above, J_c is a functional of S_1, S_2, \dots, S_M through Biot-Savart's law in which the induced magnetic flux density is determined as a definite integral of the shielding current density. This leads to the complicated dependence of J_c on S and, hence, it is very difficult to calculate the Jacobian matrix analytically. For these reasons, we apply the combination of the successive substitution method and the Newton-Raphson method to the solution of (7). In this method, the

solution of (7) is determined iteratively. In the k th cycle, the nonlinear equation,

$$F(S^*) \equiv G(S^*, J_c(S^{(k-1)})) = 0, \quad (8)$$

is first solved by use of the Newton-Raphson method to obtain S^* . Since the nodal vector J_c is a function of position only in (8), the Jacobian matrix of F with respect to S^* can be easily evaluated. Next, the approximate solution is corrected by

$$S^{(k)} = S^{(k-1)} + \gamma (S^* - S^{(k-1)}), \quad (9)$$

where the superscript (k) denotes an iteration number label and γ is an underrelaxation factor. The above iteration cycle is repeated until the series $\{S^{(k)}\}$ converges to a tolerable accuracy. The nodal vector S^{n+1} is obtained as a converged vector of $\{S^{(k)}\}$. For the case that the constant- j_c model is adopted as $j_c(B)$, the nodal vector J_c is no longer a function of S . Therefore, the Newton-Raphson method can be directly applied to the solution of (7) in this case.

By using the above method at each time step, we can solve the initial-boundary-value problem of (1) to determine the time evolution of the shielding current density. When the spatial distribution of the shielding current density is calculated, the induced magnetic flux density can be evaluated by use of Biot-Savart's law. As the measure of the shielding performance of HTS plates, we adopt two types of quantities: the shielding factor σ and the damping coefficient α . Both quantities are defined as follows: $\sigma = B_z/B_{0z}$ and $\alpha = 10 \log_{10}(\langle B^2 \rangle / \langle B_0^2 \rangle)$. Here B and B_0 are the total and the applied magnetic flux densities, respectively, and the subscript z denotes z -component of the vector. Also, the square bracket means the time average. The shielding factor σ indicates the time-dependent shielding performance, whereas the damping coefficient α represents the time-averaged one. In this sense, the desirable shielding performance should be characterized by both a weak time dependence of σ and a large absolute value of α .

IV. MAGNETIC SHIELDING ANALYSIS

The numerical code for calculating the time evolution of the shielding current density has been developed by using the method explained in the previous section. In this section, let us investigate the magnetic shielding performance of the disk-shaped HTS plate by use of the code. Throughout the present analysis, we fix the geometrical and the physical parameters as follows: $R = 20$ mm, $D = 2$ mm, $T = 77$ K, $j_{c0} = 1.5 \times 10^6$ A/m², $U_0 = 92$ meV, $\rho_f = 7.620 \times 10^{-10}$ Ω m and $\rho_c = 6.666 \times 10^{-11}$ Ω m.

Let us first investigate the influence of the B -dependence of j_c on the shielding performance of the HTS plate. In Fig. 2, we show the damping coefficients as functions of the parameter B_j in the Kim model. This figure indicates that the shielding performance of the HTS plate is not affected by the B -dependence of j_c . This is because the penetrating magnetic flux density is too small to change j_c drastically. From this result, we can conclude that the magnetic shielding analysis of the HTS plate can be performed by assuming the constant- j_c model. Hence, not

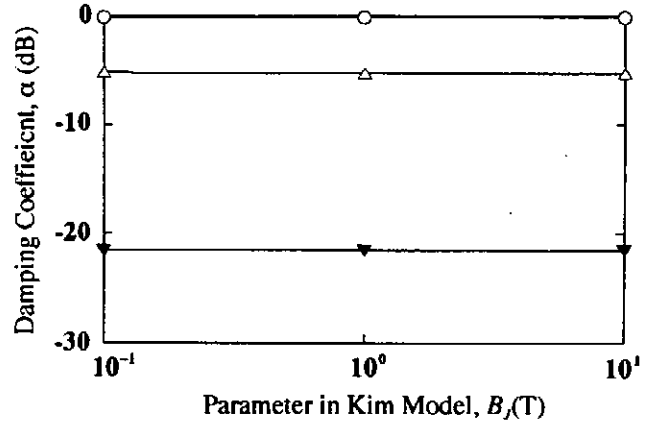
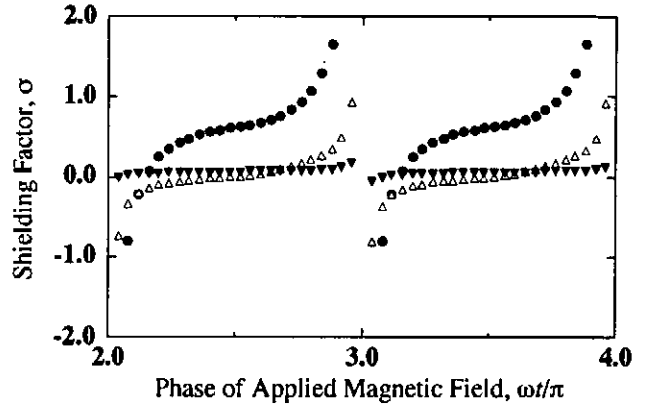
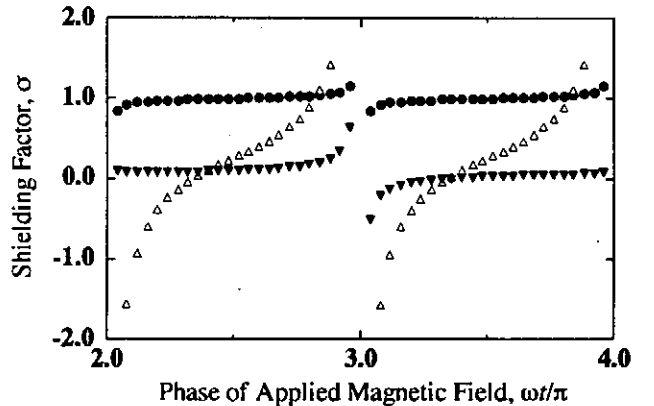


Fig. 2. Damping coefficients α as functions of the parameter B_j in the Kim model. Here, the values of α are calculated at $(z/R, r/R) = (-0.06, 0.0)$ and the amplitude B_0^* of the applied magnetic flux density is fixed as $B_0^* = 1$ T. The symbols, \circ , \triangle and ∇ , denote the values for $\omega = 10$ Hz, 100 Hz and 1 kHz, respectively.



(a)



(b)

Fig. 3. The time dependence of the shielding factor σ at $(z/R, r/R) = (-0.06, 0.0)$ in case of (a) $B_0^* = 1.0 \times 10^{-2}$ T and (b) $B_0^* = 1$ T. The symbols, \bullet , \triangle and ∇ , denote the values for $\omega = 1$ Hz, 100 Hz and 1 kHz, respectively.

the Kim model but the constant- j_c model is used in the following.

Next, we investigate the time dependence of the magnetic shielding performance. The shielding factors σ are evaluated on the symmetry axis and are depicted as a

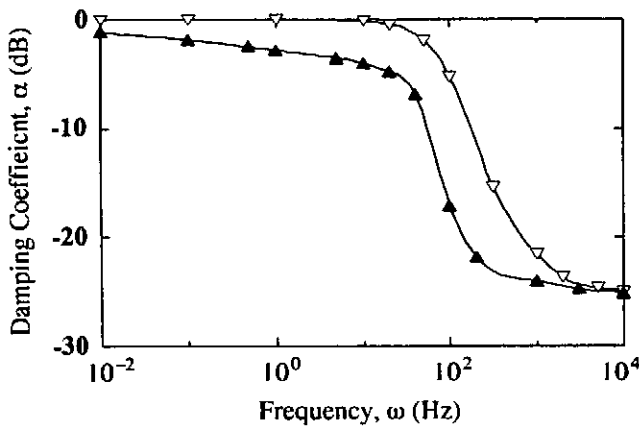


Fig. 4. Frequency dependence of damping coefficients α at $(z/R, r/R) = (-0.06, 0.0)$. \blacktriangle : $B_0^* = 1.0 \times 10^{-2}$ T and ∇ : $B_0^* = 1$ T.

function of time in Figs. 3(a) and 3(b). We see from these figures that the shielding factor σ increases monotonously from $\omega t = (n-1)\pi$ to $\omega t = n\pi$ (n : integer number). For the case with $B_0^* = 1.0 \times 10^{-2}$ T, the time dependence of σ becomes weak with an increasing frequency (see Fig. 3(a)). On the other hand, the slightly different tendency is observed for the case with $B_0^* = 1.0$ T. The shielding factor is almost always equal to unity in case of $\omega = 1$ Hz, and this means that the shielding performance is very poor in this case. As the frequency is increased above 1 Hz, the time dependence becomes remarkable. A further increase in the frequency will weaken the time dependence of the shielding factor until it is almost equal to zero (see Fig. 3(b)). From the above results, it might be said that the shielding factor has no time dependence in the high-frequency range with $\omega \gtrsim 1$ kHz and that its value is nearly equal to zero.

Finally, we investigate the frequency dependence of the magnetic shielding performance of the HTS plate. Damping coefficients α are calculated at $(z/R, r/R) = (-0.06, 0.0)$ for $B_0^* = 1.0 \times 10^{-2}$ T and 1 T, and are depicted as functions of ω in Fig. 4. The damping coefficient decreases slowly with an increasing frequency of the applied magnetic field in the low-frequency range below 10 Hz, whereas it diminishes remarkably with ω in the frequency range with $10 \text{ Hz} \lesssim \omega \lesssim 1 \text{ kHz}$. A further increase in ω will cause α to approach a constant value. In other words, the damping factor will almost approach to a saturated value in the frequency range with $\omega \gtrsim 1 \text{ kHz}$. From the above results, it might be said that the time-averaged shielding performance of the HTS plate is enhanced remarkably with an increase in the frequency.

V. CONCLUSIONS

We have developed the numerical code for analyzing the time evolution of the shielding current density on the basis of the flux flow creep model. In the code, either the Kim model or the constant- j_c model is used to the description of the B -dependence of the critical current density. By means the code, we have investigated the magnetic shielding performance of the disk-shaped HTS

plate. Conclusions obtained in the present study are summarized as follows.

- 1) The magnetic shielding performance of the HTS plate is not affected by the values of the parameter B_j in the Kim model. This result implies that the magnetic shielding analysis of the HTS plate can be performed by using the constant- j_c model.
- 2) The shielding factor has no time dependence in the high-frequency range with $\omega \gtrsim 1$ kHz and its value is nearly equal to zero. On the other hand, the damping coefficient decreases monotonously with the frequency of the applied magnetic field. In particular, it approaches to a constant value in the frequency range with $\omega \gtrsim 1$ kHz. From these results, we can conclude that the HTS plate has a desirable shielding ability in the frequency range with $\omega \gtrsim 1$ kHz even when it remains in a mixed state.

ACKNOWLEDGMENT

The authors wish to thank Prof. S. Ohshima, Yamagata University for valuable discussions from an experimental standpoint in the course of this work.

REFERENCES

- [1] S. Ohshima, and K. Okuyama, "Magnetic shielding effect of $\text{Ba}_2\text{YCu}_3\text{O}_{7-\delta}$ plates," *Jpn. J. Appl. Phys.*, vol. 29, pp. 2403-2406, November 1990.
- [2] A. Hussain, and M. Sayer, "Simple magnetic shielding experiment on high Tc superconducting bulk ceramics and thin films, metals and alloys," *Cryogenics*, vol. 32, pp. 64-68, January 1992.
- [3] S. Ohshima, H. Ohtsu, A. Kamitani, S. Kambe, and K. Okuyama, "Magnetic shielding effect of overlapped BPSCCO plates," *Proc. 5th Int. Symp. Superconductivity*, pp. 1273-1276, November 1992.
- [4] G. Mizuochi, S. Ohshima, K. Okuyama, A. Kamitani, and T. Mochizuki, "Magnetic shielding effect of BSCCO(2223) plate and composite plate," *Proc. 7th Int. Symp. Superconductivity*, pp. 1321-1324, November 1994.
- [5] A. Kamitani, M. Shibata, and S. Ohshima, "Magnetic shielding effect of multiple-layer thin superconducting plates by T-method," *IEEE Trans. Appl. Superconductivity*, vol. 7, pp. 2562-2565, 1997.
- [6] A. Kamitani, S. Ohshima, T. Yokono, and M. Natori, "Frequency dependence of magnetic shielding performance in HTS plates," *Proc. 10th Int. Symp. Superconductivity*, pp. 1365-1368, October 1998.
- [7] A. Kamitani, and S. Ohshima, "Magnetic shielding analysis of axisymmetric HTS plates in mixed state," *IEICE Trans. Electron.*, vol. E82-C, pp. 766-773, May 1999.
- [8] M. Uesaka, A. Suzuki, N. Tanaka, Y. Yoshida, and K. Miya, "A.c. magnetic properties of YBaCuO bulk superconductor in high Tc superconducting levitation," *Cryogenics*, vol. 35, pp. 243-247, 1995.
- [9] Y. Yoshida, M. Uesaka, and K. Miya, "Evaluation of dynamic magnetic force of high Tc superconductor with flux flow and creep," *Int. J. Appl. Electromagn. Mater.*, vol. 5, pp. 83-89, 1994.
- [10] Y. Yoshida, M. Uesaka, and K. Miya, "Magnetic field and force analysis of high Tc superconductor with flux flow and creep," *IEEE Trans. Magn.*, vol. 30, pp. 3503-3506, 1994.
- [11] M. Murakami, S. Gotoh, H. Fujimoto, K. Yamaguchi, N. Koshizuka, and S. Tanaka, "Flux pinning and critical currents in melt processed YBaCuO superconductors," *Supercond. Sci. Technol.*, vol. 4, pp. S43-S50, 1991.
- [12] K. W. Morton, and D. F. Mayers, *Numerical Solution of Partial Differential Equations*. Cambridge University Press, Cambridge, 1994.

On the Structure of Numerical Solutions of Flow Simulation by Implicit Scheme

Itaru Hataue

Department of Systems and Information, Kumamoto University

Kurokami 2-39-1, Kumamoto, Kumamoto 860-8555, Japan

Abstract

In the present paper, the structure of the asymptotic numerical solutions given from the implicit schemes. Analytical discussion and numerical tests on the fully implicit scheme of the Burgers' equation and its linearized form were performed. Furthermore, we tried to investigate the characteristics of ghost numerical solutions of incompressible fluid equations from the viewpoints of the effect of popular fourth order artificial viscosity terms. The calculation model adopted in the present paper was the flow around the circular cylinder and the Reynolds number was 2000. The non-dimensional governing the incompressible Navier-Stokes equations and the continuity equation were solved numerically by using the MAC(Maker-And-Cell) method and implicit temporal scheme. Unsteady dynamical structure was investigated in detail by applying the nonlinear dynamics approaches on the calculated time series data of drag coefficients. Ghost numerical solutions appear not only in the cases of explicit scheme cases but also appear in those of implicit cases. It was shown that the amplitude of fourth order artificial viscosity term and has a great influence on the structure of the asymptotic numerical solutions.

Keywords

Asymptotic Numerical Solution, Implicit scheme, Burgers' equation, Flow Simulation, Incompressible flow, Ghost solution

1 Intriduction

The development of high performance computing has made the numerical fluid dynamics calculations routine. Today, we can get the numerical turbulence easily as the result. However, complicated chaotic solutions, even when true solutions of the original differential equation approach limit cycles or fixed points, are often obtained as a consequence of the omission of the local discretization errors in the transfer from the continuous differential equations to their discretized counterparts. In particular, there is a possibility to get several types of asymptotic numerical solutions even when the same physical parameters such as the Reynolds number and the same conditions such as the boundary ones are used. Solutions which do not correspond to the true one are often called spurious solutions or ghost ones and they have been studied in detail by a lot of researchers.¹⁻⁹⁾ We also studied the characteristic behavior of the asymptotic numerical solutions of simple scalar nonlinear differential equations.⁸⁻⁹⁾ In those papers, we discussed the dependence of initial data and boundary conditions on the nonlinear instability and concluded that we may get ghost solutions which are never seen in the case of linear cases even if we adopt the more accurate scheme, e.g. high-order Runge-Kutta scheme due to many kinds of errors and the characteristics of schemes. Furthermore, I am sorry to say that this phenomenon also appears in the case of the system of fluid equations.¹⁰⁻¹¹⁾ In most cases, the approximate conditions of calculations are set to be physically reasonable. However even if we use the popular fourth order artificial viscosity terms and upwind schemes, the complicated flow structure appears in the cases of the low Reynolds numbers where the flows are expected to be laminar. The artificial viscosity terms which are added explicitly and implicitly in order to stabilize the system change the characteristics of numerical solutions. Needless to say, we can not perform calculations stably without these stabilizing terms in the cases of the high Reynolds number because the nonlinear instability grows and the calculations diverge. However the added terms bring other nonlinear instabilities and the qualitative structure of the asymptotic numerical solution changes. In other words, there is a possibility for us to get multiple stable and unstable asymptotic numerical solutions under the same physical conditions and parameters. To select correct solutions among these multiple ones depends on experimental and physical intuitions of researchers. Only one thing which has been clarified in a lot of kinds of approaches is that most of numerical and discretization errors induce the spurious nonlinear instability and the make complicated the system.

By the way, we studied the cases of explicit calculations of compressible flows in which the simultaneous equations does not need to be solved in our previous papers.¹⁰⁻¹¹⁾ When researchers in the field of computational fluid dynamics(CFD) solve the Navier-Stokes

equation numerically, they usually use implicit schemes owing to its high performance and efficiency in computations. Usefulness of implicit schemes may be originated from the unconditional stability in the linear case. However, is the high stability available also in the nonlinear case? Do not ghost solutions appear in the calculation in using very large values of Δt ? On the other hand, most of implicit schemes used in the field of CFD need the linearization. How about the effect of this linearization on the nonlinear structure of the steady state numerical solutions? In the case in which the nonlinear source terms are included in the PDE such as the reaction-diffusion equation, reaction-convection equation, reaction - convection - diffusion equation and so on, we can find quite important meanings in this linearization. However, literatures which refer to these problems in detail are few. Therefore, to analyze these problems makes a great contribution to CFD studies. In the present paper, we considered the initial boundary value problem of one-dimensional Burgers' equation and their backward Euler temporal finite difference approximations as a simple example and discussed the structure of the numerical solutions of fully implicit systems and their linearized ones. Next, we discuss the structure of numerical solutions of practical incompressible flows. One of the most popular method in the incompressible calculations is MAC(Maker-And-Cell) method¹²⁾ in which the Poisson equation for pressure has to be solved and it is necessary to solve the simultaneous equations. One of purposes in the present paper is to investigate the characteristics of ghost solutions from the viewpoints of the effect of popular fourth order artificial viscosity terms. Concretely, we compare the dependence on the amplitude of artificial viscosity term. In a lot of contributions in the field of computational fluid dynamics, computed results are discussed by using the flow visualization technique and calculating some statistical quantities and so on. Though these methods are useful to discuss the simultaneous and global structure of the computed flow fields, most of those methods are not so effective that we can not elucidate their clear unsteady characteristics in detail. In our previous papers, we applied the nonlinear dynamics approaches which were effective in analyses of the unsteady structure of numerical results of direct simulations of the practical fluid motions. Generally speaking, these analyses of the nonlinear structure are equivalent to studies of instability of dynamical system. In the present study, we adopted the flow around the circular cylinder as the simple model and discussed the difference of the unsteady structure by comparing the data reconstructed from the long period of time series of C_D (drag coefficient).

Analytical approaches on the one-dimensional Burgers' equation are discussed in Section 2. For the practical calculations for fluid motions, the numerical schemes used in the present paper are expressed briefly in Section 3. Other conditions of computations such as the grid systems, boundary conditions and so on are also described in this section. In

Section 4, the effect of artificial viscosity term are discussed in detail.

2 Analytical approach for Burgers' equation

we considered the initial boundary value problem of one-dimensional Burgers' equation(2.1) and its finite difference approximation as a simple example. Though there are infinite numbers of steady state solutions of one-dimensional Burgers' equation, only one trivial solution, $u(x)=0$, is allowed in the physical meaning.

$$\begin{cases} u_t + uu_x = \nu u_{xx}, & (0 < x < (n-1)\Delta x) \\ u(x, 0) = u^0(x), \\ u(0, t) = u((n-1)\Delta x, t) = 0. \end{cases} \quad (2.1)$$

Euler backward temporal difference scheme are applied to eq.(2.1). Derived multi-dimensional discrete dynamical system has different complex structure composed of various solutions which are not the solution which numerically diverges to infinity and no longer correspond to solution of original continuous DE. We discuss the characteristic features of two-dimensional(4 points) and three-dimensional(5 points) discrete dynamical system generated by the spatial central difference scheme, fully implicit form, eq.(2.2), and its linearized form, eq.(2.3).

$$\begin{cases} u_i^{(m+1)} = u_i^{(m)} + \Delta t \left\{ -u_i^{(m+1)} \frac{u_{i+1}^{(m+1)} - u_{i-1}^{(m+1)}}{2\Delta x} + \nu \frac{u_{i+1}^{(m+1)} - 2u_i^{(m+1)} + u_{i-1}^{(m+1)}}{(\Delta x)^2} \right\}, \\ u_i^{(0)} : \text{ (Initial data) }, \\ u_0^{(m)} = u_{n-1}^{(m)} = 0. \end{cases} \quad (0 < i < (n-1), m \geq 0) \quad (2.2)$$

$$\begin{cases} u_i^{(m+1)} = u_i^{(m)} + \Delta t \left\{ -u_i^{(m)} \frac{u_{i+1}^{(m+1)} - u_{i-1}^{(m+1)}}{2\Delta x} + \nu \frac{u_{i+1}^{(m+1)} - 2u_i^{(m+1)} + u_{i-1}^{(m+1)}}{(\Delta x)^2} \right\}, \\ u_i^{(0)} : \text{ (Initial data) }, \\ u_0^{(m)} = u_{n-1}^{(m)} = 0. \end{cases} \quad (0 < i < (n-1), m \geq 0) \quad (2.3)$$

In order to solve eq.(2.3), we must solve n -dimensional algebraic equation.

(a) Two-dimensional discrete system

Two-dimensional(4 points) discrete system by fully implicit scheme, eq.(2.4), has the two roots shown in eq.(2.5). Though one solution which has a negative sign before in

R.H.S. of eq.(2.5) corresponds to the true solution, another one corresponds to the ghost solution. The former converges on the equilibrium point-(0, 0), the latter converges on $(6\nu/\Delta x, -6\nu/\Delta x)$.

$$\begin{cases} \frac{x_1^{(m+1)} - x_1^{(m)}}{\Delta t} + x_1^{(m+1)} \frac{x_2^{(m+1)} - 0}{2\Delta x} = \nu \frac{x_2^{(m+1)} - 2x_1^{(m+1)} + 0}{(\Delta x)^2}, \\ \frac{x_2^{(m+1)} - x_2^{(m)}}{\Delta t} + x_2^{(m+1)} \frac{0 - x_1^{(m+1)}}{2\Delta x} = \nu \frac{0 - 2x_2^{(m+1)} + x_1^{(m+1)}}{(\Delta x)^2}, \end{cases} \quad (2.4)$$

and

$$x_1^{(m+1)} = \frac{-a \pm \sqrt{a^2 - 4b}}{2}, \quad x_2^{(m+1)} = z - x_1^{(m+1)}, \quad (2.5)$$

where

$$\begin{aligned} a &= -\frac{zc + 3d + 1}{c}, \quad b = \frac{x_1^{(m)} + zd}{c}, \quad c = \frac{\Delta t}{2\Delta x}, \\ d &= \nu \frac{\Delta t}{(\Delta x)^2}, \quad z = x_1^{(m+1)} + x_2^{(m+1)} = (1 - c)(x_1^{(m)} + x_2^{(m)}). \end{aligned}$$

In the case of fully implicit scheme, we can not determine which alternative solution in eq.(2.5) we should adopt. On the other hand, we can solve that problem by linearizing eq.(2.4), eq.(2.6).

$$\begin{cases} \frac{x_1^{(m+1)} - x_1^{(m)}}{\Delta t} + x_1^{(m)} \frac{x_2^{(m+1)} - 0}{2\Delta x} = \nu \frac{x_2^{(m+1)} - 2x_1^{(m+1)} + 0}{(\Delta x)^2}, \\ \frac{x_2^{(m+1)} - x_2^{(m)}}{\Delta t} + x_2^{(m)} \frac{0 - x_1^{(m+1)}}{2\Delta x} = \nu \frac{0 - 2x_2^{(m+1)} + x_1^{(m+1)}}{(\Delta x)^2}. \end{cases} \quad (2.6)$$

By the linear stability theory, eigenvalues of Jacobian matrix of the discrete map of eq.(2.6) are follows.

$$\begin{cases} \lambda_1 = \frac{(\Delta x)^2}{(\Delta x)^2 + 3\nu\Delta t}, \quad \lambda_2 = \frac{(\Delta x)^2}{(\Delta x)^2 + \nu\Delta t} \quad (\text{for } (0, 0)), \\ \lambda_1 = \frac{(\Delta x)^2 + 3\nu\Delta t}{(\Delta x)^2}, \quad \lambda_2 = \frac{(\Delta x)^2 + 3\nu\Delta t}{(\Delta x)^2 + 4\nu\Delta t} \quad (\text{for } (\frac{6\nu}{\Delta x}, -\frac{6\nu}{\Delta x})). \end{cases}$$

These results show that the origin is the stable equilibrium point because of $|\lambda_1| < 1$ and $|\lambda_2| < 1$, and $(6\nu/\Delta x, -6\nu/\Delta x)$ is the unstable equilibrium point because of $|\lambda_1| > 1$ (if $\nu > 0$).

(b) Three-dimensional discrete system

Three-dimensional(5 points) discrete system by fully implicit scheme eq.(2.7) has three roots shown in eq.(2.8). We can get three real solutions in the present case. Though one of solutions of eq.(2.8) corresponds to the true solution which converges on the equilibrium

point-(0, 0, 0), other two solutions correspond to ghost solutions. One of the ghost solutions numerically diverges to $(2\nu/\Delta x, \infty, -2\nu/\Delta x)$. Another ghost solution may be divided into several types such as 4- or 8-periodic points and so on due to the parameters $(\nu, \Delta x)$ and initial condition. We can show the existence of these attractors $((0, 0, 0), (2\nu/\Delta x, \infty, -2\nu/\Delta x)$ and 4-periodic points) practically, e.g., for the case of $\nu=1/22, \Delta x=1/11$. Therefore, we must determine the reasonable scheme among the complicated branches described above in order to get the true solution in the physical meaning in the case of fully implicit scheme.

$$\begin{cases} \frac{x_1^{(m+1)} - x_1^{(m)}}{\Delta t} + x_1^{(m+1)} \frac{x_2^{(m+1)} - 0}{2\Delta x} = \nu \frac{x_2^{(m+1)} - 2x_1^{(m+1)} + 0}{(\Delta x)^2}, \\ \frac{x_2^{(m+1)} - x_2^{(m)}}{\Delta t} + x_2^{(m+1)} \frac{x_3^{(m+1)} - x_1^{(m+1)}}{2\Delta x} = \nu \frac{x_3^{(m+1)} - 2x_2^{(m+1)} + x_1^{(m+1)}}{(\Delta x)^2}, \\ \frac{x_3^{(m+1)} - x_3^{(m)}}{\Delta t} + x_3^{(m+1)} \frac{0 - x_2^{(m+1)}}{2\Delta x} = \nu \frac{0 - 2x_3^{(m+1)} + x_2^{(m+1)}}{(\Delta x)^2}, \end{cases} \quad (2.7)$$

$$\begin{aligned} x_2^{(m+1)} &= A + B - \frac{a}{3}, \quad \omega A + \omega^2 B - \frac{a}{3}, \quad \omega^2 A + \omega B - \frac{a}{3}, \\ x_1^{(m+1)} &= \frac{x_1^{(m)} + z x_2^{(m+1)}}{1 + 2z + y x_2^{(m+1)}}, \quad x_3^{(m+1)} = \frac{x_3^{(m)} + z x_2^{(m+1)}}{1 + 2z - y x_2^{(m+1)}}, \end{aligned} \quad (2.8)$$

where

$$\begin{aligned} a &= -(x_1^{(m)} + x_2^{(m)} + x_3^{(m)}), \\ b &= \frac{-1 + (x_1^{(m)} - x_3^{(m)})(y - yz) - 6z - 10z^2 - 4z^3}{y^2}, \\ c &= \frac{(1 + 2z) \{z(x_1^{(m)} + 2x_2^{(m)} + x_3^{(m)}) + x_2^{(m)}\}}{y^2}, \\ \omega &= \frac{-1 + i\sqrt{3}}{2}, \quad y = \frac{\Delta t}{2\Delta x}, \quad z = \nu \frac{\Delta t}{(\Delta x)^2}, \\ A &= \sqrt[3]{-\frac{q}{2} + \sqrt{\frac{q^2}{4} + \frac{p^3}{27}}}, \quad B = \sqrt[3]{-\frac{q}{2} - \sqrt{\frac{q^2}{4} + \frac{p^3}{27}}}, \\ p &= b - \frac{a^2}{3}, \quad q = \frac{2a^3}{27} - \frac{ab}{3} + c. \end{aligned}$$

On the other hand, we can solve that problem by linearizing eq.(2.7), eq.(2.9).

$$\begin{cases} \frac{x_1^{(m+1)} - x_1^{(m)}}{\Delta t} + x_1^{(m)} \frac{x_2^{(m+1)} - 0}{2\Delta x} = \nu \frac{x_2^{(m+1)} - 2x_1^{(m+1)} + 0}{(\Delta x)^2}, \\ \frac{x_2^{(m+1)} - x_2^{(m)}}{\Delta t} + x_2^{(m)} \frac{x_3^{(m+1)} - x_1^{(m+1)}}{2\Delta x} = \nu \frac{x_3^{(m+1)} - 2x_2^{(m+1)} + x_1^{(m+1)}}{(\Delta x)^2}, \\ \frac{x_3^{(m+1)} - x_3^{(m)}}{\Delta t} + x_3^{(m)} \frac{0 - x_2^{(m+1)}}{2\Delta x} = \nu \frac{0 - 2x_3^{(m+1)} + x_2^{(m+1)}}{(\Delta x)^2}, \end{cases} \quad (2.9)$$

By the linear stability theory, eigenvalues of Jacobian matrix of the discrete map of eq.(2.8) for the equilibrium point(0, 0, 0) are follows:

$$\begin{cases} \lambda_1 = \frac{(\Delta x)^2}{(\Delta x)^2 + 2\nu\Delta t}, \\ \lambda_2 = \frac{2(\Delta x)^4 + (4 + \sqrt{8})(\Delta x)^2\nu\Delta t}{2(\Delta x)^4 + 8(\Delta x)^2\nu\Delta t + 4\nu^2(\Delta t)^2}, \\ \lambda_3 = \frac{2(\Delta x)^4 + (4 - \sqrt{8})(\Delta x)^2\nu\Delta t}{2(\Delta x)^4 + 8(\Delta x)^2\nu\Delta t + 4\nu^2(\Delta t)^2}. \end{cases}$$

These results show that (0, 0, 0) is the stable equilibrium point because of $|\lambda_1| < 1$, $|\lambda_2| < 1$ and $|\lambda_3| < 1$ (, if $\nu > 0$). By practical computation of eq.(2.8) in the case of $\nu=1/22$, $\Delta x=1/11$, we get only the true solution, (0, 0, 0), for all Δt values with very fast convergence speed. This linearized scheme of eq.(2.2) is quite excellent scheme to get only the true solution and calculate steady state solutions efficiently. Furthermore, we tried another linearization forms, eq.(2.10). In the present numerical experiments, we could not find any ghost numerical solutions in several dimensional discrete systems in the case of this linearization schemes, too.

$$\begin{cases} u_i^{(m+1)} = u_i^{(m)} + \Delta t \left\{ -u_1^{(m)} \frac{u_2^{(m)} - u_0^{(m)}}{2\Delta x} + \nu \frac{u_2^{(m)} - 2u_1^{(m)} + u_0^{(m)}}{(\Delta x)^2} \right\}, \\ u_i^{(m+1)} = u_i^{(m)} + \Delta t \left\{ -u_i^{(m)} \frac{u_{i+1}^{(m)} - u_{i-1}^{(m+1)}}{2\Delta x} + \nu \frac{u_{i+1}^{(m)} - 2u_i^{(m)} + u_{i-1}^{(m+1)}}{(\Delta x)^2} \right\}, \\ \quad (1 < i < (n-1), m \geq 0) \\ u_i^{(0)} : \text{(Initial data)}, \\ u_0^{(m)} = u_{n-1}^{(m)} = 0. \end{cases} \quad (2.10)$$

Generally speaking, dynamical structure of the low-dimensional($n=2,3$) discrete system is more complicated than that of the higher-dimensional ones. Therefore, the effects of linearization in implicit schemes is so effective that we may be able to get the true solution without the trouble of occurrence of ghost solutions in higher-dimensional cases. However, we have not got the almighty criterion in analyzing the nonlinear dynamical system, yet. The several methods which we suggested and used in the present paper are expected to be indispensable for studies in the field of CFD.

3 Practical Calculation of Flow Motion

3.1 The incompressible Navier-Stokes equation

The non-dimensional governing the incompressible Navier-Stokes equations and the continuity equation are given as follows:

$$\text{div} \mathbf{V} = 0, \quad (3.1)$$

$$\frac{\partial \mathbf{V}}{\partial t} + (\mathbf{V} \cdot \text{grad}) \mathbf{V} = -\text{grad} p + \frac{1}{Re} \Delta \mathbf{V}, \quad (3.2)$$

where $\mathbf{V} = (u, v)$, p and Re denote velocity vector, pressure and the Reynolds number, respectively.

3.2 Numerical algorithm

The Poisson equation for pressure can be derived on the basis of MAC method.¹²⁾

$$\Delta p = -\text{div}(\mathbf{V} \cdot \text{grad})\mathbf{V} + R \quad , \quad (3.3)$$

where

$$R = -\frac{\partial D}{\partial t} + \frac{1}{Re}\Delta D \quad , \quad D \equiv \text{div}\mathbf{V} \quad .$$

In the present study, we employed the generalized transformation of coordinates, $(x, y) \rightarrow (\xi, \eta)$, then we get the transformed Poisson equation as follows:

$$\begin{aligned} \tilde{\Delta} p = & -\frac{(y_\eta u_\xi - y_\xi u_\eta)^2 + 2(x_\xi u_\eta - x_\eta u_\xi)(y_\eta v_\xi - y_\xi v_\eta) + (x_\xi v_\eta - x_\eta v_\xi)^2}{J^2} \\ & -\frac{y_\eta u_\xi - y_\xi u_\eta + x_\xi v_\eta - x_\eta v_\xi}{J\Delta t} \quad , \end{aligned} \quad (3.4)$$

where J is the Jacobian of transformation. The Poisson equation is solved using SOR scheme. All spatial derivatives except for those of the nonlinear convection term is discretized by using the central finite difference. For those of the convection terms, we considered parameter ϵ in order to discuss the effects of fourth order artificial viscosity term,

$$f \frac{\partial u}{\partial \xi} = \frac{f_i(-u_{i+2} + 8u_{i-1} - 8u_{i+1} + u_{i-2})}{12\Delta\xi} + \epsilon \frac{|f_i|(u_{i+2} - 4u_{i-1} + 6u_i - 4u_{i+1} + u_{i-2})}{4\Delta\xi^4} \quad . \quad (3.5)$$

Eq. (3.5) is based on the third-order upwind schemes¹³⁾. In the present paper in which the two-dimensional generalized coordinates are used, ϵ_ξ shows the parameter for ξ -direction and ϵ_η for η -direction, respectively. For the time marching of the Navier-Stokes equations, the first order Euler implicit scheme is employed. In the case of the implicit scheme, the nonlinear convection term is linearized for \mathbf{V}^{n+1} as follows:

$$(\mathbf{V}^{n+1} \cdot \nabla) \mathbf{V}^{n+1} \approx (\mathbf{V}^n \cdot \nabla) \mathbf{V}^{n+1} \quad . \quad (3.6)$$

3.3 Grid systems

The O-type grid systems are used in all cases. The body surface corresponds to $K = 1$, the circle of which radius is equal to 1. Outer flow region corresponds to $K = KMAX$, the circle of which radius is set to from 60 to 70. The mesh points are strongly concentrated in

the boundary layer and the minimum spacing normal to the surface of the body is set to be less than $\frac{0.049}{\sqrt{Re}}$. Therefore this grid system is fine enough to resolve the flow structure in the boundary layer.

3.4 Boundary conditions

The boundary conditions on the body surface are as follows: The no-slip condition is used for the velocity components. The pressure p along the body surface is obtained by solving a normal momentum equation. At the far boundaries, the free-stream values are specified.

4 Results and Discussions of Practical Computation

In this section, we discuss about the computed results which are given by using the implicit temporal scheme in detail. The calculation model which is adopted in the present paper is the flow around the circular cylinder and the Reynolds number is 2000. Flows around a circular cylinder have been reported by a lot of experiments of which the results were summarized in the paper by James *et al.*¹⁴⁾ and were described in the textbook by Schlichting.¹⁵⁾ In a lot of historical studies, the larger the Reynolds number becomes, the more complicated the flow field becomes. In the range of the low Reynolds numbers, the fixed points of the time series of C_D which correspond to the laminar flow (the two recirculating standing eddies) first bifurcate (Hopf bifurcation) to the limit cycles which physically correspond to Kármán vortex street. At this bifurcation point, where the Reynolds number is about 50, this first true loss of symmetry occurs. The subcritical flow regime is located at Reynolds numbers below $1-2 \times 10^5$ and it has long been agreed that in this Reynolds number range the flow around a circular cylinder is laminar.¹⁴⁾ Furthermore, the larger Re becomes, the larger the amplitude of the time series of C_D becomes and the second bifurcation occurs which shows the onset of turbulence and a chaotic motion can be seen. Therefore, the flow field is expected to be still periodic at $Re=2000$. In the implicit Euler scheme which is used in the present paper, the nonlinear convection term is linearized like eq. (3.6). Therefore, we must solve two linear systems which are the Poisson equation for pressure and time marching step by iterative methods. The number of limit of iteration in solving the Poisson equation for pressure is 1000 times and that in time marching step is 200 times. The criterion of norm of error is below 10^{-6} in solving the Poisson equation for pressure and is below 10^{-7} in time marching step. Of course, the criterion of norm of error is never satisfied in early stage of calculations. Here we must select one physical variable which represent the qualitative unsteady feature of the whole computed system in order

to compare the structure of the numerical solutions. Time series of physical variables in a grid point is not suitable because it is difficult to select the best point without any self-will. The integrated variables such as the drag coefficient(C_D) and the lift coefficient(C_L) show the typical profile. We adopted the drag coefficient(C_D) as the variable. In order to get the remove the effect of initial condition, we adopted the sampling period of the time series of C_D from $T(\text{non-dimensional time})=400$ to 500. In this period, the flow fields are expected to be almost quasi-steady. We compared several characteristics of structure of quasi-steady flow field on the basis of nonlinear dynamics approaches such as the three-dimensional profiles of attractor which are reconstructed from the time series of C_D data. We got some asymptotic solutions such as limit cycles and so on for different parameter ϵ . Figure 1 is the comparison of the typical characteristics of structure of attractors given from the time series of C_D . Globally speaking, if we find only one clear maximum point in time history profile or the trajectory reconstructed three-dimensionally is the simple closed curve, we call this attractor "Limit cycle". In the cases of two different clear maximum points in time history data, we call them "Periodic two(P2)". We can classify these asymptotic solutions by estimating three data shown in figure 1 totally. In the present section, parameter ϵ value for ξ -direction is same as that for η -direction in all cases. Figure 2 shows the regimes in which several attractors in some ϵ values exist. Calculations in the cases of $\epsilon > 1.2$ diverged and we could not get the stable solutions in the case of $\Delta t = 0.02$. We got an interesting bifurcation sequence with the decrease of parameter ϵ as shown in this figure. It is clearly seen that the larger ϵ value becomes, the simpler structure of attractor becomes. In the region if $\epsilon > 0.8$, calculated attractor is P2 which maybe corresponds to the true solution in all Δt value cases. Because the artificial viscosity term stabilizes the system, this phenomenon is expected to be reasonable. When P2 attractors become unstable, a cusp appears and the trajectories look like tori. In the region of $\epsilon \approx 0.75$ in the case of $\Delta t = 0.02$, the P4 attractor which has five local maximum points in the time series of C_D appears. Though these P4 attractors have four clear local maximum points and one more quite fine fluctuation, we neglect this and do not call them P5 but P4. These P4 attractors become unstable and the stable P8 attractor appear. Furthermore, the stable P16 attractor appears in the cases of smaller ϵ . This (P2-P4-P8-P16) bifurcation sequences which is similar to the period-doubling one is quite interesting. However, what we must pay attention is that the unstable complicated attractors(T) also appear even if these hard criterions were satisfied. This phenomenon may be a transient one. However, though we performed longer and longer period calculations in several cases, numerical solutions never converged to the stable attractors. Furthermore, multiple stable attractors coexist around the complicated unstable attractor. In order to get the physically reasonable numerical

solutions, it becomes clear that we should add the relatively large amplitude of fourth order artificial viscosity terms. Though to add the higher order artificial viscosity terms may be a necessary condition to remove the ghost solutions, it is not still unknown what is the sufficient condition to obtain the physically reasonable numerical solutions. On the other hand, when the Δt values become small, first bifurcation points moves to the small ϵ region where ghost solutions appear becomes narrow. This result is the most important because it is quite lucky for the researchers who analyse the flow motion by using the implicit scheme.

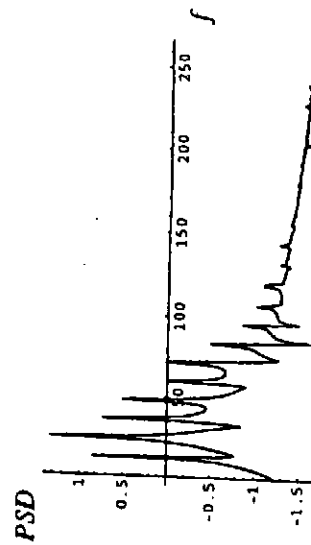
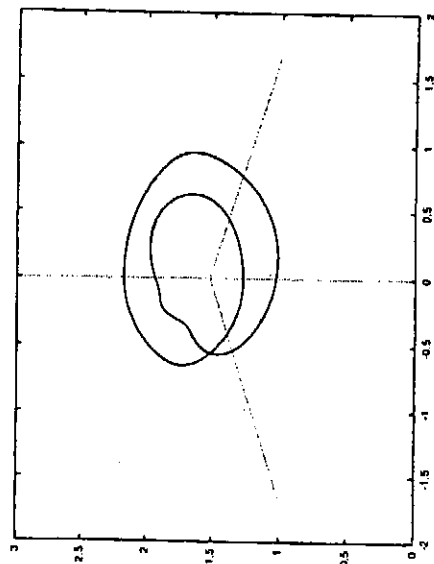
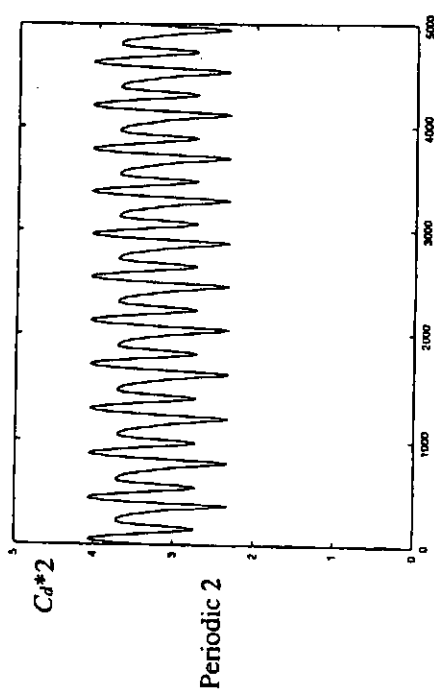
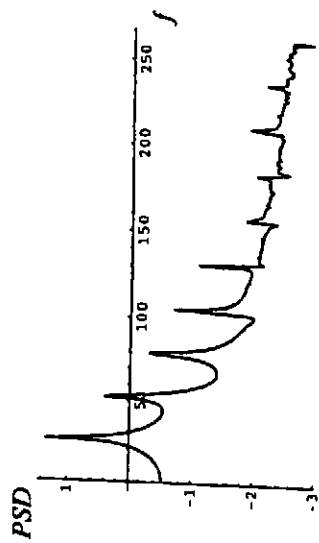
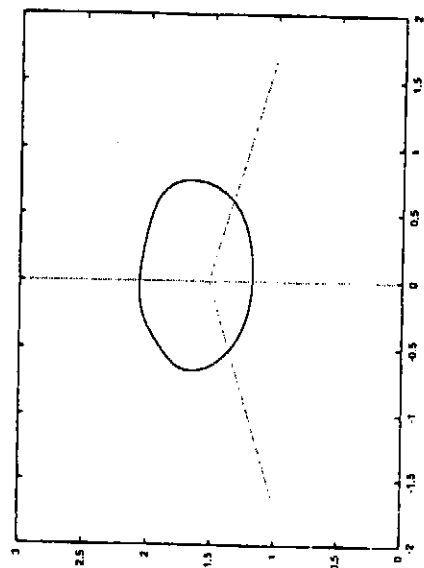
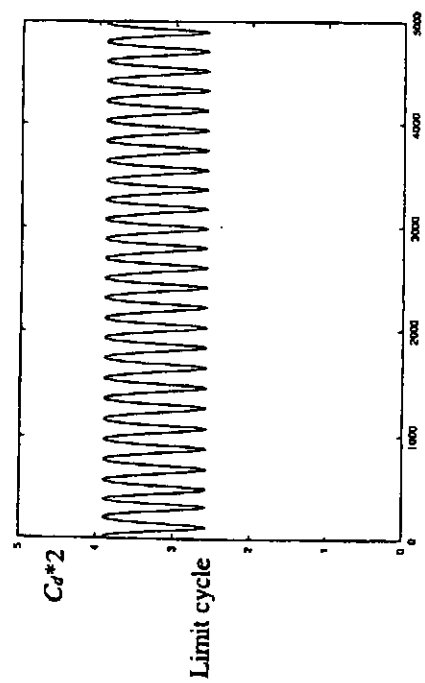
4 Conclusions

The supercomputer and the development of visualization technique have made it possible to simulate the complicated phenomenon such as flow motions as if they were open before our eyes actually. However, on the other hand, the strong nonlinearity of the computational discrete dynamical system still makes it difficult to make the computed results reliable as shown in the appearance of the ghost numerical solutions. In the present study, we showed the ghost numerical solutions appear not only in the cases of explicit scheme cases but also appear in those of implicit cases in solving the nonlinear equations analytically and numerically. In the study of fully implicit scheme of Burgers' equation, we showed that there is a possibility that the multiple steady solutions exist simultaneously. However, the ghost solutions disappear by using the effective linearization technique. Furthermore, we discussed the asymptotic numerical solutions of incompressible Navier-Stokes equations. In order to discuss the reliability of their numerical solutions, since only the usual methods used in the common analyses in the field of computational fluid dynamics is not adequate, we need more effective methods to analyze the complicated unsteady structure of the numerical solutions in detail. We proposed some nonlinear dynamics approaches which are used in the fields of mathematics, theoretical and experimental physics and so on. To study the characteristics of attractors which were constructed by the computed time series of C_D at the quasi-steady state can not only make the differences of the unsteady structure clear but also give us the important information. In particular, to evaluate the influences of degree of convergence in the iteration steps on the structure of asymptotic numerical solutions becomes clear by using nonlinear dynamics approaches. Furthermore, it is shown that some strange phenomenon occur when we use the small ϵ parameters even if the stable implicit temporal schemes are utilized. Further, as if the adequate convergence condition of the Poisson equation of the pressure was not attained in each time step, we can get the non-diverging numerical solutions which never appear

actually. As described above, we must pay much attention to the selection of suitable schemes and the discretized parameters in order to the physically reasonable results.

References

- 1) A. Stuart:SIAM Review, **31**(1989)191.
- 2) E. N. Lorenz: Physica D, **35-3**(1989)299.
- 3) H. C. Yee, P. K. Sweby and D. F. Griffiths: J. Comput. Phys., **97**(1991)249.
- 4) D. F. Griffiths, P. K. Sweby and H. C. Yee: IMA J. Num. Anal., **12**(1992)319.
- 5) A. Lafon and H. C. Yee, H. C.: AIAA Paper, 92-0419(1992).
- 6) A. R. Humphries:IMA J. Num. Anal., **13**(1993)263.
- 7) D. F. Griffiths, A. Stuart and H. C. Yee: SIAM J. Num. Anal., **29**(1992)1244.
- 8) I. Hataue: AIAA J.,**33**(1995)163.
- 9) I. Hataue: AIAA-Paper,97-0870(1997).
- 10) I.Hataue: J. of Phys. Soc. Japan, **67-6**(1998)1895.
- 11) I.Hataue: Theo. Appl. Mech., **47**(1998)205.
- 12) F. H. Harlow and J. E. Welch: Phys. Fluids, **8**(1965)2182.
- 13) T. Kawamura and K. Kuwahara: AIAA Paper,84-0340(1984).
- 14) W. D. James, S. W. Paris and G. N. Malcolm: AIAA J., **18**(1980)1066.
- 15) H. Schlichting: "*Boundary-Layer Theory*", (Mcgraw-Hill, New York, 1979).



(a) time series

(b) Plot ($Ca(t)$, $Ca(t+25\Delta t)$, $Ca(t+50\Delta t)$) in phase space

(c) power spectral density

Fig.1 Typical characteristics of structure of attractors given from the time series of Ca . ($Re=2000$)

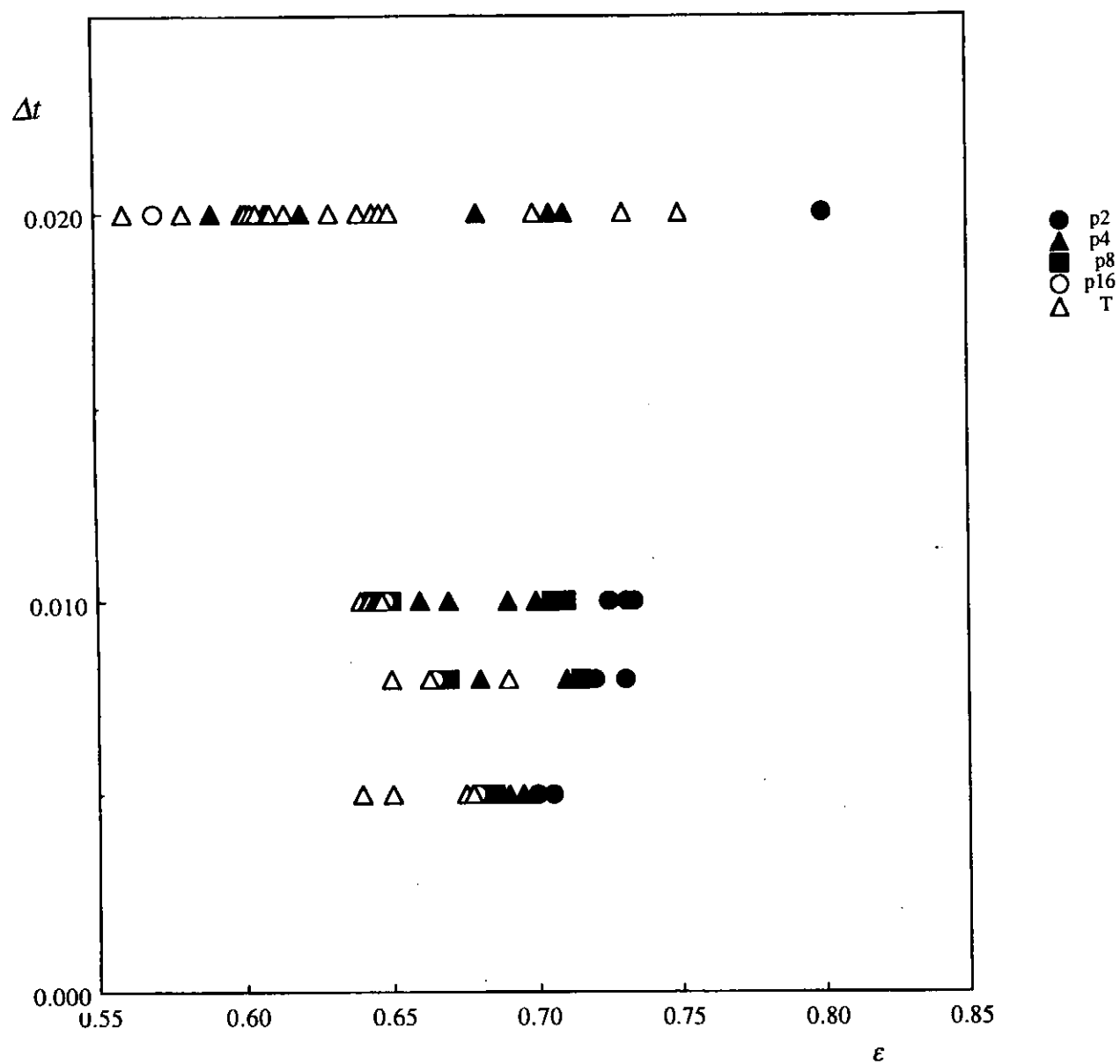


Fig.2 Plotted points show the regimes given for each ϵ value in the case of using implicit scheme.(Re=2000)

On FEM-FSM Combined Method

Applied to 2D Exterior Laplace and Helmholtz Problems

USHIJIMA, Teruo

Department of Computer Science

Faculty of Electro-Communications

The University of Electro-Communications

182-8585 Chofu-shi Chofugaoka 1-5-1 Tokyo Japan

ABSTRACT

Consider the Poisson equation $-\Delta u = f$ in a planar exterior domain of a bounded domain \mathcal{O} . Assume that $f = 0$ in the outside of a disc with sufficiently large diameter. The solution u is assumed to be bounded at infinity. Discretizing the problem, we employ the finite element method (FEM, in short) inside the disc, and the charge simulation method (CSM, in short) outside the disc. Results of mathematical analysis for this FEM-CSM combined method are reported in this paper.

In the mathematical analysis for the method, especially in the proof of an a priori error estimate for the approximate solutions obtained by the method, a relation between continuous and discrete Fourier coefficients of equi-distant piecewise linear continuous 2π -periodic function plays a key role.

CSM is a typical example of the fundamental solution method (FSM, in short), through which the solution of homogeneous partial differential equation is approximated as a linear combination of fundamental solutions of differential operator. Hence the combined method for 2D exterior Laplace problem is extendable to the planar exterior reduced wave equations. Our discretization procedure for the reduced wave equation is also described in the paper.

Keywords: two dimensional exterior Laplace problem, finite element method, charge simulation method, FEM-CSM combined method, reduced wave equation, two dimensional exterior Helmholtz problem, fundamental solution method, FEM-FSM combined method.

1. Relation between continuous and discrete Fourier coefficients for equi-distant piecewise linear continuous 2π -periodic functions

Let $f(\theta)$ be a complex valued continuous 2π -periodic function of θ . For $n \in \mathbf{Z}$, a continuous Fourier coefficient f_n of the function $f(\theta)$ is defined through

$$f_n = \frac{1}{2\pi} \int_0^{2\pi} f(\theta) e^{-in\theta} d\theta.$$

Fix a positive integer N . Set

$$\theta_1 = \frac{2\pi}{N}.$$

For any $j \in \mathbf{Z}$, denote $j\theta_1$ by θ_j . For $n \in \mathbf{Z}$, a discrete Fourier coefficient $f_n^{(N)}$ of the function $f(\theta)$

is defined through

$$f_n^{(N)} = \frac{1}{N} \sum_{j=0}^{N-1} f(\theta_j) e^{-in\theta_j}.$$

It is to be noted that we have for any continuous 2π -periodic function $f(\theta)$,

$$(1) \quad f_{n+Nr}^{(N)} = f_n^{(N)}, \quad n \in \mathbf{Z}, \quad r \in \mathbf{Z} - \{0\}.$$

Let $\hat{w}(\theta)$ be the reference roof function defined through

$$\hat{w}(\theta) = \begin{cases} 1 - |\theta| & : |\theta| \leq 1, \\ 0 & : |\theta| \geq 1. \end{cases}$$

For any $j \in \mathbf{Z}$, define a piecewise linear basis func-

tion $w_j^{(N)}(\theta)$ through the following formula:

$$w_j^{(N)}(\theta) = \hat{w}\left(\frac{\theta - \theta_j}{\theta_1}\right), \quad -\infty < \theta < \infty.$$

A complex valued function $f(\theta)$ is said to be an **equi-distant piecewise linear continuous 2π -periodic function** (with N nodal points) in this paper if $f(\theta)$ is represented as

$$f(\theta) = \sum_{j=0}^N f(\theta_j) w_j^{(N)}(\theta), \quad 0 \leq \theta \leq 2\pi,$$

with

$$f(2\pi) = f(0).$$

Introduce a function $\alpha(\theta)$ through the formula:

$$\alpha(\theta) = \frac{2(1 - \cos(\theta))}{\theta^2} \quad \text{for } \theta \neq 0, \quad \text{with } \alpha(0) = 1.$$

Theorem 1 *We have the following relation for any equi-distant piecewise linear continuous 2π -periodic function (with N nodal points) $f(\theta)$,*

$$(2) \quad f_n = \alpha(\theta_n) f_n^{(N)}, \quad n \in \mathbb{Z}.$$

Proof A straightforward calculus leads the relation. \square

Corollary *We have the following identity for any equi-distant piecewise linear continuous 2π -periodic function (with N nodal points) $f(\theta)$,*

$$(3) \quad f_{n+Nr} = \left(\frac{n}{n+Nr}\right)^2 f_n, \quad n \in \mathbb{Z}, \quad r \in \mathbb{Z} - \{0\}.$$

Proof Since we have

$$\alpha(\theta_{n+Nr}) = \left(\frac{n}{n+Nr}\right)^2 \alpha(\theta_n), \quad n \in \mathbb{Z}, \quad r \in \mathbb{Z} - \{0\},$$

Theorem 1 together with Equality (1) implies Equality (3). \square

2. Boundary bilinear forms of Steklov type for exterior Laplace problems and its CSM-approximation forms

With the full use of identities (1), (2) and (3), the author has obtained several estimates concerning differences between the boundary bilinear form of Steklov type for the exterior Laplace problems and its CSM-approximation forms. Here the abbreviation

of CSM has been employed for the charge simulation method (See [1]).

Let D_a be the interior of the disc with radius a having the origin as its center, and let Γ_a be the boundary of D_a . Let $\Omega_e = (D_a \cup \Gamma_a)^C$, which is said to be the exterior domain. We use the notation $\mathbf{r} = \mathbf{r}(\theta)$ for the point in the plane corresponding to the complex number $re^{i\theta}$ with $r = |\mathbf{r}|$ where $|\mathbf{r}|$ is the Euclidean norm of $\mathbf{r} \in \mathbb{R}^2$. Similarly we use $\mathbf{a} = \mathbf{a}(\theta)$, and $\tilde{\rho} = \tilde{\rho}(\theta)$, corresponding to $ae^{i\theta}$ with $a = |\mathbf{a}|$, and $\rho e^{i\theta}$ with $\rho = |\tilde{\rho}|$, respectively.

For functions $u(\mathbf{a}(\theta))$ and $v(\mathbf{a}(\theta))$ of $H^{1/2}(\Gamma_a)$, let us introduce the boundary bilinear form of Steklov type for exterior Laplace problem through the following formula:

$$(4) \quad b(u, v) = 2\pi \sum_{n=-\infty}^{\infty} |n| f_n \bar{g}_n,$$

where f_n , and g_n , are continuous Fourier coefficients of $u(\mathbf{a}(\theta))$, and $v(\mathbf{a}(\theta))$, respectively.

It is to be noted that the following fact:

If $u(\mathbf{a}(\theta))$ is the boundary value on Γ_a of the function $u(\mathbf{r})$ satisfying the following boundary value problem (E):

$$(E) \quad \begin{cases} -\Delta u = 0 & \text{in } \Omega_e, \\ u = \varphi & \text{on } \Gamma_a, \\ \sup_{\Omega_e} |u| < \infty, \end{cases}$$

with

$$\varphi = u(\mathbf{a}(\theta)),$$

then

$$(5) \quad b(u, v) = - \int_{\Gamma_a} \frac{\partial u}{\partial r} v d\Gamma.$$

(In (5), $d\Gamma$ is the curve element of Γ_a . Namely

$$d\Gamma = a d\theta$$

in the polar coordinate expression.)

Fix a positive number ρ so as to satisfy $0 < \rho < a$. For a fixed positive integer N , set the points $\tilde{\rho}_j, \mathbf{a}_j, 0 \leq j \leq N-1$, as follows:

$$\mathbf{a}_j = \mathbf{a}(\theta_j), \quad \tilde{\rho}_j = \tilde{\rho}(\theta_j) \quad \text{with } 0 < \rho < a.$$

The points $\tilde{\rho}_j$, and \mathbf{a}_j , are said to be the source, and the collocation, points, respectively. The arrangement of the set of points of source points and collocation points introduced as above is called the **equi-distant equally phased arrangement of source**

points and collocation points, hereafter in this paper.

The CSM approximate form for $b(u, v)$ of the first type, which is denoted by $b^{(N)}(u, v)$, is represented through the following formula (6):

$$(6) \quad b^{(N)}(u, v) = - \int_{\Gamma_a} \frac{\partial u^{(N)}}{\partial r} v^{(N)} d\Gamma,$$

where $u^{(N)}(\mathbf{r})$, and $v^{(N)}(\mathbf{r})$, are CSM-approximate solutions for $u(\mathbf{r})$, and $v(\mathbf{r})$, satisfying (E) with $\varphi = u(\mathbf{a}(\theta))$, and $\varphi = v(\mathbf{a}(\theta))$, respectively. Namely $u^{(N)}(\mathbf{r})$ is determined through the following problem (E^(N)):

$$(E^{(N)}) \quad \begin{cases} u^{(N)}(\mathbf{r}) = \sum_{j=0}^{N-1} q_j G_j(\mathbf{r}) + q_N, \\ u^{(N)}(\mathbf{a}_j) = u(\mathbf{a}_j), \quad 0 \leq j \leq N-1, \\ \sum_{j=0}^{N-1} q_j = 0, \end{cases}$$

where the set of points $\{\tilde{\rho}_j, \mathbf{a}_j : 0 \leq j \leq N-1\}$ is the equi-distant equally phased arrangement of source points and collocation points, and

$$G_j(\mathbf{r}) = E(\mathbf{r} - \tilde{\rho}_j) - E(\mathbf{r}), \quad E(\mathbf{r}) = -\frac{1}{2\pi} \log r.$$

Problem (E^(N)) is to find $N+1$ unknowns q_j , $0 \leq j \leq N$, and it is uniquely solvable for any fixed $\rho \in (0, a)$.

The CSM approximate form for $b(u, v)$ of the second type, which is denoted by $\bar{b}^{(N)}(u, v)$, is represented through the following formula (7):

$$(7) \quad \bar{b}^{(N)}(u, v) = -\frac{2\pi a}{N} \sum_{j=0}^{N-1} \frac{\partial u^{(N)}(\mathbf{a}_j)}{\partial r} v^{(N)}(\mathbf{a}_j),$$

which is the quadrature formula for $b^{(N)}(u, v)$ with the use of trapezoidal rule.

We use the following notations:

$$\begin{aligned} b(v) &= b(v, v)^{1/2}, \\ b^{(N)}(v) &= b(v, v)^{1/2}, \\ \bar{b}^{(N)}(v) &= \bar{b}^{(N)}(v, v)^{1/2}. \end{aligned}$$

Denote the totality of equi-distant piecewise linear continuous 2π -periodic functions (with N nodal points) $v(\mathbf{a}(\theta))$ by V_N :

$$V_N = \{v(\mathbf{a}(\theta)) = \sum_{j=0}^N v(\mathbf{a}_j) w_j^{(N)}(\theta)\}.$$

Let

$$N(\gamma) = \frac{\log 2}{-\log \gamma} \quad \text{with} \quad \gamma = \frac{\rho}{a}.$$

Theorem 2 We have the following relation for any $v \in V_N$.

$$\frac{1}{4\sqrt{1+2\zeta(3)}} b(v) \leq b^{(N)}(v) \leq \frac{\pi^2}{2} b(v)$$

provided that $N \geq N(\gamma)$, where

$$\zeta(3) = \sum_{r=1}^{\infty} \frac{1}{r^3}.$$

Theorem 3 For $u, v \in V_N$, we have

$$|b^{(N)}(u, v) - \bar{b}^{(N)}(u, v)| \leq 8\gamma^{2N} b^{(N)}(u) b^{(N)}(v)$$

provided that $N \geq N(\gamma)$.

3. Proof of Theorem 2

For a fixed positive integer N , introduce sets of integers \mathcal{N}_r through

$$\mathcal{N}_r = \{n : -\frac{N}{2} \leq n - Nr < \frac{N}{2}\}$$

with

$$r = 0, \pm 1, \pm 2, \dots$$

Define functions $s_n^{(N)}(\gamma)$ of $\gamma \in (0, 1)$, $1 \leq n \leq N-1$, through

$$s_n^{(N)}(\gamma) = \int_0^\gamma \frac{x^{n-1} + x^{N-n-1}}{1-x^N} dx.$$

Proposition 1 For $u, v \in V_N$, we have

$$b^{(N)}(u, v) = 2\pi \sum_{n \in \mathcal{N}_0} \Lambda_{|n|}^{(N)} f_n^{(N)} \overline{g_n^{(N)}}$$

and

$$\bar{b}^{(N)}(u, v) = 2\pi \sum_{n \in \mathcal{N}_0} \bar{\Lambda}_{|n|}^{(N)} f_n^{(N)} \overline{g_n^{(N)}},$$

where

$$\Lambda_n^{(N)} = \frac{s_n^{(N)}(\gamma^2)}{\{s_n^{(N)}(\gamma)\}^2}, \quad 1 \leq n \leq N-1$$

and

$$\bar{\Lambda}_n^{(N)} = \frac{\gamma \frac{d}{d\gamma} s_n^{(N)}(\gamma)}{s_n^{(N)}(\gamma)}, \quad 1 \leq n \leq N-1$$

and $f_n^{(N)}$, and $g_n^{(N)}$, are discrete Fourier coefficients of $u(\mathbf{a}(\theta))$, and $v(\mathbf{a}(\theta))$, respectively.

Using the representation of $\Lambda_n^{(N)}$, we obtain

Proposition 2 *If $N \geq N(\gamma)$, then*

$$\frac{n}{16} \leq \Lambda_n^{(N)} \leq 4n, \quad 1 \leq n \leq \frac{N}{2}.$$

An elemental calculus leads

Proposition 3 *It holds*

$$\frac{4}{\pi^2} \leq \alpha(\theta) \leq 1, \quad -\pi \leq \theta \leq \pi.$$

Proposition 4 *For $v \in V_N$, we have*

$$\begin{aligned} & \frac{1}{16} \left\{ 2\pi \sum_{n \in \mathcal{N}_0} |n| |g_n|^2 \right\} \\ & \leq b^{(N)}(v, v) \leq \\ & \frac{\pi^4}{4} \left\{ 2\pi \sum_{n \in \mathcal{N}_0} |n| |g_n|^2 \right\} \end{aligned}$$

provided that $N \geq N(\gamma)$.

Proof Due to Theorem 1 and Proposition 1, we have

$$b^{(N)}(v, v) = 2\pi \sum_{n \in \mathcal{N}_0} \Lambda_{|n|}^{(N)} \frac{1}{|\alpha(\theta_n)|^2} |g_n|^2.$$

Propositions 2 and 3 imply the conclusion of Proposition 4. \square

Proposition 5 *For $v \in V_N$, we have*

$$\begin{aligned} & \left\{ 2\pi \sum_{n \in \mathcal{N}_0} |n| |g_n|^2 \right\} \\ & \leq b(v, v) \leq \\ & (1 + 2\zeta(3)) \left\{ 2\pi \sum_{n \in \mathcal{N}_0} |n| |g_n|^2 \right\}. \end{aligned}$$

Proof Due to Corollary of Theorem 1, we have

$$\frac{1}{2\pi} b(v, v) = \sum_{r \in \mathbb{Z}} \sum_{n \in \mathcal{N}_0} \left| \frac{n}{n + Nr} \right|^3 |n| |g_n|^2$$

with the following notaional convention:

$$\left| \frac{n}{n + Nr} \right|_{n=r=0} = 1.$$

For $r \in \mathbb{Z} - \{0\}$, we have

$$\left| \frac{n}{n + Nr} \right| \leq \frac{1}{|r|}, \quad n \in \mathcal{N}_0.$$

Therefore

$$b(v, v) \leq \left(1 + 2 \sum_{r=1}^{\infty} \frac{1}{r^3} \right) \left\{ 2\pi \sum_{n \in \mathcal{N}_0} |n| |g_n|^2 \right\}.$$

Hence the second inequality of the conclusion is valid, while the 1st one is trivial by definition of $b(u, v)$. \square

Propositions 4 and 5 complete the proof of Theorem 2.

4. Proof of Theorem 3

Proposition 6 *For an integer $n \in [1, N - 1]$, define B_n through the following formula:*

$$B_n = \sum_{p \in \mathbb{Z}} \sum_{q \in \mathbb{Z}} \left\{ \gamma^{|n+Np|} \frac{\gamma^{|n+Nq|}}{|n + Nq|} \right\}.$$

Then we have

$$s_n^{(N)}(\gamma^2) \leq B_n \leq (1 + 8\gamma^2) s_n^{(N)}(\gamma^2)$$

provided that $N \geq N(\gamma)$.

Proof A lengthy but straightforward calculus leads the conclusion. \square

Proposition 7 *For $N \geq N(\gamma)$, we have*

$$\Lambda_n^{(N)} \leq \bar{\Lambda}_n^{(N)} \leq (1 + 8\gamma^2) \Lambda_n^{(N)}.$$

Proof Let

$$\Gamma_n = s_n^{(N)}(\gamma).$$

Then we have

$$\Lambda_n^{(N)} = \frac{s_n^{(N)}(\gamma^2)}{\Gamma_n^2},$$

and

$$\bar{\Lambda}_n^{(N)} = \frac{B_n}{\Gamma_n^2}.$$

Hence Proposition 6 implies the conclusion. \square

The proof of Theorem 3 is now straightforward. In fact, we have

$$b^{(N)}(u, v) - \bar{b}^{(N)}(u, v)$$

$$= 2\pi \sum_{n \in \mathcal{N}_0} (\Lambda_{|n|}^{(N)} - \bar{\Lambda}_{|n|}^{(N)}) f_n^{(N)} \overline{g_n^{(N)}}.$$

Hence it holds

$$\begin{aligned} & |b^{(N)}(u, v) - \bar{b}^{(N)}(u, v)| \\ & \leq 2\pi \left\{ \sum_{n \in \mathcal{N}_0} |\Lambda_{|n|}^{(N)} - \bar{\Lambda}_{|n|}^{(N)}| |f_n^{(N)}|^2 \right\}^{1/2} \\ & \quad \times \left\{ \sum_{n \in \mathcal{N}_0} |\Lambda_{|n|}^{(N)} - \bar{\Lambda}_{|n|}^{(N)}| |g_n^{(N)}|^2 \right\}^{1/2}. \end{aligned}$$

Let $N \geq N(\gamma)$. Proposition 7 implies

$$0 \leq |\Lambda_{|n|}^{(N)} - \bar{\Lambda}_{|n|}^{(N)}| \leq 8\gamma^2 \Lambda_{|n|}^{(N)}, \quad n \in \mathcal{N}_0.$$

Therefore we get

$$\begin{aligned} & |b^{(N)}(u, v) - \bar{b}^{(N)}(u, v)| \\ & \leq 8\gamma^2 \times \left\{ 2\pi \sum_{n \in \mathcal{N}_0} \Lambda_{|n|}^{(N)} |f_n^{(N)}|^2 \right\}^{1/2} \\ & \quad \times \left\{ 2\pi \sum_{n \in \mathcal{N}_0} \Lambda_{|n|}^{(N)} |g_n^{(N)}|^2 \right\}^{1/2} \end{aligned}$$

provided that $N \geq N(\gamma)$. Due to Proposition 1 we have the conclusion of Theorem 3.

5. Application to mathematical analysis of an FEM-CSM combined method for exterior Laplace problems

Fix a simply connected bounded domain \mathcal{O} in the plane. Assume that the boundary \mathcal{C} of \mathcal{O} is sufficiently smooth. The exterior domain of \mathcal{C} is denoted by Ω .

Fix a function $f \in L^2(\Omega)$ whose support, $\text{supp}(f)$, is bounded.

Choose a so large that the open disc D_a may contain the union $\mathcal{O} \cup \text{supp}(f)$ in its interior.

The following Poisson equation (E) is employed as a model problem.

$$(E) \quad \begin{cases} -\Delta u = f & \text{in } \Omega, \\ u = 0 & \text{on } \mathcal{C}, \\ \sup_{|r| > a} |u| < \infty. \end{cases}$$

The intersection of the domain Ω and the disc D_a is said to be the interior domain, denoted by Ω_i :

$$\Omega_i = \Omega \cap D_a.$$

Consider the Dirichlet inner product $a(u, v)$ for $u, v \in H^1(\Omega_i)$:

$$a(u, v) = \int_{\Omega_i} \text{grad} u \text{ grad} v \, d\Omega.$$

Since the trace $\gamma_a v$ on Γ_a is an element of $H^{1/2}(\Gamma_a)$ for any $v \in H^1(\Omega_i)$, the boundary bilinear form of Steklov type $b(u, v)$ is well defined for $u, v \in H^1(\Omega_i)$. Therefore we can define a continuous symmetric bilinear form:

$$t(u, v) = a(u, v) + b(u, v)$$

for $u, v \in H^1(\Omega_i)$.

Let $F(v)$ be a continuous linear functional on $H^1(\Omega_i)$ defined through the following formula:

$$F(v) = \int_{\Omega_i} f v \, d\Omega.$$

A function space V is defined as follows:

$$V = \{v \in H^1(\Omega_i) : v = 0 \text{ on } \mathcal{C}\}.$$

Using these notations, the following weak formulation problem (II) is defined.

$$(II) \quad \begin{cases} t(u, v) = F(v), & v \in V, \\ u \in V. \end{cases}$$

Admitting the equivalence between the equation (E) and the problem (II), we consider the problem (II) and its approximate ones hereafter.

Fix a positive number ρ so as to satisfy $0 < \rho < a$. For a fixed positive integer N , set the points $\bar{\rho}_j, \mathbf{a}_j, 0 \leq j \leq N-1$, as in the equi-distant equally phased arrangement of source points and collocation points defined in Section 2.

A family of finite dimensional subspaces of V :

$$\{V_N : N = N_0, N_0 + 1, \dots\}$$

is supposed to have the following properties:

$$(V_N - 1) \quad V_N \subset C(\bar{\Omega}_i).$$

$$(V_N - 2) \quad \begin{cases} \text{For any } v \in V_N, v(\mathbf{a}(\theta)) \text{ is an equi-distant} \\ \text{piecewise linear continuous } 2\pi\text{-periodic} \\ \text{function with respect to } \theta. \end{cases}$$

$$(V_N - 3) \quad \begin{cases} \min_{v_N \in V_N} a(v - v_N) \leq \frac{C}{N} \|v\|_{H^2(\Omega_i)}, \\ v \in V \cap H^2(\Omega_i). \end{cases}$$

In the property $(V_N - 3)$, C is a constant independent of N and v , and

$$a(v) = a(v, v)^{1/2}, \quad v \in V.$$

An explanation concerning a construction method of the family of spaces $\{V_N : N = N_0, N_0 + 1, \dots\}$ is added here. Let a polygonal domain $\Omega_i^{(N)}$ be an approximate domain of the interior domain Ω_i . A triangulation of $\Omega_i^{(N)}$ yields a standard piecewise linear continuous finite element space \hat{V}_N . Adding a modification for triangles which have their edges on the boundary of $\Omega_i^{(N)}$ through the way of curved element due to Zlámal[6], we can change \hat{V}_N to a space contained in $C(\bar{\Omega}_i)$. A family $\{V_N : N = N_0, N_0 + 1, \dots\}$ which satisfies conditions $(V_N - 1), (V_N - 2), (V_N - 3)$, can be constructed through the procedure just mentioned.

For $u, v \in H^1(\Omega_i) \cap C(\bar{\Omega}_i)$, we define bilinear forms $t^{(N)}(u, v)$ and $\bar{t}^{(N)}(u, v)$ as follows.

$$t^{(N)}(u, v) = a(u, v) + b^{(N)}(u, v),$$

and

$$\bar{t}^{(N)}(u, v) = a(u, v) + \bar{b}^{(N)}(u, v).$$

Now two approximate problems $(\Pi^{(N)})$ and $(\bar{\Pi}^{(N)})$ are stated as follows.

$$(\Pi^{(N)}) \quad \begin{cases} t^{(N)}(u_N, v) = F(v), & v \in V_N, \\ u_N \in V_N. \end{cases}$$

$$(\bar{\Pi}^{(N)}) \quad \begin{cases} \bar{t}^{(N)}(\bar{u}_N, v) = F(v), & v \in V_N, \\ \bar{u}_N \in V_N. \end{cases}$$

With the aide of Theorems 2 and 3 and other necessary discussions, we can show the following error estimate.

Theorem 4 For a constant C , we have the following estimate.

$$\left. \begin{aligned} \|u - u_N\|_{H^1(\Omega_i)} \\ \|u - \bar{u}_N\|_{H^1(\Omega_i)} \end{aligned} \right\} \leq \frac{C}{N} \|u\|_{H^2(\Omega_i)}.$$

In the above, the constant C is independent of the solution u of (Π) and N .

6. Reduced wave problem in the outside of an open disc

Let k be the length of the wave number vector. Consider the following reduced wave problem (E_f) in the exterior domain Ω_e of the circle Γ_a with radius a having the origin as its center.

$$(E_f) \quad \begin{cases} -\Delta u - k^2 u = 0 & \text{in } \Omega_e, \\ u = f & \text{on } \Gamma_a, \\ \lim_{r \rightarrow \infty} \sqrt{r} \left\{ \frac{\partial u}{\partial r} - iku \right\} = 0. \end{cases}$$

In the above, f is a complex valued continuous function on Γ_a .

The solution $u = u(\mathbf{r})$ of the problem (E_f) is represented as

$$u = \sum_{n=-\infty}^{\infty} f_n \frac{H_n^{(1)}(kr)}{H_n^{(1)}(ka)} e^{in\theta},$$

where f_n is the continuous Fourier coefficient of the function $f(\mathbf{a}(\theta))$,

$$f_n = \frac{1}{2\pi} \int_{-\pi}^{\pi} f(\mathbf{a}(\theta)) e^{-in\theta} d\theta,$$

and $H_n^{(1)}(z)$ is the n -th Hankel function of the first kind.

The boundary bilinear form $b(u, v)$ of Steklov type corresponding to the problem (E_f) is given by the following formula:

$$b(u, v) = 2\pi \sum_{n=-\infty}^{\infty} \mu_n |f_n \bar{g}_n|,$$

where for $n = 0, 1, 2, \dots$

$$\mu_n = k \frac{\dot{H}_n^{(1)}(ka)}{H_n^{(1)}(ka)}, \quad \dot{H}_n^{(1)}(z) = \frac{d}{dz} H_n^{(1)}(z).$$

7. FSM approximate problem for the reduced wave problem in the outside of an open disc

Fix a positive number ρ so as to satisfy $0 < \rho < a$. For a fixed positive integer N , set the points $\bar{\rho}_j, \mathbf{a}_j, 0 \leq j \leq N-1$, as the equi-distant equally phased arrangement of source points and collocation points defined in Section 2.

An FSM, (fundamental solution method), approximate problem $(E_f^{(N)})$ of the problem (E_f) is defined through the following :

$$(E_f^{(N)}) \quad \begin{cases} u^{(N)}(\mathbf{r}) = \sum_{j=0}^{N-1} q_j G_j(\mathbf{r}), \\ u^{(N)}(\mathbf{a}_j) = f(\mathbf{a}_j), \quad 0 \leq j \leq N-1. \end{cases}$$

We use basis functions $G_j(\mathbf{r})$ in this problem represented as follows with the use of the constant multiple of the fundamental solution of Helmholtz equation, $H_0^{(1)}(kr)$,

$$G_j(\mathbf{r}) = H_0^{(1)}(k|r - \rho e^{-i\theta_j}|), \quad 0 \leq j \leq N-1.$$

8. FSM approximate form for the boundary bilinear form of Steklov type

Setting

$$g(\theta) = H_0^{(1)}(k|ae^{i\theta} - \rho|),$$

we define for $l \in \mathbb{Z}$,

$$g_l = g(\theta_l).$$

The two-sided infinite sequence $\{g_l : l = 0, \pm 1, \pm 2, \dots\}$ has the period N . Further it is symmetric with respect to $N/2$. A **wave transmission vector** $\mathbf{g} \in \mathbb{R}^N$ is defined through

$$\mathbf{g} = (g_l)_{0 \leq l \leq N-1}.$$

And a **wave transmission matrix** G is defined through

$$G = (g_{jk})_{0 \leq j, k \leq N-1},$$

$$g_{jk} = g_{k-j}, \quad 0 \leq j, k \leq N-1.$$

It is to be noted that the matrix G is a complex valued symmetric cyclic square matrix of order N , which is not hermitian symmetric. Namely we have

$$g_{jk} = g_{kj}, \quad 0 \leq j, k \leq N-1.$$

Noticing the collocation condition:

$$\sum_{k=0}^{N-1} G_k(\mathbf{a}_j) q_k = f(\mathbf{a}_j),$$

and the following identities:

$$\begin{aligned} G_k(\mathbf{a}_j) &= H_0^{(1)}(k|ae^{i\theta_j} - \rho e^{i\theta_k}|) \\ &= H_0^{(1)}(k|e^{i\theta_j} - \gamma e^{i\theta_k}|) \\ &= H_0^{(1)}(k|e^{i\theta_{j-k}} - \gamma|) \\ &= g(\theta_{j-k}) \\ &= g_{kj} \\ &= g_{jk}, \end{aligned}$$

we see that the problem $(E_f^{(N)})$ is represented as

$$(E) \quad G\mathbf{q} = \mathbf{f},$$

where \mathbf{q} and \mathbf{f} are defined as follows.

$$\mathbf{q} = \begin{pmatrix} q_0 \\ q_1 \\ \vdots \\ q_{N-1} \end{pmatrix}, \quad \mathbf{f} = \begin{pmatrix} f(\mathbf{a}_0) \\ f(\mathbf{a}_1) \\ \vdots \\ f(\mathbf{a}_{N-1}) \end{pmatrix}.$$

Denote eigenvalues of the matrix G by λ_j , $0 \leq j \leq N-1$. Then we have the following representation:

$$\lambda_j = \sum_{l=0}^{N-1} g_l \omega^{jl}, \quad 0 \leq j \leq N-1,$$

where

$$\omega = e^{i\theta_1}, \quad \theta_1 = \frac{2\pi}{N}.$$

The eigenvector $\vec{\varphi}_j$ of G corresponding to the eigenvalue λ_j with the unit length is given by

$$\vec{\varphi}_j = \frac{1}{\sqrt{N}} (\omega^{jk})_{0 \leq k \leq N-1}.$$

The set of N vectors $\{\vec{\varphi}_j, 0 \leq j \leq N-1\}$ forms an orthogonal system of basis of \mathbb{C}^N . All the eigenvalues of G differ from zero if and only if the matrix G is regular. Therefore the problem $(E_f^{(N)})$ is uniquely solvable if and only if the following condition holds good:

$$(8) \quad \lambda_j \neq 0, \quad 0 \leq j \leq N-1.$$

Hereafter the unique solvability condition (8) is assumed.

The FSM approximate form for $b(u, v)$ of the first type, which is denoted by $b^{(N)}(u, v)$, is represented through the following formula (9):

$$(9) \quad b^{(N)}(u, v) = - \int_{\Gamma_a} \frac{\partial u^{(N)}}{\partial r} \overline{v^{(N)}} d\Gamma,$$

where $u^{(N)}(\mathbf{r})$, and $v^{(N)}(\mathbf{r})$, are FSM-approximate solutions for $u(\mathbf{r})$, and $v(\mathbf{r})$, satisfying (E_f) with $f = u(\mathbf{a}(\theta))$, and (E_f) with $f = v(\mathbf{a}(\theta))$, respectively. Namely $u^{(N)}(\mathbf{r})$ is determined through the problem $(E_f^{(N)})$ with $f = u(\mathbf{a}(\theta))$. In the right hand side of (9), $\overline{v^{(N)}}$ is the complex conjugate of $v^{(N)}(\mathbf{r})$.

The FSM approximate form for $b(u, v)$ of the second type, which is denoted by $\bar{b}^{(N)}(u, v)$, is represented through the following formula (10):

$$(10) \quad \bar{b}^{(N)}(u, v) = - \frac{2\pi a}{N} \sum_{j=0}^{N-1} \frac{\partial u^{(N)}(\mathbf{a}_j)}{\partial r} \overline{v^{(N)}(\mathbf{a}_j)},$$

which is the quadrature formula for $b^{(N)}(u, v)$ with the use of trapezoidal rule.

Let H_j be the radial derivative towards the coordinate origin of the function $G_j(\mathbf{r})$ of the variable \mathbf{r} . Namely

$$H_j(\mathbf{r}) = -\frac{\partial}{\partial r} G_j(\mathbf{r}), \quad 0 \leq j \leq N-1.$$

We define for $l \in \mathbb{Z}$,

$$h_l = H_0(\mathbf{a}_l).$$

The two-sided infinite sequence $\{h_l : l = 0, \pm 1, \pm 2, \dots\}$ has the period N . Further it is symmetric with respect to $N/2$. A **wave derivative vector** $\mathbf{h} \in \mathbb{R}^N$ is defined through

$$\mathbf{h} = (h_l)_{0 \leq l \leq N-1}.$$

And a **wave derivative matrix** H is defined through

$$H = (h_{jk})_{0 \leq j, k \leq N-1},$$

$$h_{jk} = h_{k-j}, \quad 0 \leq j, k \leq N-1.$$

The matrix H is a complex valued symmetric cyclic square matrix of order N .

Consider the value of the exterior normal derivative on the boundary Γ_a with respect to the exterior domain Ω_e of the solution $u^{(N)}(\mathbf{r})$ of the problem $(E_r^{(N)})$. The value at the point $\mathbf{r} = \mathbf{a}_j$ is the j -th component of the vector $H\mathbf{q}$. Namely, using \mathbf{q} of the problem (E) in this Section, we have

$$\left(\frac{\partial u^{(N)}}{\partial n_e}(\mathbf{a}_j) \right)_{0 \leq j \leq N-1} = H\mathbf{q}.$$

Now a matrix representation of FSM approximate boundary bilinear form $\bar{b}^{(N)}(u, v)$ can be given in the following Theorem 5.

Theorem 5 *Let the function $h(\theta)$ be defined through the following formula:*

$$h(\theta) = -k \cdot \frac{a - \rho \cos \theta}{|ae^{i\theta} - \rho|} \cdot H_1^{(1)}(k|ae^{-i\theta} - \rho|).$$

For integers $j = 0, 1, \dots, N-1$, setting

$$h_j = h(\theta_j), \quad h_j^{(N)} = \frac{1}{N} \sum_{k=0}^{N-1} h_k \omega^{-jk},$$

let

$$\mathbf{h} = (h_j)_{0 \leq j \leq N-1}.$$

Supposing the unique-solvability condition:

$$\lambda_j \neq 0, \quad 0 \leq j \leq N-1,$$

put

$$\mathbf{c} = G^{-1}\mathbf{h} = (c_j)_{0 \leq j \leq N-1}.$$

Defining the value of c_j for any integer j so as that the sequence $c_j : j = 0, \pm 1, \pm 2, \dots$ may have the period N , set

$$b_{jk} = \frac{2\pi a}{N} c_{k-j}, \quad 0 \leq j, k \leq N-1.$$

Then we have

$$\bar{b}^{(N)}(u, v) = (B\mathbf{u}, \mathbf{v}), \quad B = (b_{jk})_{0 \leq j, k \leq N-1},$$

where

$$\mathbf{u} = (u(\mathbf{a}(\theta_j)))_{0 \leq j \leq N-1}, \quad \mathbf{v} = (v(\mathbf{a}(\theta_j)))_{0 \leq j \leq N-1}.$$

In Theorem 5, $(B\mathbf{u}, \mathbf{v})$ is the usual inner product in \mathbb{C}^N .

It is to be noted that the following representations hold.

$$c_j = \sum_{l=0}^{N-1} \frac{1}{\lambda_l} h_l^{(N)} \omega^{jl}, \quad 0 \leq j \leq N-1.$$

$$b_{jk} = \frac{2\pi a}{N} \sum_{l=0}^{N-1} \frac{1}{\lambda_l} h_l^{(N)} \omega^{(k-j)l}, \quad 0 \leq j, k \leq N-1.$$

The eigenvalue of the matrix B is given by the following formula for an integer l with $0 \leq l \leq N-1$,

$$\mu_l^{(N)} = \frac{1}{N} \sum_{j=0}^{N-1} \omega^{jl} \left\{ \sum_{m=0}^{N-1} \frac{\omega^{jm}}{\lambda_m} \left(\sum_{n=0}^{N-1} h_n \omega^{-nl} \right) \right\},$$

with the corresponding eigenvector $\vec{\varphi}_l$.

The following formula holds good as a spectral representation of the FSM approximate boundary bilinear form $\bar{b}(u, v)$.

$$\bar{b}^{(N)}(u, v) = 2\pi \sum_{n \in \mathbb{N}_0} \mu_{|n|}^{(N)} f_n^{(N)} \overline{g_n^{(N)}},$$

where $f_n^{(N)}$, and $g_n^{(N)}$, are the discrete Fourier coefficients of the function $f(\theta) = u(\mathbf{a}(\theta))$, and $f(\theta) = v(\mathbf{a}(\theta))$, respectively.

9. FEM-FSM combined method for the reduced wave problem in the exterior of a general scattering body

Fix a simply connected bounded domain \mathcal{O} in the plane. Assume that the boundary \mathcal{C} of \mathcal{O} is sufficiently smooth. The exterior domain of \mathcal{C} is denoted by Ω . Let g be a function representing the plane wave with the wave number vector (l, m) . More precisely, set

$$g(x, y) = e^{i(lx + my)}, \quad l^2 + m^2 = k^2.$$

Consider the following reduced wave problem (E).

$$(E) \quad \begin{cases} -\Delta u - k^2 u = 0 & \text{in } \Omega, \\ u + g = 0 & \text{on } \mathcal{C}, \\ \lim_{r \rightarrow \infty} \sqrt{r} \left\{ \frac{\partial u}{\partial r} - iku \right\} = 0. \end{cases}$$

As in the case of Poisson equation in Section 5, the intersection of the domain Ω and the disc D_a is said to be the interior domain, denoted by Ω_i .

For complex valued functions $u, v \in H^1(\Omega_i)$, consider the Dirichlet inner product $a(u, v)$:

$$a(u, v) = \int_{\Omega_i} \text{grad} u \text{ grad} \bar{v} \, d\Omega,$$

where \bar{v} represents the complex conjugate of v . Further L^2 inner product for $u, v \in L^2(\Omega_i)$ is denoted by $m(u, v)$:

$$m(u, v) = \int_{\Omega_i} u \bar{v} \, d\Omega.$$

Since the trace $\gamma_a v$ on Γ_a is an element of $H^{1/2}(\Gamma_a)$ for any $v \in H^1(\Omega_i)$, we can see the boundary bilinear form of Steklov type $b(u, v)$ is well defined for $u, v \in H^1(\Omega_i)$ (See, for example, Zebic[5]). Therefore we can define a continuous bilinear form:

$$t(u, v) = a(u, v) - k^2 m(u, v) + b(u, v)$$

for $u, v \in H^1(\Omega_i)$. Hereafter, denoting the function space $H^1(\Omega_i)$ by W , let

$$V = \{v \in W : v = 0 \text{ on } \mathcal{C}\}.$$

With these notations, the following weak formulation problem (II) is defined.

$$(II) \quad \begin{cases} t(u, v) = 0, & v \in V, \\ u + g = 0 & \text{on } \mathcal{C}, \\ u \in W. \end{cases}$$

Admitting the equivalence between the equation (E) and the problem (II), we consider the problem (II) and its approximate ones hereafter.

Fix a positive number ρ so as to satisfy $0 < \rho < a$. For a fixed positive integer N , set the points $\tilde{\rho}_j, \mathbf{a}_j, 0 \leq j \leq N-1$, as in the equi-distant equally phased arrangement of source points and collocation points defined in Section 2.

A family of finite dimensional subspaces of W ,

$$\{W_N : N = N_0, N_0 + 1, \dots\},$$

is supposed to have the following properties:

$$(W_N - 1) \quad W_N \subset C(\bar{\Omega}_i).$$

$$(W_N - 2) \quad \begin{cases} \text{For any } v \in W_N, v(\mathbf{a}(\theta)) \text{ is an equi-distant} \\ \text{piecewise linear continuous } 2\pi\text{-periodic} \\ \text{function with respect to } \theta. \end{cases}$$

Define an approximate space V_N of V through

$$V_N = W_N \cap V.$$

For $u, v \in H^1(\Omega_i) \cap C(\bar{\Omega}_i)$, set

$$\tilde{t}^{(N)}(u, v) = a(u, v) - k^2 m(u, v) + \tilde{b}^{(N)}(u, v).$$

Fix an element g_N of W_N which coincides with g at the nodal points on the interior boundary \mathcal{C} .

Now we can set the following approximate problem $(\bar{\Pi}^{(N)})$.

$$(\bar{\Pi}^{(N)}) \quad \begin{cases} \tilde{t}^{(N)}(\bar{u}_N, v) = 0, & v \in V_N, \\ \bar{u}_N + g_N = 0 & \text{on } \mathcal{C}, \\ \bar{u}_N \in W_N. \end{cases}$$

Thus we have formulated an FEM-FSM combined method for the reduced wave problem in the exterior of a general scattering body.

10. Spectral representation of the wave transmission matrix G

Now the author is trying to find answers of the following problems.

Unique solvability of the problem $(\bar{\Pi}^{(N)})$.

Convergence of its solution \bar{u}_N to the genuine solution u .

Estimate of the difference between \bar{u}_N and u .

The following is a preliminary consideration for the first problem.

Applying Graf's addition theorem ([4] pp.359-361) for the 0-th order Hankel function of the first kind

to the present basis functions $G_j, 0 \leq j \leq N-1$, we obtain an analytical representation for the eigenvalues of the matrix G . Namely we have the following Theorem 6.

Theorem 6 Define $\lambda_j, 0 \leq j \leq N-1$, as follows.

$$\lambda_j = N \left(\sum_{r=-\infty}^{\infty} J_{j+N_r}(\kappa) J_{j+N_r}(\gamma\kappa) + i \sum_{r=-\infty}^{\infty} N_{j+N_r}(\kappa) J_{j+N_r}(\gamma\kappa) \right),$$

where $J_n(z)$, and $N_n(z)$, are the n -th order Bessel, and Neumann, functions, respectively, and

$$\kappa = ka, \quad \gamma = \frac{\rho}{a}.$$

Then $\lambda_j, 0 \leq j \leq N-1$, are the eigenvalues of the wave transmission matrix G . The eigenvector $\vec{\varphi}_j$ with the unit length corresponding to the eigenvalue λ_j is represented as

$$\vec{\varphi}_j = \frac{1}{\sqrt{N}} (\omega^{jk})_{0 \leq k \leq N-1}.$$

From the above representation for the eigenvalues of the matrix G , we have

$$\operatorname{Re} \lambda_j = N \times \sum_{r=-\infty}^{\infty} J_{j+N_r}(\kappa) J_{j+N_r}(\gamma\kappa).$$

The right hand side of the above equality with $\gamma = 1$ yields

$$N \times \sum_{r=-\infty}^{\infty} \{J_{j+N_r}(\kappa)\}^2 > 0.$$

Hence, for the fixed N , tending γ sufficiently near to 1, we have that all the eigenvalues $\lambda_j, 0 \leq j \leq N-1$, differ from zero, and that the wave transmission matrix G is regular. The regularity of G would likely hold good in more general setting. Under the assumption of the regularity of G , we have the representation formula for the solution of FSM approximate problem $(E_f^{(N)})$ for the reduced wave problem in the outside of an open disc in the following Theorem 7.

Theorem 7 Assume the unique solvability condition:

$$\lambda_j \neq 0, \quad 0 \leq j \leq N-1.$$

Then the solution $u^{(N)}(\mathbf{r})$ of the problem $(E_f^{(N)})$ is represented as follows.

$$u^{(N)}(\mathbf{r}) = \sum_{j=0}^{N-1} f_j^{(N)} \frac{\varphi_j^{(N)}(\mathbf{r})}{\varphi_j^{(N)}(\mathbf{a}_0)},$$

where $f_j^{(N)}, 0 \leq j \leq N-1$, are the discrete Fourier coefficients of the function $f(\theta) = u(\mathbf{a}(\theta))$, and

$$\varphi_j^{(N)}(\mathbf{r}) = N \sum_{r=-\infty}^{\infty} H_{j+N_r}^{(1)}(\delta\kappa) J_{j+N_r}(\gamma\kappa) e^{i(j+N_r)},$$

$$0 \leq j \leq N-1$$

with

$$\delta = \frac{r}{a}.$$

It is to be noted that the eigenvalues λ_j of the transmission matrix G is represented as

$$\lambda_j = \varphi_j^{(N)}(\mathbf{a}_0), \quad 0 \leq j \leq N-1.$$

References

- [1] Katsurada, M. and Okamoto, H., A mathematical study of the charge simulation method I, J. Fac. Sci. Univ. Tokyo, Sect. IA, Math, Vol. 35, pp. 507-518 (1988).
- [2] Ushijima, T., Some remarks on CSM approximate solutions of bounded harmonic function in a domain exterior to a circle, in Japanese, Abstract of 1998 Annual Meeting of Japan Society for Industrial and Applied Mathematics, pp. 60-61 (1998.9.12).
- [3] Ushijima, T., An FEM-CSM combined method for 2D exterior Laplace problems, in Japanese, Abstract of Applied Mathematics Branch in Fall Joint Meeting of Mathematical Society of Japan, pp.126-129 (1998.10.3).
- [4] Watson, G. N., A Treatise on the Theory of Bessel Functions, Second Edition, Cambridge at the University Press, 1966.
- [5] Zebic, A., Equation de Helmholtz: Étude numérique de quelques préconditionnements pour la methode GMRES, Rapport de Recherche de INRIA, Numéro 1802, Décembre 1992.
- [6] Zlámal, M., Curved elements in the finite element method. I, SIAM J. Numer. Anal. Vol. 10, pp. 229-240 (1973).

Publication List of NIFS-PROC Series

- NIFS-PROC-1 *"U.S.-Japan on Comparison of Theoretical and Experimental Transport in Toroidal Systems Oct. 23-27, 1989", Mar. 1990*
- NIFS-PROC-2 *"Structures in Confined Plasmas –Proceedings of Workshop of US-Japan Joint Institute for Fusion Theory Program–"; Mar. 1990*
- NIFS-PROC-3 *"Proceedings of the First International Toki Conference on Plasma Physics and Controlled Nuclear Fusion –Next Generation Experiments in Helical Systems– Dec. 4-7, 1989" Mar. 1990*
- NIFS-PROC-4 *"Plasma Spectroscopy and Atomic Processes –Proceedings of the Workshop at Data & Planning Center in NIFS–"; Sep. 1990*
- NIFS-PROC-5 *"Symposium on Development of Intensified Pulsed Particle Beams and Its Applications February 20 1990"; Oct. 1990*
- NIFS-PROC-6 *"Proceedings of the Second International TOKI Conference on Plasma Physics and Controlled Nuclear Fusion , Nonlinear Phenomena in Fusion Plasmas -Theory and Computer Simulation-"; Apr. 1991*
- NIFS-PROC-7 *"Proceedings of Workshop on Emissions from Heavy Current Carrying High Density Plasma and Diagnostics"; May 1991*
- NIFS-PROC-8 *"Symposium on Development and Applications of Intense Pulsed Particle Beams, December 6 - 7, 1990"; June 1991*
- NIFS-PROC-9 *"X-ray Radiation from Hot Dense Plasmas and Atomic Processes"; Oct. 1991*
- NIFS-PROC-10 *"U.S.-Japan Workshop on "RF Heating and Current Drive in Confinement Systems Tokamaks" Nov. 18-21, 1991, Jan. 1992*
- NIFS-PROC-11 *"Plasma-Based and Novel Accelerators (Proceedings of Workshop on Plasma-Based and Novel Accelerators) Nagoya, Japan, Dec. 1991"; May 1992*
- NIFS-PROC-12 *"Proceedings of Japan-U.S. Workshop P-196 on High Heat Flux Components and Plasma Surface Interactions for Next Devices"; Mar. 1993*
- NIFS-PROC-13 **【NIFS シンポジウム**
 「核燃焼プラズマの研究を考えるー現状と今後の取り組み方」
 1992年7月15日、核融合科学研究所」1993年7月
*NIFS Symposium "Toward the Research of Fusion Burning Plasmas -Present Status and Future strategy-"
 ", 1992 July 15, National Institute for Fusion Science"; July 1993 (in Japanese)*
- NIFS-PROC-14 *"Physics and Application of High Density Z-pinches", July 1993*
- NIFS-PROC-15 岡本正雄、講義「プラズマ物理の基礎」
 平成5年度 総合大学院大学1994年2月
 M. Okamoto,
 "Lecture Note on the Bases of Plasma Physics" Graduate University for Advanced Studies Feb. 1994
 (in Japanese)
- NIFS-PROC-16 代表者 河合良信
 平成5年度 核融合科学研究所共同研究
 研究会報告書「プラズマ中のカオス現象」
 *"Interdisciplinary Graduate School of Engineering Sciences" Report of the meeting on Chaotic Phenomena
 in Plasma Apr. 1994 (in Japanese)*
- NIFS-PROC-17 平成5年度 NIFS シンポジウム 報告書
 「核融合炉開発研究のアセスメント」平成5年11月29日-30日 於 核融合科学研究所
 *"Assessment of Fusion Reactor Development" Proceedings of NIFS Symposium held on November 29-30,
 1993 at National Institute for Fusion Science" Apr. 1994 (in Japanese)*
- NIFS-PROC-18 *"Physics of High Energy Density Plasmas Produced by Pulsed Power" June 1994*
- NIFS-PROC-19 K. Morita, N. Noda (Ed.),

** Proceedings of 2nd International Workshop on Tritium Effects in Plasma Facing Components at Nagoya University, Symposion Hall, May 19-20, 1994", Aug. 1994*

- NIFS-PROC-20 研究代表者 阿部 勝憲 (東北大学・工学部)
所内世話人 野田信明
平成 6 年度 核融合科学研究所共同研究 [研究会] 「金属系高熱流束材料の開発と評価」成果報告書
K. Abe and N. Noda (Eds.),
"Research and Development of Metallic Materials for Plasma Facing and High Heat Flux Components"
Nov. 1994 (in Japanese)
- NIFS-PROC-21 世話人: 森田 健治 (名大工学部)、金子 敏明 (岡山理科大学理学部)
「境界プラズマと炉壁との相互作用に関する基礎過程の研究」研究会報告
K. Morita (Nagoya Univ.), T. Kaneko (Okayama Univ. Science) (Eds.)
"NIFS Joint Meeting "Plasma-Divertor Interactions" and "Fundamentals of Boundary Plasma-Wall Interactions" January 6-7, 1995 National Institute for Fusion Science" Mar. 1995 (in Japanese)
- NIFS-PROC-22 代表者 河合 良信
プラズマ中のカオス現象
Y. Kawai,
"Report of the Meeting on Chaotic Phenomena in Plasma, 1994" Apr. 1995 (in Japanese)
- NIFS-PROC-23 K. Yatsui (Ed.),
"New Applications of Pulsed, High-Energy Density Plasmas"; June 1995
- NIFS-PROC-24 T. Kuroda and M. Sasao (Eds.),
"Proceedings of the Symposium on Negative Ion Sources and Their Applications, NIFS, Dec. 26-27, 1994",
Aug. 1995
- NIFS-PROC-25 岡本 正雄
新古典輸送概論 (講義録)
M. Okamoto,
"An Introduction to the Neoclassical Transport Theory" (Lecture note), Nov. 1995 (in Japanese)
- NIFS-PROC-26 Shozo Ishii (Ed.),
"Physics, Diagnostics, and Application of Pulsed High Energy Density Plasma as an Extreme State";
May 1996
- NIFS-PROC-27 代表者 河合 良信
プラズマ中のカオスとその周辺非線形現象
Y. Kawai,
"Report of the Meeting on Chaotic Phenomena in Plasmas and Beyond, 1995", Sep. 1996 (in Japanese)
- NIFS-PROC-28 T. Mito (Ed.),
"Proceedings of the Symposium on Cryogenic Systems for Large Scale Superconducting Applications", Sep.
1996
- NIFS-PROC-29 岡本 正雄
講義「核融合プラズマ物理の基礎 - I」
平成 8 年度 総合研究大学院大学 数物科学研究科 核融合科学専攻 1996年 10月
M. Okamoto
"Lecture Note on the Fundamentals of Fusion Plasma Physics - I" Graduate University for Advanced Studies; Oct. 1996 (in Japanese)
- NIFS-PROC-30 研究代表者 栗下 裕明 (東北大学金属材料研究所)
所内世話人 加藤 雄大
平成 8 年度核融合科学研究所共同研究「被損傷材料の微小体積強度評価法の高度化」研究会 1996年 10月 9日 於: 核融合科学研究所
H. Kurishita and Y. Katoh (Eds.)
NIFS Workshop on Application of Micro-Indentation Technique to Evaluation of Mechanical Properties of Fusion Materials, Oct. 9, 1996, NIFS; Nov. 1996 (in Japanese)
- NIFS-PROC-31 岡本 正雄
講義「核融合プラズマ物理の基礎 - II」
平成 8 年度 総合研究大学院大学 数物科学研究科 核融合科学専攻 1997年 4月
M. Okamoto
"Lecture Note on the Fundamentals of Fusion Plasma Physics - II" Graduate University for Advanced

Studies; Apr. 1997 (in Japanese)

- NIFS-PROC-32 代表者 河合 良信
平成8年度 核融合科学研究所共同研究 研究会報告「プラズマ中のカオスとその周辺非線形現象」
Y. Kawai (Ed)
Report of the Meeting on Chaotic Phenomena in Plasmas and Beyond, 1996; Apr. 1997 (mainly in Japanese)
- NIFS-PROC-33 H. Sanuki,
Studies on Wave Analysis and Electric Field in Plasmas; July 1997
- NIFS-PROC-34 プラズマ対向機器・PSI・熱・粒子制御合同研究会報告
平成9年6月27日(金)9:00~16:20 核融合科学研究所・管理棟4F第1会議室
1997年10月
T. Yamashina (Hokkaido University)
Plasma Facing Components, PSI and Heat/Particle Control June 27, 1997, National Institute for Fusion Science T. Yamashina (Hokkaido University); Oct. 1997 (in Japanese)
- NIFS-PROC-35 T. Watari,
Plasma Heating and Current Drive; Oct. 1997
- NIFS-PROC-36 T. Miyamoto and K. Takasugi (Eds.)
Production and Physics of High Energy Density Plasma; Production and Physics of High Energy Density Plasma; Oct. 1997
- NIFS-PROC-37 (Eds.) T. Fujimoto, P. Beiersdorfer,
Proceedings of the Japan-US Workshop on Plasma Polarization Spectroscopy and The International Seminar on Plasma Polarization Spectroscopy January 26-28, 1998, Kyoto; June 1998
- NIFS-PROC-38 (Eds.) Y. Tomita, Y. Nakamura and T. Hayashi,
Proceedings of the Second Asian Pacific Plasma Theory Conference APPTC '97, January 26-28, 1998, Kyoto; Aug. 1998
- NIFS-PROC-39 (Ed.) K. Hirano,
Production, Diagnostics and Application of High Energy Density Plasmas; Dec. 1998
- NIFS-PROC-40 研究代表者 加古 孝(電気通信大学)
所内世話人 渡辺 二太
平成10年度核融合科学研究所共同研究 研究会「プラズマ閉じ込めに関連する数値計算手法の研究」
Ed. by T. Kako and T. Watanabe
Proceeding of 1998-Workshop on MHD Computations "Study on Numerical Methods Related to Plasma Confinement Apr. 1999
- NIFS-PROC-41 (Eds.) S. Goto and S. Yoshimura,
Proceedings of The US-Japan Workshop and The Satellite Meeting of ITC-9 on Physics of High Beta Plasma Confinement in Innovative Fusion System, Dec. 14-15, 1998, NIFS, Toki; Apr. 1999
- NIFS-PROC-42 (Eds.) H. Akiyama and S. Katsuki,
Physics and Applications of High Temperature and Dense Plasmas Produced by Pulsed Power; Aug. 1999
- NIFS-PROC-43 (Ed.) M. Tanaka,
Structure Formation and Function of Gaseous, Biological and Strongly Coupled Plasmas; Sep. 1999
- NIFS-PROC-44 (Ed.) T. Kato and I. Murakami,
Proceedings of the International Seminar on Atomic Processes in Plasmas, July 29-30, 1999, Toki, Japan; Jan. 2000
- NIFS-PROC-45 (Eds.) K. Yatsui and W. Jiang,
Physics and Applications of Extreme Energy-Density State, Nov. 25-26, 1999, NIFS; Mar. 2000
- NIFS-PROC-46 研究代表者 加古 孝(電気通信大学)
所内世話人 渡辺 二太
平成11年度核融合科学研究所共同研究 研究会「プラズマ閉じ込めに関連する数値計算手法の研究」
Ed. by T. Kako and T. Watanabe
Proceeding of 1999-Workshop on MHD Computations "Study on Numerical Methods Related to Plasma Confinement June. 2000